AN EXPERIMENTAL AND NUMERICAL STUDY OF RETROFITTED MASONRY WALLS UNDER CYCLIC LOADING

BY

BASHEER HASAN ALI AL-GOHI

A Dissertation Presented to the
DEANSHIP OF GRADUATE STUDIES

KING FAHD UNIVERSITY OF PETROLEUM & MINERALS

DHAHRAN, SAUDI ARABIA

In Partial Fulfillment of the
Requirements for the Degree of

DOCTOR OF PHILOSOPHY

In

CIVIL ENGINEERING

MAY 2013

KING FAHD UNIVERSITY OF PETROLEUM & MINERALS
DHAHRAN- 31261, SAUDI ARABIA

DEANSHIP OF GRADUATE STUDIES

This thesis, written by **BASHEER HASAN ALI ALGOHI** under the direction his thesis advisor and approved by his thesis committee, has been presented and accepted by the Dean of Graduate Studies, in partial fulfillment of the requirements for the degree of **DOCTOR OF PHILOSOPHY IN CIVIL ENGINEERING.**

Dr. Mohammed H. Baluch
(Advisor)

13 MAY 2013

Dr. Nedal T. Ratrout
Department Chairman

Kalimur Rahman

Dr. Muhammad K. Rahman
(Co-Advisor)

Dr. Salam A. Zummo
Dean of Graduate Studies

Dr. Ali H. Al-Gadhib
(Member)

26/5/13

Date

Dr. Abul Kalam Azad
(Member)

Dr. Alfarabi M. Sharif
(Member)

DEDICATED TO

MY BELOVED PARENTS

AND

MY BROTHERS & SISTERS

AND

MY WIFE AND MY KIDS

ACKNOWLEDGMENTS

First and foremost, I thank Allah (subhana wa taala) for endowing me with health, patience, and knowledge to complete this work.

Acknowledgement is due to the King Fahd University of Petroleum & Minerals for the support given to this research through its excellent facilities and for granting me the opportunity to pursue my graduate studies with financial support.

I acknowledge, with deep gratitude and appreciation, the inspiration, encouragement, valuable time and guidance given to me by Dr. Mohammed Baluch, who served as my major advisor. Thereafter, I am deeply indebted and grateful to Dr. Mohammad K. Rahman, my co-advisor, for his extensive guidance, continuous support, and personal involvement in all phases of this research. I am also grateful to my other committee members, Dr. Ali Al-Gadhib, Dr. Abul Kalam Azad, Dr. Alfarabi M. Sharif for their constructive guidance, valuable advice and cooperation.

I would like to offer my acknowledgement to Dr. Alper Ilki and Dr. Cem Demir from Istanbul Technical University (ITU) who helped and trained me in preparing the experimental set-up and procedure utilized in this study.

I also acknowledge the sincere and untiring efforts of Engr. Imran who assisted me during all stages of my experiments. Thanks and acknowledgment are due to the laboratory technician Eng. Omer for his tremendous help.

Great thanks to Zamil Steel for donating steel frame to conduct the experiment in this study.

Thanks are also due to Simulia - Dassault Systèmes for helping me in ABAQUS simulation software.

I am also indebted to the department chairman, Dr. Nedal T. Ratrout, and to other faculty members for their support.

Thanks are due to my colleagues at the University for their friendship during my graduate studies.

Finally, I would like to express my deepest gratitude to my mother, father, brothers, sisters, my wife, my children, and all other relatives, for their emotional and moral support throughout my academic career and also for their love, patience, encouragement and prayers.

TABLE OF CONTENTS

LIST OF TABLES

LIST OF FIGURES

ABSTRACT

Full Name : [Basheer Hasan Ali Al-Gohi]

Thesis Title : [AN EXPERIMENTAL AND NUMERICAL STUDY OF RETROFITTED MASONRY WALLS UNDER CYCLIC LOADING]

Major Field : [CIVIL & ENVIRONMENTAL ENGINEERING]

Date of Degree : [May-2013]

Masonry wall as a building block of masonry structures has attracted tremendous attention from several research directions. It has been studied extensively for architectural features, structural aspects and properties of materials utilized for construction. Taking the structural point of view, masonry structures have been studied extensively for better understanding of its behavior. One of the greatest motivations for this direction of research is that historical structures represent valuable treasures for the countries culturally and economically. Attempts are being exerted for preserving, maintaining and strengthening historical structures so that they can still be in good conditions for longer periods of time.

In this study, masonry walls made from sandstone and lime mortar that represent a form of heritage structures in Riyadh have been studied experimentally and numerically using elastoplastic-damage model as originally developed by Lubliner et al (1989) and further extended by Lee and Fenves (1998).

In the experimental part, three walls were tested under a combination of axial and lateral loading. Two of the walls were unreinforced masonry walls (URM) and the third wall was reinforced using CFRP.

In the numerical simulation, Finite Element Software ABAQUS was used in the study . The masonry wall was modeled pursuing two different approaches. In the first approach, the masonry blocks and lime mortar layers were modeled as a continuum material using solid elements. In the second approach the masonry block was modeled as a continuum material whereas the lime mortar was modeled as an interface layer. Tests was also conducted on the wall ingredient materials to extract the mechanical properties needed to be included in the numerical simulation.

Numerical simulation using ABAQUS was carried out for walls tested by other researchers as well.

An interesting general behavior of walls was concluded in which almost all walls having an aspect ratio close to one behave in a similar manner and have almost identical interaction relationship between lateral strength and the axial force applied to the wall.

ملخص الرسالة

الاسم الكامل: بشير حسن علي الجوحي

عنوان الرسالة: دراسة معملية وعددية لجدران بنائية مقواه ومعرضة لأحمال دورية.

التخصص: هندسة مدنية

تاريخ الدرجة العلمية: مايو 2013

الجدران البنائية كوحدة بناء انشائية للمباني جذبت الكثير من اهتمام كثير الباحثين. تم دراسة الجدران البنائية من عدة نواحي تشمل النواحي المعمارية، النواحي الانشائية، ونواحي المادة المكونة للمواد البنائية. بأخذ الناحية الإنشائية للجدران البنائية، فقد تم دراسة الجدران البنائية من الناحية الإنشائية بشكل مكثف من اجل الوصول الى معرفة وفهم طريقة تصرف الجدران البنائية عند تعرضها للأحمال. أحد العوامل التي تدفع نحوا البحث في هذا التجاه هو أهمية المباني التاريخية المكونة من الجدران البنائية والتي تشكل كنز مهم للكثير من البلدان حول العالم من الناحية التاريخية والناحية الاقتصادية. هناك محاولات حثيثة من اجل الحفاظ على هذه المباني وأيضا تقويتها وتدعيمها إذا دعت الحاجة بحيث تظل هذه المباني في حالة جيدة لأكبر وأطول فترة ممكنة من الزمن.

في هذه الرسالة، تم عمل تجارب معملية وأيضا دراسة تحليلية عددية لجدران مصنوعة من الحجر الرملي الموجود في منطقة الرياض. الدراسة العددية تمت باستخدام نظرية المرونة واللدونة مقرونة بمستوى الضرر الحاصل في المادة. هذه النظرية تم انشائها وتطويرها في جامعة كاليفورنيا بركلي ومن ثم أدرجت في برنامج أبكس.

في التجارب المعملية تم فحص واختبار ثلاثة جدران بحيث أن كل جدار تم تحميله محوريا ومن ثم جانبيا. اثنين من هذه الجدران كانت بدون أي تقوية (جدران في حالتها الطبيعية) والجدار الثالث تم تقويته بواسطة الياف الكربون.

في الدراسة العددية، تم استخدام طريقة العناصر المتناهية عن طريق برنامج أبكس بحيث تم تحليل الجدران البنائية بهذه الطريقة عن طريق استراتيجيتين: الاستراتيجية الاولي تم اعتمادا فرضية ان كل من الوحدان البنائية ومونة البناء هي مواد متصلة وذلك عن طريق استخدام العناصر الصلبة. في الاستراتيجية الثانية تم فرض الوحدات البنائية مواد متصل بيمنا مونة البناء تم الاستعاضة عنها بطبقات ربط بينية. العديدة من التجارب المخبرية أجريت على المواد المكونة للجدران البنائية من اجل الحصول على خصائص المواد الازم معرفتها من اجل تشغيل التحليلات العددية.

تحليلات عددية أخرى أجريت أيضا على جدران بنائية اختبرت بواسطة باحثين اخرين من اجل الوصول الى صيغة موحده لطريقة تصرف الجدران البنائية عند تحميلها محوريا وجانبيا.

تم الحصول على نتائج رائعة حيث تم الوصول الى معرفة كيفية تصرف الجدران البنائية المعرضة لأحمال محورية وجانبية. تم اكتشاف ان جميع الجدران البنائية والتي لديها نسبة ابعدا تتقرب من واحد، فإنها تتصرف بنفس الطريقة تقريبا عند النظر الى مقاومة الجدران للأحمال الجانية كمعادلة لمقدار الحمل المحوري المسلط على الجدار.

CHAPTER 1

INTRODUCTION

Masonry wall as a building blocks of masonry structures has attracted tremendous attention from several research directions. It has been studied architecturally, mineralogically and structurally. Taking the structural point of view, masonry structures have been studied extensively for better understanding of its behavior. One of the greatest motivations for this direction of research is that historical structures represent valuable treasures for the countries culturally and economically. Attempts are being exerted for preserving, maintaining and strengthening historical structures so that they can still be in good conditions for longer period of time. One of the most hazard that can damage masonry structures are the earthquakes.

1.1 Earthquake Hazard.

Earthquake is a major hazard that some countries worldwide are facing. These earthquakes result in loss in human life and economy. It has been reported that, masonry buildings show high level of damage due to earthquake loading as compared to modern reinforced concrete and steel constructions. This is because of the fact that masonry structures are poorly designed to withstand such loading and also it is the nature of the masonry construction in which the masonry walls are weak to resist seismic movements, especially with the movements that result in out of plane vibrations. Earthquake damage can happen due to direct effect of ground motion as seen in many earthquake events worldwide. A lot of destruction occurs in the infrastructures, residential and commercial structures which in turn results in loss of life and has a major effect on the economy. Fig 1.1 shows a major destruction that happened due to earthquake that hit Haiti in January 2010. A lot of death was reported in this earthquake and economic crisis hit the country. A violence was also reported as a consequence of non-availability of food which added extra complication to the situation.

Earthquake effect can also happen indirectly in a form of tsunamis which can be more dangerous and result is catastrophic destruction. The tsunami which hit Japan in March 2011 is an example of the amount of damage and destruction that can happen as a result of earthquake Fig 1.2.

Figure 1.1 Damaged Buildings in Port-au-Prince, Haiti, after 7.0 Earthquake, January 2010

Figure 1.2 A large Ferry Boat Rests Inland Amidst Destroyed Houses after a 9.0 Earthquake and Subsequent Tsunami Struck Japan in March 2011

1.2 Seismicity of Arabian Peninsula

It is well know that on our planet Earth, there are seven or eight major tectonic plates (depending on how they are defined) and many minor plates. Most of the major earthquakes occur at the plate boundaries due to the movement of the tectonic plates. Fig 1.3 show a depiction of Earth tectonic plates provided by USGS (U.S Geological Survey). Majority of the boundaries of the pates are located in the oceans and seas. Some of these faults is also pesent within the earth land as can be seen in Carrizo Plain, which is one of the easiest places to view surface fractures of the San Andreas Fault, which traverses below the plain (Fig 1.4).

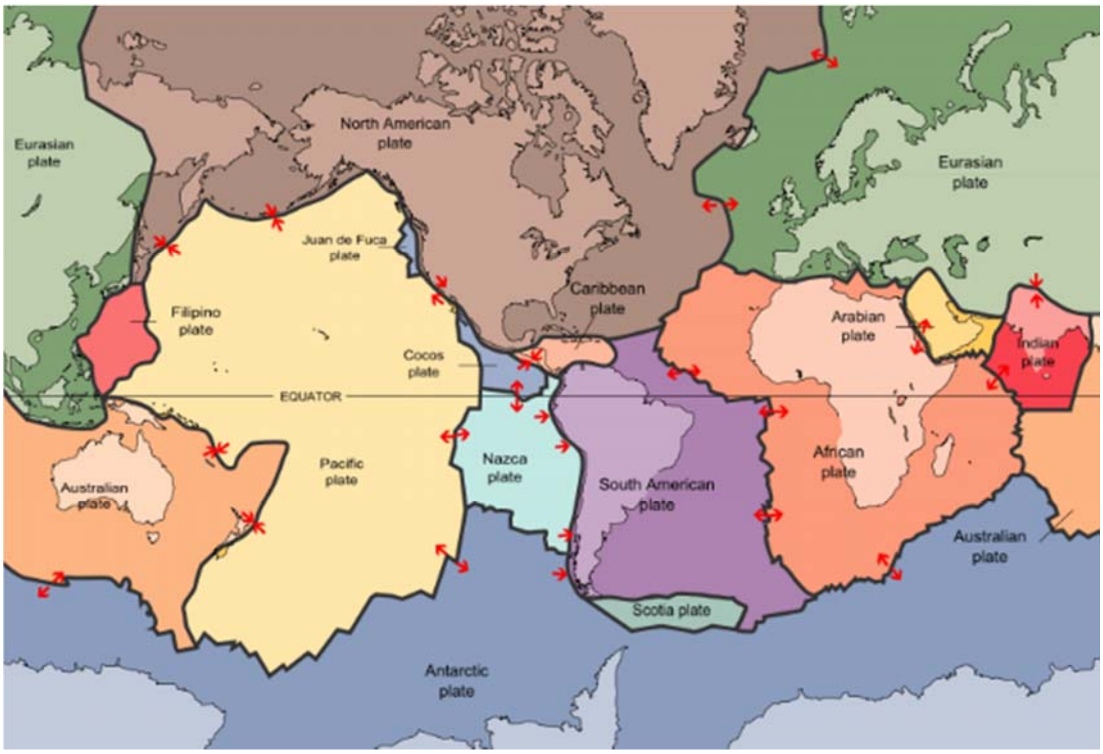

Figure 1.3 The 15 Major Earth Tectonic Plates (USGS)

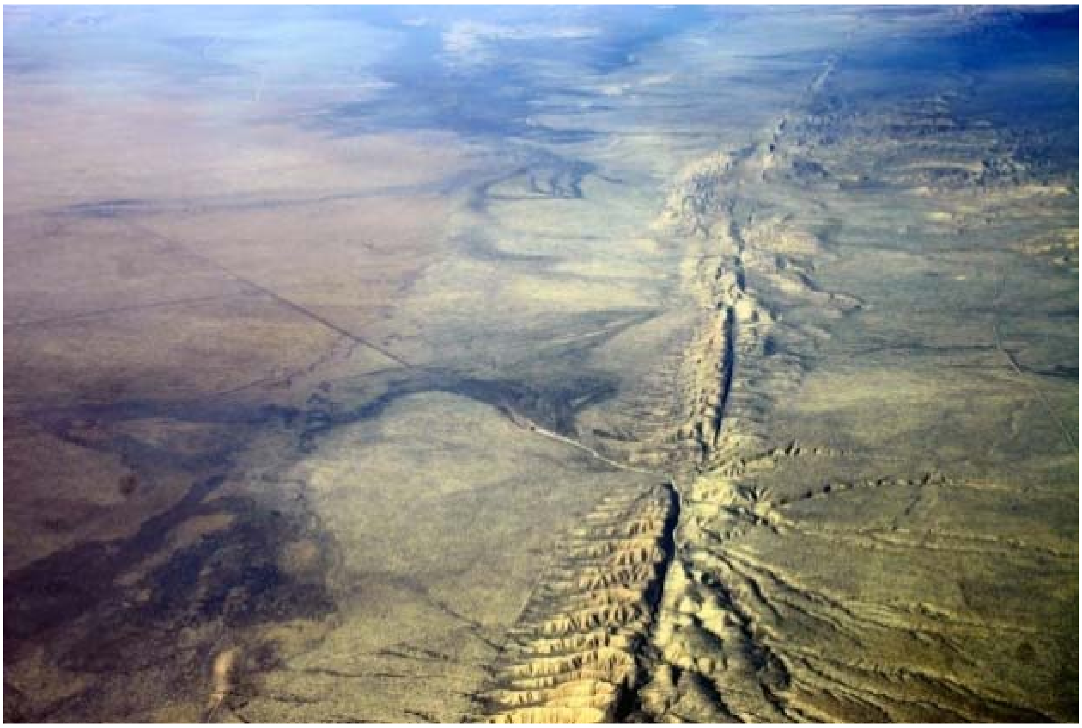

Figure 1.4 Carrizo Plain, Northwest of Los Angeles

It is clear that the Arabian plate is a small plate compare to other plates. The Eastern and northern margins of the Arabian plate consist of the Zagros and Makran Mountains in Iran, and the Taurus Mountains in southern Turkey, and these form a convergent zone where the Arabian plate collides with the Eurasian plate. The Dead Sea transform fault system in the northwestern part of the Arabian plate extends from the northern part of the Red Sea to the Taurus Mountains in southern Turkey, passing through the Gulf of Aqaba and the Dead Sea. The Owen fracture zone on the south-east edge of the Arabian plate extends from the eastern part of the Gulf of Aden to the Makran Mountains. The Arabian plate moves in a northeasterly direction between the Owen fracture zone and the Dead Sea fault with widening of the Red Sea and Gulf of Aden, and collision or subduction with the Makran, Zagros, and Taurus Mountains Figs 1.5 and 1.6.

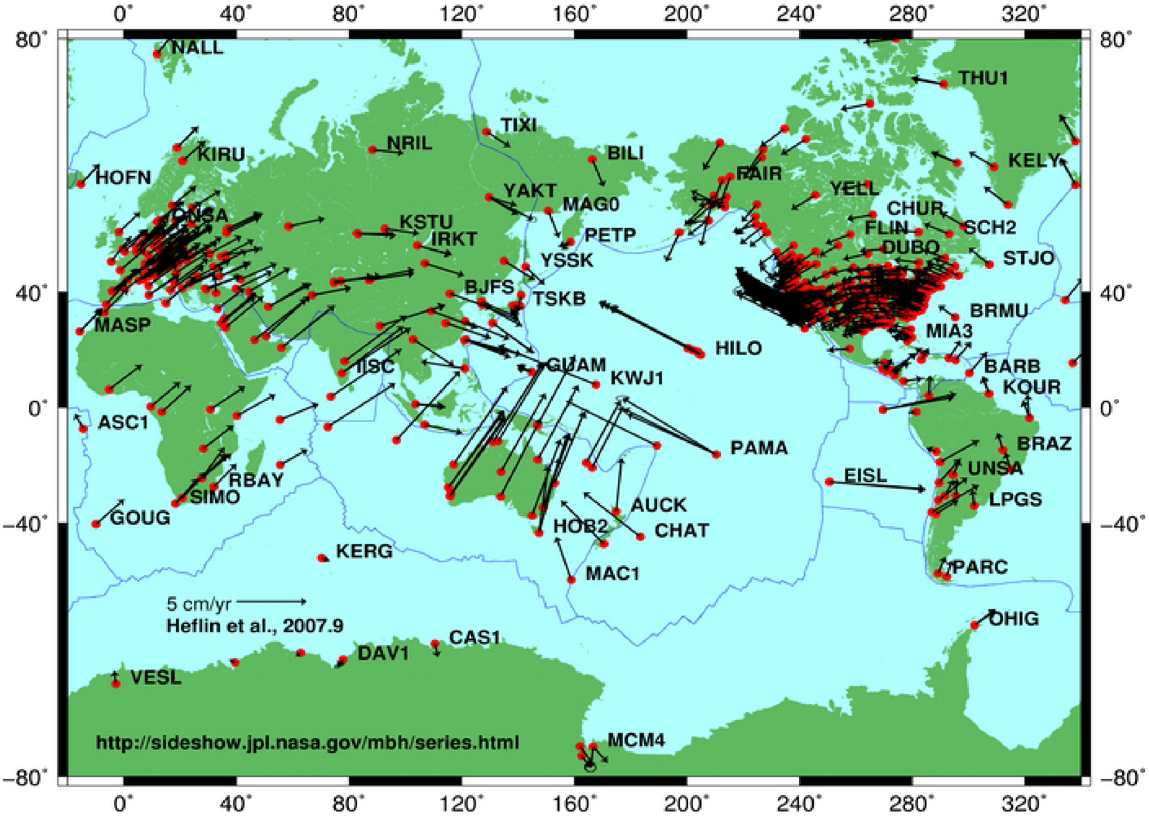

Figure 1.5 Plate Tectonic Movements Measured by GPS Devices (NASA).

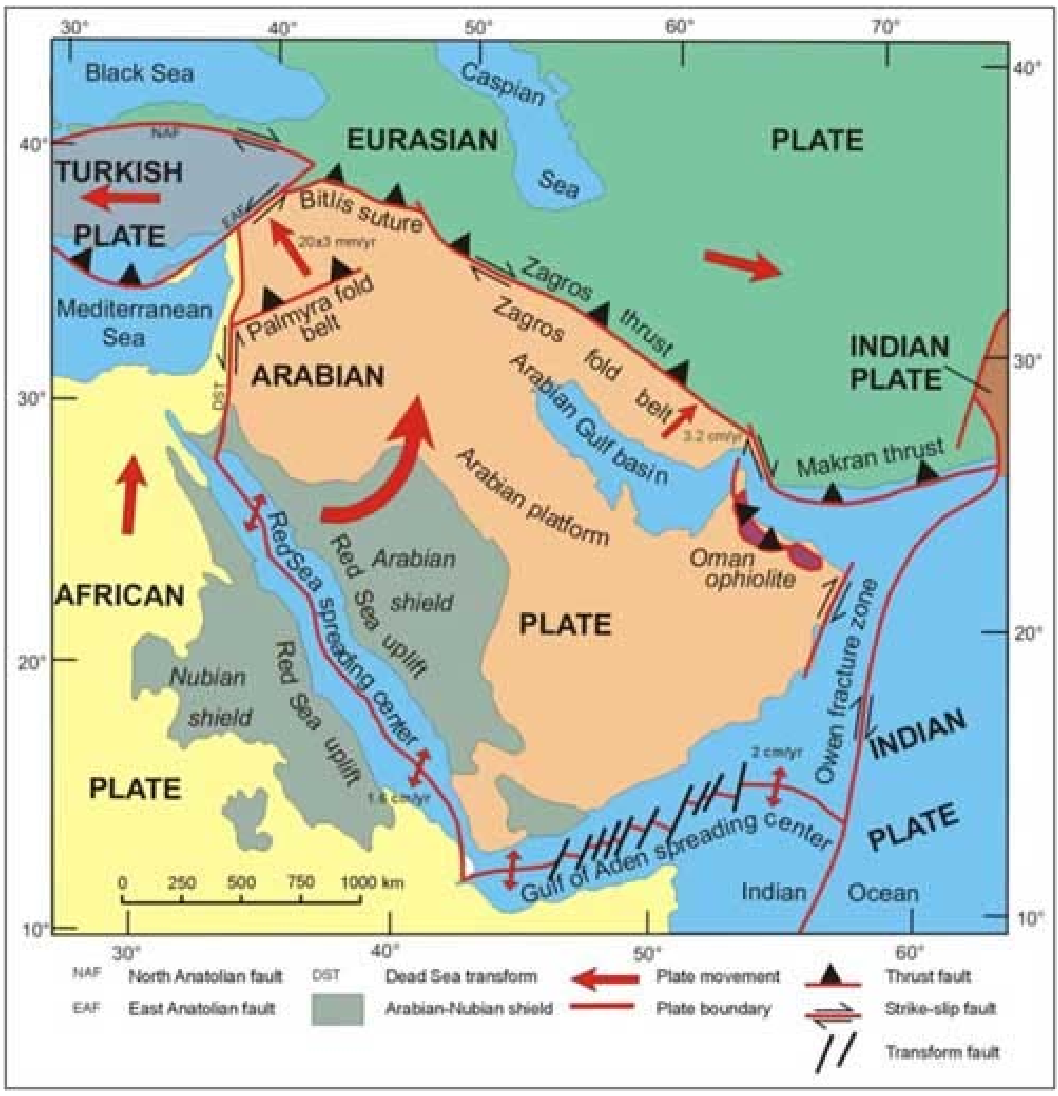

Figure 1.6 Arabian Plate Boundaries and Relative Movements (Johnson 1998)

It has been reported by NASA that 358,214 earthquake events occurred worldwide between 1963 and 1998 (Fig 1.7). In addition, USGS has issued a map for the major earthquake events that occurred worldwide between 1900 and 2010 (Fig 1.8). Among those events, at least 2 major earthquakes happened in Arabian plate. The first one was in Dhamar, North Yemen (near the southern border of Saudi Arabia) which accrued on December 13, 1982 with magnitude of 6.0. It was the first instrumentally recorded earthquake in the Dhamar region. As many as 2,800 people were killed and 1,500 injured. The second major earthquake was in Jordan (near the northern border of Saudi Arabia). It occurred in Gulf of Aqaba (also known as Nuweiba earthquake) on November 22, 1995, at 06:15 local time (04:15 UTC) and registered a magnitude of 7.3 on the Richter scale. The epicenter was located in the central segment of the Gulf of Aqaba (the narrow body of water that separates Egypt's Sinai Peninsula from the western border of Saudi Arabia). At least 8 people were killed and 30 were injured in the meizoseismal area. Saudi Arabia was affected by this earthquake. Two women were reported dead and one person was killed and two were injured slightly at Al Bad and damage was reported there as well as the towns of Al-`Ula and Haql. During several independent field studies, cracks and other ground deformations were observed on both the Egyptian and Saudi Arabian sides of the gulf. A series of cracks were discovered in Saudi Arabia near 28°35' N and 29°05' N during a field survey that was done there in 1996.

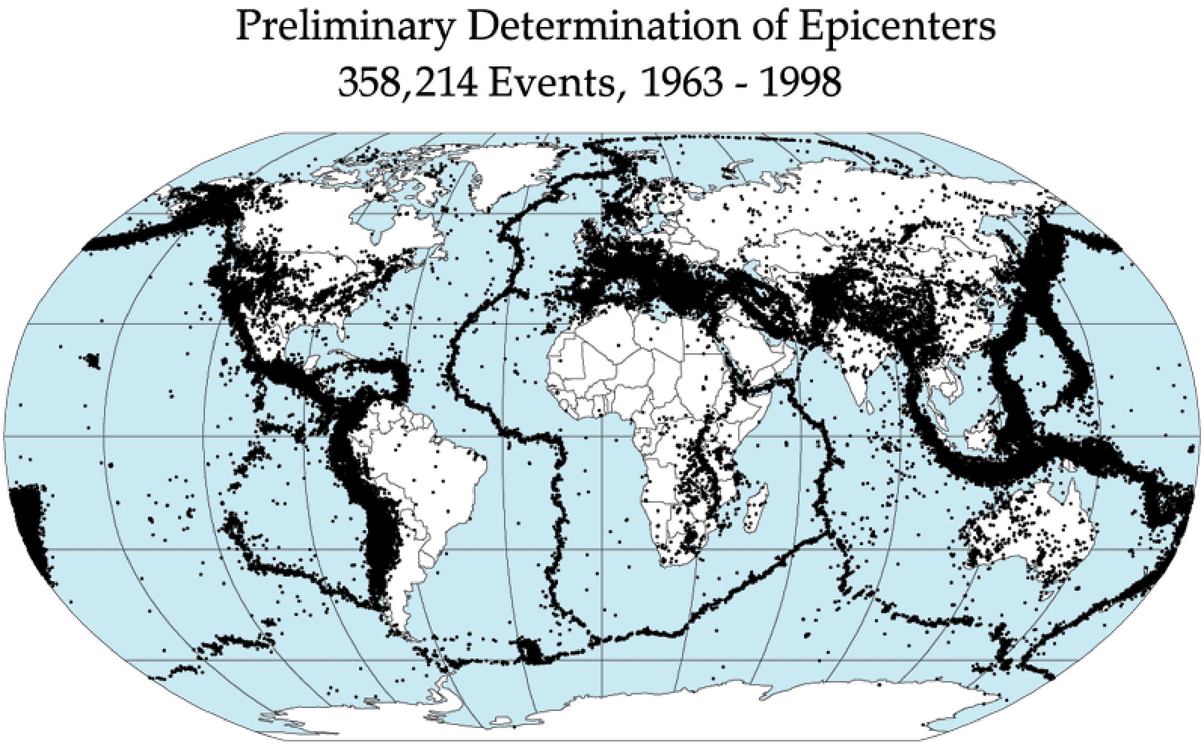

Figure 1.7 Global Earthquake Eepicenters, 1963-1998

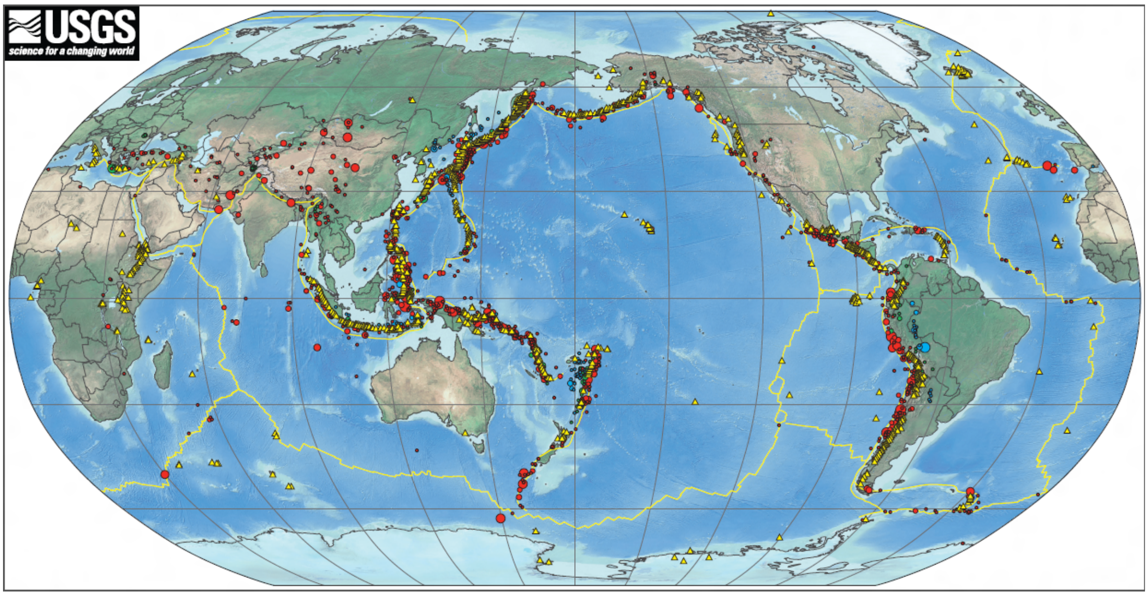

Figure 1.8 Seismicity of the Earth 1900-2010 (USGS)

1.3 Earthquake Due to Volcanic Activates.

Earthquake may also happen as a result of volcanic activities in which the lava movement under the earth crust exerts a high pressure on the crust trying to escape to outside. This process is generally associated with earthquake activities. Saudi Arabia has such type of actives especially in the western and northern western part of the country. The last volcanic activity reported was in Al-Ais area near Medina, May 2009. The resulting earthquake measured 5.8 on the Richter scale. At least 3000 earthquakes has been recorded within one month in which 30 of them measured 3.7 on the Richter scale. Fig 1.9 -1.12 shows some aspects and consequences of the earthquake.

Figure 1.9 Volcano Caused the Earthquake, 9 Km South East Al-Ais

Figure 1.10 Earth fault Resulted from Al-Ais Earthquake.

Figure 1.11 Earth Fault Resulted from Al-Ais Earthquake.

Figure 1.12 A close view of the Earth Fault Resulted from Al-Ais Earthquake.

Saudi geological survey has issued a map for the recent activities in the Kingdom. This map shows quite large number of activities, particularly in the western part of the country as shown in Fig 1.13. Some of these activities were measured more than 5.0 on Richter scale.

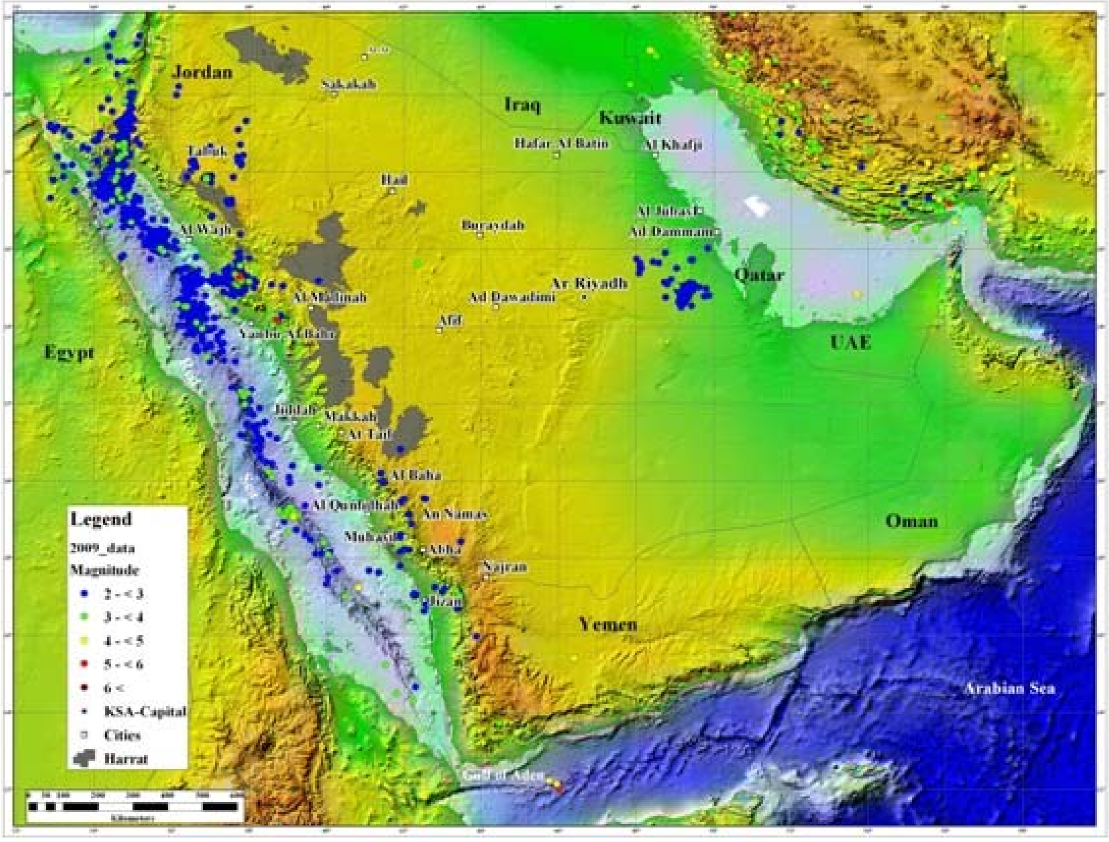

Figure 1.13 Earthquake Epicenter in Saudi Arabia and other Countries up to 2010.

It can be seen that there is potential earthquake hazard in some areas especially western part of Saudi Arabia. Due to this hazard, Saudi authority has put laws in those areas in which the seismic design is now mandatory for any new construction in the area. The Saudi authorities have also constructed a network of seismic recording stations the spread though out the country as show in Fig 1.14.

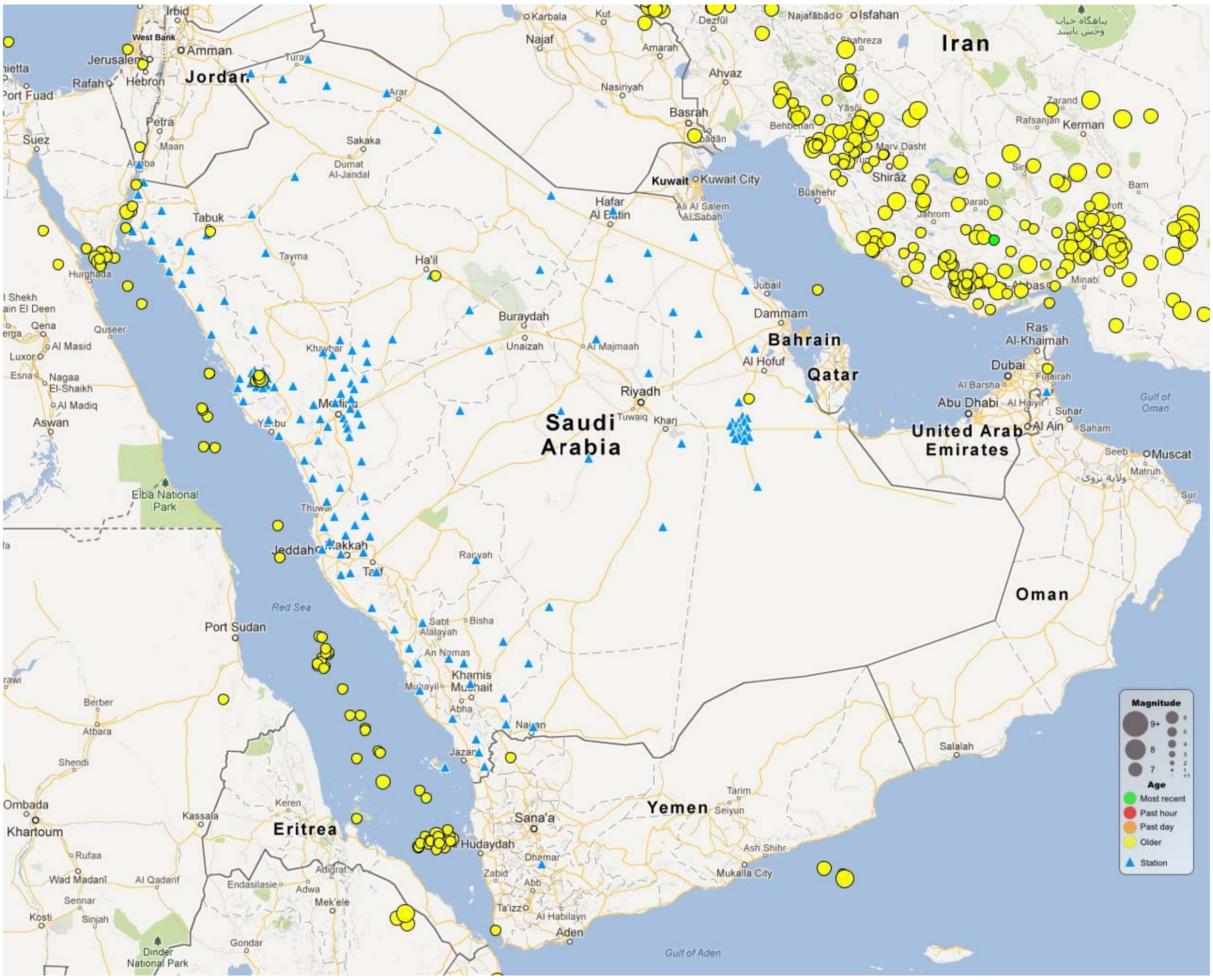

Figure 1.14 Seismic Recording Station in Saudi Arabia.

1.4 Earthquake and Heritage Structures.

Unreinforced masonry (URM) construction is one of the oldest type of structures in human history. It was used by almost all civilizations in different areas all around the world. Different kind of constructions have been constructed using masonry walls including low rise buildings, high rise buildings, dams, channels, stardoms, bridges, lighthouse, mosques, churches, and so many other type of constructions (Figs 1.15-1.17). Masonry type of construction is still being used up to present day in many urban areas as bearing walls, and in other areas in heritage type of construction. Masonry components are also used in modern buildings, especially as infill walls. According to the work done by Abrams (1992) and Filiatrault et al (2001), URM has been recognized, following nearly every medium to strong earthquake, as one of the most vulnerable forms of construction. From the past experience of earthquakes, well-engineered and constructed URM buildings possess good characteristics and can withstand such earthquakes. Most reports mentioned that the majority of deaths in a major earthquake event result from failure of seismically deficient URM structures due to their inability to dissipate energy through inelastic deformation in an earthquake.

Heritage structures were mainly built with masonry type of construction. Such heritage buildings represent human treasures as well as they are considered to be a major source of tourist related income to governments and countries all around the world. One example of such effect of heritage structure is Turkey, which hosts most of humane heritage structures aged back up to early time of civilization. These historical structures have a major effect on the economy of Turkey in which about 33 millions tourists have reported to arrive to the turkey in 2011, which makes more than 17 billion $ dollars of income.

Figure 1.15 Blue Mosque, Istanbul, Turkey, built from 1609 to 1616.

Figure 1.16 The Coliseum, Rome, Italy, the largest ever structure built in the Roman Empire , built from 72 AD 80 AD

Figure 1.17 Roman Aqueduct, Segovia, Spain.

1.5 Heritage Structures in Saudi Arabia.

Saudi Arabia and all other countries in the Arabian Island have rich heritage construction which is spread all over the country. Some of these structures were built using rocks and lime mortar and others were built using mud. A lot of damage happened to some of those structures. Recently, several projects for restoration and rehabilitation such structures are taking places. Jeddah city is considered one of the places that hold many heritage structures. Saudi Arabia authorities have lunched a project for restoration of Jeddah old city. Figs 1.18-1.21 show some of the old buildings in Jeddah.

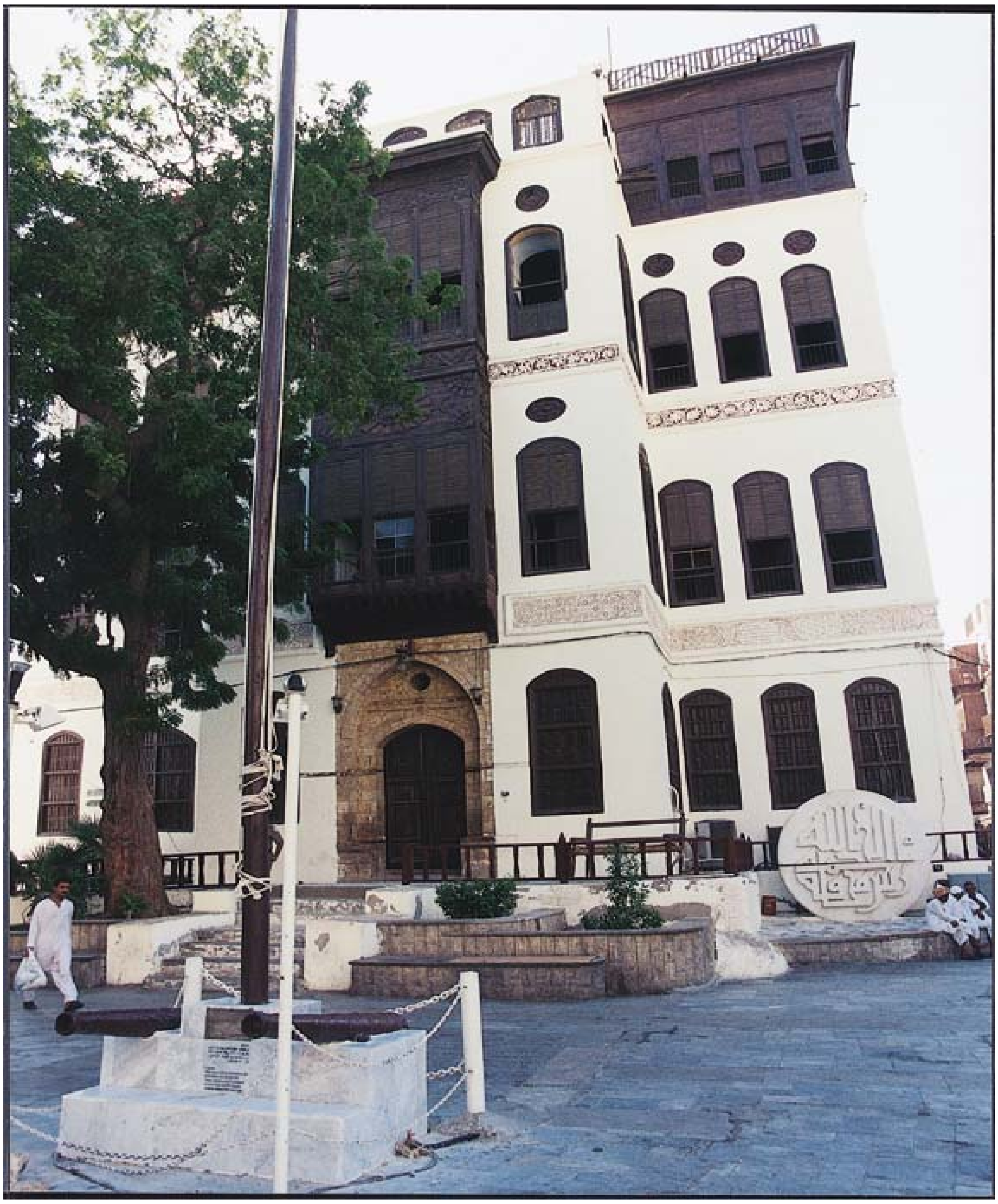

Figure 1.18 New and Old Building

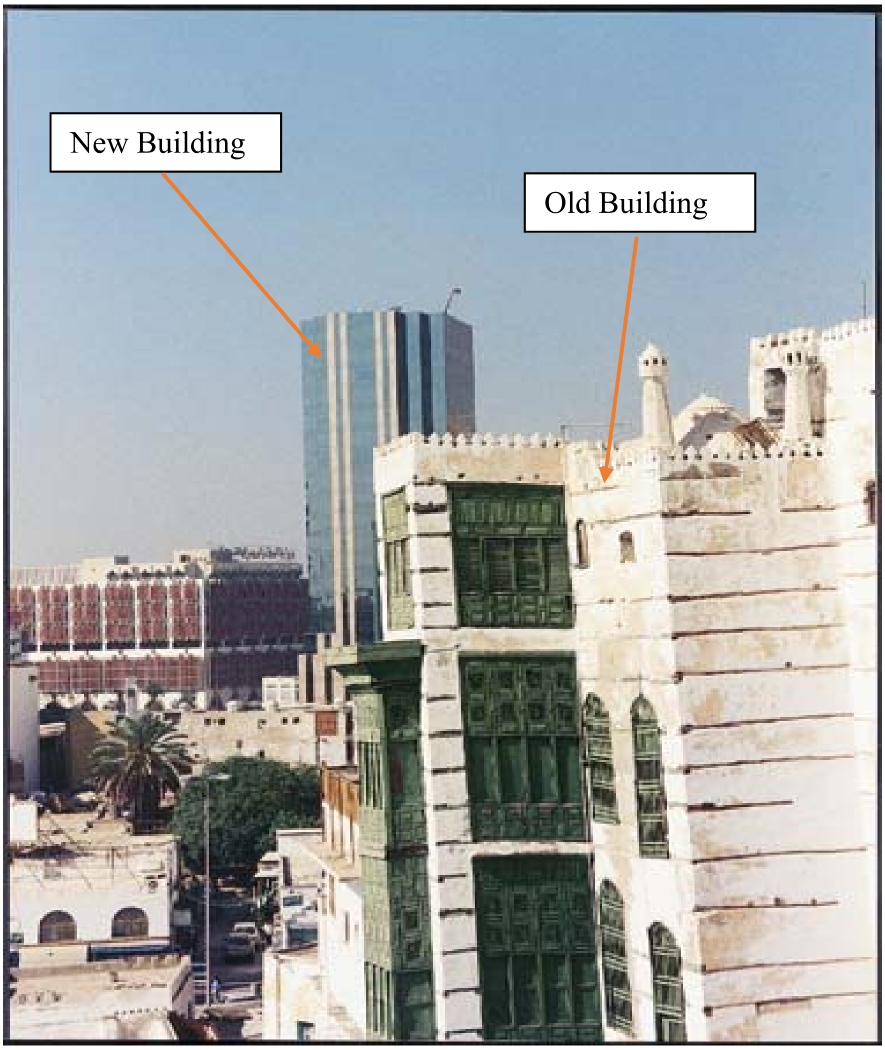

Figure 1.19 Old Building after Restoration

Figure 1.20 Old Building before Restoration

Figure 1.21 Collapse of an Old Building in Jeddah.

Diriyah in Riyadh is also one of the historical places in Saudi Arabia. It includes old city and also historical palaces and Castles. The Saudi authorities launched a project for restoration of the historical buildings and places in Diriyah. Fig 1.22 shows some of the old buildings in Diriyah.

Figure 1.22 Historical Palces in Diriyah-Riyadh

In the Eastern Province, many historical places exist. One of those places is Tarout Castle in Tarout Island. This castle is reported to be built 4300 B.C. A lot of damage due to non-documented reasons has affected the castle and there is a government project to restore and retrofit the castle as shown in Fig 1.23 and 1.24

Figure 1.23 Tarout Castle in Qatif, built 4300 BC

Figure 1.24 Close vies of Tarout Castle in Qatif, built 4300 BC

1.6 Summary

The previous review shows that there exists a strong need to develop an expertise in the area of earthquake engineering in general and in heritage structures restoration and retrofitting in particular to maintain and preserve such structures in good conditions against any damage that may occur during a seismic event. In order to accomplish this, there is a strong need to understand the behavior and response of such structures to seismic loading. This understanding of wall behavior will allow engineers to make correct decisions in the right time to either strengthen or retrofit these structures. Based on that, a project is underway in the Department of Civil and Environmental at KFUPM to assess the behavior of walls made from sandstone and lime mortar that represent a form of heritage structures in Riyadh.

Several studies have been carried out targeting the understanding of the behavior of URM and the retrofitting of URM when subjected to seismic loading. Some of these studies are experimental, whilst others are either numerical or combined approaches. Several techniques of seismic retrofitting of masonry structures have been developed and practiced in seismically active areas including Turkey, Iran, Mexico, Portugal, Greece, Italy, Japan, United States and many other countries all around the world.

Masonry walls plays an important role in seismic response of the whole masonry structure according to the configurations of the masonry wall in the structure. It has been reported (Vasconselos 2005) that if the wall does not fail in the out of plane failure mode , then the resistant mechanism of the unreinforced masonry building under seismic action is assured by in-plane behavior of masonry walls. Several type of tests have been used in investigating the behavior of masonry walls.

In general, masonry walls show five modes of failure depending on loading and geometry conditions, which is measured in terms of aspect ratio (ratio of height to width). Walls having an aspect ratio close to 1.0 generally fail in the following modes: (i) rocking mode, (ii) sliding mode, (iii) staggered head/bed joint failure, (iv) cracks through wall blocks, and (v) crushing of wall blocks or bricks. Based on research conducted on behavior of URM, it can be concluded that walls subjected to in-plane loading follow similar failure patterns.

Behavior of masonry walls subjected to both axial and cyclic lateral loading has been investigated extensively by different researchers worldwide. Such investigations are very important due to the need to preserve the heritage structures subjected to seismic activities. It has been reported that, the Gulf area is being subjected to an increasing trend in seismic activities which means that there is a strong need to study the effect of seismic loading on heritage structures in local areas of Gulf. Gulf area has a rich collection of heritage structures that are spread throughout the Gulf countries. Different kind of masonry walls were used to construct such structures including single and multi-leaf masonry walls. In this study, the behavior of masonry walls subject to seismic loading is assessed by conducting an experimental and numerical study on walls subjected to pre-axial compression force and lateral cyclic displacement load. The walls tested in this study were typical form of heritage construction used in Riyadh, Saudi Arabia. The walls consists of one single leaf with lime mortar between stone units at head and bed joints.

In order to arrive at a firm understanding of the behavior of walls subjected to pre-axial compression force and cyclic loading, walls are modeled in an ABAQUS environment, using a plastic-damage model as originally developed by Lubliner (1989) and further extended by Lee and Fenves (1998) at University of California, Berkley. Micro-modeling analysis level was used in which both stone bricks and lime mortar are modeled using continuum approach as an elasto-plastic damage to capture the true behavior when subject to cyclic loading. Different kind of material tests were conducted to extract the material properties needed in the FEM simulation.

The model yields interesting interactive collapse mechanisms that result as the axial loading on the wall is increased. Different modes of failure have been observed in this study.

CHAPTER 2

LITERATURE REVIEW

2.1 Introduction

Masonry wall has been used since the early civilization. It was used mainly as a load carrying structure. The world is full of heritage structures that are highly valuable. Those structures have been suffered from several aggressive agents that tend to destroy them. One of the most severe and over the centuries disastrous agents is the earthquakes. Masonry wall is still used nowadays as infill in the reinforced concrete frame structures. In order to maintain the treasure of heritage structures as well as preservation of humans live, masonry walls need to be investigated and studied to characterize the mechanical properties and behavior of them to several loading conditions. As mentioned before, earthquake is the main issue that threatens and shortens the life of such masonry structures. The masonry walls could be single leaf or multi-leaves which may be filled with rubble in between leaves. Several researchers have investigated the behavior of masonry walls.

2.2 Research Survey.

Demir (2012) studied the effect of cyclic loading on heritage masonry wall representing an ancient historical Mosque in Istanbul which is *Bayezid II Mosque*. In his work, Demair tested 6 masonry walls which were 1/3 scale down of the real masonry walls of the Mosque. The walls were multi-leaves walls with rubble infill between the two layers of the wall. The dimensions of the walls were 1.2 m by 1.2 m and had a thickness of 30 cm. Some of the walls were prepared with clamps between units to represent the real situation in the mosque. The loading type was quasi-static cyclic loading.

The variables in Demir's experiments were clamped or unclamped and level of axial loads exerted on the walls. These variables are summarized in Table No. 2.1.

Table 2.1 variables in Demir's experiments

Sample	Clamped or Not	Axial Load (MPa)	Axial Stress Mpa
M-25-C	Yes	0.25	0.25
M-50-C	Yes	0.50	0.5
M-75-C	Yes	0.75	0.75
M-100-C	Yes	1.00	1.0
M-50	No	0.50	0.5

The lateral displacements were recorded against the lateral strength associated with that displacement. In his study, Demir found that the mosque walls exhibit different behavior and strength according to the level of axial stress exerted on the wall. Mode of failure was noted to vary according to the variation of axial load. Demir also reported a ductile behavior of the walls when the level of axial stress is low compared to the axial capacity of the wall. Demir performed a finite element analysis using ABAQUS. Although Demir was able to get good agreements between the experiment and FEM analysis, the range of axial load used in the FEM analysis was limited to that used in the real experiment.

Li et al (2005) investigated the behavior of masonry concrete walls subjected to diagonal loading. They also investigated the effect of NSM (near surface mounted) reinforcement using GFRP and stainless steel bars on the strength of masonry walls. The authors discussed their results in the framework of a mechanistic model. In the current study presented in this manuscript, finite element simulations, using elasto-plastic damage model, have also been conducted on the concrete masonry walls tested by Li (2005). The loading types adopted in this study are axial and lateral loading, in which the effect would be similar to that of diagonal loading adopted by Li et al (2005). Finite element simulation has been conducted for this type of wall using a number of initial axial load intensities, as high as the full axial capacity of the wall, so that the interaction diagram in the axial and lateral load space can be determined. The geometry of the walls adopted by Li et al (2005) was 1625 mm by 1625 mm by 152 mm thickness. The concrete masonry units had dimensions of 406 mm by 203 mm by 152 mm thickness. A type N mortar (ASTM C270) was used to build the walls.

Vasconcelos (2005) studied the seismic performance of masonry walls made of granite stone. She did an in-plane loading test on three types of masonry walls, namely, WS (walls composed of units with regular shape and dimensions and dry joints), WI (walls consisted of the assembly of irregular hand cut and bed joints), WR (walls composed of units with variable shape and dimensions randomly assembles with low strength mortar). The walls have dimensions of 1m x 1.2 m. The WS walls were subjected to in-plane monotonic loading. The other two types of walls were subjected to cyclic loading. All three types of walls were subjected to pre-axial compression stress of 0.5, 0.87 and 1.25 MPa. Vasconcelos reported that, the failure modes depend clearly on the level of axial load and on the textural arrangement. She concluded that, for low to moderate axial loads, the flexural/rocking mechanism prevails, whereas, for high levels of pre-compression, the lateral response is either characterized by mixed flexural/shear/toe crushing or by shear failure. Vasconcelos also reported that masonry walls subjected to high levels of pre-compression, exhibit a brittle failure. It was verified that masonry stone walls exhibit large nonlinear deformation up to the collapse state.

Senthivel and Lourenco (2009) have conducted a finite element analysis for modeling of deformation characteristic of historical stone masonry shear wall. They have idealized the simulation as two dimensional nonlinear finite elements. Their numerical study was based on experimental test carried out by Vasconcelos. Plasticity theory based on micro modeling technique has been adopted in their analysis. The stone units were modeled using eight node continuum plane stress elements with full Gauss integration. The joints and unit-joints interfaces were modeled using six node zero thickness line interface elements with Lobatto integration. The numerical and material properties needed for the simulation were extracted from the experimental work of Vasconcelos study. They used a FORTRAN Finite element program developed by Lourenco (1996). They have found that, heel, toe, center and local point of application of load on the shear wall are the critical regions. They also found that, failure in these regions mainly controlled the overall behavior of the shear walls. They have concluded that, failure patterns and load deformation response of the walls are highly influenced by the axial pre-compression and material properties. According to their results, they have found a good agreement between the FEM and experimental results. Although the FORTRAN program was used to simulate monotonic loading, it can’t be used to simulate cyclic loading.

Gabor et al (2006), have conducted numerical and an experimental analysis of the in-plane shear behavior of hollow brick masonry panels subjected to diagonal loading. The non-linear behavior of masonry was modeled considering elastic-perfectly plastic behavior of the mortar joint. The researchers used micro-modeling approach to the walls so that for mortar, elastic-perfectly plastic formulation (Drucker–Prager) is adopted with non-associated plasticity to describe the evolution of the plastic strains. The bricks were considered full elastic material. The FEM environment was ANSYS. They have extracted the parameters needed in the FEM simulation using tests conducted on prisms. The experimental study was conducted on masonry panels having dimensions of 870 mm by 840 mm by 100 mm. The researchers have concluded that, there is a good agreement between the results of the experimental and numerical studies. The FEM predicted, with good accuracy, the ultimate loads, ultimate strains, plastic strain evolution, and failure modes.

Da Porto, F et al (2010), have conducted and experimental and numerical study on defining the in-plane cyclic behavior of three types of load-bearing masonry walls, assembled with perforated clay units, and various types of head and bed joints. Three types of clay masonry were studied: units with mortar pockets (PO), tongue-and-groove units (TG), and edge-ground units with thin-layer mortar joints (TM). According to experimental results, a methodical process of model calibration was carried out in order to obtain one single set of parameters that can be used with different modeling strategies and can describe various types of test. Experimental behavior was reproduced by four types of nonlinear finite-element models. Both macromodeling and micromodeling strategies, implementing either the isotropic damage or orthotropic plastic model, were adopted. Results allow some conclusions to be drawn about the adopted experimental procedures, the behavior of the three masonry types, and the reliability of the modeling strategies in order to use the most consistent one to carry out parametric analyses. The walls were made with vertically perforated clay units. Masonry made with pockets for mortar infill (Po), according to Eurocode EN1996-1-1 (European Committee for Standardization 2005), is classified as having fully filled head joints as mortar is provided over a minimum of 40% of the unit width. Masonry made with tongue-and-groove units (TG) was built with dry mechanical interlocking between units at the head joints. Thin-layer joint masonry (TM) was built using thin layer mortar at the bed joints and dry mechanical interlocking between the units at the head joints. Almost 150 tests on mortar and units were conducts. 51 tests were conducted on large masonry assemblage with dimensions of $1000 \times 1250 \times 300$ mm. the walls tested with applying central and constant vertical loads of 17, 22, 27, and 33% of the mean compressive strength measured by the uniaxial compression tests. Experimental results were reproduced by means of both macromodeling and micromodeling strategies. A plane stress state was assumed in all adopted models, implementing actual experimental boundary conditions and loading schemes. Eight-node elements with a Gauss integration scheme were used in continuum models and for masonry units. In the discrete models, six-node zero thickness interface elements with the Lobatto integration scheme were also adopted for head and bed joints. The results shows a good agreement between experimental and numerical studies. Francesca also reported that Orthotropic models and the isotropic micromodel are more suitable and isotropic models, in particular the isotropic micromodel, described shear-compression tests accurately.

Chaimoon et al (2007), have conducted a numerical study of unreinforced masonry walls under shear-compression fracture using inelastic material behavior with compression cap in the failure surface. According to Chaimoon, a simplified micro-modeling approach is used wherein the two masonry components: bricks and mortar joints are modeled separately. The mortar joint, which is the plane of weakness, is represented through interface nodes of zero thickness. The formulation derived by Attard and Tin-Loi (2007) for the numerical simulation of fracture in concrete is extended to model shear compression failure in masonry. According to Chaimoon, the advantages of this formulation are that, as with the discrete crack models, there is no length scale required.

The formulation also allows the tracking of interacting and/or branching cracks without re-meshing. The formulation of Attard and Tin-Loi (2007) is based on a linear complementarity formulation as in Bolzon et al and uses a mathematical programming algorithm to obtain solutions to a non-holonomic rate form within a quasi-prescribed displacement approach. The inelastic failure surface of a structure is an assembled piecewise-linear failure surface. Compressive failure was not taken into account. The results of simulations of failure in masonry walls showed that the inclusion of brick failure was very important with reasonable predictions when compared to experimental results. The formulation, however, was limited because of the existence of unacceptably high compressive stresses at the wall toe.

2.3 Type of Cycle Loading.

The behavior of masonry structures have been studied by different researchers using different testing technique. The main difference between those techniques is the loading nature such as quasi-static monotonic or cyclic loading, shaking table loading, and pseudo-dynamic loading. According to Gerardin and Negro (2000), the dynamic shaking table is the most realistic test to accurately simulate seismic loading. Pesudo-dynamic tests is similar to shaking table test. In the quasi static loading however, the rate of loading is low. Although the quasi static loading cannot capture the inertia effect, it is the most common technique used to evaluate the behavior of masonry walls because this test is simple relative to other testing techniques and allow more accurate measurements of forced and displacements and the record of damage evolutions. The results of quasi-static loading are more conservative compare to the dynamic test in which the inertia effect adds more resistance to the wall in case of dynamic testing. The lateral loading in quasi-static loading can be extracted from real seismic lading as shown in Fig 2.1 (Tomaževič)

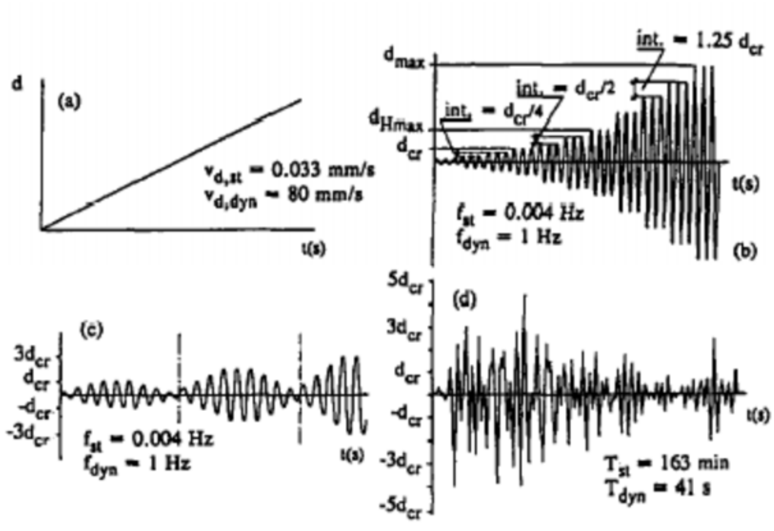

Figure 2.1 Typical lateral displacement time histories used to simulate seismic loading (Tomaževič,1999).

CHAPTER 3

THEORETICAL PRELIMINARIES

3.1 Introduction.

Numerical investigation of masonry wall subjected on in plane loading have been investigated quite much in recent decades. It is well known that masonry structures are a composite material as it consists of mortar and bricks in which each material has its own material properties. Moreover, the interaction between constituent materials raises extra challenges to the problem. Another source of complexity when dealing with masonry structures is the consequence of loading in which cracks formed within the material will generate new surfaces within each material. This lead to contact problem between the two crated surfaces at the sides of the cracks. Loading is also add more complexity to the problem under consideration. Dynamic lading which involve earthquake loading is extremely difficult and complex to be modeled using numerical technique.

When investigating numerical studies conducted by many researchers, it can be concluded that, finite element method is the most numerical technique used technique in solving masonry mechanics problem. The availability of sophisticated commercial software makes dealing with mechanics of masonry wall easy. When considering all of complexity included in masonry mechanics, finite element method needs a lot of resources in terms of material properties, processing time and storage capacity. Therefore, many simplifications have been adopted and incorporated when conducting fine element analysis. These simplifications included, idealization of 3D problem to 2D, simplification in material constitutive models, simplification and idealizations in loading type, and simplification in level of analysis.

Three different types of computational methods have been utilized be the research community to simulate the behavior of masonry structures under static and dynamic loadings. These computational methods are generally categorized into three groups namely: (i) micro-scale, (ii) macro-scale, and (iii) meso-scale (Kiarash, M. D 2012). In the macro- and meso-scale analysis of masonry buildings, the general behavior of the structure is important, and not the detailed behavior of each component. Although micro-scale modeling takes the most computational resources (size and time), it has the most accuracy level and gives accurate response of the structure beside the exact path of cracks and exact shape of failure pattern. Analysis methods based on meso- and macro-scale approaches are usually accompanied by simplifying assumptions to improve the computational efficiency, and clearly, the accuracy of the analysis is less than in the micro-analysis case.

In the micro and mesoe scale analysis, three main techniques have been implemented in analysis of masonry structures. The first techniques is based on interface assumption of mortar and places of potential cracks within masonry unites. In this model masonry brick are modeled as continuum based (elastic or inelastic) material and the mortar is molded as interface material. This model have been investigated by many researchers (Roelfsta, Bazent, Lourenco, Page, Cusatis, and Giblert). In case of cracks with the bricks themselves, interface are introduced at the places where potential cracks can happen. In the interface element approach the interface element modeled based on elasto-plastic behavior. The interface element was originally molded so that only tensile and shear failure could happen in the normal compression however, no crash is allowed in the interface element. Lourenco modified this model and added a cape to the compression curve of the interface material in which interface element will crash when reaching certain level of normal stress. Although the interface element was molded based on nonlinear behavior, the bricks was assumed to behave elastically.

The second technique used in simulating masonry and concrete structures is that based on Discrete Element Method (DEM). In this technique the continuum elements are replaced by system of discrete element in which the materials are discretized into collection of rigid bodies connected and interact by friction. This approached was investigated by Cundall.

The third FEM techniques is the lattice model. In this model the material was replaced by truss elements with different material poetries of the truss elements. The lattice model have been developed so that the truss elements have been changed by beam element with three degree of freedom in 2D and six degree of freedom in 3D (Harnnikoff and Cusatis).

In the current study, continuum based approach was adopted in which masonry brick and mortar where modeled as continuum material. The interaction between mortar and bricks was assumed perfect. This assumption was based on the fact that the cracks in the mortar joist mostly happen within the mortar themself. So treating the mortar as a continuum material with week properties will accurately give the effect of interface. The advantage of this model is that the true failure of wall as well as the crack pattern within mortar can be captured efficiently.

Several constitutive models have been proposed and used to simulate masonry mechanics. In the discrete approach, the unidirectional members can have simple elastic properties or it can have also elasto-plastic properties. In general the behavior can be captured though the degrees of freedom at the nodes of the element.

In the interface model, the bricks are assumed elastic and all nonlinearity will be lumped in the interface element (Lourenco). Most of proposed interface element consider Mohr-Coulomb as a yield surface with adding compression cap and tension cutoff (Lourenco). The proposed yield surface in the $\tau - \sigma$ space is shown in Fig 3.1.

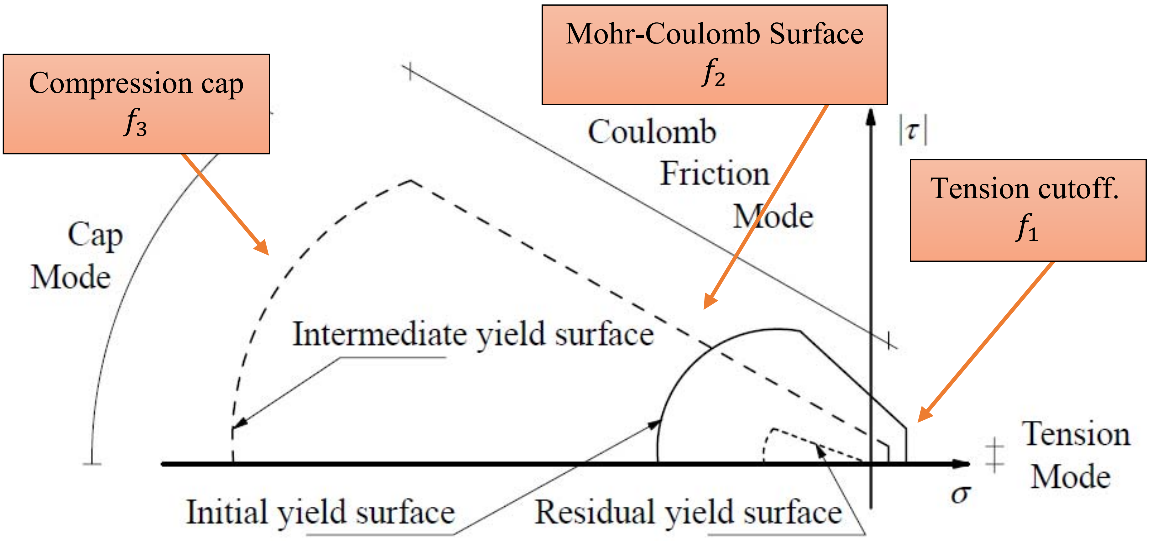

Figure 3.1 Yield surface of Interface Proposed by Lourenco

Remarkable work have been done by Lourenco in numerical simulation of masonry wall based on interface modeling approach. In his work, Lourenco suggested nullity composite yield surface that includes tension, shear and compression failure with softening of each surfaces. These yield surfaces that shown in Fig 3.1 are described as follows:

Tension cutoff surface:

$$f_1(\sigma, \kappa_1) = \sigma - f_t(\kappa_1) \tag{3.1}$$

Mohr-Coulomb surface:

$$f_2(\sigma, \kappa_2) = \tau + \sigma\, Tan(\phi(\kappa_2)) - c(\kappa_2) \tag{3.2}$$

Compression cap:

$$f_3(\sigma, \kappa_3) = C_{nn}\sigma^2 + C_{ss}\tau^2 + C_{nn}\sigma - \bar{\sigma}^2(\kappa_3) \tag{3.3}$$

Where f_t, $c(\kappa_2)$, and $\bar{\sigma}^2(\kappa_3)$ are functions of κ and some other material parameters.

The expansion and contraction (herding and softening) of the yield surfaces are controlled by parameter κ_i which is a function of plastic strain rate, state of stress and other factors.

$$\kappa_i = \kappa_i(\dot{\varepsilon}^p, \sigma, ..) \tag{3.4}$$

Although Lourenco's cap model provided a novel way of get the behavior of masonry wall, it did not take into account the degradation of stiffness of the material when performing cyclic loading. Several experiments have been reinforce that idea that, when unloading for any point bend yield limit, the loading slop (stiffness) is less than the initial slop (Stiffness) of the load displacement curve. In Lourinco model however, the unloading path will follow same slop as the initial slope of the load displacement curve.

To take into account the degradation of the stiffness of the material when unloading, reduction of initial stiffness has to be introduced. The best technique to address this issue is though damage mechanics. In damage mechanics, the stiffness is reduces continually through damage parameter that increasingly evolve during loading. The evolution of damage parameter is controlled by state of plastic strain and the energy dissipated during loading.

In concrete and granular material, the degradation of stiffness was observed and investigated by many researchers (E. P Popove, L. Kachanov, G. Z. Voyiadjis, Jean Lemaître, Pijaudier-Cabot, Jean-Louis Chaboche, Milan Jirasek, and Peter Grassl, Lubliner, and, Lee and Fenves). Damage quantity can be taken as a scalar quantity in which the damage is assumed isotropic or it can be also vector and tensor quantities. For concrete, the damage is well known to be anisotropic. One clear fact about concrete is that damage in tension is different than that in compression. So taking the case of isotropic damage and applied it to concrete will not give accurate results. When considering the simplest damage approach, concrete can be modeled with at least two isotropic damage parameters. One is compression damage parameter and the other is tension damage parameter. This assumption have been studied by Lubliner and further developed by Lee and Fenves at university of California Berkeley. In his model, Lubliner suggested that concrete can be modeled in the frame work of damage machines using two damage parameters namely compression damage (d_c) and tension damage (d_t). This means that the compression as well as tension damage parameter is considered to be isotropic quantities. The damage parameters controls the evolution of yield surface and also controls the degradation of the stiffness of the material. The damage parameters themself are functions of plastic strain rat. This model has been incorporated in ABAQUS finite element software. This incorporated model results in successful and sophisticated approach to simulate concrete and granular material under general loading conditions including cyclic loading.

In this study, the walls were modeled in an ABAQUS environment, using a plastic-damage model. As mentioned before, this model has been originally developed by Lubliner et al. 1989 and further extended by Lee and Fenves 1998. The wall blocks and the lime mortar, are modeled as elasto-plastic with scalar damage paramtes (tenstin damage and compression damage) using yield surfaces that are generalization of the Drucker-Prager model. In this model, new terms are included that account for hardening and softening in compression and softening in tension, with parameters calibrated to the experimentally measured stress-plastic strain data from uniaxial compressive and tensile tests for both the blocks and the mortar. Scalar form of damage is built into the model to account for stiffness degradation.

In general, masonry walls subjected to in plane loading case faille in any one of five failure modes. Those modes are: (i) sliding, (ii) rocking, (iii) staggered head/bed joint failure, (iv) cracks through wall blocks, and (v) crushing of wall blocks or bricks. Investigated those mode of failure was not fully addressed and studied be research community neither experimentally nor numerically. Moreover, the interaction between lateral and axial loading have not been investigated experimentally at all. Some attempts were made to relate the uniaxial force to lateral force using mechanistic approach as framework of analysis. On goal of this study is to address this issue numerically in which FEM analysis have been conducted to walls taking the full range of axial force starting with zero axial force up to full axial capacity of the wall. Some of the numerical results for the interactive collapse mechanism are compared to available experimental data. It has been noted that the relation between axial and lateral forces followed a parabolic curve type. A proposed interaction curve have been suggested in this study as a result of full FEM simulation. To generalize the observation found in this study, FEM analysis have been also done to walls tested by other researchers. Comparison and analysis have been done to data resulted from all FEM simulation. Interesting and universal relationship have been resulted from all simulations. In the following section, a review and introduction to mechanistic models are presented.

3.2 Mechanistic Analysis.

As mentioned before, masonry walls subjected to in-plane loading exhibit different mechanistic response based on the intensity of axial loading applied and wall aspect ratio. Failure patterns and load deformation response of the walls are also highly influenced by the axial pre-compression and material properties (Senthivel, R., Lourenço P. B 2009, ACI Committee 440 (2002).). The different modes of failure (as a function of axial load) include (i) sliding, (ii) rocking, (iii) staggered head/bed joint failure, (iv) cracks through wall blocks, and (v) crushing of wall blocks or bricks (Filiatrault, A 2001, Demir, C (2012), Li, T (2005), Vasconcelos, G. F (2005), Kiarash, M. D (2012), Haider. W (2007), Senthivel, R., Lourenço P. B (2009), Yi, T (2004), Basoenondo, E. A (2004), Haach, V. G (2009), Voon, K. C (2007), Al-Gohi, B. (2010), ACI Committee 440 (2002)). Several attempts have been conducted toward understanding and predicting the behavior of masonry walls using mechanistic framework of analysis. Each failure mode is characterized by different failure pattern, sequences, and gives different levels of lateral resistance. These modes of failures can be summarized as follows:

3.2.1 Sliding Failure

For walls subject to low levels of axial compression loading and/or having a low friction coefficient μ due to poor mortar, horizontal cracks in bed joints may form a sliding plane extending along the bed joints through the length of the wall. This results in the upper part of the wall sliding relative to the lower part (Fig. 3.2). As in ACI Guidelines (ACI

Committee 440 (2002).), Li et al (2005) propose that, the shear strength of the reinforced wall can be expressed as

$$V_n = V_m + V_r \tag{3.5}$$

where V_m and V_f are the shear resistance of the masonry and the contribution of any provided reinforcement to the shear strength of the wall. For in-plane loading of URM, failure is usually due to debonding at the mortar-block interface and shear sliding along the bed joints with cracks developing in a stepped manner. Using a Mohr-Coulomb failure criterion, the shear strength can be modeled as

$$\tau = \tau_0 + \mu\sigma_n \tag{3.6}$$

where τ_0 is the shear bond strength, μ is the coefficient of internal friction, and σ_n is the normal compressive stress on the wall. Paulay and Priestley (1992) recommend approximating the cohesion τ_0 by 3% of the masonry gross area compressive strength f'_m and internal friction μ in the range of 0.3 to 1.2. With the walls tested by Li et al (2005) being subjected to diagonal compression, the shear capacity for sliding shear along the wall bed joints can be shown to be

$$V_{m,1} = \tau \times A_n = A_n(\tau_0 + \mu\sigma_n) \tag{3.7}$$

Where:

A_n is the sliding shear area.

τ_0 is the shear bond strength.

μ is the coefficient of internal friction.

σ_n is the normal stress.

The lateral resistance of the wall ($V_{m,1}$) is generally low in this mode of failure.

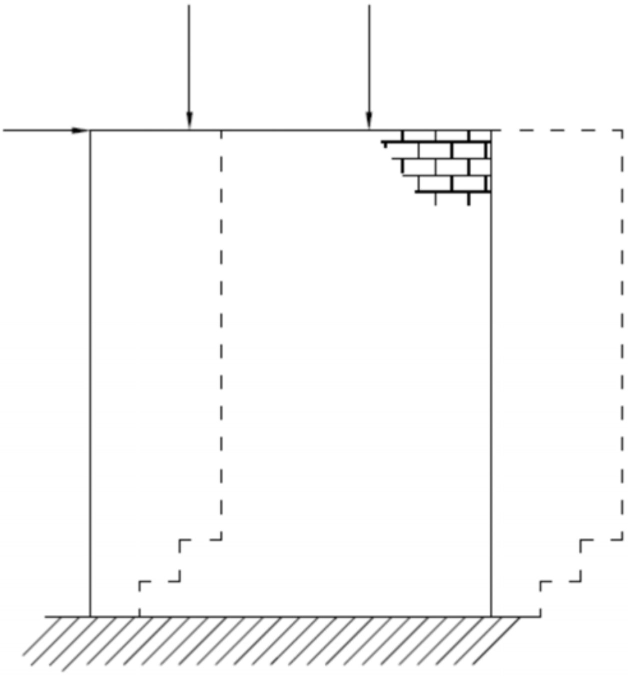

Figure 3.2 Sliding failure mode

Crisafulli et al, (1995) have suggested a more realistic distribution of normal and shear stresses acting on a block. Assuming that the variation of the normal stresses is linear with a zero value at the center of the block and maximum at the edges and that failure occurs in the joints for low levels of axial stress, it results that

$$V_{m,2} = \tau \times A_n = A_n(\tau_0^* + \mu^* \sigma_n) \tag{3.8}$$

Where:

$$\tau_0^* = \frac{\tau_0}{1 + 1.5\mu\, b/d}, \quad \mu^* = \frac{\mu}{1 + 1.5\mu\, b/d}$$

d is the block length.

b is the block depth.

3.2.2 Rocking and Toe Crushing Failure.

Walls with a higher axial loading and stronger mortar type may be set into a rocking motion. Due to the mechanism of this type of response, toe of the wall is generally subjected to high compression force because the entire force is transferred to the base through the toe contact area. This generally results into a local crushing at the toe of the wall, followed by general collapse of the wall. (Fig. 3.3).

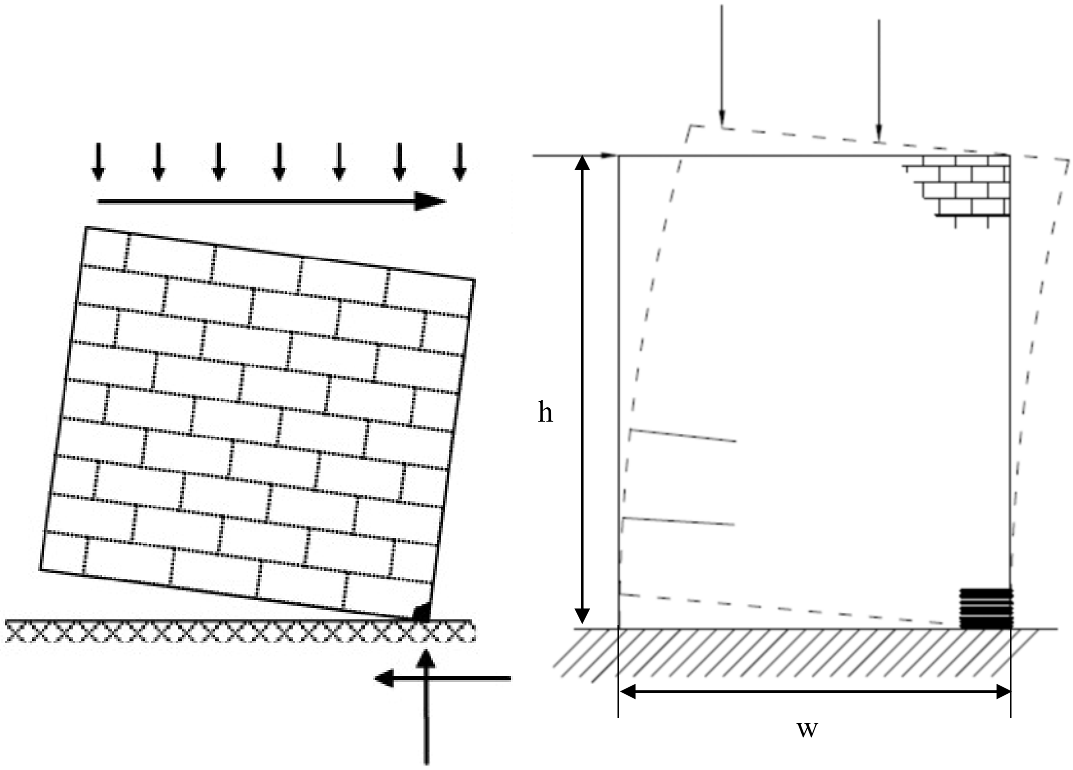

Figure 3.3 Rocking and Toe Crushing Failure mode

3.2.3 Staggered Head/Bed Joint Failure

This mode of failure is generally accompanied with higher axial force on the walls. In this case, the wall is not able to slide along a bed joint nor to rotate due to the high confinement. This results in redistribution of the force within the wall and the energy is dissipated trough staggered cracking of the head and bed joints of the wall. The lateral resistance of the wall is this case is higher than the previous modes. This type of failure is very common in dry contact masonry walls or walls with weak mortar relative to bricks (Fig 3.4).

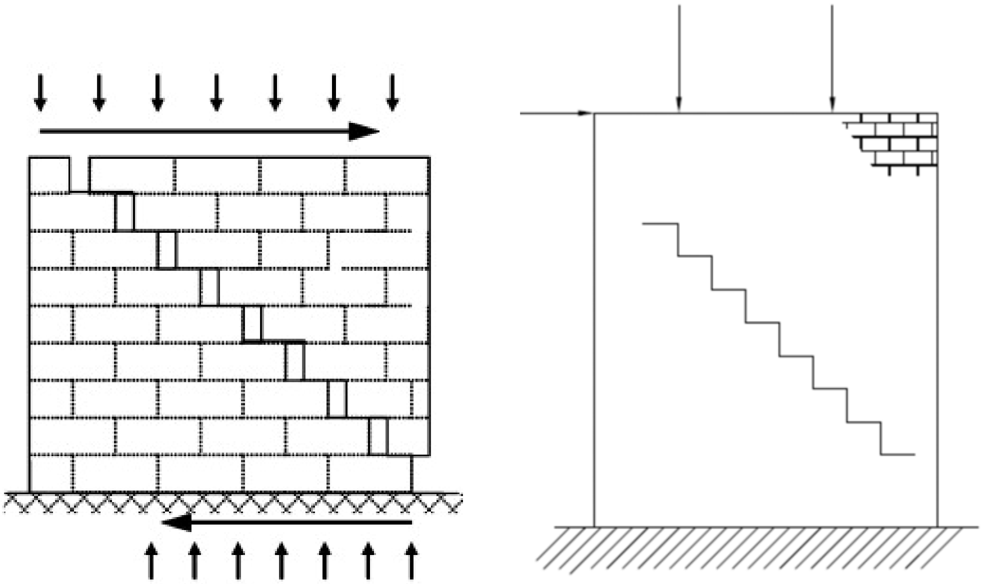

Figure 3.4 Staggered head/bed joint failure mode

3.2.4 Cracks Through Wall Blocks

In this failure mode, the degree of confinement is higher than in the previous modes. This prevents the wall from sliding in a staggered pattern. In this failure mode, the combination of axial and lateral forces results in an initiation of the cracks through the wall bricks due to principal diagonal tensile stress exceeding the tensile strength of the brick (Fig 3.5).

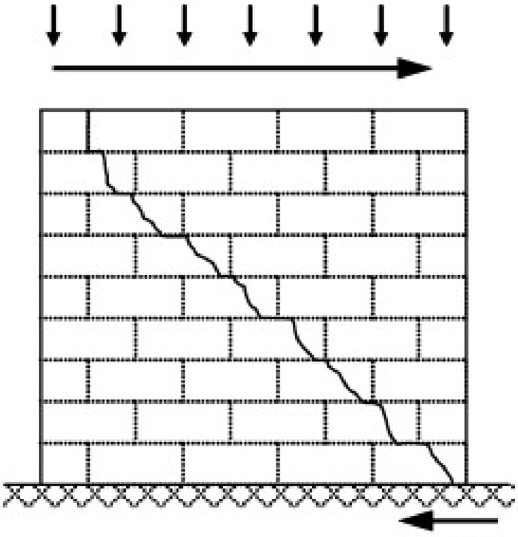

Figure 3.5 Cracks through Wall Blocks

Assuming that this failure occurs when the maximum tensile stress becomes equal to the tensile strength of the masonry, f'_{tb}, it may be shown that the lateral shear required to induce the tensile crack in the masonry block may be found from Eq. (3.9), Li et al (2005), Paulay et al (1992)

$$V_{m,3} = \frac{f'_{tb}}{2.3}\sqrt{1 + \frac{\sigma_n}{f'_{tb}}} \times A_n \qquad (3.9)$$

Where:

σ_n is the axial pre-compression, taken positive in Eq 3.9

Generally, the level of axial force is around 40-60% of wall axial capacity. The lateral resistance of the wall in this case is the highest of all the failure modes.

3.2.5 Crushing of Wall Blocks or Bricks.

In this failure mode, wall is subjected to extremely high axial force. Major damage to the wall results due to the high axial force (before the application of lateral force) in terms of high compression induced cracks in the wall bricks. The level of axial force in this case is generally 70-90 % of the wall axial capacity. In this case, the wall is weak in lateral resistance and the level of lateral resistance is low compared to the case when the axial force is less (Fig 3.6).

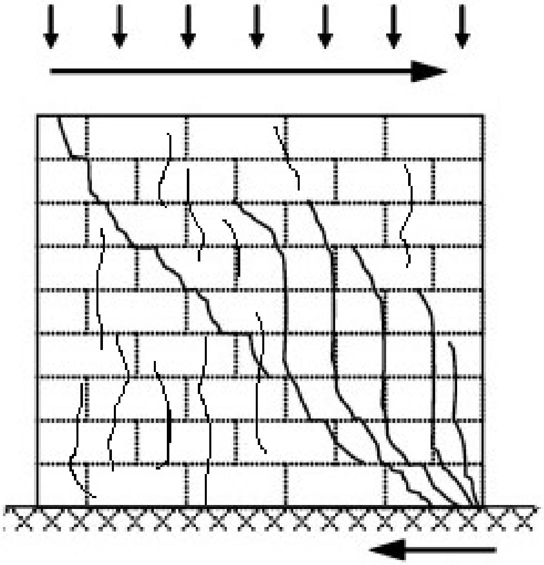

Figure 3.6 Crushing of Wall Blocks or Bricks

For this case, according to Li et al (2005), when the compressive stress approaches the wall axial capacity, the shear force to cause failure may be found from Eq. 3.10.

$$V_{m,4} = (f'_m - \sigma_n)\frac{2d}{3b}A_n \qquad (3.10)$$

Where:

f'_m is the compressive strength of the masonry wall.

d is the block length.

b is the block depth.

Li et al (2005) have plotted the transverse lateral capacity based on Eqs. 3.7, 3.9, and 3.10 and the results are shown in Fig. 3.7.

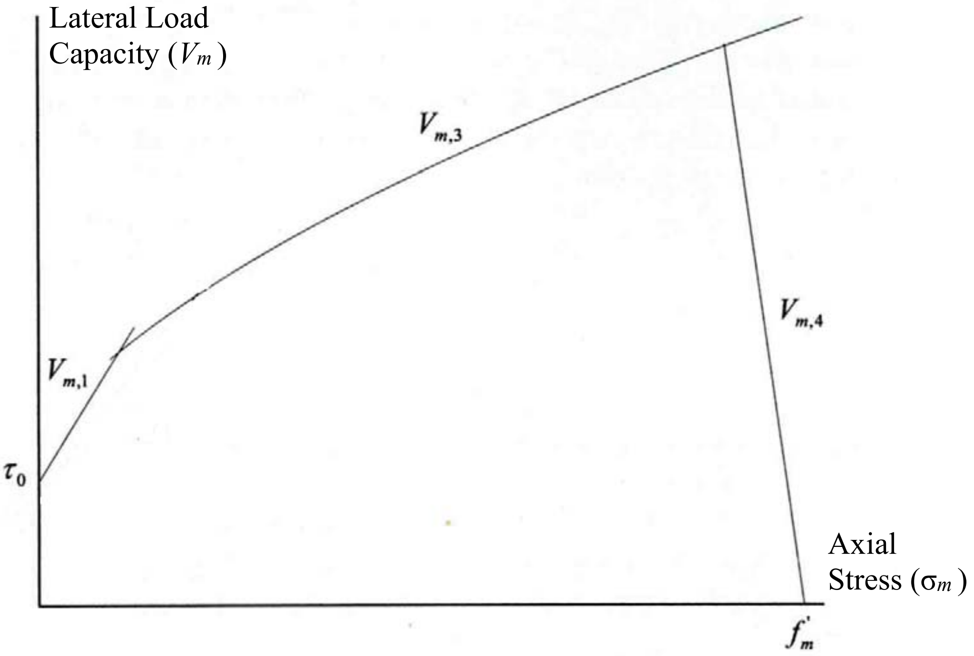

Figure 3.7 Shear-axial Interaction Diagram for URM Walls (Li et al)

Fig. 3.7 shows that, the lateral strength of walls increases with increase in the level of axial stress applied to the wall up to a certain limit, after which the lateral strength of the wall sharply reduces. As shown in Fig. 3.7, the curve is composed of three line segments with clear and sharp boundaries between the segments.

This behavior have also been suggested by Mann and Müller (1982) due to a set of remarkable experiments carried out on shear-walls (see Fig. 3.8).

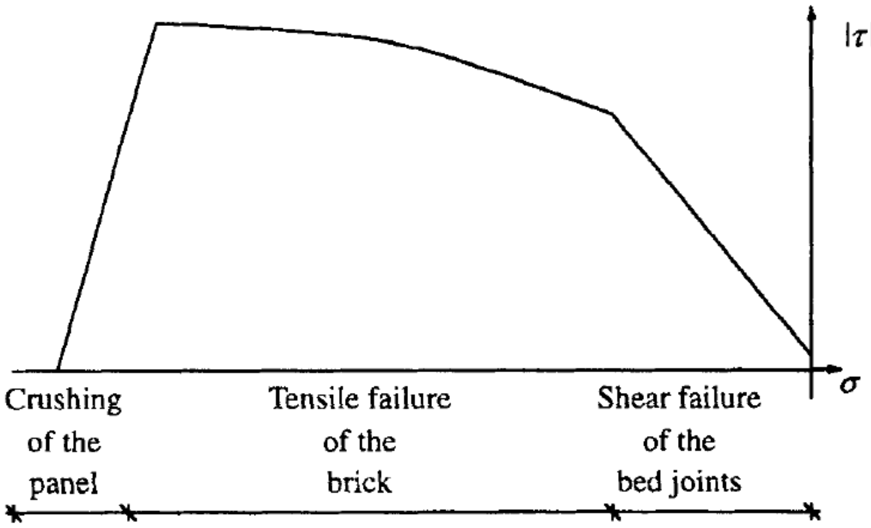

Figure 3.8 Shear-axial Interaction Diagram for URM Walls (Mann and Müller).

Form the above-mentioned observations it can be seen that, the lateral strength of the wall is directly proportion to the axial load up to approximate 50-70% of the axial load capacity of the wall. This followed by inversely proportion in relation between lateral strength and axial load. It has to be mentioned in this regard that the proposed relationship is composed of three segmental lines with clear and sharp boundaries. In reality, the transition between these three segments should be rather smooth and continues. Based on this, a propionic relationship would be much more appropriate to capture the relationship between axial loading and lateral strength of the wall.

This relation between axial load and lateral strength of the wall has not been studied in the frames work of the FEM. One of the objectives of this study is to explore the behavior of masonry wall when level of axial load is high compare to axial capacities of the walls. A newly proposed formula will be presented in this study, which relate the lateral strength to level of axial load excreted on the wall.

As mentioned before, continuum based approach using Concrete Plastic Damage Model was adopted in this study where both masonry bricks and lime mortar were modeled as continuum material. Review of the Concrete Plastic Damage Model is presented in next section.

3.3 Review of Plastic Damage Model

This section essentially follows the development given in the ABAQUS 6.12 Manual work. Some new comments and details given to better understand the elasto-plastic damage model of Lubliner et al (1989) and Lee & Fenves (1998). **C**oncrete **D**amage **P**lasticity (CDP) is one of the possible constitutive models that can efficiently and accurately describe the behavior of granular type materials under different conditions of loading. Several laboratory tests are necessary to identify the CDP model. Those tests have been introduced by Kachanov (1986) and further developed by Rabotnov (1969) and others. The elastic-plastic response of the concrete damaged plasticity model is described in terms of the effective stress $\bar{\sigma}$ and the hardening variable $\tilde{\varepsilon}^{pl}$ with scalar isotropic damage.

$$\bar{\sigma} = D_0^{el} : (\varepsilon - \varepsilon^{pl}) \in \{\bar{\sigma} | F(\bar{\sigma}, \tilde{\varepsilon}^{pl}) \leq 0\} \tag{3.11}$$

$$\dot{\tilde{\varepsilon}}^{pl} = h(\bar{\sigma}, \tilde{\varepsilon}^{pl}) . \hat{\tilde{\varepsilon}}^{pl} \tag{3.12}$$

$$\dot{\varepsilon}^{pl} = \dot{\lambda} \frac{\partial G(\bar{\sigma})}{\partial \bar{\sigma}} \tag{3.13}$$

Where:

$\dot{\lambda}$ and F obey the Kuhn-Tucker conditions: $\dot{\lambda}F = 0;\ \dot{\lambda} \geq 0; F \leq 0$. The Cauchy stress is calculated in terms of the stiffness degradation variable, $d = d(\bar{\sigma}, \tilde{\varepsilon}^{pl})$, and the effective stress as:

$$\sigma = (1 - d)\bar{\sigma} \tag{3.14}$$

The constitute relations for the elastic-plastic response, Eq. 3.11-3.13 , are decoupled from the stiffness degradation response, Eq. 3.14, which makes the model attractive for an effective numerical implementing.

In general, the CDP mode consists of following fundamental concepts: (i) strain rate decomposition, (ii) stress strain relation, (iii) stiffness degradation and hardening rule, (iv) yield function, and (v) flow rule.

3.3.1 Strain Rate Decomposition

An additive strain rate decomposition is assumed for the rate-independent model:

$$\dot{\varepsilon} = \dot{\varepsilon}^{el} + \dot{\varepsilon}^{pl} \tag{3.15}$$

where $\dot{\varepsilon}$ is the total strain rate, $\dot{\varepsilon}^{el}$is the elastic part of the strain rate, and $\dot{\varepsilon}^{pl}$ is the plastic part of the strain rate.

3.3.2 Stress Strain Relation

The stress-strain relations are governed by scalar damaged elasticity:

$$\sigma = (1 - d)D_0^{el}\!:(\varepsilon - \varepsilon^{pl}) = D^{el}\!:(\varepsilon - \varepsilon^{pl}) \tag{3.16}$$

$$D^{el} = D_0^{el}(1 - d) \tag{3.17}$$

Where:

σ is Cauchy stress tensor

d is the scalar stiffness degradation variable, which can take values in the range from zero (undamaged material) to one (fully damaged material).

ε is the strain tensor,

ε^{pl} is the plastic strain tensor,

D_0^{el} the initial (undamaged) elastic stiffness of the material,

D^{el} is the degraded elastic stiffness tensor.

The effective stress tensor is defined as:

$$\bar{\sigma} = D_0^{el} : (\varepsilon - \varepsilon^{pl}) \quad (3.18)$$

In the formulation, it is necessary to propose the evolution of the scalar degradation variable to be a function of effective stress and effective plastic strain.

$$d = d(\bar{\sigma}, \tilde{\varepsilon}^{pl}) \quad (3.19)$$

In CDP model, the stiffness degradation is initially isotropic and defined by degradation variable d_c in a compression zone and variable d_t in tension zone.

Thus, the Cauchy stress tensor σ is related to the effective stress tensor $\bar{\sigma}$ through the scalar degradation parameter (1- d):

$$\sigma = (1 - d)\bar{\sigma} \quad (3.20)$$

3.3.3 Stiffness Degradation and Hardening Rule.

Damage states in tension and compression are characterized independently by two hardening variables, $\tilde{\varepsilon}_c^{pl}$, and $\tilde{\varepsilon}_t^{pl}$, which are referred to equivalent plastic strains in tension and compression, respectively.

The evolution equations of the hardening variables $\tilde{\varepsilon}_t^{pl}$ and $\tilde{\varepsilon}_c^{pl}$ are conveniently formulated by considering uniaxial loading conditions first and then extended to multiaxial conditions.

3.3.4 Uniaxial Conditions

It is assumed that the uniaxial stress-strain curves can be converted into stress versus plastic strain curves of the form:

$$\sigma_t = \sigma_t\left(\tilde{\varepsilon}_t^{pl}, \dot{\tilde{\varepsilon}}_t^{pl}, ..\right) \tag{3.21}$$

$$\sigma_c = \sigma_c\left(\tilde{\varepsilon}_c^{pl}, \dot{\tilde{\varepsilon}}_c^{pl}, ..\right) \tag{3.22}$$

where the subscripts *t* and *c* refer to tension and compression, respectively; $\dot{\tilde{\varepsilon}}_t^{pl}$and $\dot{\tilde{\varepsilon}}_c^{pl}$are the equivalent plastic strain rates, $\tilde{\varepsilon}_t^{pl} = \int_0^t \dot{\tilde{\varepsilon}}_t^{pl} dt$ and $\tilde{\varepsilon}_c^{pl} = \int_0^t \dot{\tilde{\varepsilon}}_c^{pl} dt$ are the equivalent plastic strains. Under uniaxial loading conditions, the effective plastic strain rates are given as:

$$\dot{\tilde{\varepsilon}}_t^{pl} = \dot{\tilde{\varepsilon}}_{11}^{pl} \tag{3.23}$$

$$\dot{\tilde{\varepsilon}}_c^{pl} = -\dot{\tilde{\varepsilon}}_{11}^{pl} \tag{3.24}$$

When the concrete specimen is unloaded from any point on the strain softening branch of the stress-strain curves, the unloading response is observed to be weakened: the elastic stiffness of the material appears to be damaged (or degraded). The degradation of the elastic stiffness is significantly different between tension and compression tests; in either case, the effect is more pronounced as the plastic strain increases. The degraded response of concrete is characterized by two independent uniaxial damage variables, d_t and , d_c which are assumed to be functions of the plastic strains:

$$d_t = d_t\left(\tilde{\varepsilon}_t^{pl}, ..\right) \tag{3.25}$$

$$d_c = d_c\left(\tilde{\varepsilon}_c^{pl}, ..\right) \tag{3.26}$$

The evaluation of the damage parameter have been studied extensively and it can take several forms. The most used model for describing the variation of the damage parameter d is based on the pastic energy dissipated during loading in which d will be the ratio between plastic energy dispiated up to certain plastic strain and the total plastic energy. This can be descripted as shown in Eq 3.27.

$$d_t = \frac{\int_0^{\tilde{\varepsilon}_t^{pl}} d_t\left(\tilde{\varepsilon}_t^{pl}\right)}{\int_0^{\tilde{\varepsilon}_{tf}^{pl}} d_t\left(\tilde{\varepsilon}_t^{pl}\right)} \tag{3.27}$$

Eq. 3.27 can be interpreted as shown in Fig. 3.9.

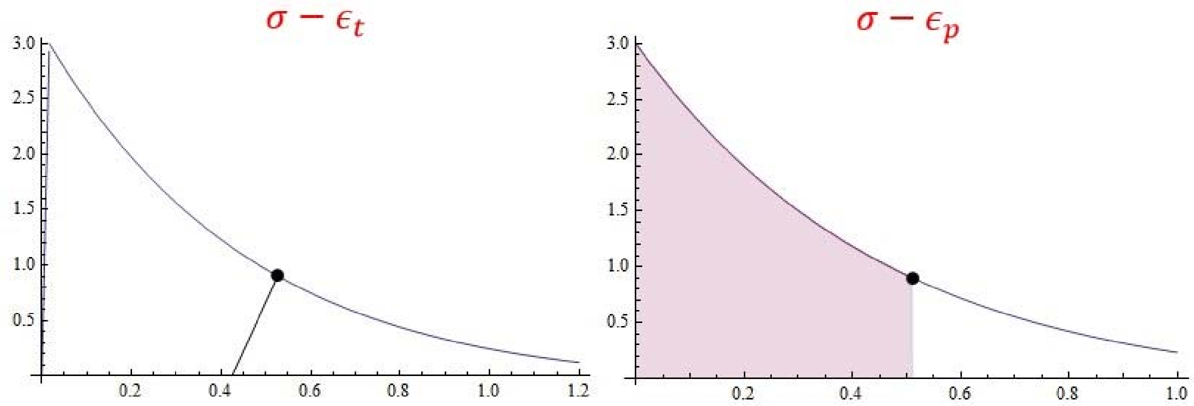

Figure 3.9 Variation of Tension Damage Parameter d_t

The shaded area in the right side of Fig 3.9 represent the level of damage in the stress-plastic strain space. The percentage of this area with respect the total area is the amount of scalar damage at the continuum point.

Similarly, the compression damage can be calculated as shown in Eq 3.28

$$d_c = \frac{\int_0^{\tilde{\varepsilon}_c^{pl}} d_c\left(\tilde{\varepsilon}_c^{pl}\right)}{\int_0^{\tilde{\varepsilon}_{cf}^{pl}} d_c\left(\tilde{\varepsilon}_c^{pl}\right)} \tag{3.28}$$

The graphical interpretation of Eq 3.28 is shown in Fig 3.10.

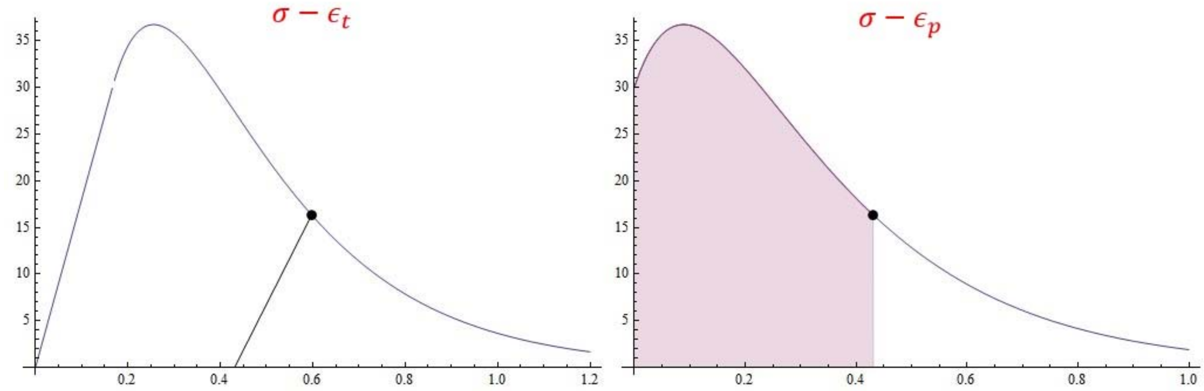

Figure 3.10 Variation of Compression Damage Parameter d_c

The uniaxial degradation variables are increasing functions of the equivalent plastic strains. They can take values ranging from zero, for the undamaged material, to one, for the fully damaged material as shown in Fig. 3.11.

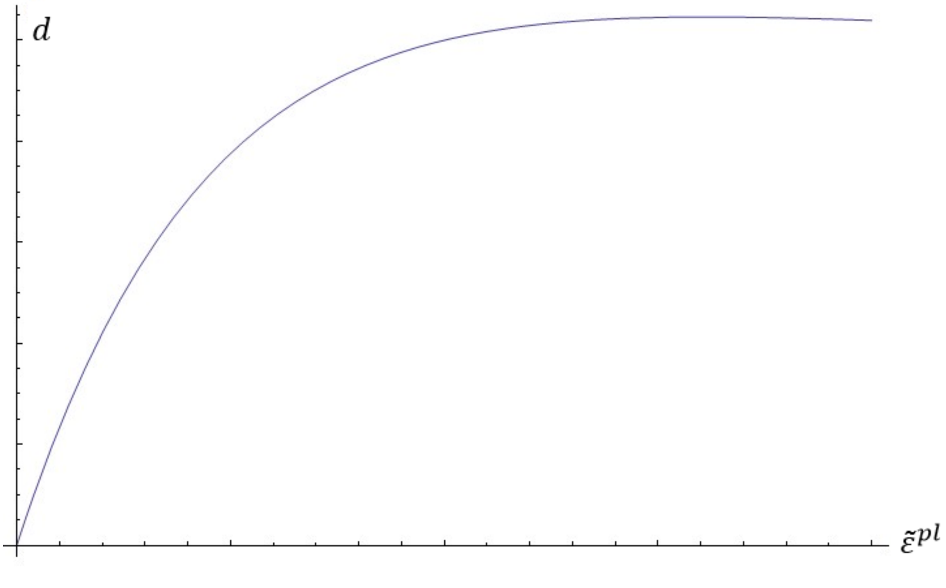

Figure 3.11 Variation Damage Parameter d with Respect to Effective Plastic Strain $\tilde{\varepsilon}^{pl}$

If E_0 is the initial (undamaged) elastic stiffness of the material, the stress-strain relations under uniaxial tension and compression loading are, respectively:

$$\sigma_t = (1 - d_t)E_0\left(\varepsilon_t - \tilde{\varepsilon}_t^{pl}\right) \tag{3.29}$$

$$\sigma_c = (1 - d_c)E_0\left(\varepsilon_c - \tilde{\varepsilon}_c^{pl}\right) \tag{3.30}$$

The effective uniaxial cohesion stresses, $\bar{\sigma}_t$ and, $\bar{\sigma}_c$ are

given as

$$\bar{\sigma}_t = \frac{\sigma_t}{(1-d_t)} = E_0\left(\varepsilon_t - \tilde{\varepsilon}_t^{pl}\right) \tag{3.31}$$

$$\bar{\sigma}_c = \frac{\sigma_t}{(1-d_c)} = E_0\left(\varepsilon_c - \tilde{\varepsilon}_c^{pl}\right) \tag{3.32}$$

The effective uniaxial cohesion stresses determine the size of the yield (or failure) surface.

3.3.5 Multiaxial Conditions

The evolution equations for the hardening variables must be extended for the general multiaxial conditions. Based on Lee and Fenves (1998) it is assumed that the equivalent plastic strain rates are evaluated according to the expressions:

$$\dot{\tilde{\varepsilon}}_t^{pl} = r(\hat{\bar{\sigma}})\dot{\hat{\varepsilon}}_{max}^{pl} \tag{3.33}$$

$$\dot{\tilde{\varepsilon}}_c^{pl} = -(1 - r(\hat{\bar{\sigma}}))\dot{\hat{\varepsilon}}_{min}^{pl} \tag{3.34}$$

where $\dot{\hat{\varepsilon}}_{max}^{pl}$ and $\dot{\hat{\varepsilon}}_{min}^{pl}$ are, respectively, the maximum and minimum eigenvalues of the plastic strain rate tensor $\dot{\hat{\varepsilon}}^{pl}$ and

$$r(\hat{\bar{\sigma}}) = \frac{\sum_{i=1}^{3}\langle\hat{\bar{\sigma}}_i\rangle}{\sum_{i=1}^{3}|\hat{\bar{\sigma}}_i|}\ , \quad 0 \leq r(\hat{\bar{\sigma}}) \leq 1 \tag{3.35}$$

is a stress weight factor that is equal to one if all principal stresses $\hat{\bar{\sigma}}_i$, $(i = 1, 2, 3)$ are positive and equal to zero if they are negative. In uniaxial loading conditions, Eqs 3.33 and 3.34 reduce to the uniaxial definitions Eqs 3.23 and 3.24, since $\dot{\tilde{\varepsilon}}^{pl}_{max} = \dot{\tilde{\varepsilon}}^{pl}_{11}$ in tension, and $\dot{\tilde{\varepsilon}}^{pl}_{min} = \dot{\tilde{\varepsilon}}^{pl}_{11}$ in compression.

If the eigenvalues of the plastic strain rate tensor $(\hat{\dot{\varepsilon}}_i, i = 1{,}2{,}3\ )$ are ordered such that $\dot{\tilde{\varepsilon}}^{pl}_{max} = \hat{\dot{\varepsilon}}_1 \geq \hat{\dot{\varepsilon}}_2 \geq \hat{\dot{\varepsilon}}_3 = \dot{\tilde{\varepsilon}}^{pl}_{min}$, the evolution equation for general multiaxial stress conditions can be expressed in the following matrix form:

$$\dot{\tilde{\varepsilon}}^{pl} = \begin{bmatrix} \dot{\tilde{\varepsilon}}^{pl}_t \\ \dot{\tilde{\varepsilon}}^{pl}_c \end{bmatrix} = h(\hat{\bar{\sigma}}, \tilde{\varepsilon}^{pl}).\, \hat{\dot{\varepsilon}}^{pl} \tag{3.36}$$

where

$$h\left(\hat{\bar{\sigma}}, \tilde{\varepsilon}^{pl}\right) = \begin{bmatrix} r(\hat{\bar{\sigma}}) & 0 & 0 \\ 0 & 0 & (r(\hat{\bar{\sigma}}) - 1) \end{bmatrix} \tag{3.37}$$

and

$$\hat{\dot{\varepsilon}}^{pl} = \begin{bmatrix} \hat{\dot{\varepsilon}}^{pl}_1 \\ \hat{\dot{\varepsilon}}^{pl}_2 \\ \hat{\dot{\varepsilon}}^{pl}_3 \end{bmatrix} \tag{3.38}$$

$$\dot{\tilde{\varepsilon}}^{pl} = \begin{bmatrix} \dot{\tilde{\varepsilon}}^{pl}_t \\ \dot{\tilde{\varepsilon}}^{pl}_c \end{bmatrix} = \begin{bmatrix} r(\hat{\bar{\sigma}}) & 0 & 0 \\ 0 & 0 & (r(\hat{\bar{\sigma}}) - 1) \end{bmatrix} . \begin{bmatrix} \hat{\dot{\varepsilon}}^{pl}_1 \\ \hat{\dot{\varepsilon}}^{pl}_2 \\ \hat{\dot{\varepsilon}}^{pl}_3 \end{bmatrix} = \begin{bmatrix} r(\hat{\bar{\sigma}}) \hat{\dot{\varepsilon}}^{pl}_1 \\ (r(\hat{\bar{\sigma}}) - 1)\ \hat{\dot{\varepsilon}}^{pl}_3 \end{bmatrix} \tag{3.39}$$

Elastic stiffness degradation

The plastic-damage concrete model assumes that the elastic stiffness degradation is isotropic and characterized by a single scalar variable, *d*:

$$D^{el} = (1 - d) D^{el}_0;\ \ 0 \leq d \leq 1 \tag{3.40}$$

The definition of the scalar degradation variable *d* must be consistent with the uniaxial monotonic responses (d_t, and d_c,), and it should also capture the complexity associated with the degradation mechanisms under cyclic loading. For the general multiaxial stress conditions, ABAQUS assumes that:

$$(1-d)=(1-s_t d_c)(1-s_c d_t), \quad 0 \leq s_t, s_c \leq 1 \tag{3.41}$$

similar to the uniaxial cyclic case, only that s_t and s_c are now given in terms of the function $r(\hat{\bar{\sigma}})$ as

$$s_t = 1 - w_t r(\hat{\bar{\sigma}});\ 0 \leq w_t \leq 1 \tag{3.42}$$

$$s_c = 1 - w_c(1 - r(\hat{\bar{\sigma}}));\ 0 \leq w_c \leq 1 \tag{3.43}$$

It can be easily verified that Eq. 3.41 for the scalar degradation variable is consistent with the uniaxial response.

The experimental observation in most quasi-brittle materials, including concrete, is that the compressive stiffness is recovered upon crack closure as the load changes from tension to compression. On the other hand, the tensile stiffness is not recovered as the load changes from compression to tension once crushing micro-cracks have developed. This behavior, which corresponds to $w_t = 0$ and $w_c = 1$, is the default used by ABAQUS. Based on that, the damage parameter will be as follows:

$$s_t = 1.0 \tag{3.44}$$

$$s_c = 1 - \left(1 - r(\hat{\bar{\sigma}})\right) = r(\hat{\bar{\sigma}}) \tag{3.45}$$

$$(1-d)=(1-d_c)(1-r(\hat{\bar{\sigma}})d_t), \quad 0 \leq s_t, s_c \leq 1 \tag{3.46}$$

Fig 3.12 illustrates the variation of the global damage parameter d in the case of uniaxial cyclic loading assuming the default behavior.

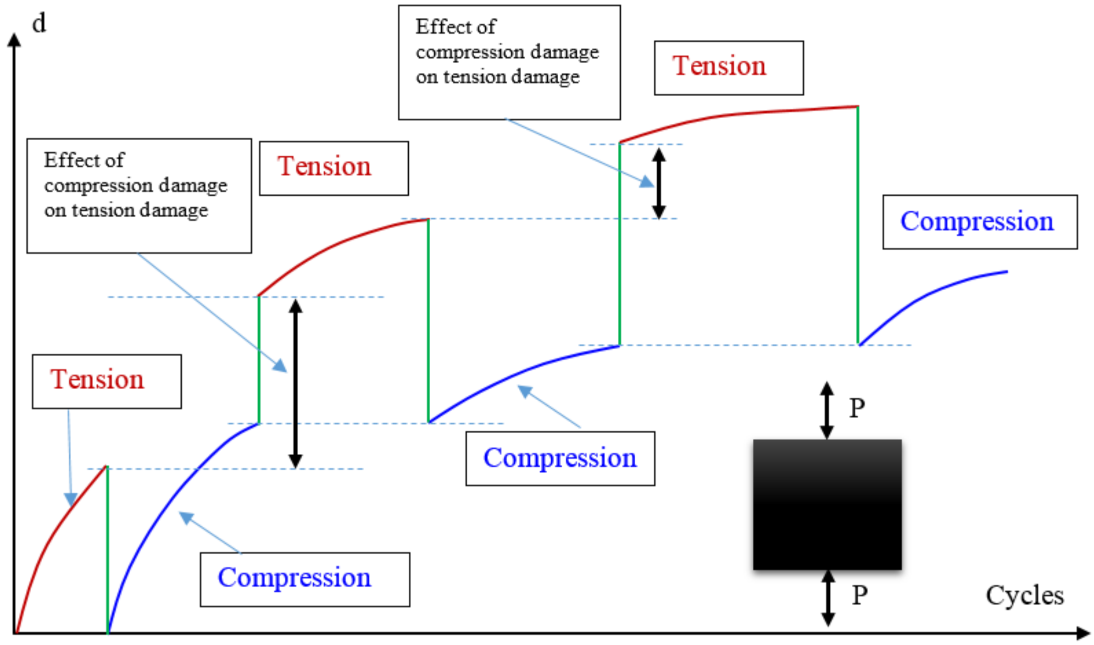

Figure 3.12 Variation of the global damage parameter d with respect to variation of cycles from tension to compression

The variation of the stress with respect to time and cycles is shown in Fig. 3.13

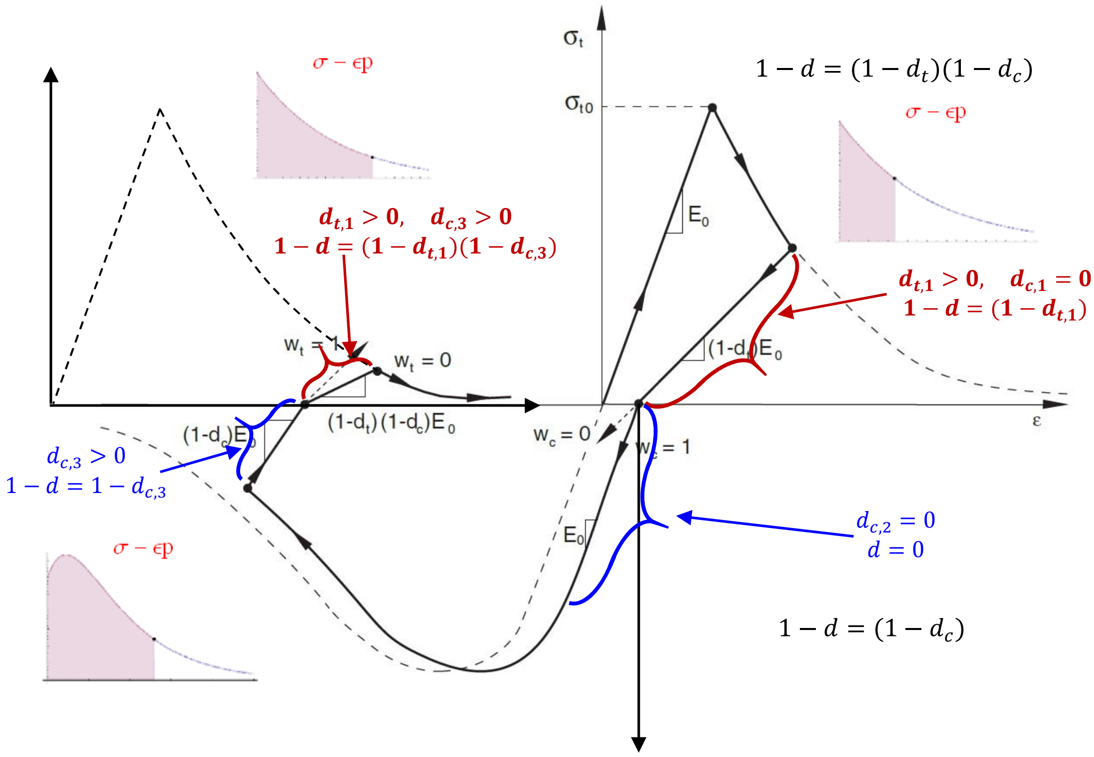

Figure 3.13 Uniaxial load cycle (tension-compression-tension) assuming default values of the stiffness recovery factors.

Cracking (tension) and crushing (compression) in concrete are represented by increasing values of the hardening (softening) variables. These variables control the evolution of the yield surface and the degradation of the elastic stiffness.

3.3.6 Yield Function

The yield function $F(\bar{\sigma}, \tilde{\varepsilon}^{pl})$ represents a surface in effective stress space, which determines the states of failure or damage. For the inviscid plastic-damage model the yield function can be expressed as:

$$F(\bar{\sigma}, \tilde{\varepsilon}^{pl}) \leq 0 \qquad (3.47)$$

The plastic-damage concrete model uses a yield condition based on the yield function originally proposed by Lubliner et al. (1989) and incorporates the modifications proposed subsequently by Lee and Fenves (1998) to account for different evolution of strength under tension and compression. In terms of effective stresses the yield function takes the form (the classical two-parameters Drucker-Prager model is a special case of Eq. 3.48)

$$F(\bar{\sigma}, \tilde{\varepsilon}^{pl}) = \frac{1}{1-\alpha}\left(\bar{q} - 3\alpha\bar{p} + \beta(\tilde{\varepsilon}^{pl})\langle\hat{\bar{\sigma}}_{max}\rangle - \gamma\langle-\hat{\bar{\sigma}}_{max}\rangle\right) - \bar{\sigma}_c\left(\tilde{\varepsilon}_c^{pl}\right) \leq 0 \quad (3.48)$$

Where:

α, γ are dimensionless material constants;

$\bar{p}$ is the effective hydrostatic pressure;

$$\bar{p} = -\frac{1}{3}\bar{\sigma}_{ii} = -\frac{1}{3}\bar{I}_1 \quad (3.49)$$

$\bar{q}$ is the Mises equivalent effective stress;

$$\bar{q} = \sqrt{\frac{3}{2}\bar{s}_{ij}s_{ij}} = \sqrt{3\bar{J}_2} \quad (3.50)$$

$\bar{s}_{ij}$ is the deviatoric component of effective stress $\bar{\sigma}$

$\hat{\bar{\sigma}}_{max}$ is the algebraically maximum eigenvalue of $\bar{\sigma}$.

The function $\beta(\tilde{\varepsilon}^{pl})$ is given as

$$\beta(\tilde{\varepsilon}^{pl}) = \frac{\bar{\sigma}_c\left(\tilde{\varepsilon}_c^{pl}\right)}{\bar{\sigma}_t\left(\tilde{\varepsilon}_c^{pl}\right)}(1-\alpha) - (1+\alpha) \quad (3.51)$$

$\bar{\sigma}_c, \bar{\sigma}_t$ are the effective tensile and compressive cohesion stress, respectively, and obtained from 1-D tests in uniaxial compression and uniaxial tension (stress-plastic strain data), and expressed as:

$$\bar{\sigma}_c\left(\tilde{\varepsilon}_c^{pl}\right) = \frac{\sigma_c}{(1-d_c)} = E_0\left(\varepsilon_c - \tilde{\varepsilon}_c^{pl}\right) \quad (3.52)$$

$$\bar{\sigma}_t\left(\tilde{\varepsilon}_t^{pl}\right) = \frac{\sigma_t}{(1-d_t)} = E_0\left(\varepsilon_t - \tilde{\varepsilon}_t^{pl}\right) \quad (3.53)$$

The $\beta(\tilde{\varepsilon}^{pl})$ parameter controls the size of the yield surface in regions where $\hat{\bar{\sigma}}_{max} \geq 0$ whereas γ controls the shape of the trace of yield surface in the deviatoric plane for stress states of biaxial and triaxial compression $\hat{\bar{\sigma}}_{max} \leq 0$

In biaxial compression, with $\hat{\bar{\sigma}}_{max} = 0$, Eq. 3.48 reduces to the well-known Drucker-Prager yield condition. The coefficient α can be determined by direct application of yield criteria as given by Eq. 3.48 for equal biaxial compression and for uniaxial compression (for both cases, $\hat{\bar{\sigma}}_{max} = 0$) and solving for α, one obtains:

$$\alpha = \frac{(\sigma_{b0}/\sigma_{c0})-1}{2(\sigma_{b0}/\sigma_{c0})-1} \tag{3.54}$$

where:

σ_{c0} is the uniaxial compression strength of concrete.

σ_{b0} is the biaxial compression strength of concrete.

Typical experimental values of the ratio $\sigma_{b0}/\sigma_{c0}$for concrete are in the range from 1.10 to 1.16, yielding values of α between 0.08 and 0.12 (Lubliner et al, (1989)).

The coefficient γ enters the yield function only for stress states of triaxial compression, when $\hat{\bar{\sigma}}_{max} \leq 0$. This coefficient can be determined by comparing the yield conditions along the tensile and compressive meridians. By definition, the *tensile meridian* (TM) is the locus of stress states satisfying the condition $\hat{\bar{\sigma}}_{max} = \hat{\bar{\sigma}}_1 \geq \hat{\bar{\sigma}}_2 = \hat{\bar{\sigma}}_3$, and the *compressive meridian* (CM) is the locus of stress states such that $\hat{\bar{\sigma}}_{max} = \hat{\bar{\sigma}}_1 = \hat{\bar{\sigma}}_2 \geq \hat{\bar{\sigma}}_3$, where , $\hat{\bar{\sigma}}_1, \hat{\bar{\sigma}}_2$, and $\hat{\bar{\sigma}}_3$ are the eigenvalues of the effective stress tensor.

One may show in general:

$$\bar{s}_1 = \frac{2}{\sqrt{3}}\sqrt{J_2}cos\ \theta \tag{3.55}$$

$$\bar{s}_2 = \frac{2}{\sqrt{3}}\sqrt{J_2}cos\ \left(\frac{2\pi}{3} - \theta\right) \tag{3.56}$$

$$\bar{s}_3 = \frac{2}{\sqrt{3}}\sqrt{J_2}cos\ \left(\frac{2\pi}{3} + \theta\right) \tag{3.57}$$

Where $\bar{s}_i$ are the principal values of the effective deviatoric stress tensor $\bar{s}_{ij}$, and θ is the angle of similarity measured from the projection of $\bar{\sigma}_1$ in the deviatoric plane. For the tensile meridian, $= 0^o$, whereas for the compression meridian, $\theta = 60^o$.

Substituting the appropriate values of θ in expressions for $\bar{s}_i$ and expressing $\bar{\sigma}_1$ in terms of $\bar{s}_1$

$$(\hat{\bar{\sigma}}_{max})_{TM} = \bar{\sigma}_1 = \bar{s}_1 - \bar{p} = \frac{2}{\sqrt{3}}\sqrt{J_2} - \bar{p} = \frac{2\bar{q}}{3} - \bar{p} \tag{3.58}$$

$$(\hat{\bar{\sigma}}_{max})_{CM} = \bar{\sigma}_1 = \bar{s}_1 - \bar{p} = \frac{1}{\sqrt{3}}\sqrt{J_2} - \bar{p} = \frac{\bar{q}}{3} - \bar{p} \tag{3.59}$$

With $\hat{\bar{\sigma}}_{max} < 0$, the corresponding yield conditions are:

$$\left(\frac{2}{3}\gamma + 1\right)\bar{q} - (\gamma + 3\alpha)\bar{p} = (1 - \alpha)\bar{\sigma}_c \quad (TM) \tag{3.60}$$

$$\left(\frac{1}{3}\gamma + 1\right)\bar{q} - (\gamma + 3\alpha)\bar{p} = (1 - \alpha)\bar{\sigma}_c \quad (CM) \tag{3.61}$$

Let $K_c = \bar{q}_{(TM)}/\bar{q}_{(CM)}$ for any given value of the hydrostatic pressure $\bar{p}$ with $\hat{\bar{\sigma}}_{max} < 0$; then:

$$K_c = \frac{\gamma+3}{2\gamma+3} \tag{3.62}$$

The fact that K_c is constant does not seem to be contradicted by experimental evidence (Lubliner et al (1989)). The coefficient γ is, therefore, evaluated as

$$\gamma = \frac{3(1-K_c)}{2K_c-1} \tag{3.63}$$

It was suggested by Lubliner (1989) that, the value of K_c ranging from 0.66 to 0.8.

If $\hat{\bar{\sigma}}_{max} > 0$, the yield conditions along the tensile and compressive meridians reduce to:

$$\left(\frac{2}{3}\beta + 1\right)\bar{q} - (\beta + 3\alpha)\bar{p} = (1-\alpha)\bar{\sigma}_c \quad (TM) \tag{3.64}$$

$$\left(\frac{1}{3}\beta + 1\right)\bar{q} - (\beta + 3\alpha)\bar{p} = (1-\alpha)\bar{\sigma}_c \quad (CM) \tag{3.65}$$

Let $K_t = \bar{q}_{(TM)}/\bar{q}_{(CM)}$ for any given value of the hydrostatic pressure $\bar{p}$ with $\hat{\bar{\sigma}}_{max} > 0$; then:

$$K_t = \frac{\beta+3}{2\beta+3} \tag{3.66}$$

When the value of $\beta(\tilde{\varepsilon}^{pl})$ and γ are set to zero, then the well know Drucker-Prager surface rustles as shown in Figs 3.14 and 3.15.

$$F(\bar{\sigma}, \tilde{\varepsilon}^{pl}) = \frac{1}{1-\alpha}\left(\bar{q} - 3\alpha\bar{p} + \cancel{\beta(\tilde{\varepsilon}^{pl})\langle\hat{\bar{\sigma}}_{max}\rangle - \gamma\langle-\hat{\bar{\sigma}}_{max}\rangle}\right) - \bar{\sigma}_c\left(\tilde{\varepsilon}_c^{pl}\right) \leq 0 \tag{3.67}$$

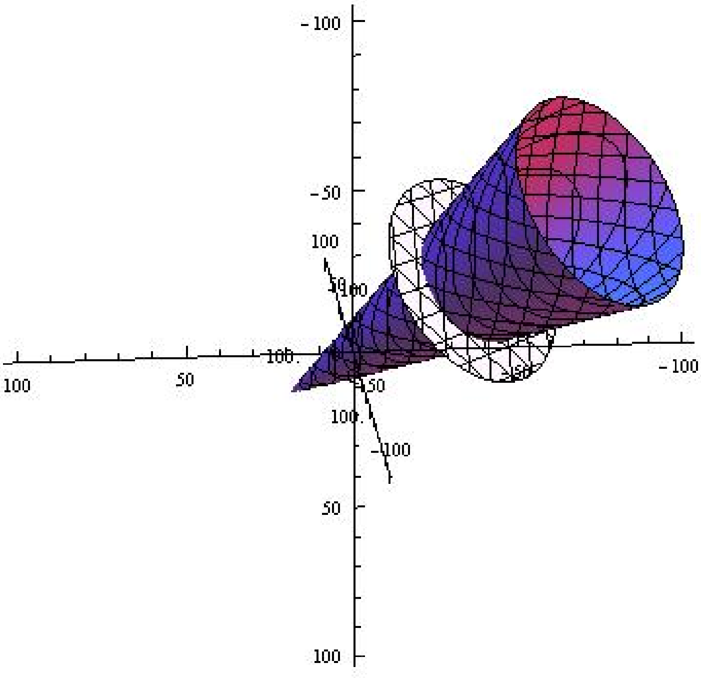

Figure 3.14 Drucker-Prager surface (Eq 3.67)

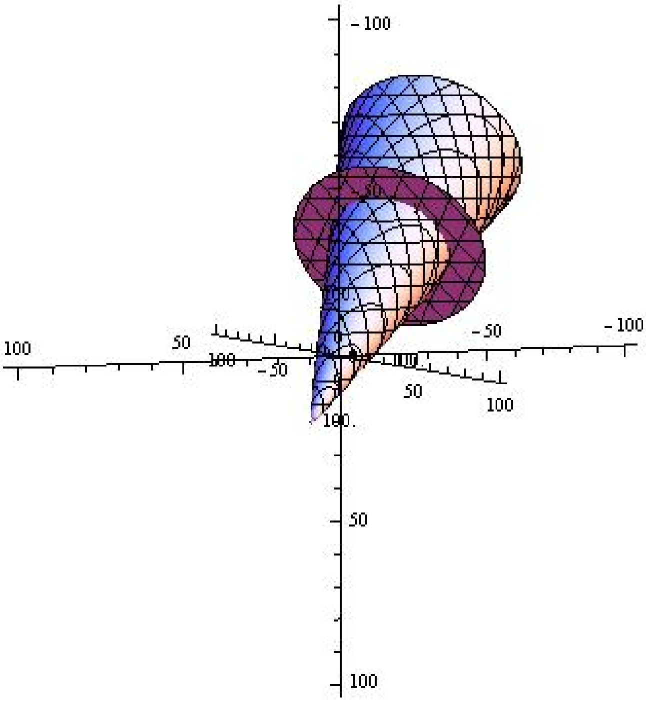

Figure 3.15 Drucker-Prager surface (Eq 3.67)

The Drucker-Prager surface is well known to have a circular shape in the deviatoric plane as show in Fig. 3.16

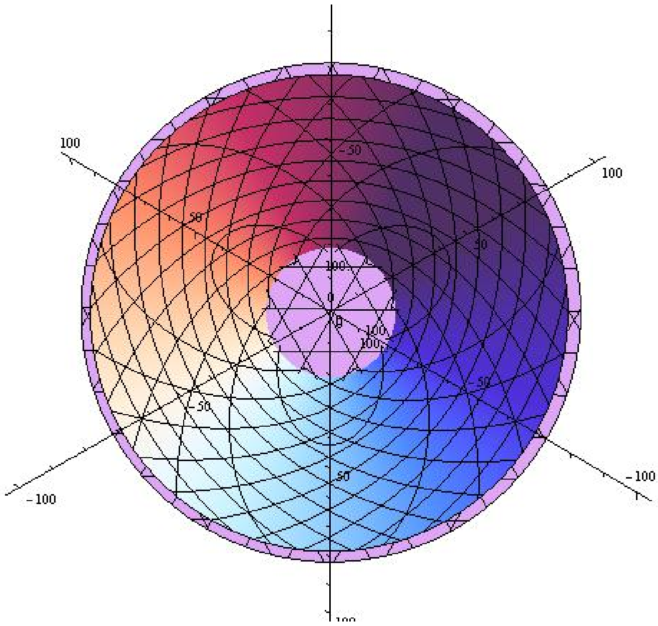

Figure 3.16 View of Drucker-Prager surface (Eq 3.67) in the deviatoric plane

When the $\beta(\tilde{\varepsilon}^{pl})$ and γ parameters are effective (not equal to zero) the 3D surface of the yield function presented in Eq 3.67 is shown in Fig. 3.17 and 3.18.

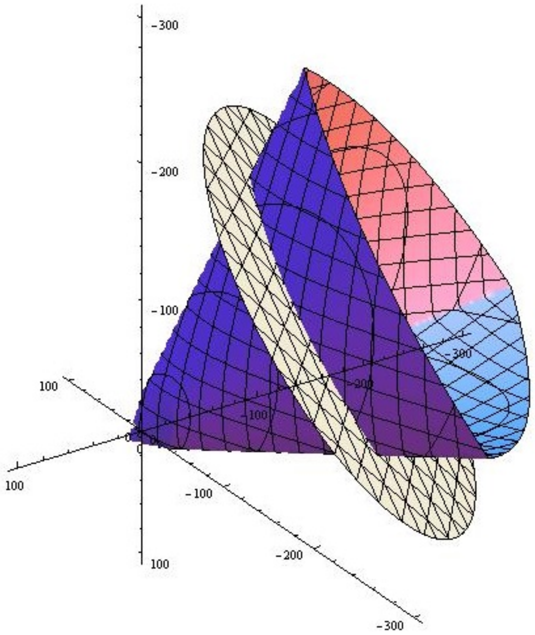

Figure 3.17 3D surface view of the yield function presented in Eq 3.48

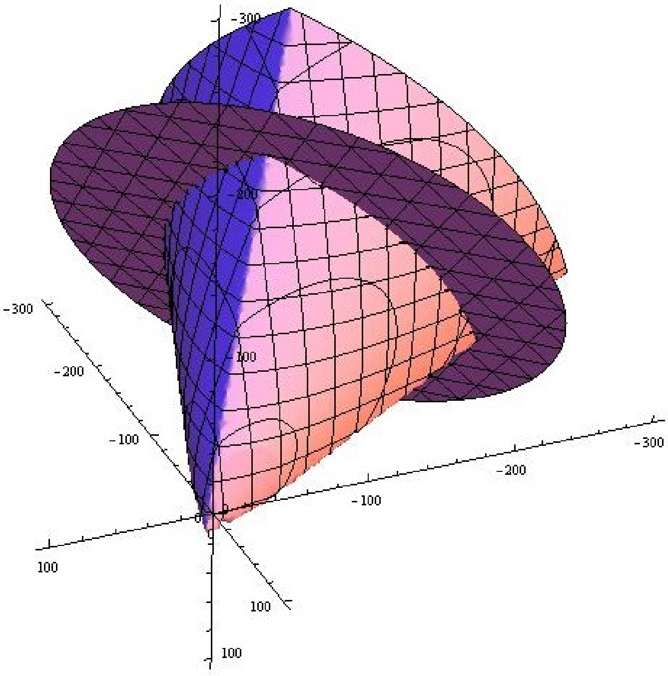

Figure 3.18 3D surface view of the yield function presented in Eq 3.48

In the deviatoric plane, the surface is close to triangular shape as shown in Fig. 3.19.

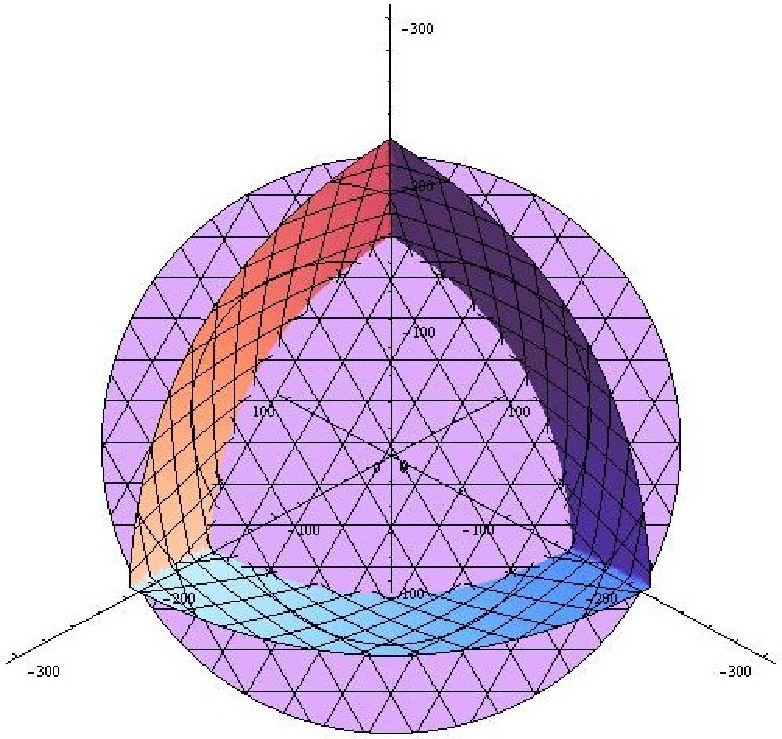

Figure 3.19 View in the deviatoric plane of the yield function presented in Eq 3.48

Typical yield surfaces are shown in Fig 3.20 in the deviatoric plane for $\hat{\hat{\sigma}}_{max} \leq 0$ and in Fig 3.21 for plane-stress conditions. Eq. 3.66, when plotted, would trace locus of yield surface in deviatoric plane for $\hat{\hat{\sigma}}_{max} > 0$.

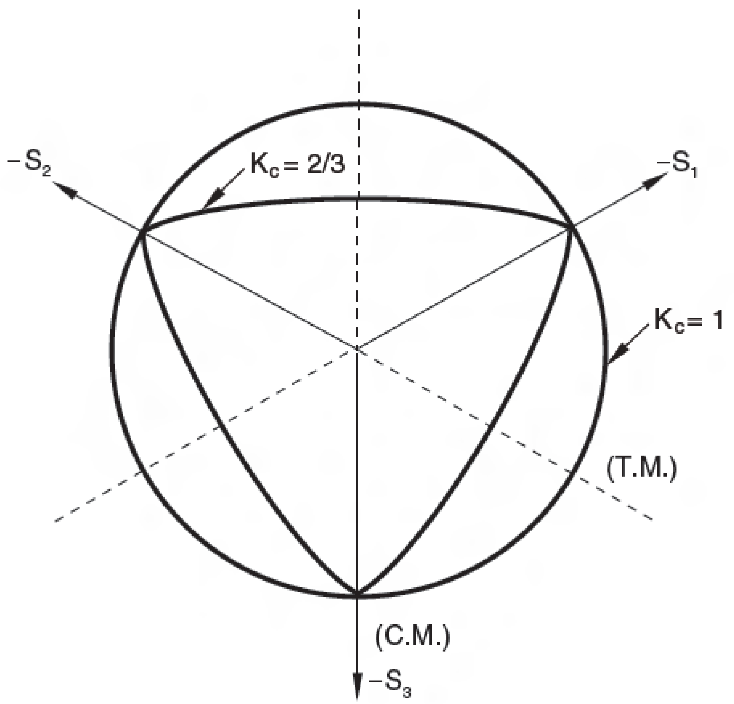

Figure 3.20 Yield surfaces in the deviatoric plane, corresponding to different values of K_c

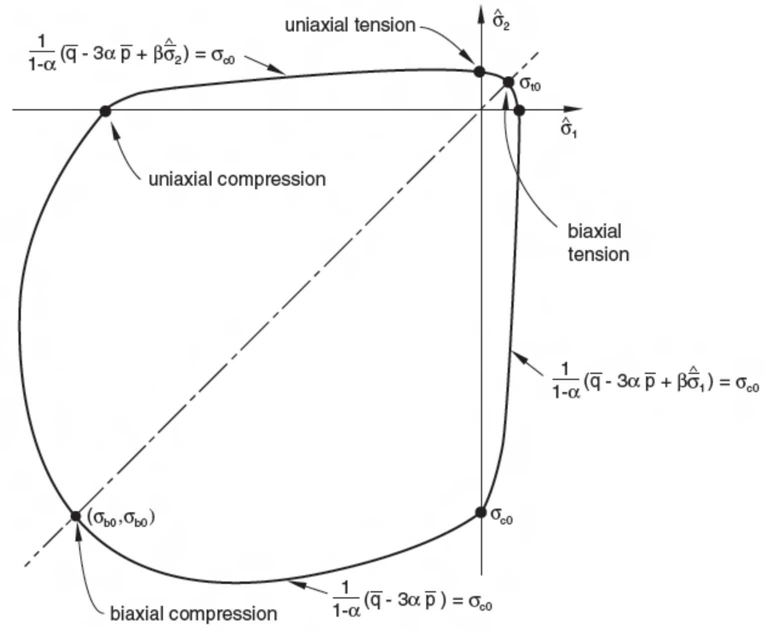

Figure 3.21 Yield surface in plane stress.

3.3.7 Flow Rule

Plastic flow is governed by a flow potential function $G(\bar{\sigma})$ according to nonassociative flow rule:

$$\dot{\varepsilon}^{pl} = \dot{\lambda}\frac{\partial G(\bar{\sigma})}{\partial \bar{\sigma}} \tag{3.68}$$

where $\dot{\lambda}$ is the nonnegative plastic multiplier. The plastic potential is defined in the effective stress space. The model uses nonassociated plasticity, therefore requiring the solution of nonsymmetric equations. The fundamental group of the constitutive parameters consists of four values, which identify the shape of the flow potential surface and the yield surface. In this model for the flow potential G, the Drucker-Prager hyperbolic function is accepted in the form:

$$G = \sqrt{(\epsilon\sigma_{t0}\tan\psi)^2 + \bar{q}^2} - \bar{p}\tan\psi \tag{3.69}$$

where ψ is the dilation angle measured in the *p–q* plane at high confining pressure; σ_{t0} is the uniaxial tensile stress at failure; and ϵ is a parameter, referred to as the eccentricity, that defines the rate at which the function approaches the asymptote (the flow potential tends to a straight line as the eccentricity tends to zero).This flow potential, which is continuous and smooth, ensures that the flow direction is defined uniquely.

Graphical representation of potential function $G(\bar{\sigma})$ is shown in Figs. 3.22 and 3.23

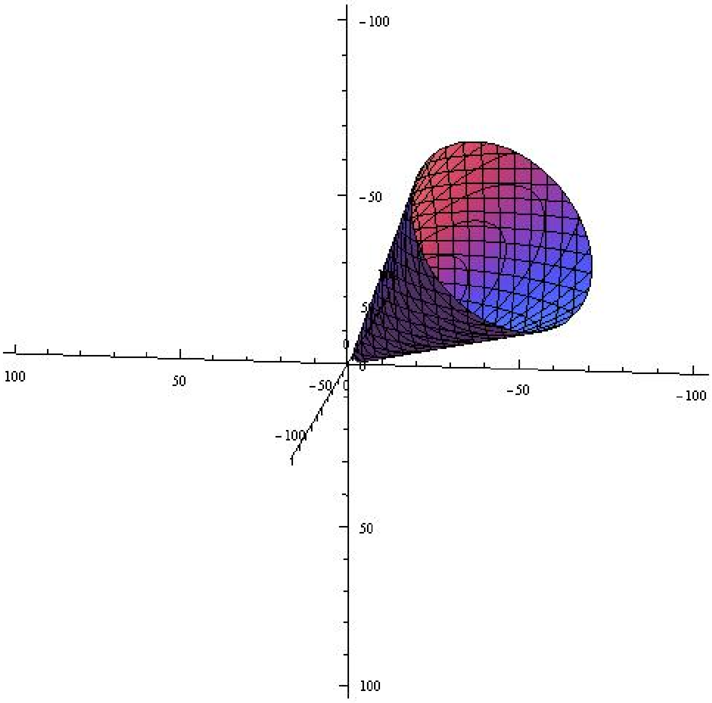

Figure 3.22 3D surface view of the potential function presented in Eq 3.69

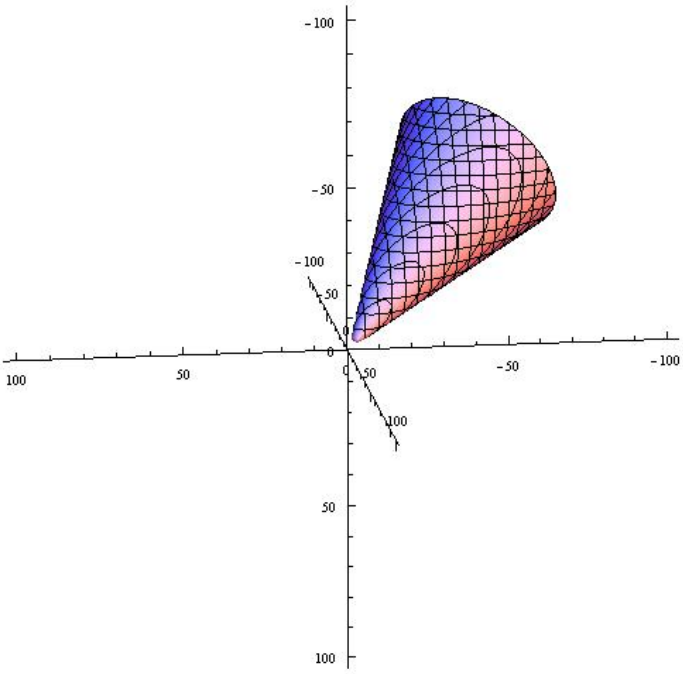

Figure 3.23 3D surface view of the potential function presented in Eq 3.69

The function asymptotically approaches the linear Drucker-Prager flow potential at high confining pressure stress and intersects the hydrostatic pressure axis at 90°.

For the propose of compression, the yield function $F(\bar{\sigma}, \tilde{\varepsilon}^{pl})$ and the plastic potential function $G(\bar{\sigma})$ are plotted together and shown in Figs. 3.24 and 3.25.

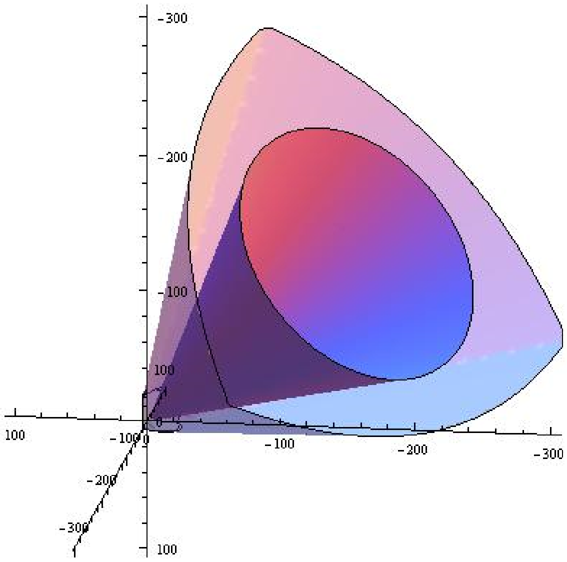

Figure 3.24 3D surface view of the yield function $F(\bar{\sigma}, \tilde{\varepsilon}^{pl})$ (Eq 3.48) and potential function $G(\bar{\sigma})$ (Eq 3.69)

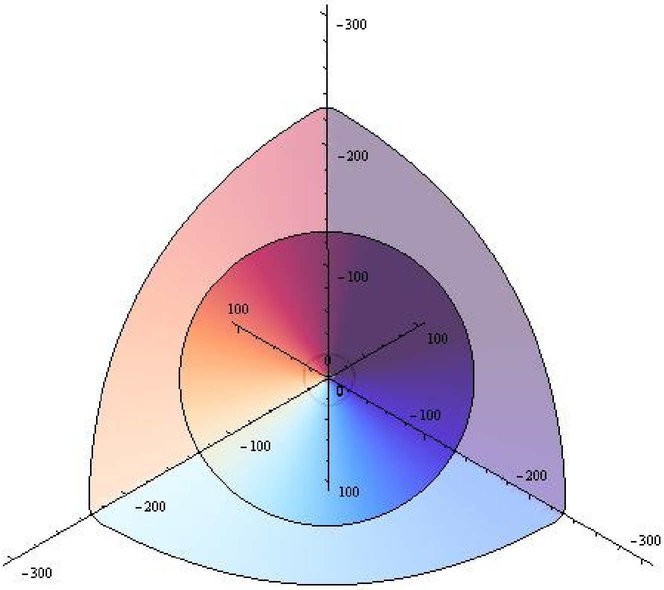

Figure 3.25 View in the deviatoric plane of the yield function $F(\bar{\sigma}, \tilde{\varepsilon}^{pl})$ and potential function $G(\bar{\sigma})$

3.4 Review of the Interface Modeling Approach.

As mentioned before, two different approach was adopted in this study. The first approach was continuum-based approach in which both sandstone and lime mortar was modeled as continuum material. The interface between the two material was assumed perfect bond. The second approach was interface base approach in which sandstone was modeled as continuum material whereas the lime mortar was modeled as interface. In ABAQUS/Explicit, the surface-base-cohesive approach was adopted. Surface based cohesive behavior is primarily intended for situations in which the interface thickness in negligibly small. In this surface-based behavior adopted in this model, the contacted surfaces are the surfaces of the adjacent bricks themselves which means that, the lime mortar thickness have been assumed to be zero as the nature of the surface-based cohesive behavior suggested. Three main ingredients of the surface based cohesive behavior namely:

- Linear elastic traction-separation model.
- Damage model
    1. Damage initiation.
    2. Damage evolution.

3.4.1 Linear Elastic Traction-Separation Model.

In the linear elastic traction separation model, the behavior can be molded either though coupled or uncoupled low. In the coupled low behavior, the traction stress vector is related to the separation vector though a full-populated stiffens matrix as shown in Eq 3.70

$$\begin{Bmatrix} t_n \\ t_s \\ t_t \end{Bmatrix} = \begin{bmatrix} K_{nn} & K_{ns} & K_{nt} \\ K_{ns} & K_{ss} & K_{st} \\ K_{nt} & K_{st} & K_{tt} \end{bmatrix} \begin{Bmatrix} \delta_n \\ \delta_s \\ \delta_t \end{Bmatrix} = \mathbf{K\delta} \tag{3.70}$$

For the uncoupled behavior, the off diagonal terms are set to be zero as shown in Eq. 3.71

$$\begin{Bmatrix} t_n \\ t_s \\ t_t \end{Bmatrix} = \begin{bmatrix} K_{nn} & 0 & 0 \\ 0 & K_{ss} & 0 \\ 0 & 0 & K_{tt} \end{bmatrix} \begin{Bmatrix} \delta_n \\ \delta_s \\ \delta_t \end{Bmatrix} = \mathbf{K\delta} \tag{3.71}$$

If the stiffness values of the material in the three normal direction are not specified, they will have the default values provided by ABAQUS.

3.4.2 Damage Model

Damage modeling allows simulate the degradation and failure of the bond between two cohesive surfaces. The failure mechanism consists of two ingredients: a damage initiation criterion and a damage evolution law. The initial response is assumed to be linear. However, once a damage initiation criterion is met, damage can occur according to a user-defined damage evolution law. Fig 3.26 shows a typical traction-separation response with a failure mechanism.

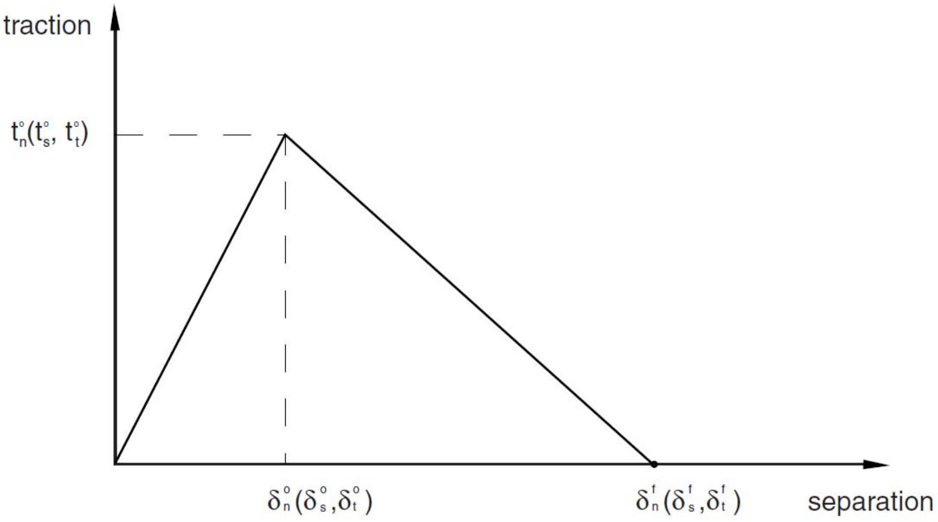

Figure 3.26 Traction separation criteria used for interface modeling.

Where:

t_n^0 is the peak value of the contact stress in the normal direction

t_s^0, t_t^0 are the peak values of the contact stress in the two orthogonal tangential directions.

δ_n^0 is peak value of the contact separation in the normal direction.

$\delta_s^0,\ \delta_t^0$ are peak value of the contact separation in the two orthogonal tangential directions.

δ_n^f is the maximum value of the contact separation in the normal direction.

$\delta_s^f,\ \delta_t^f$ are the maximum value of the contact separation in the two orthogonal tangential directions.

It has to be mentioned that cohesive surfaces do not undergo damage under pure compression.

Damage of the traction-separation response for cohesive surfaces is defined within the same general framework used for conventional materials except the damage behavior is specified as part of the interaction properties for the surfaces. Multiple damage response mechanisms are not available for cohesive surfaces: cohesive surfaces can have only one damage initiation criterion and only one damage evolution law.

3.4.2.1 Damage Initiation.

Damage initiation refers to the beginning of degradation of the cohesive response at a contact point. The process of degradation begins when the contact stresses and/or contact separations satisfy certain damage initiation criteria that you specify. Several damage initiation criteria are available in ABAQUS. In this study, quadratic stress criterion was adopted. The Quadratic stress criterion is descripted as follows:

$$\left\{\frac{\langle t_n\rangle}{t_n^0}\right\}^2+\left\{\frac{t_s}{t_s^0}\right\}^2+\left\{\frac{t_t}{t_t^0}\right\}^2=1.0 \tag{3.72}$$

where:

t_n is the actual applied value of the contact stress in the normal direction.

t_s, t_t are the applied value of the contact stress in the two tangential directions.

Damage is assumed to initiate when a quadratic interaction function involving the stress ratios (as defined in Eq 3.72) reaches a value of one.

After that, the damage evolution was controlled based on fracture energy which was found from the traction-separation (stress displacement) curve of the lime mortar.

3.4.2.2 Damage Evolution.

The damage evolution law describes the rate at which the cohesive stiffness is degraded once the corresponding initiation criterion is reached. A scalar damage variable, *D*, represents the overall damage at the contact point. It initially has a value of 0. If damage evolution is modeled, *D* monotonically evolves from 0 to 1 upon further loading after the initiation of damage. The contact stress components are affected by the damage according to:

$$t_n = \begin{cases} (1-D)\bar{t}_n, & \bar{t}_n > 0 \\ \bar{t}_n, & otherwise \end{cases} \tag{3.73}$$

$$t_s = \begin{cases} (1-D)\bar{t}_s, & \bar{t}_s > 0 \\ \bar{t}_s, & otherwise \end{cases} \tag{3.74}$$

$$t_t = \begin{cases} (1-D)\bar{t}_t, & \bar{t}_t > 0 \\ \bar{t}_t, & otherwise \end{cases} \tag{3.75}$$

Where $\bar{t}_n$, $\bar{t}_s$ and $\bar{t}_t$ are the contact stress components predicted by the elastic traction-separation behavior for the current separations without damage. The evolution of the damage parameter *D* is described by several methods. In this study, the fracture energy was adopted for describing the evolution of the damage parameter *D*. The fracture energy is equal to the area under the traction-separation curve.

3.4.2.3 Evolution Based on Energy

Damage evolution can be defined based on the energy that is dissipated as a result of the damage process (also called the fracture energy). The fracture energy is equal to the area under the traction-separation curve (Fig 3.27).

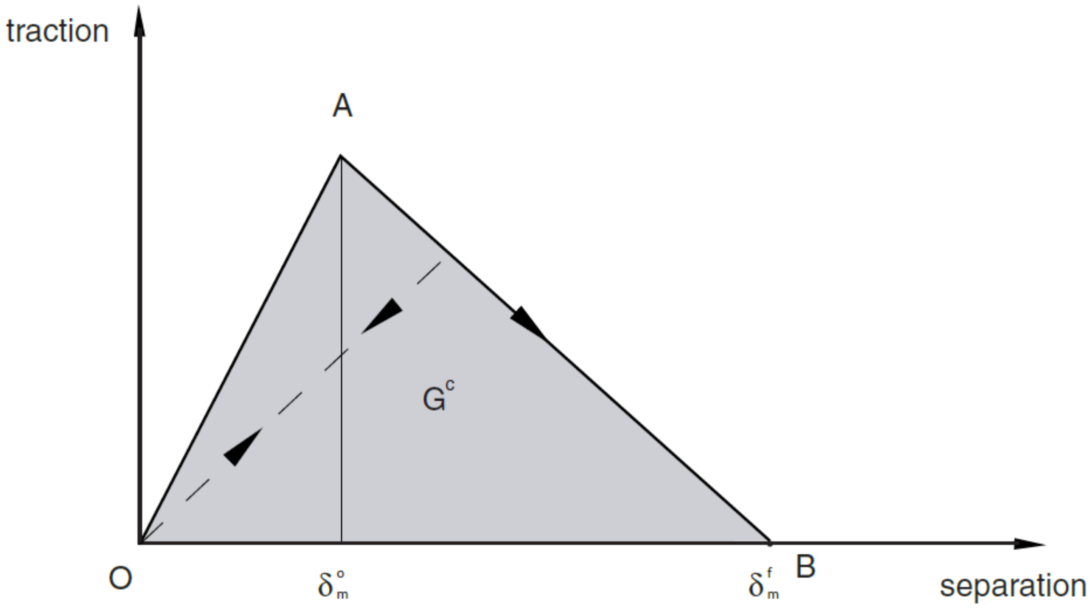

Figure 3.27 Fracture energy equal the area under traction-separation curve.

Fracture energy can be specified as a property of the cohesive interaction and it can be chosen either a linear or an exponential softening behavior. ABAQUS ensures that the area under the linear or the exponential damaged response is equal to the fracture energy.

In this study, power law was adopted to specify the evolution of the damage. The power law criterion states that failure under mixed-mode conditions is governed by a power law interaction of the energies required to cause failure in the individual (normal and two shear) modes. It is given by:

$$\left\{\frac{G_n}{G_n^C}\right\}^{\alpha} + \left\{\frac{G_s}{G_s^C}\right\}^{\alpha} + \left\{\frac{G_t}{G_t^C}\right\}^{\alpha} = 1.0 \qquad (3.76)$$

where:

G_n^C is the critical fracture energy required to cause failure in the normal direction.

G_s^C, G_t^C are the critical fracture energies required to cause failure in the first, and the second shear directions.

G_n is the actual fracture energy corresponding to the t_n traction stress in the normal direction.

$G_s,\ G_t$ are the actual fracture energies corresponding to the t_s and t_t traction stresses in the first, and the second shear directions.

α is the power law exponent.

CHAPTER 4

EXPERIMENTAL INVESTIGATIONS

4.1 Introduction

Masonry walls subjected to both axial as well as horizontal cyclic loading have been studied quite well by several researches as mentioned previously. All experimental programs aim at better understanding of behavior of walls under such loading and then protecting masonry structures against any hazard that my case damage to the masonry walls.

In this study, several experimental tests have been carried out (in order to carry out nonlinear simulation), including sandstone and lime mortar mechanical properties tests, prisms compression tests, bond test between brick and mortar, and complete wall tests under in-plane cyclic loading. The tests conducted in this study were as follows:

1. Mechanical properties tests of sandstone.
2. Mechanical properties tests of lime mortar.
3. Prism compression test
4. Sandstone-mortar interaction test
5. Full-scale wall test.

The data found from the above-mentioned tests will be used in the numerical simulation. Flow chart of the experimental and numerical programs is shown in Fig 4.1

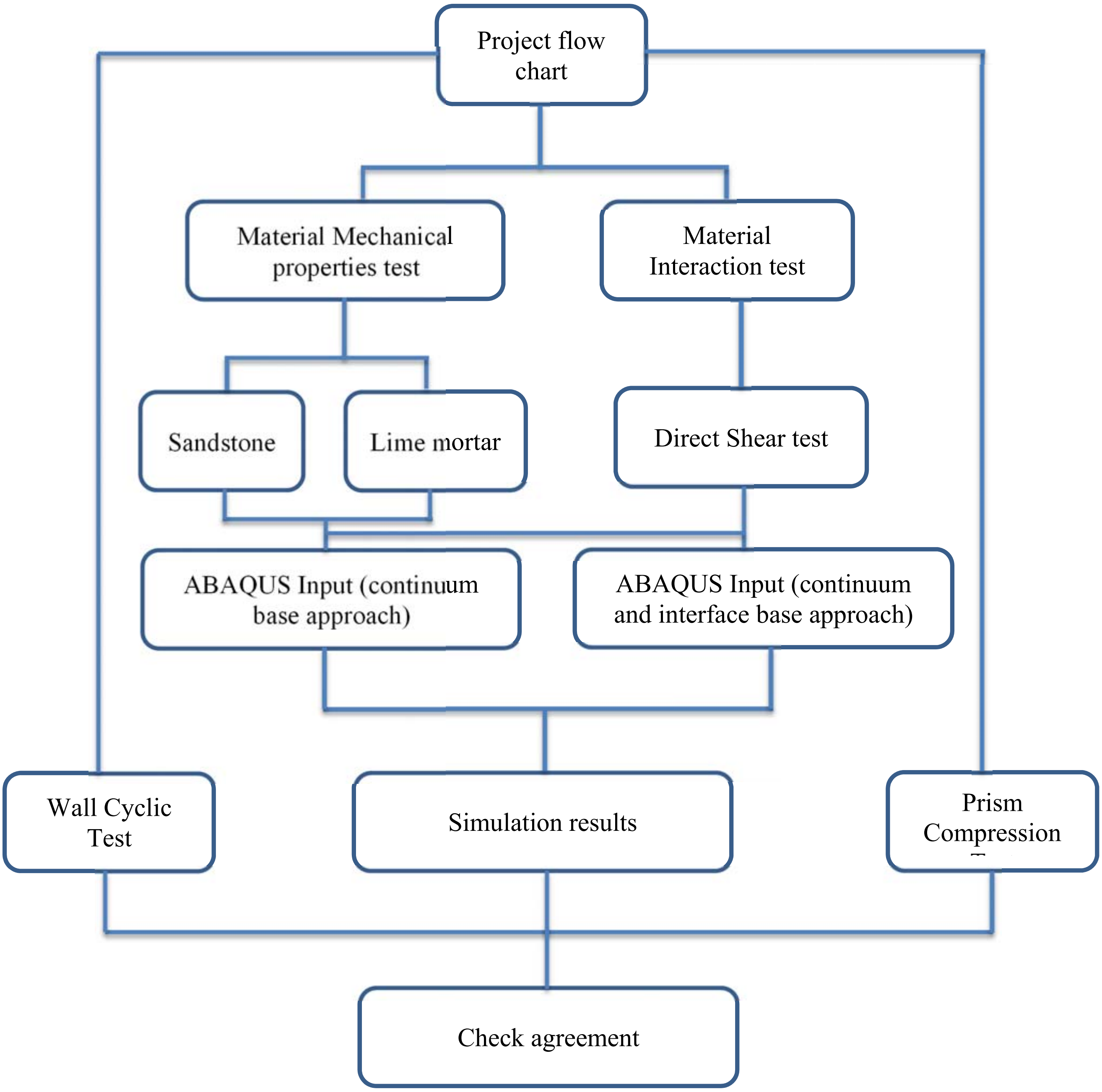

Figure 4.1 Flow Chart of the Experimental Investigation

4.2 Mechanical Properties of Sandstone.

Three main tests have been conduction to sandstone material. Those tests were

- Compression tests
- Tension tests
- Three point bend test

Tests procedures and details were all based on ASTM specifications

4.2.1 Sandstone Uniaxial Compression Test.

For compression test, cylindrical specimens were used to find the compressive behavior of the sandstone material. Specimens have been prepared according to the ASTM D 4543. According to ASTM, the ratio of height to diameter should be less than 2.5 and more than 2.0. For that, the dimensions of the specimens were chosen (Fig 4.2)

$$L = 150\ mm, D = 74\ mm$$

$$2.0 < \frac{L}{D} = \frac{150}{74} = 2.03 < 2.5$$

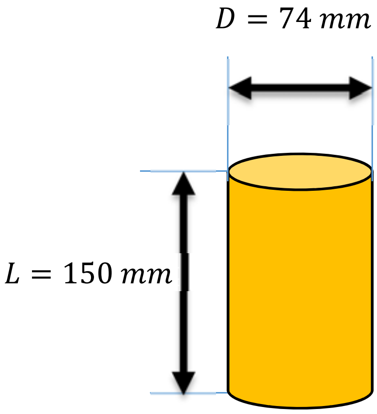

Figure 4.2 Dimensions of cylinders test under uniaxial compression

Cylindrical specimens have been prepared by coring from a sandstone rocks plate using a coring machine. Due to the nature of coring process, the outer surfaces of the cylinders were not perfectly smooth. Because of that, an abrasive process have been done to the surface of the cylinders using sandpaper (Figs 4.3).

Figure 4.3 Coring and polishing process of sandstone cylinders.

For testing the specimens in uniaxial compression, procedure have been followed in according to ASTM D 2938 – 95. Two type of compression tests were conducted namely:

i. Compression test to find only the ultimate strength of the material,
ii. Test conducted to find all mechanical properties (ultimate strength, stress strain curve, Young Modulus and Poisson's ratio).

In the first type of compression test (i), the target was to find only the ultimate strength of sandstone. This test was conducted using ELE compression testing machine. Specimens were measured in three different location to find height and diameter as shown in Table 4.1.

Table 4.1 Dimension of sandstone samples used in uniaxial compression test

Name	h mm	D mm	h/D -
SCTS-1	150.29	73.67	2.04
SCTS-2	151.96	73.51	2.07
SCTS-3	150.21	73.09	2.06
SCTS-4	152.19	73.51	2.07
SCTS-5	152.11	73.41	2.07
SCTS-6	152.30	73.25	2.08
SCTS-7	150.15	74.02	2.03
SCTS-8	150.02	73.26	2.05

The test was a load control test and the loading rate was fixed at 0.5 KN per second (Figs 4.4 and 4.5). Table 4.2 shows the compression test result of the specimens.

Figure 4.4 Sandstone cylinders made ready for uniaxial compression test.

Figure 4.5 Cylinders under compression test in ELE compression testing machine

Table 4.2 Ultimate strength of the sandstone cylindrical specimens

Name	Strength Mpa
SCTS-1	26.86
SCTS-2	25.54
SCTS-4	37.47
SCTS-5	31.05
SCTS-7	35.90
SCTS-8	30.27

The test result of the compression test reveals that, the average capacity of the sandstone was about 28 MPa with standard deviation of 6.7. The standard deviation of the results was around 6.7. Normal distribution of the result is shown in Fig 4.6

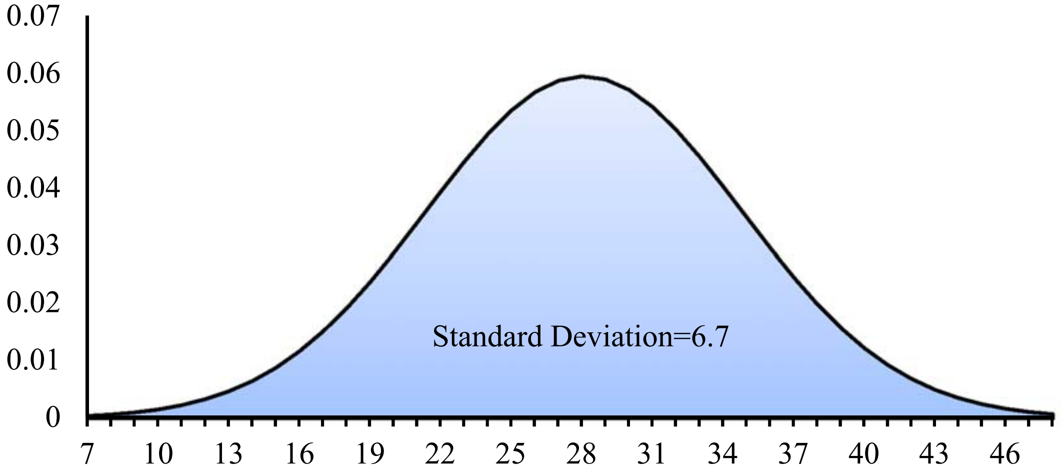

Figure 4.6 Normal Distribution of the sandstone compression test result.

In the second compression test (ii), complete stress strain curve (including the softening branch) was targeted because it is essential to be used in the numerical simulation. For that, displacement control test were adopted with slow loading rate of 0.1 mm per minute (1.6 μm/s). Two PLC-60-11 cross type; strain gauges were used in two opposite sides of the cylinders to efficiently capture the behavior of the cylinders under test and to find Young modulus, and Poisson's ratio (Figs 4.7). The texture of one of the samples after testing is shown in Fig 4.8.

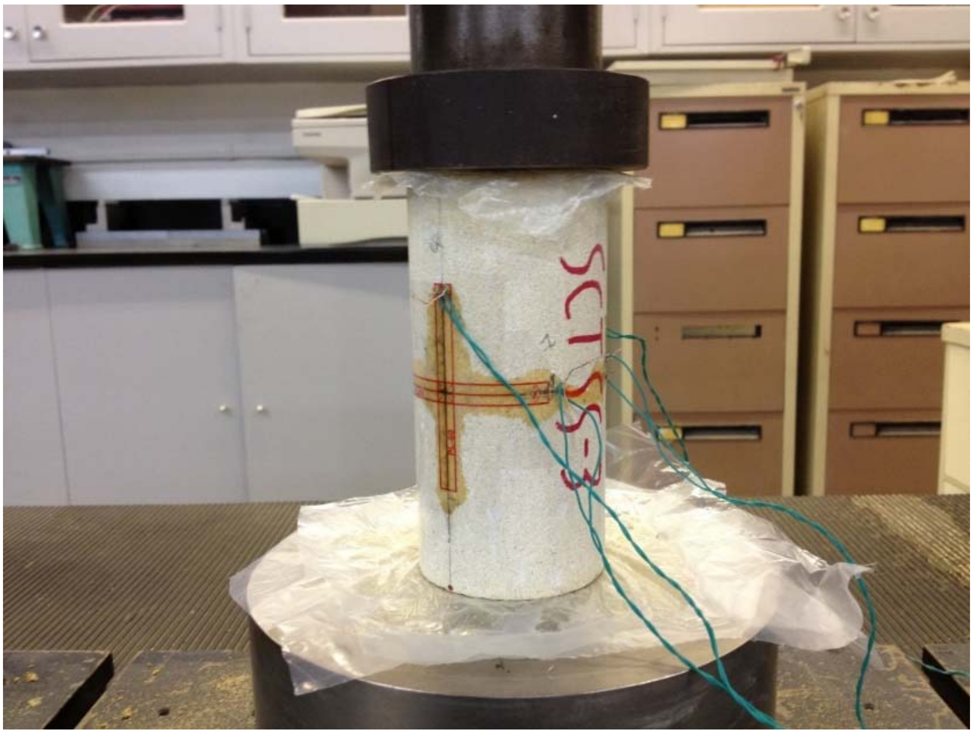

Figure 4.7 PLC-60-11 cross type; strain gauges attached to cylinder under uniaxial compression test

Figure 4.8 Texture of the samples after testing.

Stress strain curves were plotted as shows in Fig 4.9 and 4.10. Due to the nature of the strain gauges, it is not possible to capture the stress-strain curve in the softening branch. For that, the stress-strain curves where found using the displacement between the end loading plates (Fig 4.10). The test were conducted using LLOYD LR 300 K testing machine.

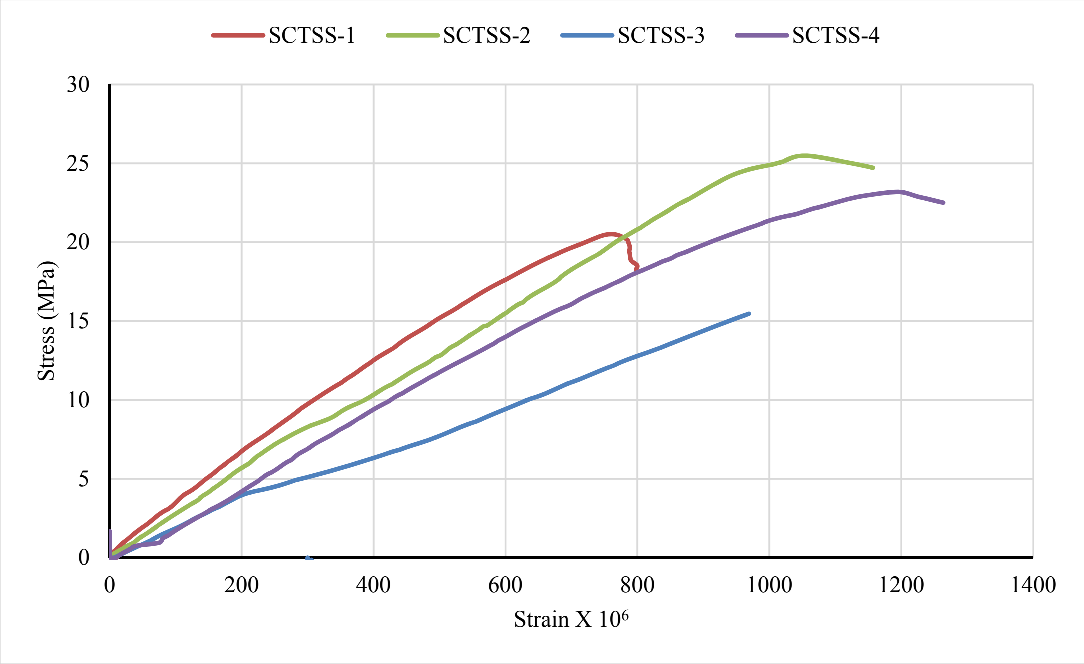

Figure 4.9 Stress Strain curves of sandstone compression test using data from strain gauges.

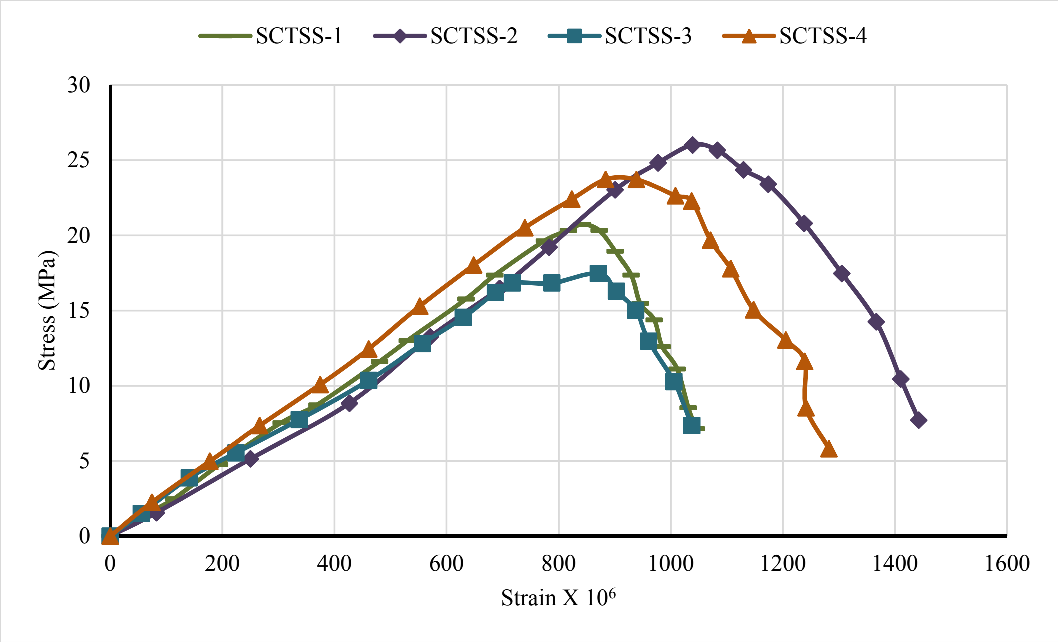

Figure 4.10 Stress Strain curves of sandstone compression test using Displacement data.

The modulus of elasticity was found and calculated considering 1/3 of the ultimate strength of the sandstone material. The modulus of elasticity was in the range of 27000 MPa.

The lateral behavior of the sandstone has also been captured though the horizontal strain gages. Fig 4.11 shows the variation of axial loading versus circumferential strain.

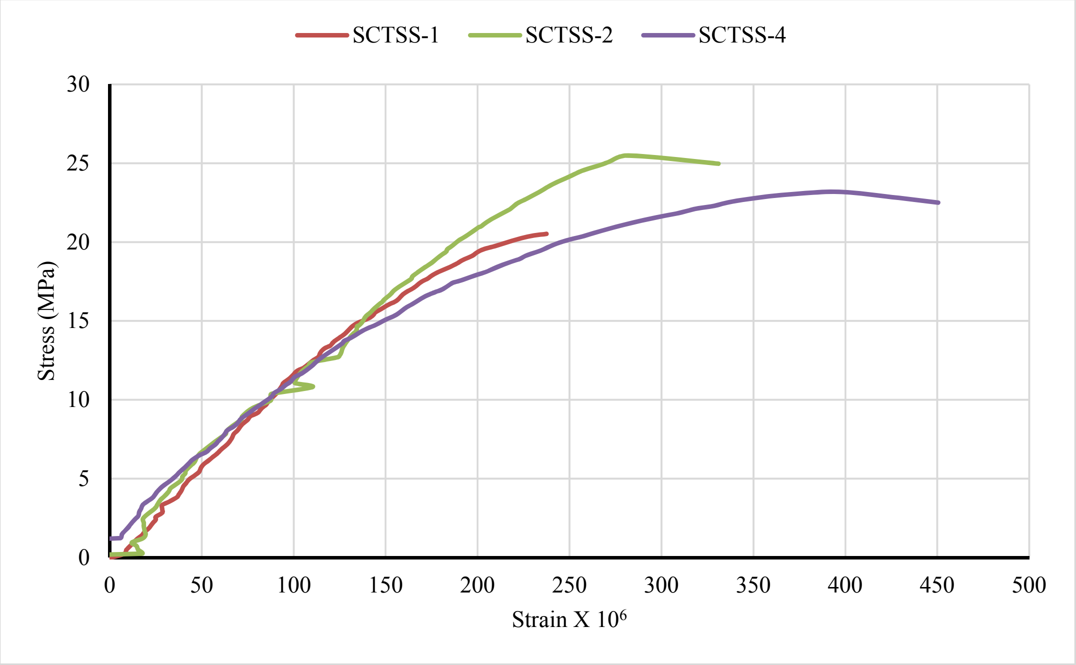

Figure 4.11 Stress Lateral Strain curves of sandstone compression test using stain gages data.

Poisson’s ratio result for the test was in the range of 0.3

The volumetric strain was also calculated in this study. Volumetric strain measures the dilatation of the material. The volumetric strain is calculated as follows:

$$\varepsilon_v = \frac{\Delta V}{V_0} = \varepsilon_a + 2\varepsilon_l$$

Where:

ε_a is the axial strain

ε_l is the lateral circumferential strain.

The variation of axial strain, lateral strain, and volumetric strain are shown in Fig 4.12.

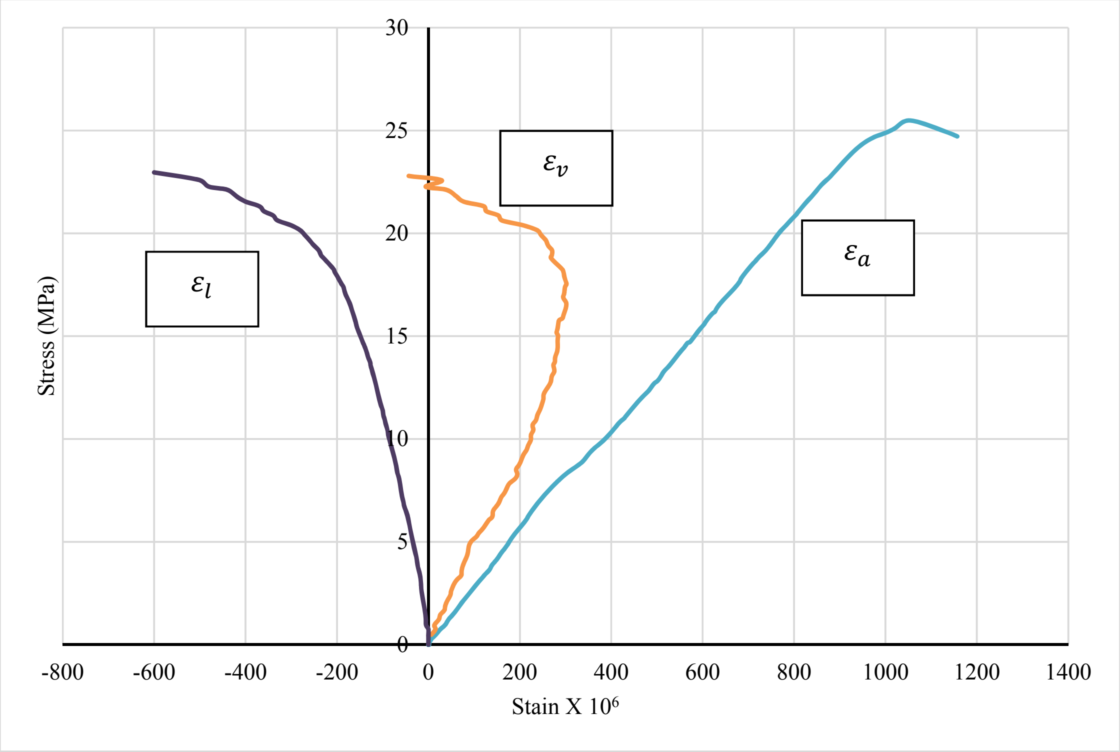

Figure 4.12 Vertical, Lateral, and volumetric strain.

The density of sandstone material was also found. Table 4.3 shows the measured density of the samples

Table 4.3 Destiny of sandstone material

Name	Density Kg/m^3
SCTSS-1	2156.35
SCTSS-2	2170.637
SCTSS-3	2074.564
SCTSS-4	2145.708
SCTSS-5	2056.247

The density of sandstone material was in the range of 2120.0 Kg/m^3

4.2.2 Sandstone Uniaxial Tension Test.

In tension test, three types of tests have been adopted namely,

i. Split test,
ii. Dog-bone tension test,
iii. Direct tension test.

4.2.3 Split Tension Tests

This test is a standard test used to find indirectly the tensile strength of Intact Rock Core Specimens. ASTM D 3967 and C 496 covers testing apparatus, specimen preparation, and testing procedures for determining the splitting tensile strength of rock by diametral line compression of a disk.

According to ASTM, each specimen has to satisfy the following dimension criteria:

$$0.2 \leq \frac{t}{D} \leq 0.75$$

In this study, diameters of the samples were fixed due to constraint in coring machine (Fig 4.13). The thickness of the specimens was calculated as follows:

$$\mathrm{D} = 75\ \mathrm{mm}, \quad \frac{\mathrm{t}}{\mathrm{D}} = 0.2\ \mathrm{to}\ 0.75, \quad \mathrm{t} = 75 \times (0.2\ \mathrm{to}\ 0.75) = 15\ \mathrm{to}\ 56\ \mathrm{mm}.$$

Taken a tolerance of $\pm 2\ mm$, thickness of 40 mm has been chosen in this study which means that:

$$0.2 < \frac{\mathrm{t}}{\mathrm{D}} = \frac{40 \pm 2}{75 \pm 2} \approx 0.533 \pm 0.04 < 0.75$$

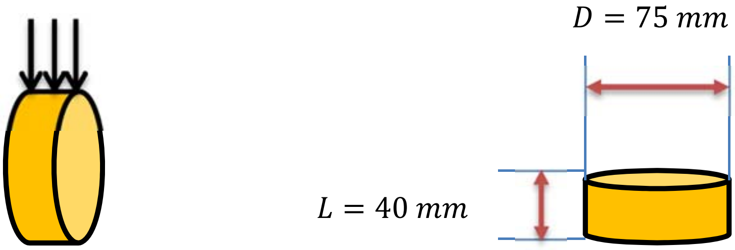

Figure 4.13 Dimension of sandstone samples tested in split test

To prepare the specimens, a sandstone rock has been caut into a plate of dimension 45 by 45 by 4 cm. After that, specimens (that were used in the split test) were cored from this plate. Due to nature of coring process, the surface of the sandstone discs have to be polished to make the surface smooth and to make the spacimens as much as possible right cylindrical disk. Following some pictures shows the procedure of coring and smoothing the surfaces of the disc spacimens (Figs 4.14 and 4.15).

Figure 4.14 Coring process of sandstone samples for split test.

Figure 4.15 Cylinders after coring and polishing.

The split test has been conducted using universal ELE compression testing machine. Specimens have been numbered and measured in three different locations to find the dimensions of the specimens. Table 4.4 gives information about all tested specimens in split test

Table 4.4 Dimensions of sandstone samples for split test

Name	t mm	D mm	t/D -
SSPT-1	37.69	73.63	1.51413
SSPT-2	39.56	73.87	1.437755
SSPT-3	39.61	72.98	1.960031
SSPT-4	39.63	73.95	2.411341
SSPT-5	39.34	74.02	2.382906
SSPT-6	39.53	73.88	2.136092
SSPT-7	39.40	73.87	2.340651
SSPT-8	39.42	73.94	2.380429
SSPT-9	39.31	73.97	2.561464
SSPT-10	39.46	74.00	2.158296
SSPT-11	39.55	74.00	2.131614
SSPT-12	39.52	73.89	1.89694
SSPT-13	39.51	73.99	2.003328

The test conducted was a load control test due to the nature of the equipment. The load rate adopted in this test was 0.5 KN/s. Figs 4.16 and 4.17 show the samples under test and also show the texture of the fractured surfaces.

Figure 4.16 Sandstone specimen under split test

Figure 4.17 Sandstone specimen after split test

The average split tensile strength was around 2.1 MPa with standard deviation of 0.33. A total of 13 samples where tested under this test and all results from split test are show in Table 4.5. The normal distribution of the results is shown in Fig 4.18.

Table 4.5 Split tension test results of sandstone samples.

Name	Tensile Strength MPa
SSPT-1	1.51
SSPT-2	1.44
SSPT-3	1.96
SSPT-4	2.41
SSPT-5	2.38
SSPT-6	2.14
SSPT-7	2.34
SSPT-8	2.38
SSPT-9	2.56
SSPT-10	2.16
SSPT-11	2.13
SSPT-12	1.90
SSPT-13	2.00

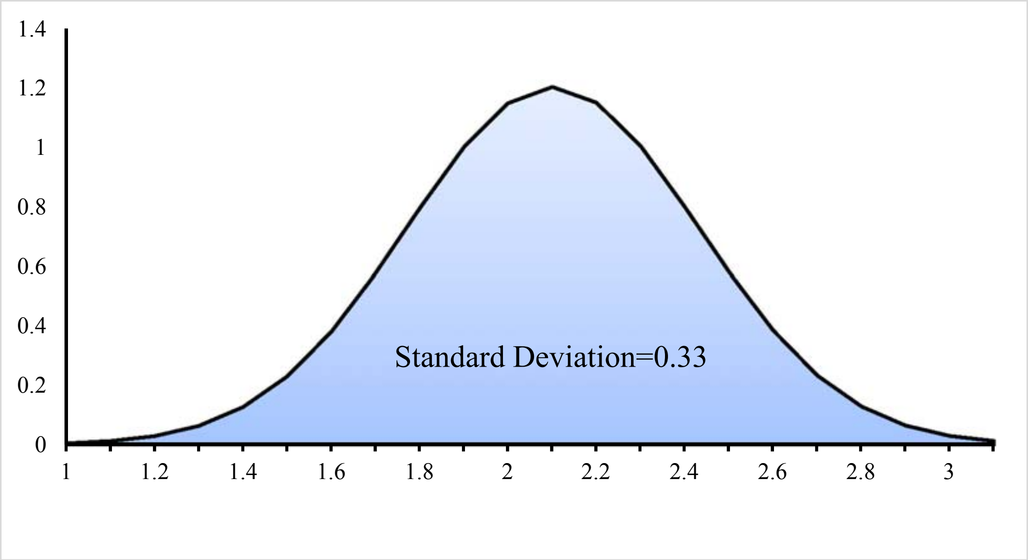

Figure 4.18 Normal distribution of the split test result.

4.2.4 Briquette Tension Test

Briquette test has also conducted to sandstone samples. Samples were shaped to the correct shape for test. This test was conducted to verify the result found form split test. The test results in approximately same tension strength of the sandstone material. Figs 4.19 and 4.20 shows the sample test under Briquette tension test.

Figure 4.19 Sandstone sample for Briquette tension test.

Figure 4.20 Configuration of Briquette tension test.

Only few samples were used in this test as the purpose of the test is only verification to split test. The tension strength of the sandstone result from this test was 3.0 MPa.

4.2.5 Direct Tension Test.

In the direct tension test, the testing equipment, testing procedure and testing rate are very important and essential to capture the correct behavior specially the softening branch of the stress strain curve in the uniaxial tension test. One of the main goal of this study is to conduct the numerical analysis on the behavior of masonry wall subjected to in plane loading. The complete stress strain curve in tension including the softening branch of the cure are very important input in the nonlinear finite element simulation.

It is well known that the shape of the softening branch depends on the boundary conditions (Van Vliet, Ramos 2000, & Vasconcelos 2005). Cracks initiation induced eccentricity in the loading. This eccentricity lead to fast fracturing of the specimen when end supports are pinned. However, when the end supports are fixed, eccentricity originated by the crack opening is balanced by the introduction of bending moments. This lead to generation of multiple cracks. Small differences were noticed (Van Vliet, 2000; Van Mier et al.,1996) in which the fracture is generally larger relative to the ones achieved in uniaxial tension tests conducted using pin-ended platens. The differences between the two behaviors are shown schematically in Fig 4.21. It has to be noted that, the fixed end support type has to induce zero moment at the beginning of the test to get result that is more accurate. Achieving this zero moment at the beginning of the test is usually difficult. Due to this difficulty and because the differences between the results of fixed end support and pined end support are close to each other, pin type of supports were adopted in this study.

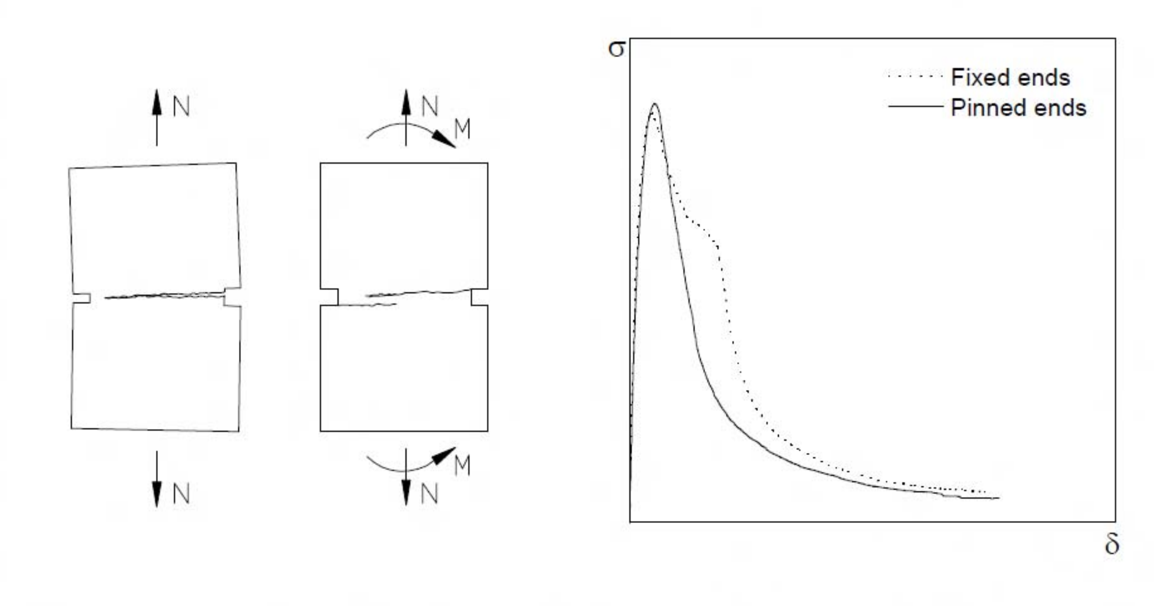

Figure 4.21 Effect of boundary condition on behavior of samples under direct tension test, Vasconcelos (2005).

According to Vasconcelos (2005) when performing direct tensile test to un-notched specimen, uncertainty about the location of the cracks will arise. Based on that, specimens dimensions adopted in this study was chosen in according to the suggested dimensions by Ramos (2001) and Vasconcelos (2005) the specimens were prismatic shape of 80mm height, 50mm length and 40mm width were considered. To capture the behavior of the cracked surfaces, notches have been introduced to the prisms in two opposite faced so that the crack will happen in the targeted area. The top and bottoms faces of the prisms were prepared to be rough so that good adhesion is achieved between the specimen and the epoxy that will glue the specimen to the loading plates. The test procedure was conducted in according to ASTM D 2936. Specimen's dimensions are shown in Figs 4.22-4.24.

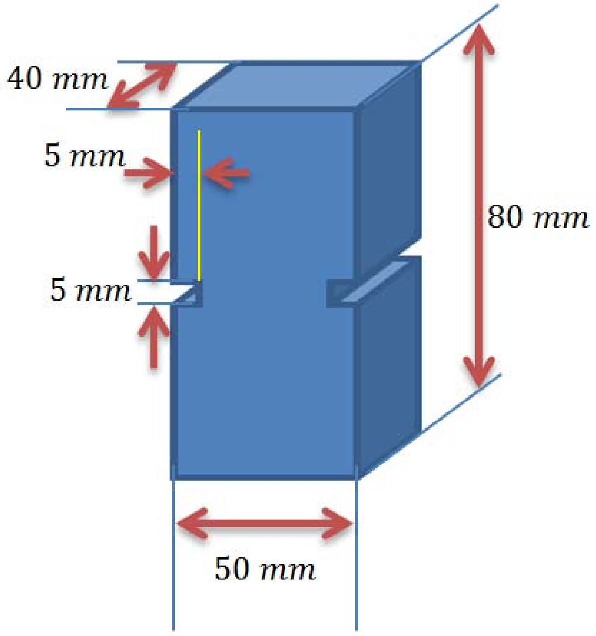

Figure 4.22 Sandstone specimen depiction and dimension

Figure 4.23 Sandstone specimen with introduced notches.

Figure 4.24 Sandstone specimen ends were made rough for better adhesion.

The ends of specimen were attached firmly to the loading plat using DEVCON glue. Two hinged supports where introduced at the center of lading plate and then the whole set up was attached to the loading machine. Two strain gauges where attached to the un-notched faces of the specimen and two PI-shape Displacement Transducer (PI-5) were attached to the specimen on the notched faces to measure the displacement through the notch. The loading rate was slow of 0.05 mm/min (0.83 μm/s) to capture the softening branch of the stress-strain curve. Specimen under loading is shown in Figs 4.25 and 4.26.

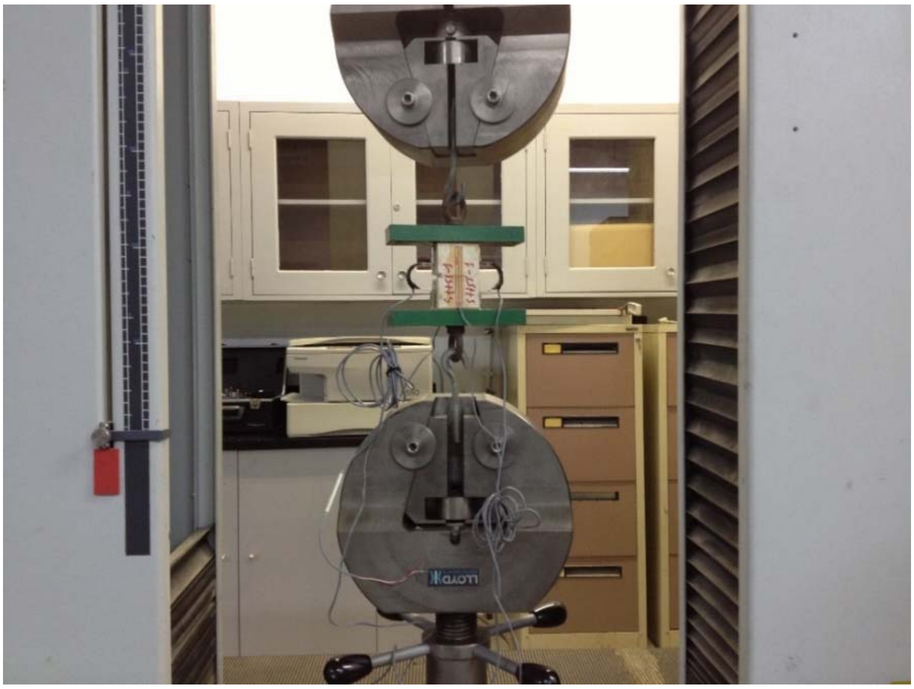

Figure 4.25 Sandstone samples in direct tension test.

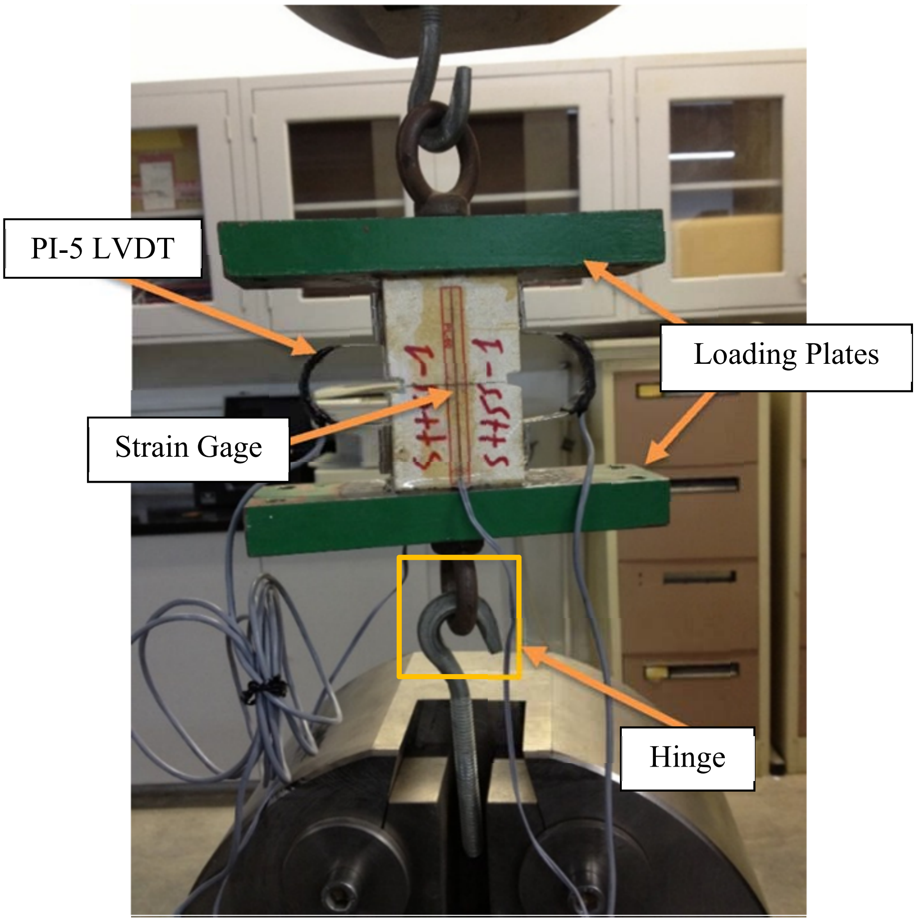

Figure 4.26 Configuration of Direct tension test

The stress strain curve reveals that, the sandstone behavior is very brittle under uniaxial tension test. Typical result of direct tension test is shown in Fig. 4.27

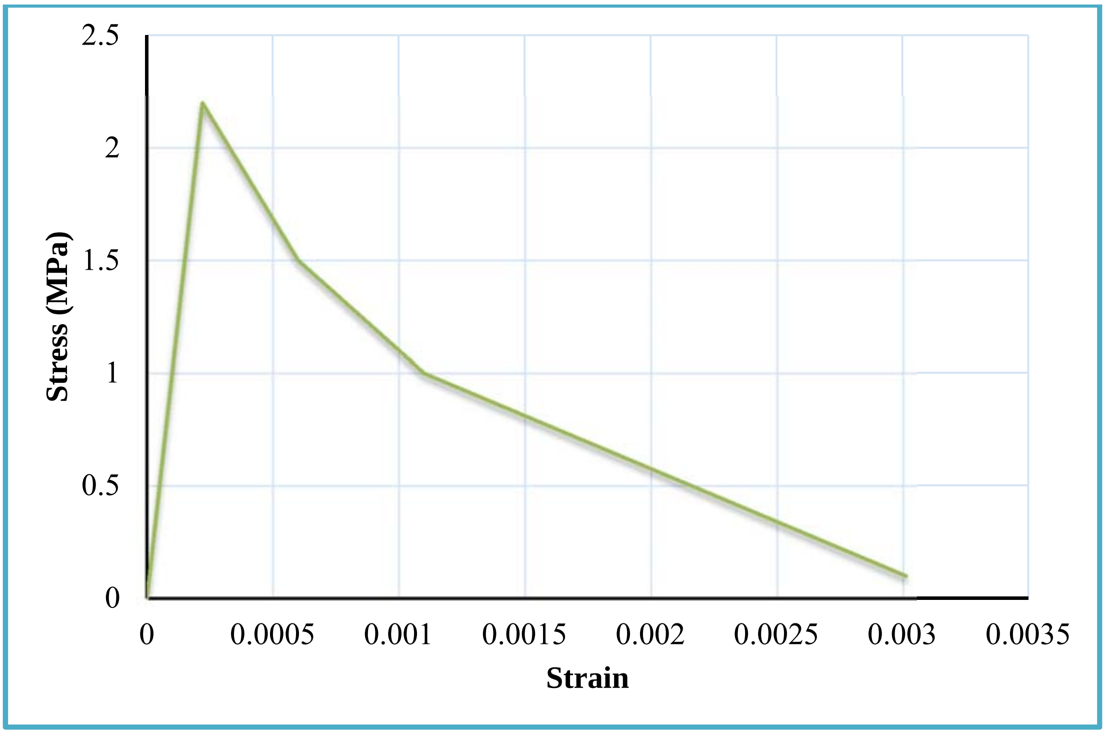

Figure 4.27 Stress-Strain curve of sandstone specimen under direct tension test.

4.3 Mechanical Properties Test of Lime Mortar.

Mortar is one of the constituent that composes the masonry wall. It is well known that mortar affect the behavior of the masonry structures (Edgell and Haseltine 2005). In this study, ready mixed Lime Mortar LM70 from Dry Mortar Company (DMC LM70 Technical details.) was used for construction of the walls and prisms. Fig 4.28.

Figure 4.28 Ready mixed Lime Mortar LM70

The lime ready mixed lime mortar consists of hydrated lime and white cement and also some other additives. This lime mortar is manufactured in according to M5, EN 998-2, ASTM C270 type N; ASTM C150, and ASTM C144. The water mix ratio specified be the manufacturer (w/m) is 0.3.

The need to perform mechanical studied for lime mortar is because it is needed in the numerical analysis. In the numerical simulation, two different approaches were adopted namely:

i. Continuum passed approach in which both sandstone and lime mortar were treated as continuum material,

ii. Interface approach in which sandstone was modeled as a continuum material whereas the lime mortar was modeled as an interface between sandstone units.

For both approaches, different kind of material parameters are needed to be input in the FEM. For that, several type of tests had to be conducted including, uniaxial compression test, uniaxial tension test, and direct shear. The continuum based approach needs different types of material properties. The tests conducted on lime mortar are shown in the following section. All lime mortar specimens were prepared though casting process and then cured for 28 days.

4.3.1 Lime Mortar Uniaxial Compression Test.

For compression test of lime mortar, cylindrical specimens were used to find the compressive behavior of the LM70 material. Specimens were prepared by casting cylinders in standard cylindrical mold. The tests and samples have been prepared according to the ASTM C 39. The dimensions of the specimens were:

$$L = 150\ mm, D = 75\ mm$$

$$\frac{L}{D} = \frac{150}{74} = 2.0$$

Figs 4.29 and 4.30 shows the configuration and sizes of the cylinders to be tested under compression test.

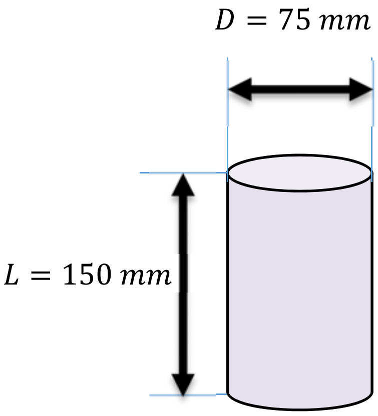

Figure 4.29 Dimensions of Lime mortar cylinders test under uniaxial compression

Figure 4.30 Lime Mortar cylindrical Specimens.

Lime mortar cubes were also used to measure the compression strength of the lime mortar. ASTM C 109 had been followed to measure the compressive strength of lime mortar cube specimens (Fig 4.31)

Figure 4.31 Lime Mortar cubic Specimens.

For testing the specimens in uniaxial compression, procedure have been followed in according to ASTM C39 & C109. Two type of compression test where conducted namely:

i. Compression test to find only the ultimate strength of the material,
ii. Compression test conducted to find all mechanical properties (ultimate strength, stress strain curve, young modulus and Poisson’s ratio).

In the first type of compression test (i), compression test were conducted for only finding the ultimate strength of the lime mortar. This test was conducted using ELE compression testing machine. The test was a load control type with loading rate of 0.5 KN per second. Dimensions of specimens have been found though measurements at different locations. The density of the material also found in this study (Table 4.6) . After that the specimens were tested under uniaxial compression test. Figs 4.32 and 4.33 shows both cylinders and cubes under compression test.

Figure 4.32 Lime mortar cylinder after compression test in ELE compression testing machine

Figure 4.33 Lime mortar cube under compression test in ELE compression testing machine

Table 4.6 Dimensions and Densities of Lime Mortar samples.

Name	h mm	Average h mm	D mm	h/D -	Area mm^2	Volume mm^3	Wight g	Density Kg/m^3
LMCTS-1	150.39	150.39	76.20	1.97	4560.3	685845	1104.2	1609.98
LMCTS-2	151.10	151.10	76.20	1.98	4560.3	689060.1	1122.3	1628.74
LMCTS-3	150.44	150.44	76.20	1.97	4560.3	686073.1	1093.1	1593.27
LMCTS-4	150.18	150.18	76.20	1.97	4560.3	684876	1094.7	1598.39
LMCTS-5	150.34	150.34	76.20	1.97	4560.3	685605.6	1092.7	1593.77
LMCTS-6	150.14	150.14	76.20	1.97	4560.3	684682.1	1101.8	1609.21
LMCTS-7	150.24	150.24	76.20	1.97	4560.3	685126.8	1075.7	1570.07
LMCTS-8	150.21	150.21	76.20	1.97	4560.3	685001.4	1093.7	1596.64
LMCTS-9	150.04	150.04	76.20	1.97	4560.3	684248.9	1078.4	1576.03
LMCTS-10	150.06	150.06	76.20	1.97	4560.3	684317.3	1095.4	1600.72

Table 4.7 shows the uniaxial compression strength of the lime mortar cylindrical samples and Table 4.8 shows the uniaxial compression strength of the lime mortar cubical samples. It has been noted that, the compression strength of lime mortar was noted to be low as the nature of the material says. The maximum load applied to the samples were recorded and then the uniaxial compression strength of the material were calculated. For the compression strength resulted for testing of cylinders, the average strength recorded was in the range of 1.8 MPa with standard deviation of 0.28. Fig 4.34

Table 4.7 Ultimate strength of the lime mortar cylindrical specimens

Name	Compression Strength MPa
LMCTS-1	1.14
LMCTS-2	2.24
LMCTS-3	1.78
LMCTS-4	1.71
LMCTS-5	1.93
LMCTS-6	1.86
LMCTS-7	1.64
LMCTS-8	1.90
LMCTS-9	1.65
LMCTS-10	1.91

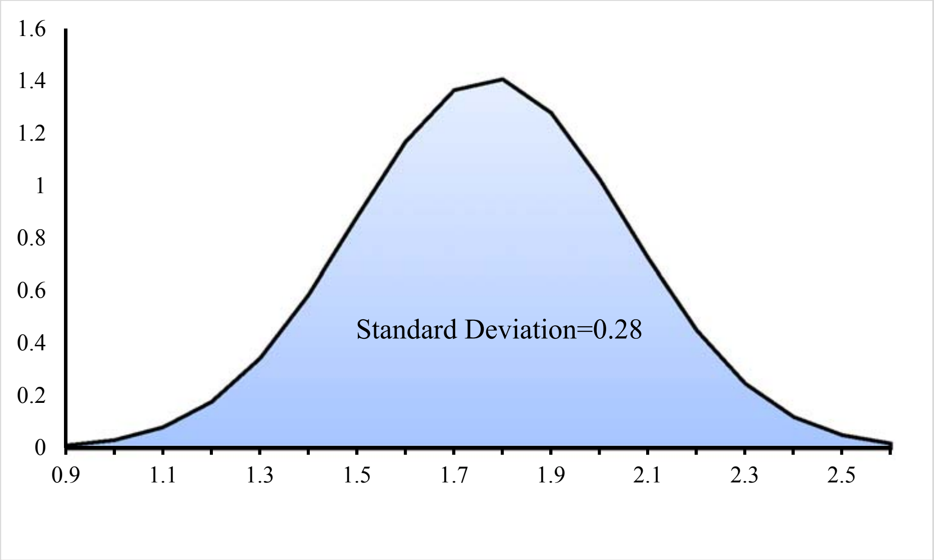

Figure 4.34 Normal Distribution of the Lime mortar cylinder compression test result.

For the compression strength of lime mortar cubes, the average strength recorded was in the range of 2.0 MPa with standard deviation of 0.26 Fig 4.35

Table 4.8 Ultimate strength of the lime mortar cube specimens

Name	Compression Strength MPa
LMCCTS-1	1.80
LMCCTS-2	2.12
LMCCTS-3	2.05
LMCCTS-4	1.70
LMCCTS-5	2.00
LMCCTS-6	2.04
LMCCTS-7	1.82
LMCCTS-8	2.13
LMCCTS-9	1.73
LMCCTS-10	2.56

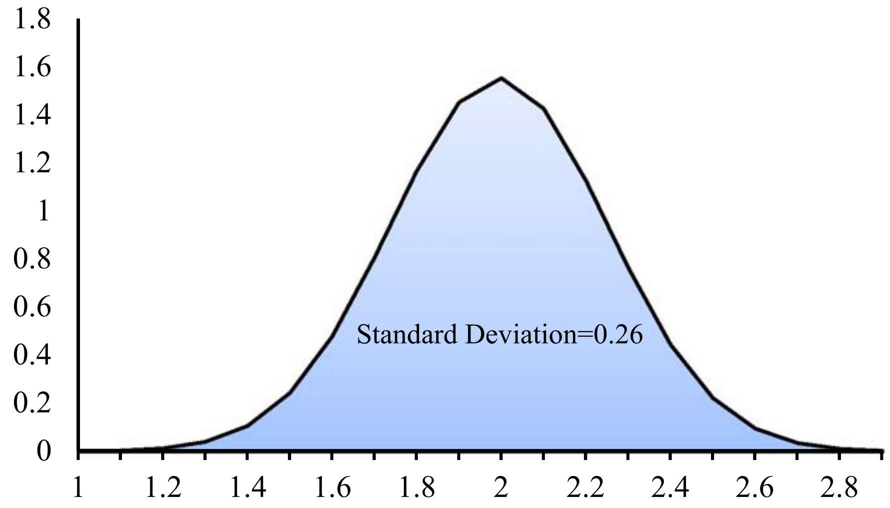

Figure 4.35 Normal Distribution of the lime mortar cube compression test result.

The test result of the compression test reveals that, the average capacity of the lime mortar was in the range of 2.0 Mpa.

In the second compression test (ii), complete stress strain curve (including the softening branch) was targeted because it is essential to be used in the numerical simulation. For that, displacement control test was adopted with slow loading rate of 0.1 mm per minute (1.6 μm/s). Two PLC-60-11 cross type; strain gauges were used in two opposite sides of the cylinders to efficiently capture the behavior of the cylinders under test and to find young modulus, and Poisson's ratio (Fig 4.36).

Figure 4.36 PLC-60-11 cross type; strain gauges attached to lime mortar cylinder under uniaxial compression test

Stress strain curves were plotted as shown in Fig 4.37. Due to the nature of the strain gauges, it is not possible to capture the stress-strain curve in the softening branch. For that, the stress-strain curves where found using the displacement between the end loading plates Fig 4.38. The test where conducted using LLOYD LR 300 K testing machine.

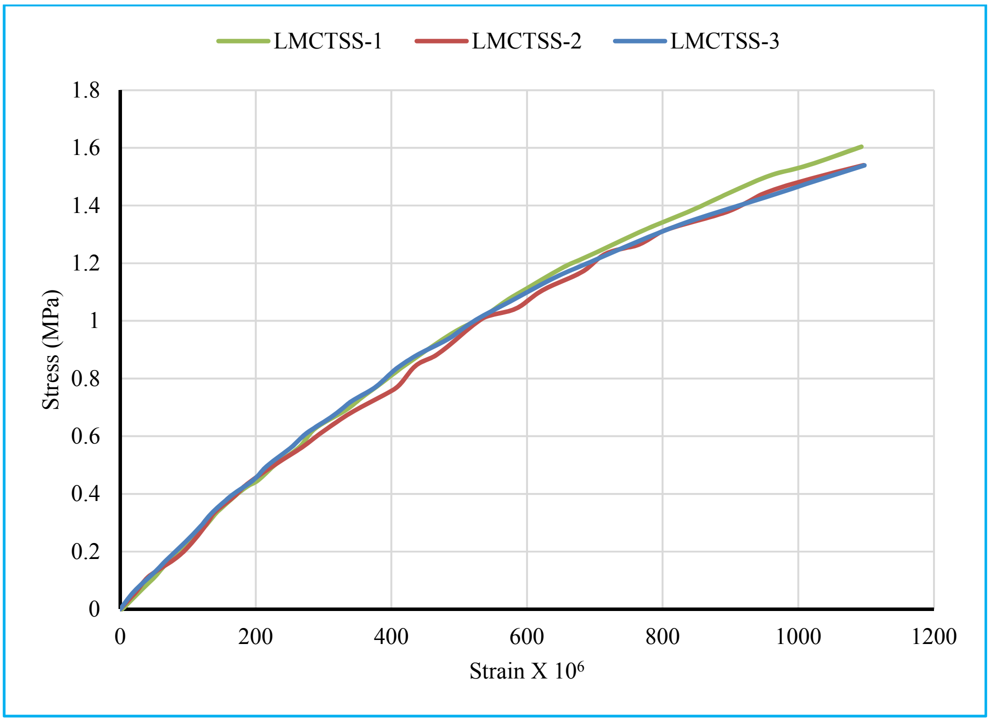

Figure 4.37 Strain curves of Lime mortar compression test using data form strain gauges.

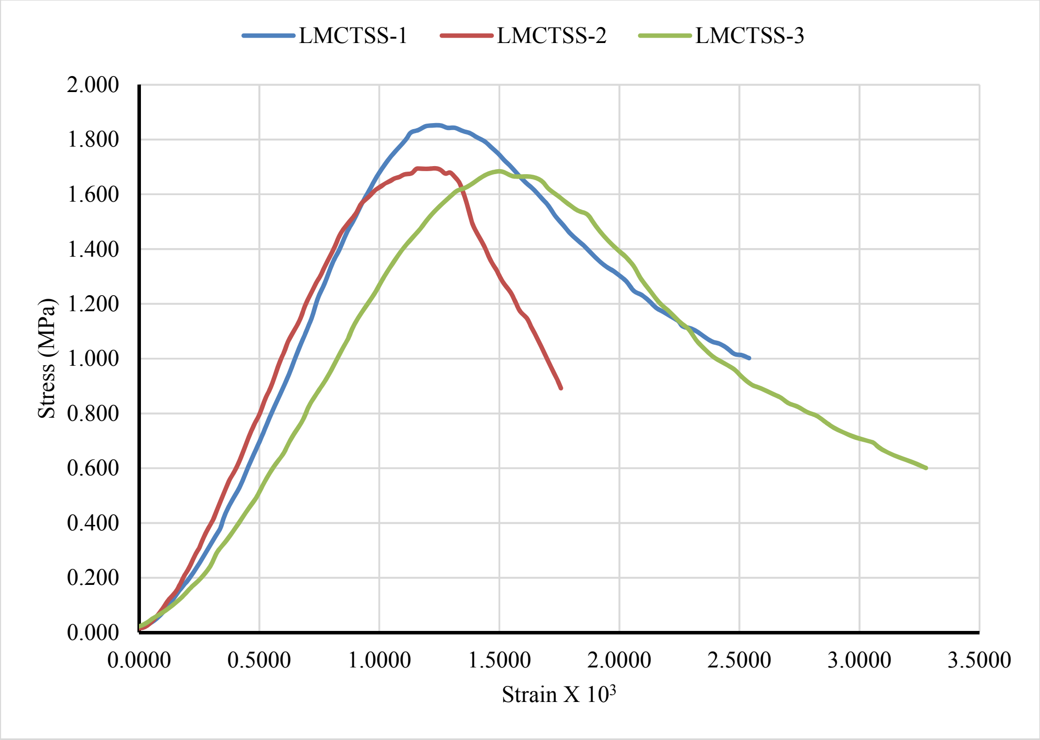

Figure 4.38 Strain curves of Lime mortar compression test using displacement data.

The lateral behavior of the sandstone also have been captured though the horizontal strain gages. Fig 4.39 shows the variation of axial loading versus circumferential strain. Poisson’s ratio result for the test was in the range of 0.25.

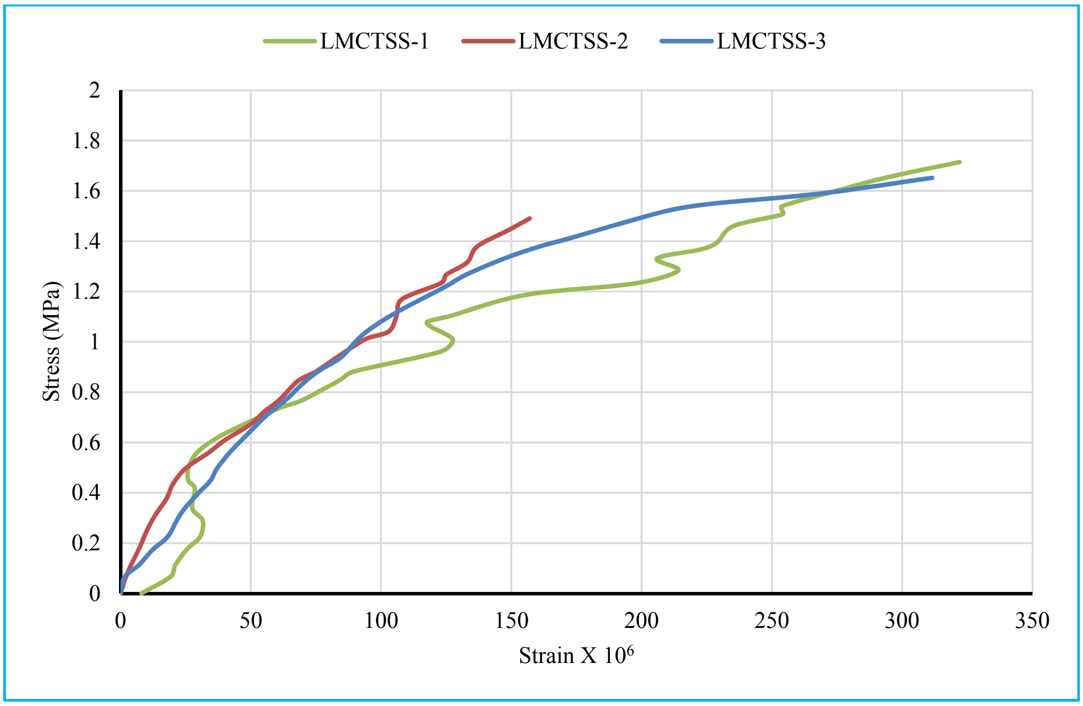

Figure 4.39 Stress Lateral Strain curves of Lime mortar compression test using stain gages data.

4.3.2 Lime Mortar Uniaxial Tension Test.

As mentioned before, tension properties of lime mortar material is also need to be used in the numerical analysis. For this porous, tension test has been conducted to lime mortar samples. In tension test, three types of tests have been adopted namely:

i. Split test,
ii. Briquette tension test,
iii. Direct tension test,

4.3.3 Split Test.

Split test where conducted in this study to indirectly find the tension strength of the Lime Mortar. Specimens, equipment and test procedure where conducted in accordance with ASTM D 3967 and C496. Samples were casted and cured for 28 days and then tests under split test. Based on the specifications, dimensions of the samples were chosen to be 75 x 150 mm (Fig 4.40). Dimensions of each specimen was found by measuring the specimen at different location (Table 4.9).

Table 4.9 Dimensions of lime mortar cylinders used in compression test.

Name	h mm	Average h mm	D mm	t/D -
LMSPT-1	150.15	150.15	76.20	1.97
LMSPT-2	150.53	150.53	76.20	1.98
LMSPT-3	150.52	150.52	76.20	1.98
LMSPT-4	150.66	150.66	76.20	1.98
LMSPT-5	150.36	150.36	76.20	1.98
LMSPT-6	149.82	149.82	76.20	1.97
LMSPT-7	150.08	150.08	76.20	1.97
LMSPT-8	150.39	150.39	76.20	1.98
LMSPT-9	150.24	150.24	76.20	1.97
LMSPT-10	149.89	149.89	76.20	1.97

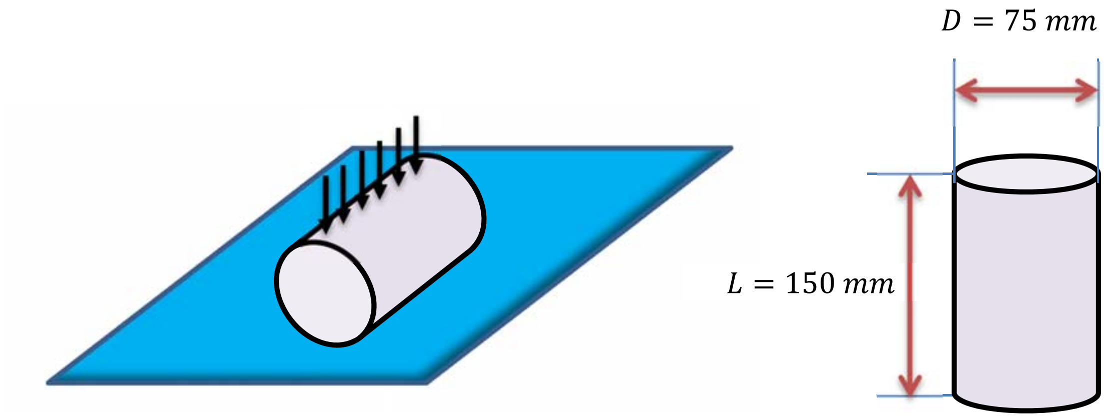

Figure 4.40 Depiction of lime mortar used in split test.

Due to the nature of the equipment used in the test, load control test was used in the test. The loading rate adopted in this test was 0.5 KN/s. Fig 4.41 show the samples under test.

Figure 4.41 Lime mortar specimen under split test.

A total number of 10 samples were test in this test. It has been noted that, the split tension strength of the lime mortar is low compare to the split tension test of the sandstone. The average split tensile strength was in the range of 0.24 MPa with standard deviation of 0.034 (Fig 4.42). Test results are show in Table 4.10.

Table 4.10 Split test result of lime mortar

Name	Split Tensile Strength MPa
LMSPT-1	0.26
LMSPT-2	0.21
LMSPT-3	0.28
LMSPT-4	0.22
LMSPT-5	0.23
LMSPT-6	0.26
LMSPT-7	0.20
LMSPT-8	0.27
LMSPT-9	0.22
LMSPT-10	0.27

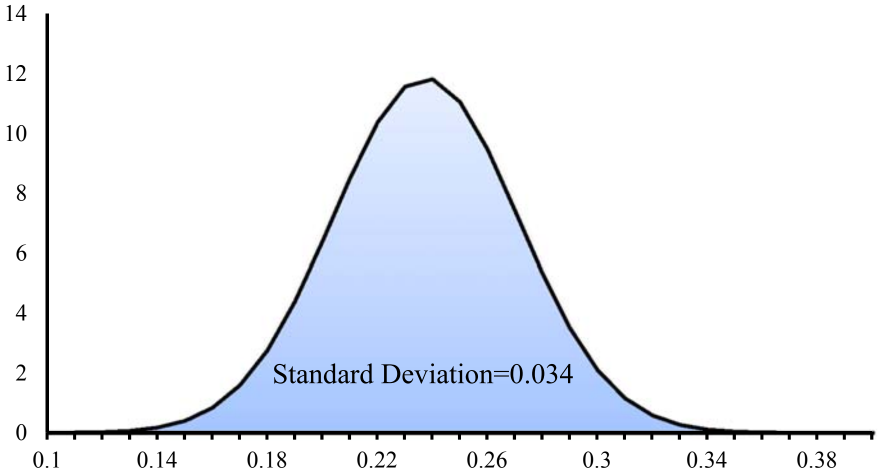

Figure 4.42 Normal Distribution of Lime Mortar split test result.

4.3.4 Briquette Tension Test.

In the Briquette test, samples were prepared using Briquette molds. This test where conduct to verify the result found from split test. Figs 4.43 and 4.44 show the sample test under Briquette tension test.

Figure 4.43 Lime mortar Briquette samples.

Figure 4.44 Lime Mortar Briquette samples under test.

A total number of 16 specimens were tested in Briquette test. The Briquette tension test results are little bit higher than that found from split test. Table 4.11 shows the results of Briquette tension test. The standard deviation of the results is 0.075. The normal distribution of the results are shown in Fig 4.45.

Table 4.11 Tension test result of doge bone lime mortar samples

Name	Tension Strength MPa
LMDTTS-1	0.43
LMDTTS-2	0.49
LMDTTS-3	0.36
LMDTTS-4	0.31
LMDTTS-5	0.36
LMDTTS-6	0.38
LMDTTS-7	0.29

LMDTTS-8	0.37
LMDTTS-9	0.56
LMDTTS-10	0.44
LMDTTS-11	0.31
LMDTTS-12	0.39
LMDTTS-13	0.28
LMDTTS-14	0.42
LMDTTS-15	0.32
LMDTTS-16	0.39

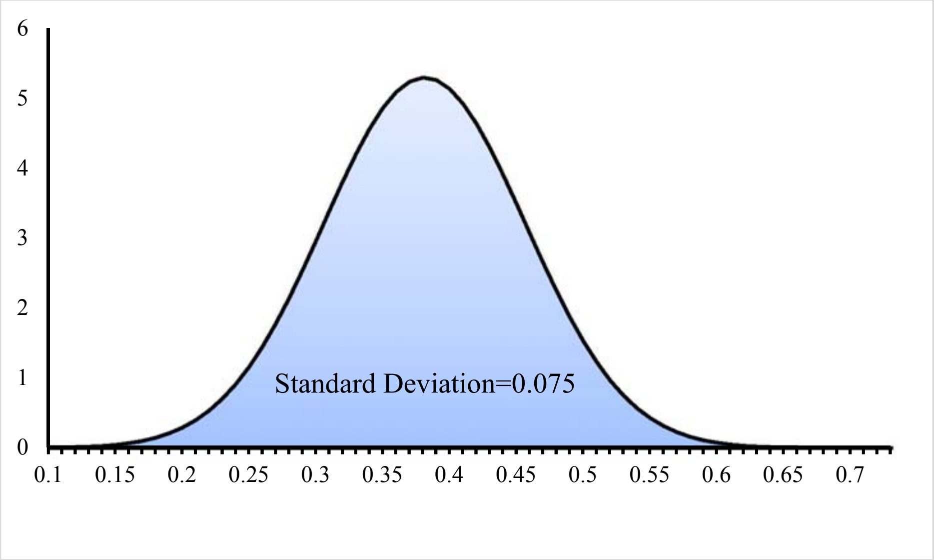

Figure 4.45 Normal distribution of Lime Mortar Briquette tension test result.

It has been noted that the average tension strength of the lime mortar results from this test is in the range of 0.38 MPa which is more than the strength found form the split test. This can attributed to the fact that the fracture area in the Briquette tension test is varying during the test. The area used to calculate the strength was based on the narrows part of the samples however; some samples were ruptured in different level of the samples resulting in more rupture area.

4.3.5 Direct Tension Test.

As mentioned in the direct tension test of the sandstone, the testing equipment, testing procedure and testing rate are very important and essential to capture the correct behavior specially the softening branch of the stress strain curve in the uniaxial tension test. The specimens were prismatic shape of 80mm height, 50mm length and 40mm width were considered. To capture the behavior of the cracked surfaces, notches have been introduced to the prisms in two opposite faced so that the crack will happen in the targeted area.

The ends of specimen were attached firmly to the loading plat using DEVCON glue. Same procedure has been followed as that adopted in direct tension test of sandstone material. Lime mortar shipment under direct tension test is shown in Fig 4.46.

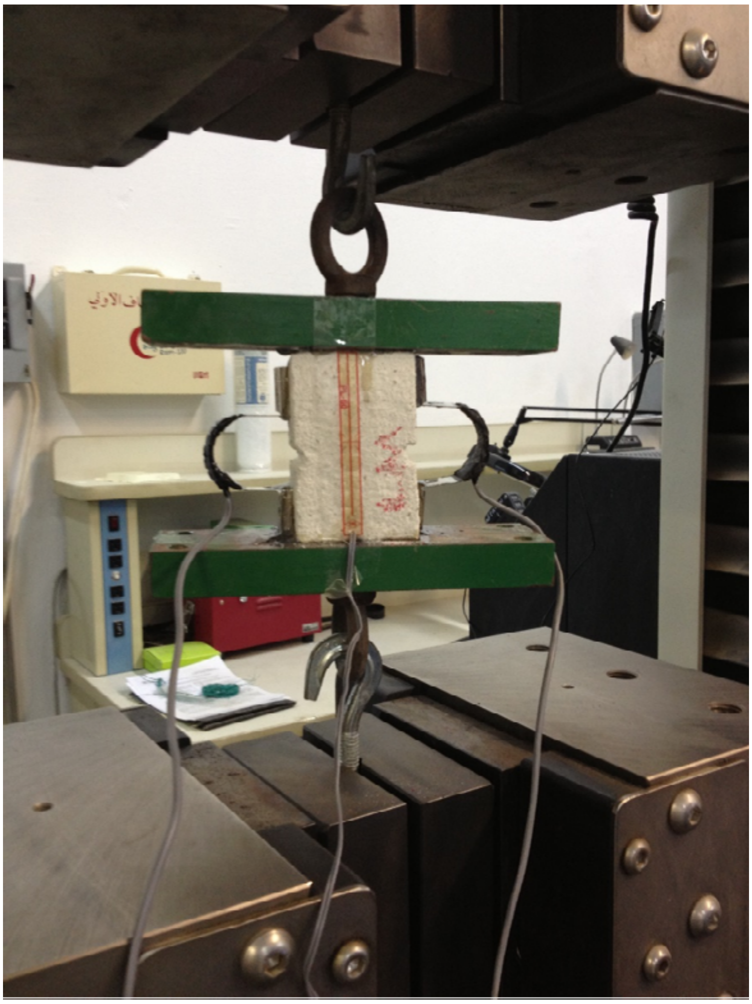

Figure 4.46 Configuration of Direct tension test

The stress strain curve is shown in Fig. 4.47

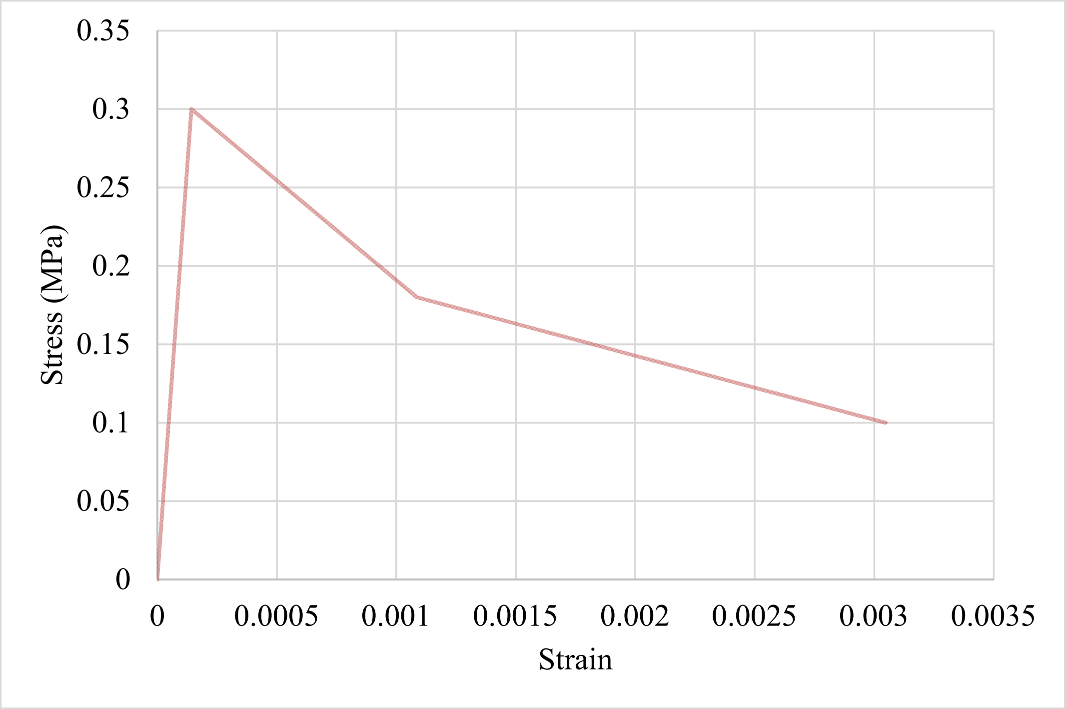

Figure 4.47 Stress-Strain curve of sandstone specimen under direct tension test.

4.4 Sandstone Lime Mortar Interface Test.

The interaction properties between sandstone and the lime mortar was needed in the interface FEM simulation. In this test, direct shear test has been conducted using double shear test approach. The configuration of the setup is shown in Figs. 4.48 and 4.49

Figure 4.48 Specimen under Direct shear test.

Figure 4.49 Specimen after testing in direct shear test.

The coefficient of friction has been found in this test. Fig 4.48 shows the force displacement curve of specimen tested under 2 MPa normal stress. The friction coefficient found from this test is 0.7.

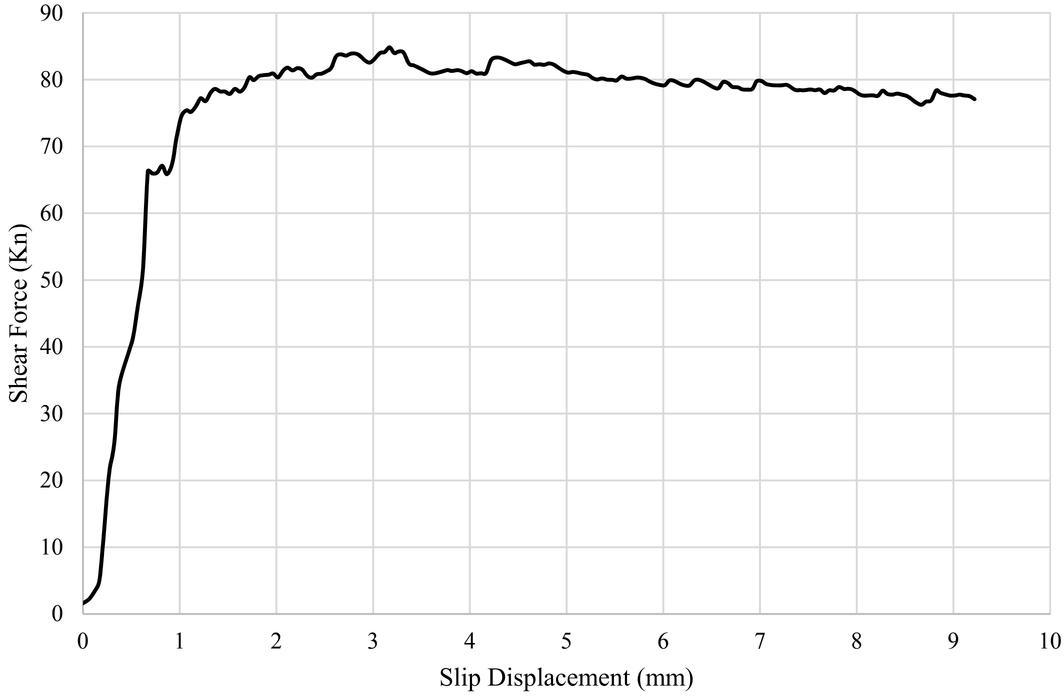

Figure 4.50 Force displacement rustled from direct shear test.

4.5 Prism Compression Test.

Behavior of masonry walls under pure compression force is needed in this study especially when doing the numerical analysis. Normally, compression test of full scale wall is rather difficult due to the necessity of high capacity machine to produce high force. This limitation usually lead to test a repetitive prism that give same behavior of the wall. In this study, compression test was carried out to prism repressing the Sandston masonry walls. ASTM C 1314 and European Standard EN1052-1(1999) provide a specifications and description of the test. According to the standards, masonry specimens should include at least one head joint in the central course centrally placed. The size of the prism in this study was limited to the capacity of the equipment available in the labs.

The prism was constructed using the same bricks that were used to construct the walls. The head and bed joints were made of ready mixed DMC lime mortar LM70 (LM70 Technical details). A total number of two masonry prisms specimens were tested under pure compression test.

Prisms, as well as walls, were built using two different sandstone brick sizes. The larger brick had dimensions of 300 x 150 x 200 mm, and the small brick had dimensions of 150 x 150 x 200 mm. Both head and bead joints were limited to be 10 mm in thickness. Shape and size of the bricks used in building prisms and walls are shown in Fig 4.51.

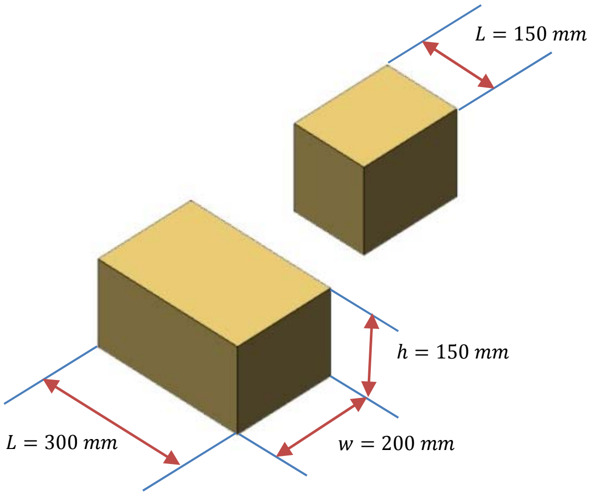

Figure 4.51 Dimensions of sandstone units

As mentioned, prism and walls were built using ready mixed DMC lime mortar LM70 with 10 mm head and bed joints. Prism and walls were then subjected to a curing period as specified in the LM70 specifications. Shape and configurations of prism are shown in the Figs 4.52-4.54.

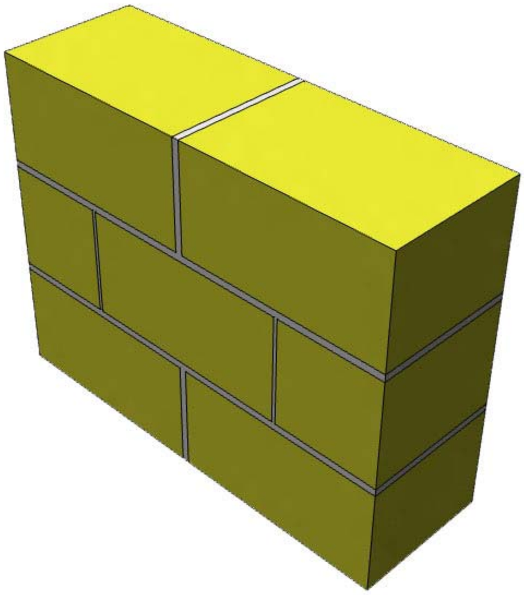

Figure 4.52 Isometric view of the sandstone prism.

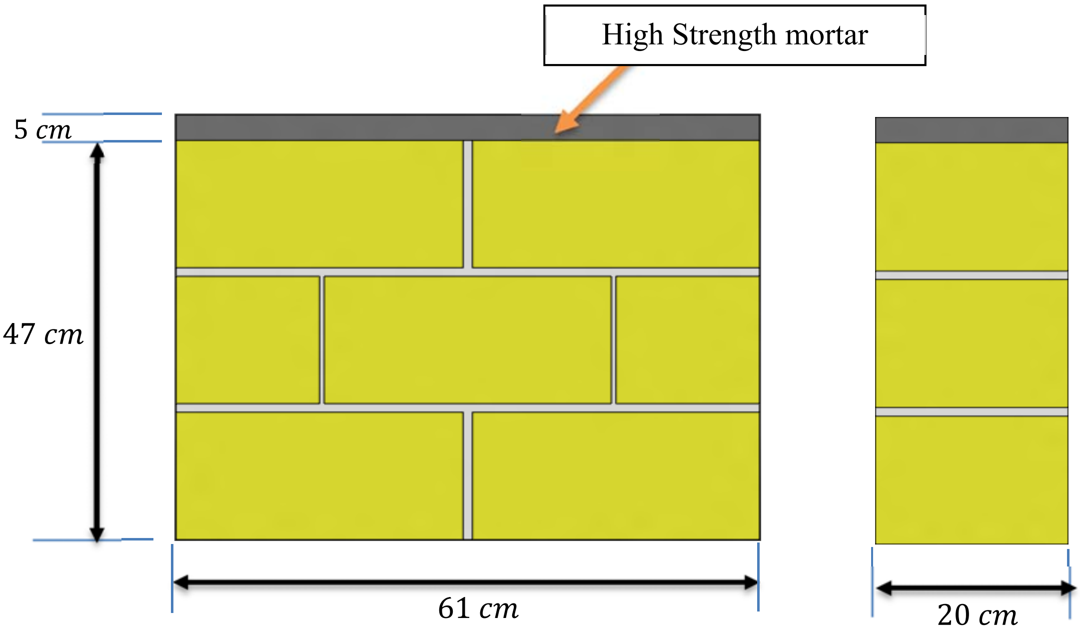

Figure 4.53 Dimensions and configuration of the sandstone prism

Figure 4.54 Sandstone Prisms under curing period.

The prisms were constructed on top of long and thick steel plate so that the movement of the prims were easy. The first course of the prism where built on the top of the steel plate using a high strength mortar EMACO S88 CT provided by BASF. Continuous curing was provide to the prisms for 28 days. The tests were conducted using Enerpac hydraulic jack and steel frame available in the reaction floor of the heavy equipment lab. Due to the nature of prims construction, the top side of the prism was not perfectly flat. Because of this, a thick layer of high strength mortar EMACO S88 CT was placed at the top of the prism so that the stress is uniformly distributed on the top side of the wall without any stress localization or concentration (Figs 4.55 and 4.56). Two thick steel plates were place at top and bottom sides of the prims so that a uniform stress is exerted on the prims.

Figure 4.55 High strength layer on top of the Sandstone prism.

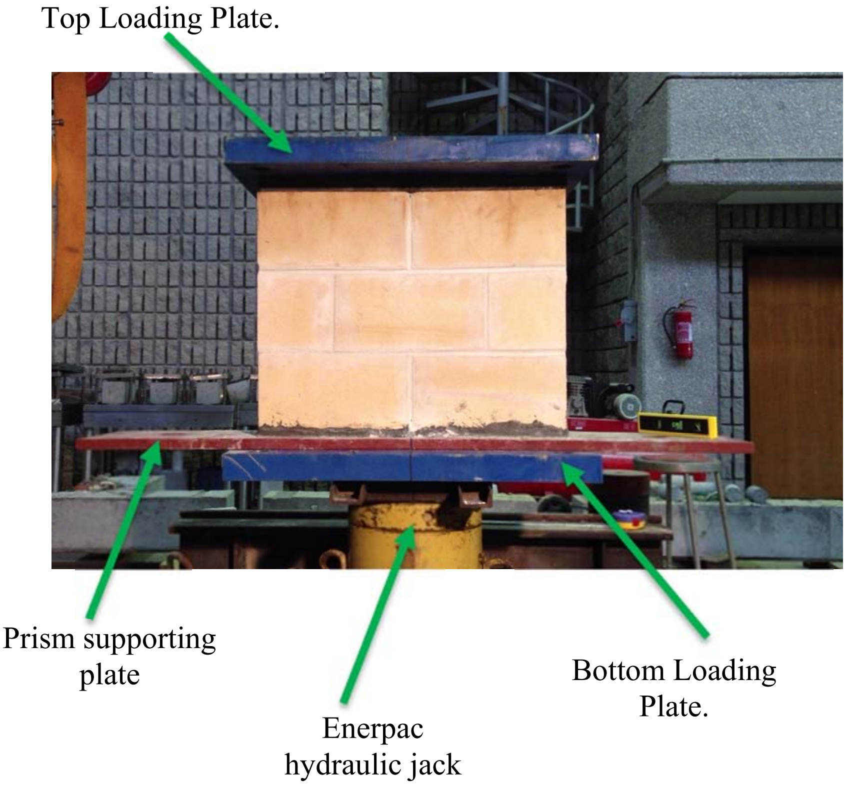

Figure 4.56 Configuration of testing setup of the Sandstone prism

Enerpac hydraulic jack was first placed on top of steel built-up section and then a thick steel plate was placed on top of the jack. The prism was then placed on top of the thick loading plate and then another thick steel loading plate was place at the top of the prism. In order to get a uniform axial loading, the prism has to be aligned vertically and horizontally. For this purpose, Laser leveler (Fig 4.57) was used to accurately place the prims in the proper position with the probe alignment (Fig 4.58).

Figure 4.57 Laser leveler used for alignment

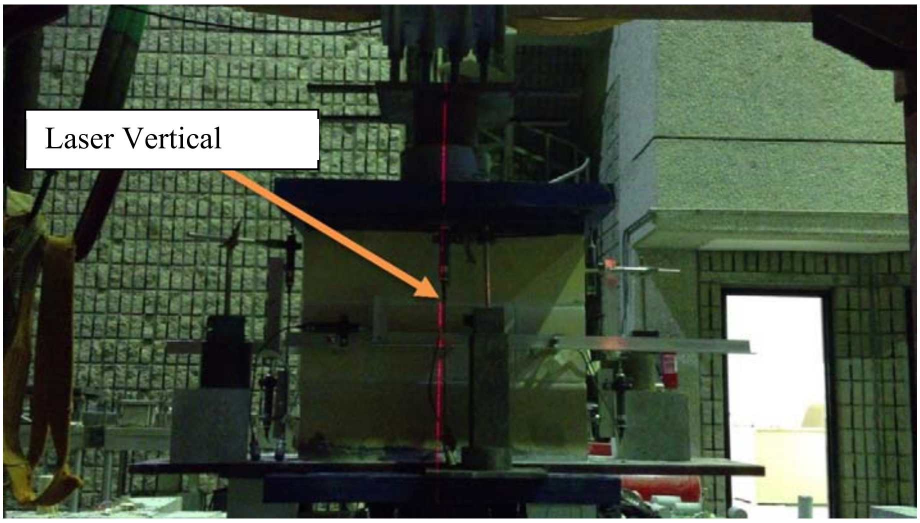

Figure 4.58 Sample under alignment process.

Vertical as well as horizontal displacement of the prism were captured using four vertical CDP-25 LVDs and two horizontal CDP-25 LVDTs. A set of threaded bars were attached firmly to the prism by gluing them indies a wholes previously drilled in the prim body. DEVECON epoxy was used to glue the threaded bars inside the holes. Some of the LVDTs were bolted to the threaded bares using aluminum L shape sections. The vertical LVDTs was attached to the prism supporting plate to measure the displacement between the prism’s top and bottom end plates. Figs 4.59 and 4.60 show the configuration of one of the tested prisms.

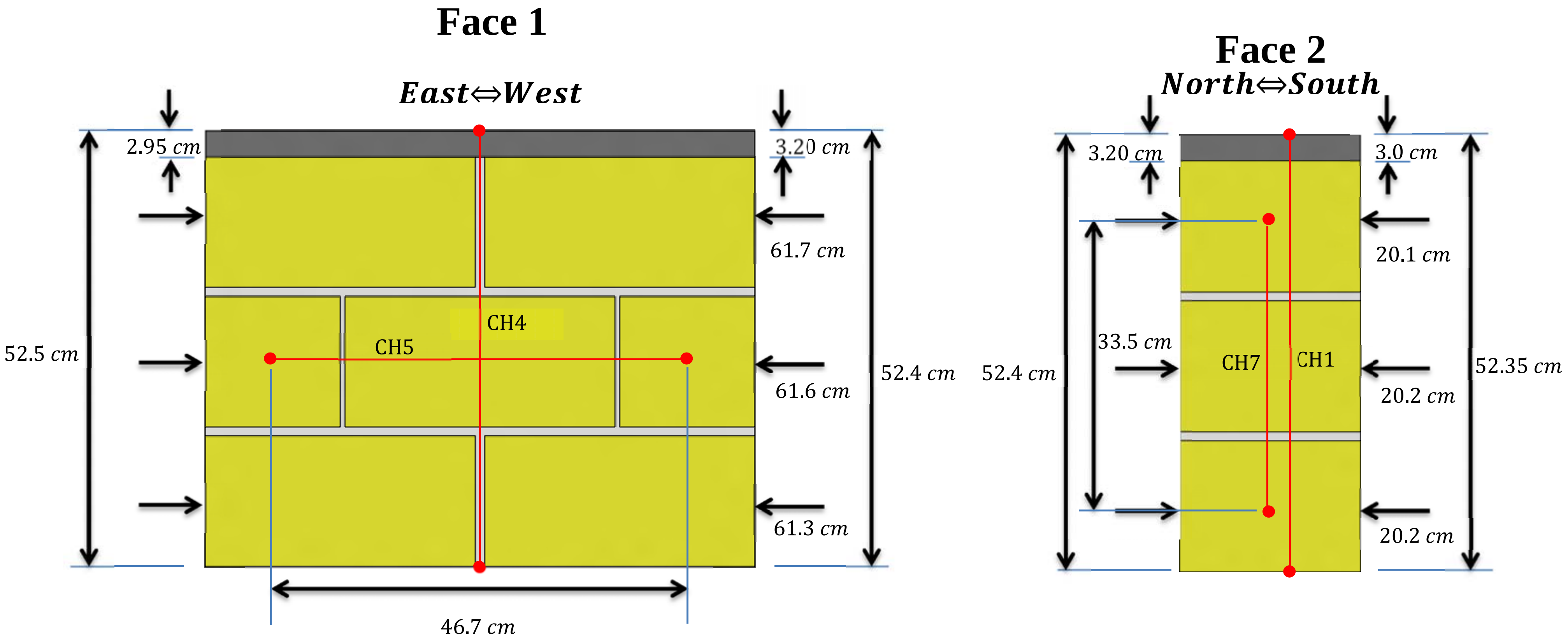

Figure 4.59Dimensions and LVDTs configuration of Sandstone Prism 2

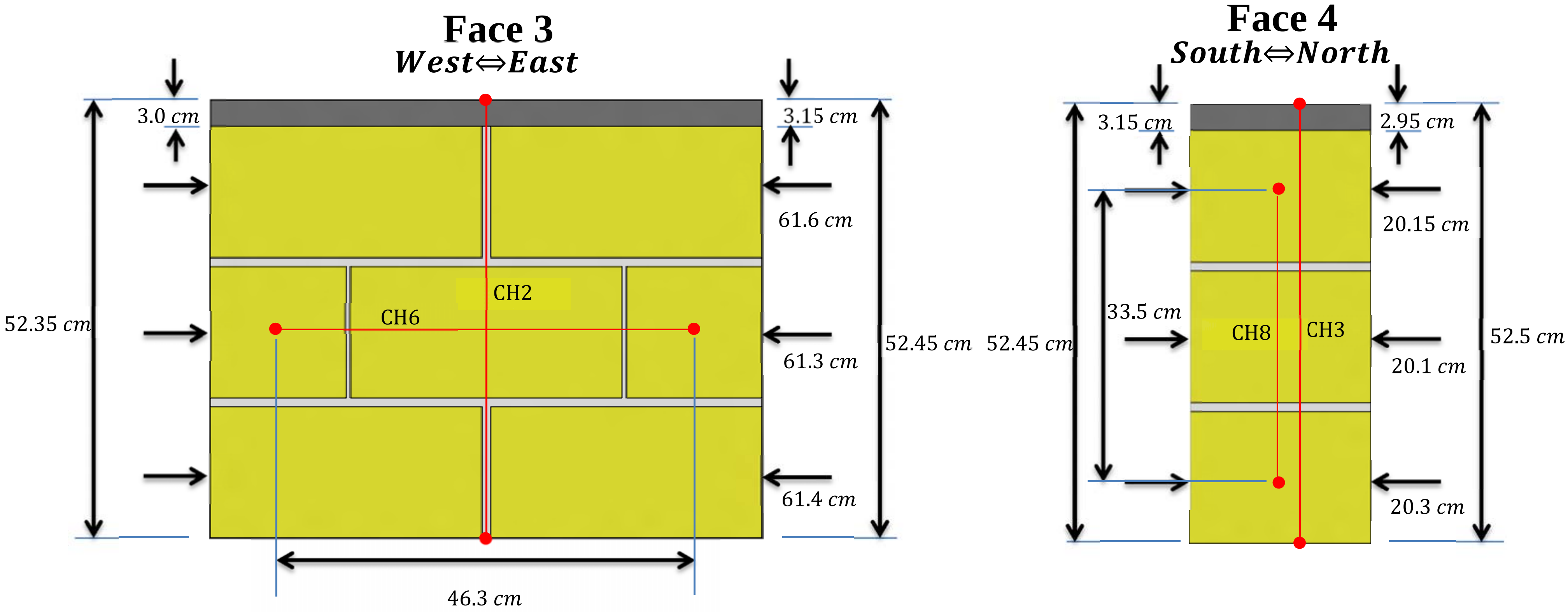

Figure 4.60 Dimensions and LVDTs configuration of Sandstone Prism 2

The axial force was exerted on the prism though a strong steel frame attached to the reaction floor. The axial load was recorded though a load cell of 2000 KN capacity placed between the prism and the steel frame. Some steel plates has to be used to fill the gap between the top of the prism and the steel frame. The data was acquired using TOKYO SOKKI data logger. Table 4.12 shows the total number of channels used in the experiment. The setup configuration is shown in Fig 4.61.

Table 4.12 Channels used in the prism compression experiment

Channel type	Channels	Number
CLC -Load Cells	0	1
CDP-25	1,2,3,4,5,6,7,8	8
Total		9

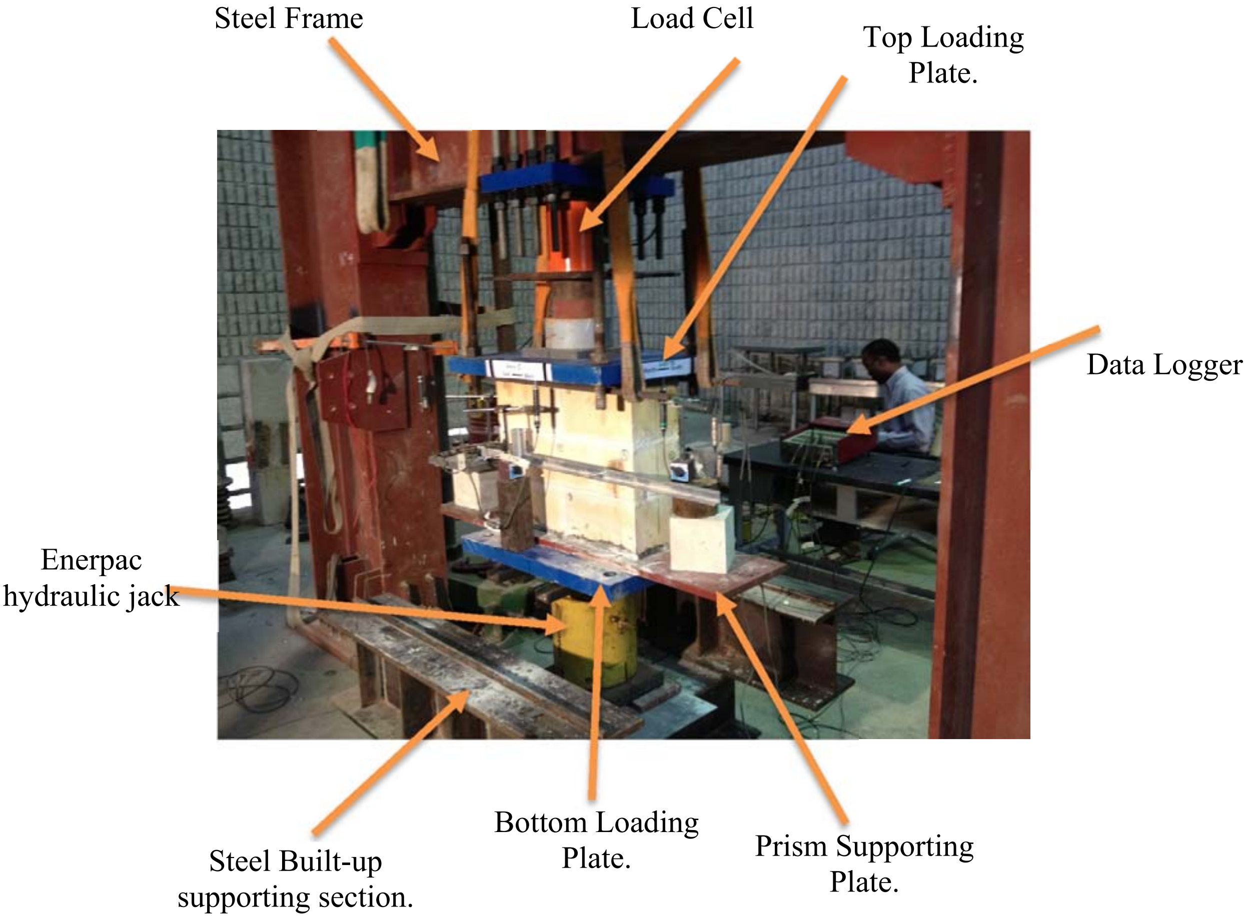

Figure 4.61 Test setup and configuration of sandstone prism

A displacement control test was adopted with an average test speed of $3 - 5\ \mu m/s$ so that the softening branch of the force-displacement curve could be captured. During the experiment, the cracks was noted and marked on the prims side by side with the associated load. To simplify the recording process of the cracks, prism brick units were numbered and sketched on paper. All cracks and associated loads was recorded graphically. The total duration of the test was 45 minutes, including cracks capturing process. The prims was first experienced a longitudinal crack and then diagonal cracks started to appear which was associated with growing of other cracks. The failure was quite uniform up to collapse. Figs 4.62-4.65 show wall during and after final collapse.

Figure 4.62 Sandstone prims during collapse.

Figure 4.63 Sandstone prism after collapse.

Figure 4.64 Sandstone Masonry prism after collapse.

Figure 4.65 Sandstone Masonry prism after collapse.

The axial strength of the two prisms are presented in Table 4.13.

Table 4.13 Axial compression strength of the prisms

Prism	Average Width mm	Average Thickness mm	Max force Kn	Stress MPa
Prism-1	617.8	201.7	1620.16	13.02
Prism-2	614.8	201.8	1754.07	14.20

Vertical load verses vertical displacements of the two prisms were recorded and shown in Fig. 4.66.

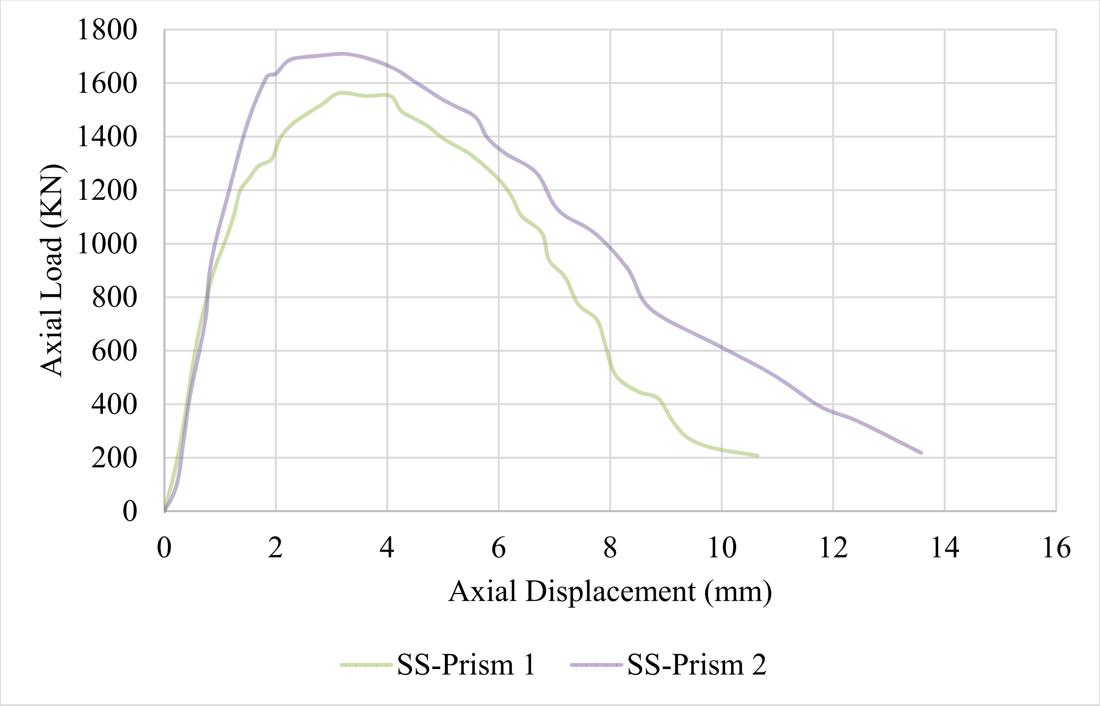

Figure 4.66 Vertical force versus vertical displacement of uniaxial compression test of Sandstone prisms.

4.6 Full Scale Masonry Walls Test

The main objective of this study is to examine the behavior of walls subjected to in-plane cyclic loading. For this purpose, three wall samples were built using sandstone units and lime mortar at head and bed joints (Fig 4.67). The walls were built directly on top of a steel U channel in the reaction floor near the testing setup so that transporting the wall from place to place were achieved without damaging the wall samples. The walls then were subjected to curing process for about three weeks with continuous water curing. After curing, the wall was then placed in the proper position within a steel frame fabricated for purpose of testing the wall under cyclic loading.

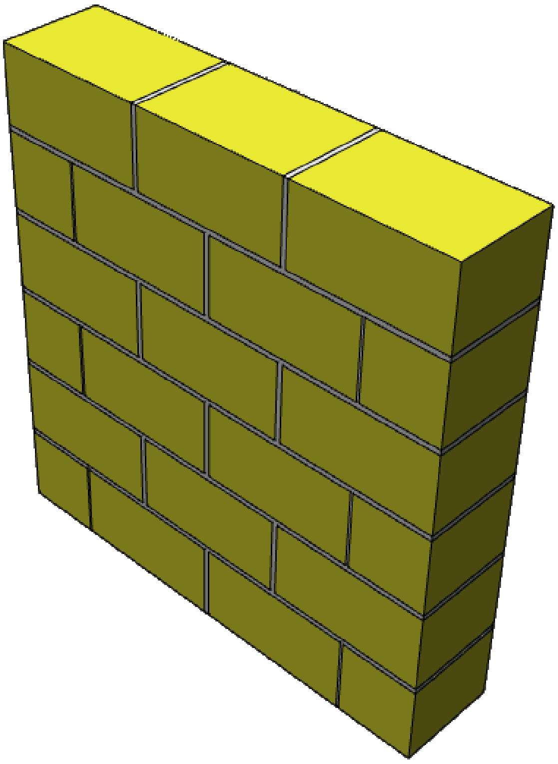

Figure 4.67 Isometric view of the sandstone wall.

Placing of the wall is a critical issue in which the wall has to be perfectly aligned vertically and horizontally so that it is in consistence with the cyclic hydraulic jack actuator to prevent any out of plane action and also to prevent eccentricity when applying load. Laser leveler was used so that perfect alignment could be achieved.

A total of three walls were tested in this study. Two of them were unreinforced masonry walls and the third one was masonry wall reinforced with CFRP. Each one of those wall were subjected to different level of pre-axial compression stress. The notation used for the distinct types of walls was based on vertical pre-compression levels.

For the purpose of testing, steel frame was constructed on the reaction floor Fig 4.68. This frame was used to exert the axial load on the wall. The axial stress was exerted on the wall using specific equipment fabricated for this test. The equipment consisted of two hydraulic jacks and controller Figs 4.69-4.71. One of the hydraulic jack (named Jack A) exerts only compression force and the other (Named Jack B) can exerts both compression and tension force. The two hydraulic jacks were designed so that the force exerted on the walls is slow.

Figure 4.68 Constructed steel frame.

Figure 4.69 Hydraulic jack Controller.

Figure 4.70 Hydraulic jack A exerts only axial force.

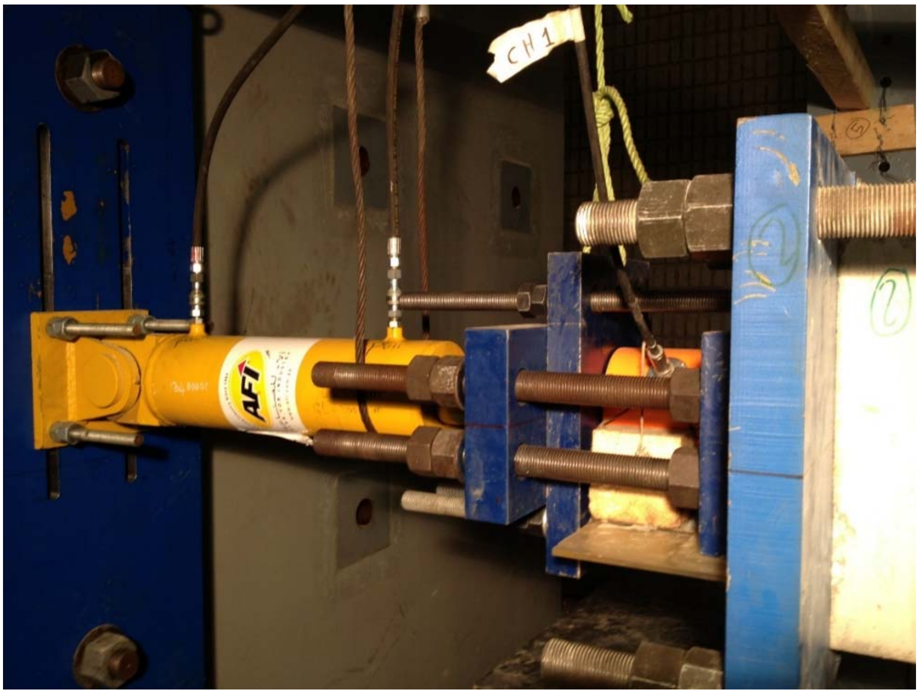

Figure 4.71 Push Pull hydraulic jack B.

The axial as well as horizontal forces were exerted on the wall though a stiff concrete beam attached to the top of the wall. High strength mortar (BASF EMACO S88C) were used to attached the stiff concrete beam to the top of the wall. This high strength mortar ensures uniform distribution of the axial and horizontal force on the wall without any stress localization.

The wall movements and deformations were captured and recorded using several LVDTs attached to the wall at different positions. Total number of channels used in the test and type of those channels based on their reading are shown in Table 4.14. Fig 4.72 and 4.73 show configuration and positions of LVDTs attached to the wall.

Table 4.14 Channels used in the wall cyclic experiment

Channel type	Channels	Number
Load Cells	0,1	2
CDP LVDT-100	2	1
CDP-25	3,4,5,6	4
PATRIOT LVDT	7,8,9,10,11	5
Total		12

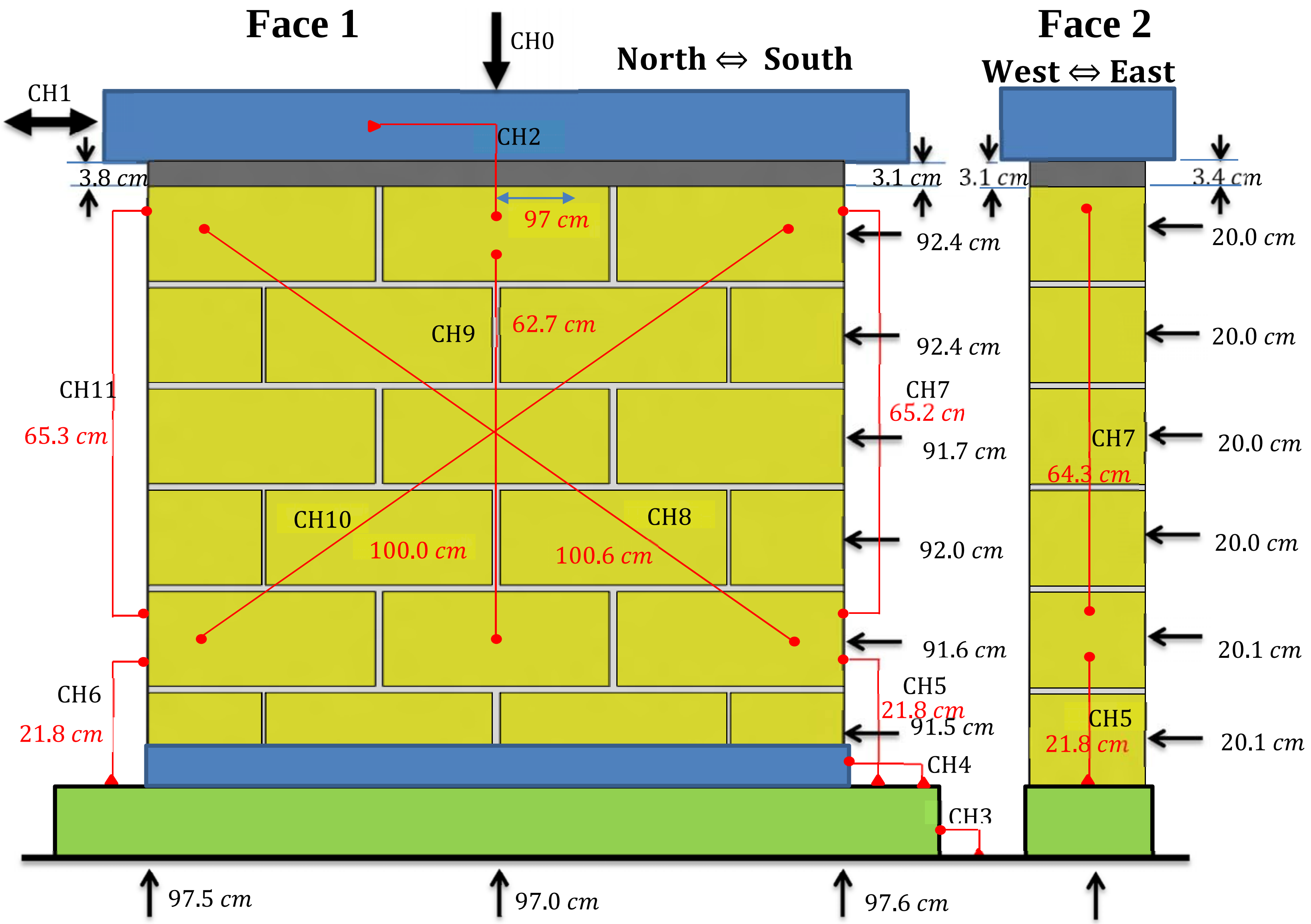

Figure 4.72 Dimensions and LVDTs configuration of wall-1.7.

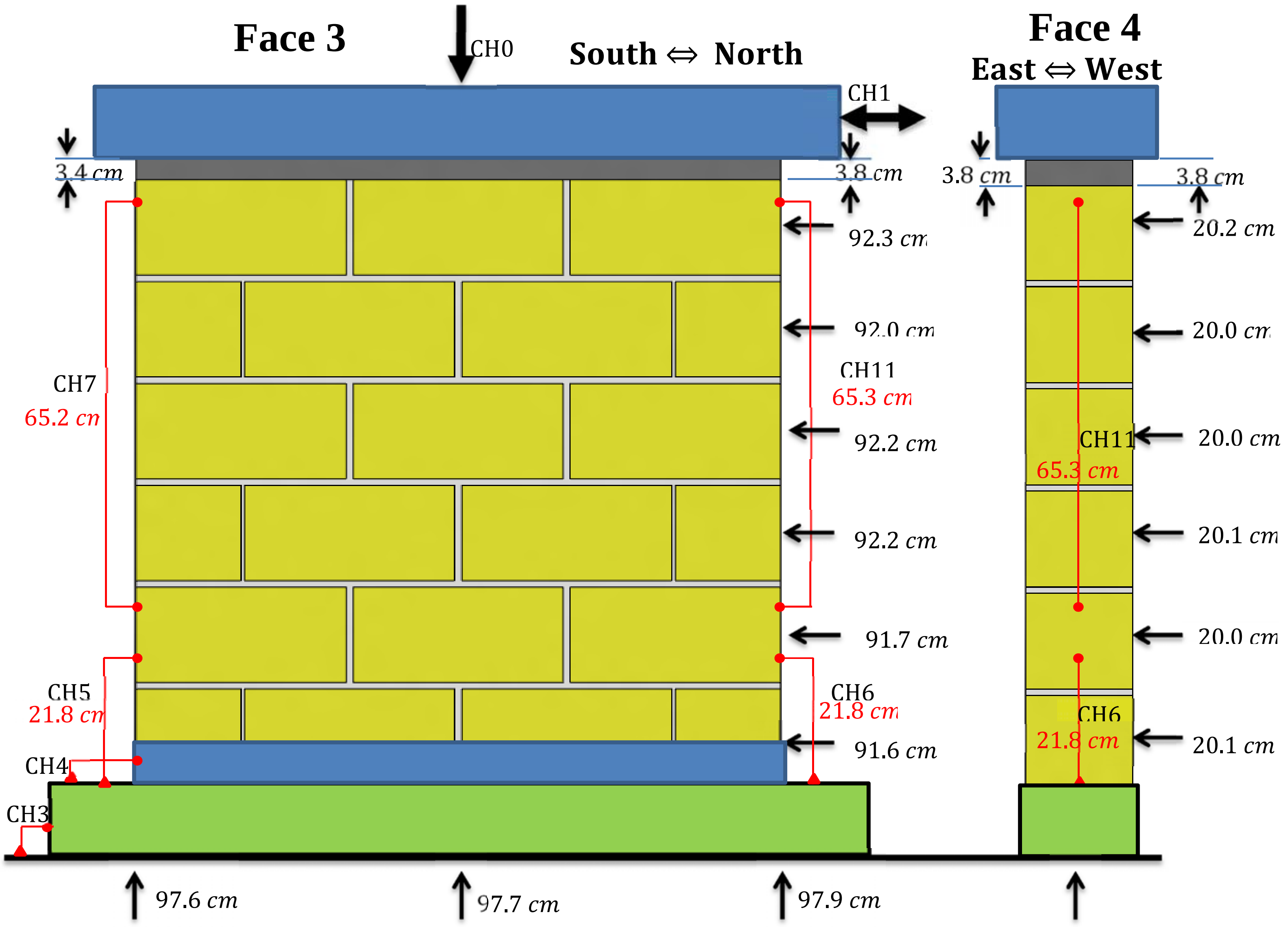

Figure 4.73 Dimensions and LVDTs configuration of wall-1.7

The axial force was exerted on walls with high axial force using Enerpac hydraulic jack which has a capacity of 2000 KN. This jack was then named Jack C. At first, the sandstone walls were placed on top of built-up steel section attached firmly to the reaction floor though two high 5 cm diameter strength big bolts. The wall was then firmly attached to this built-up section using two high strength bolts.

The axial forced exerted by the hydraulic Jack A or C was distributed to the top area of the wall though two beams. One of these two beams is a stiff concrete beam fabricated for this purpose. The other beam is stiff I steel section. At first, the concrete beam was placed and attached to the top side of the wall though thick layer of high strength mortar EMACO S88 CT. During the lateral loading of the wall, the top side of the wall as well as the attached concrete beam have to move freely so that the desired lateral load exerted on the wall can be achieved. The I steel beam was then placed on top of the concrete beam. The Jack A or C was then placed on top of the steel I beam. The hydraulic jack A or C and the steel beam were stationary in which movements (in-plane and out of plane) was prevented using a set of in-plane and out of plane support. The concrete beam, however, has to move freely in-plane to exert the lateral displacement to the top of the wall. To allow the lateral movement of the stiff concrete beam, as well as the top of the wall attached to the concrete beam, a set of cylindrical round bars were placed between the steel beam and the concrete beam. To prevent the damage of the top side of the concrete beam and also to facilitate the rotation of the round bars, thick steel plate was used to cover the top side of the concrete beam. This steel plate was firmly attachment to the beam using previously prepared bolt attached to the inside of the concrete beam at the time of casting.

As mentioned before, the wall was attached firmly to the built-up steel section. This was achieved by attaching the U wall support to the built-up steel section using two high strength blots. To prevent the wall from sliding in the first course, two L steel section were used at the two bottom ends of the wall. These two L section was attached to the U section using the same bolts used to attach the U wall support section to the built-up section. The gaps between the L section and the wall was then filled using EMACO S88 CT high strength mortar.

The horizontal load is transmitted to the wall through the concrete beam that attached to the horizontal Jack B. One side of Jack B was attached to the end of the concrete beam and the other side was reacted agents strong vertical reaction wall. Unfortunately, the horizontal Jack B was not designed for recording the exerted load. Due to this limitation, a fabricated setup was prepared and attached to the tip of the horizontal Jack B from one side and to the end of the stiff concrete beam on the other sided. This fabricated setup allowed recording the lateral load exerted on the wall using only one load cell. The horizontal Jack B was then attached to the reaction wall through a thick steel plate and strong hinge that allow only vertical rotation of Jack B. The configuration of the setup is shown in Fig. 4.74-4.80

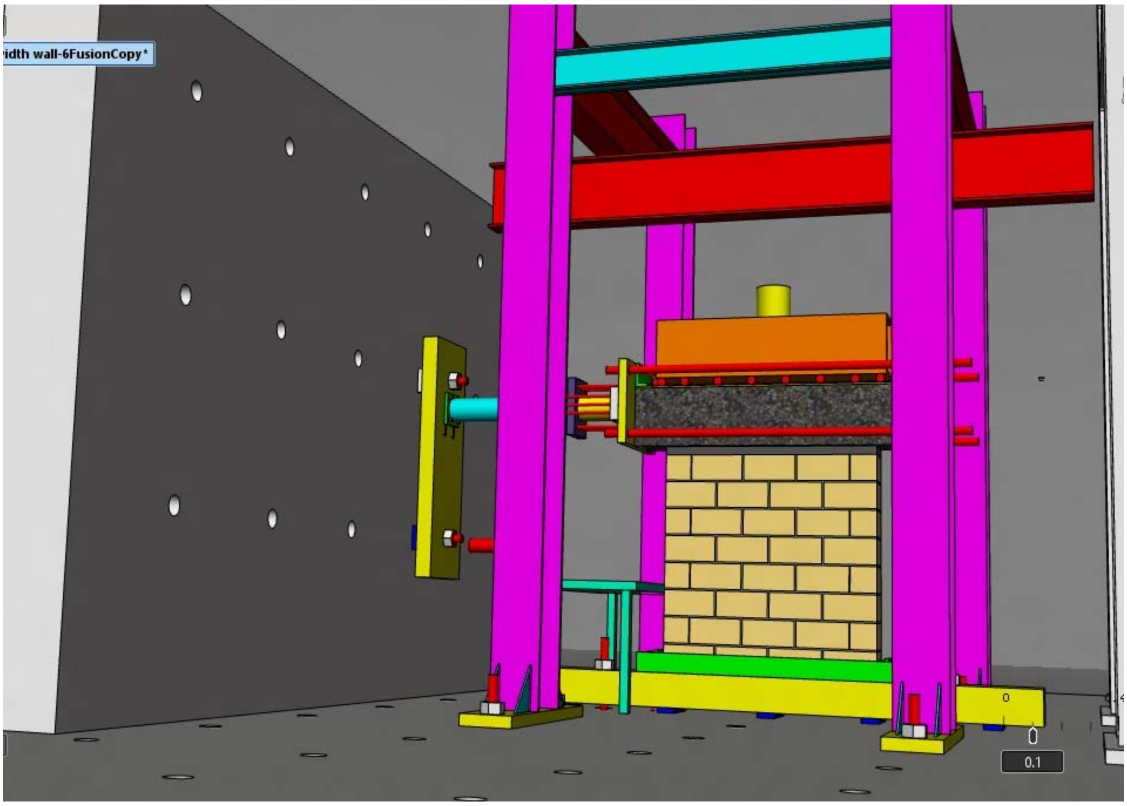

Figure 4.74 Cyclic test setup.

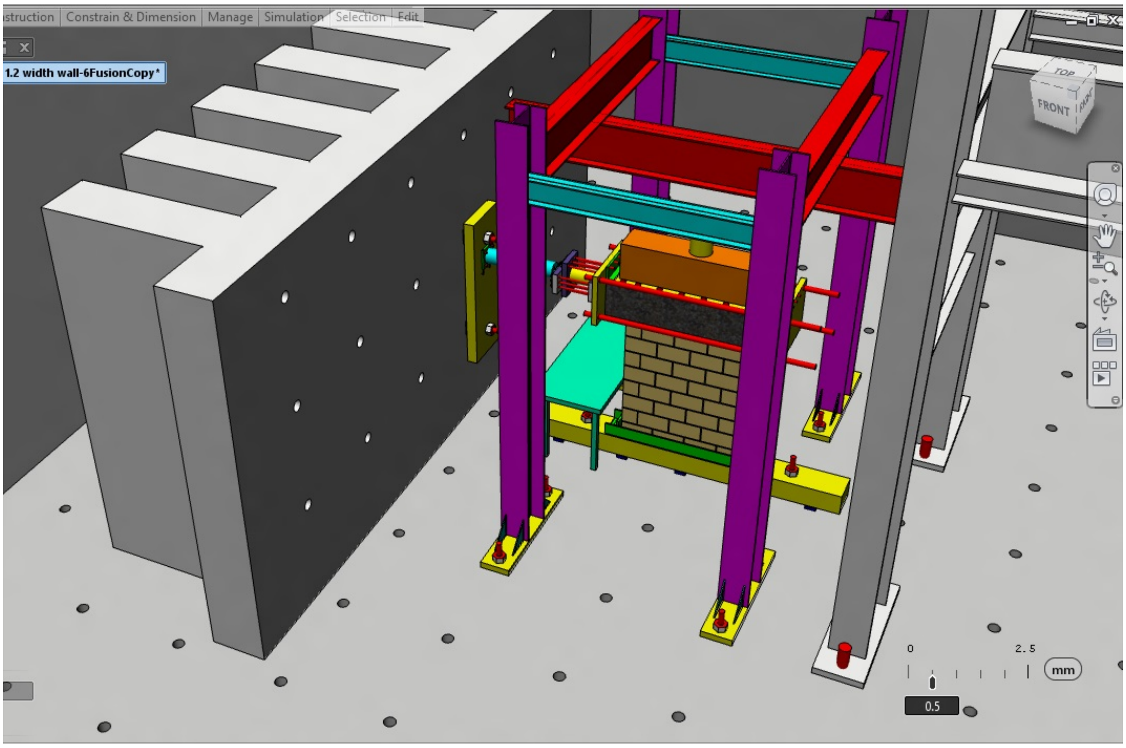

Figure 4.75 Cyclic test setup.

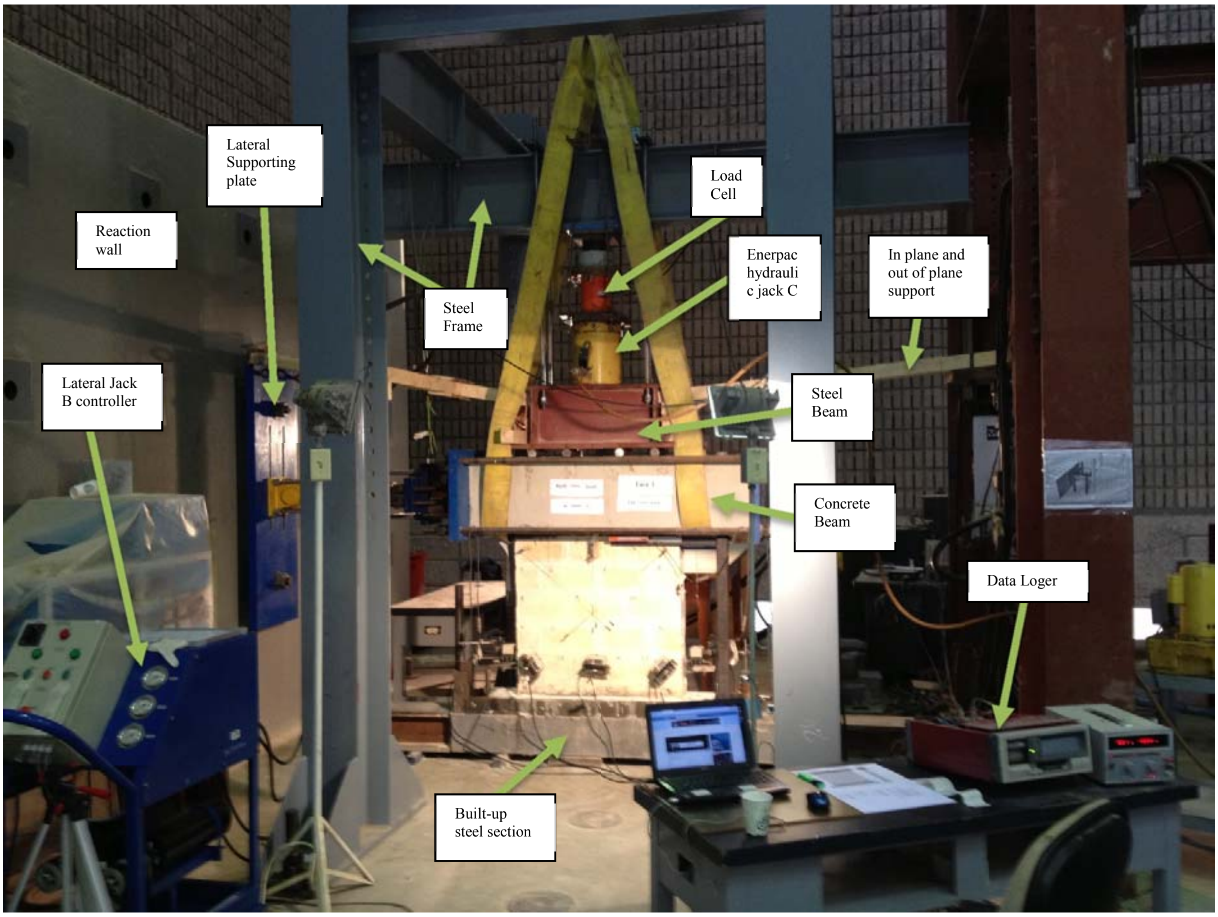

Figure 4.76 Cyclic test setup of Wall-1.7

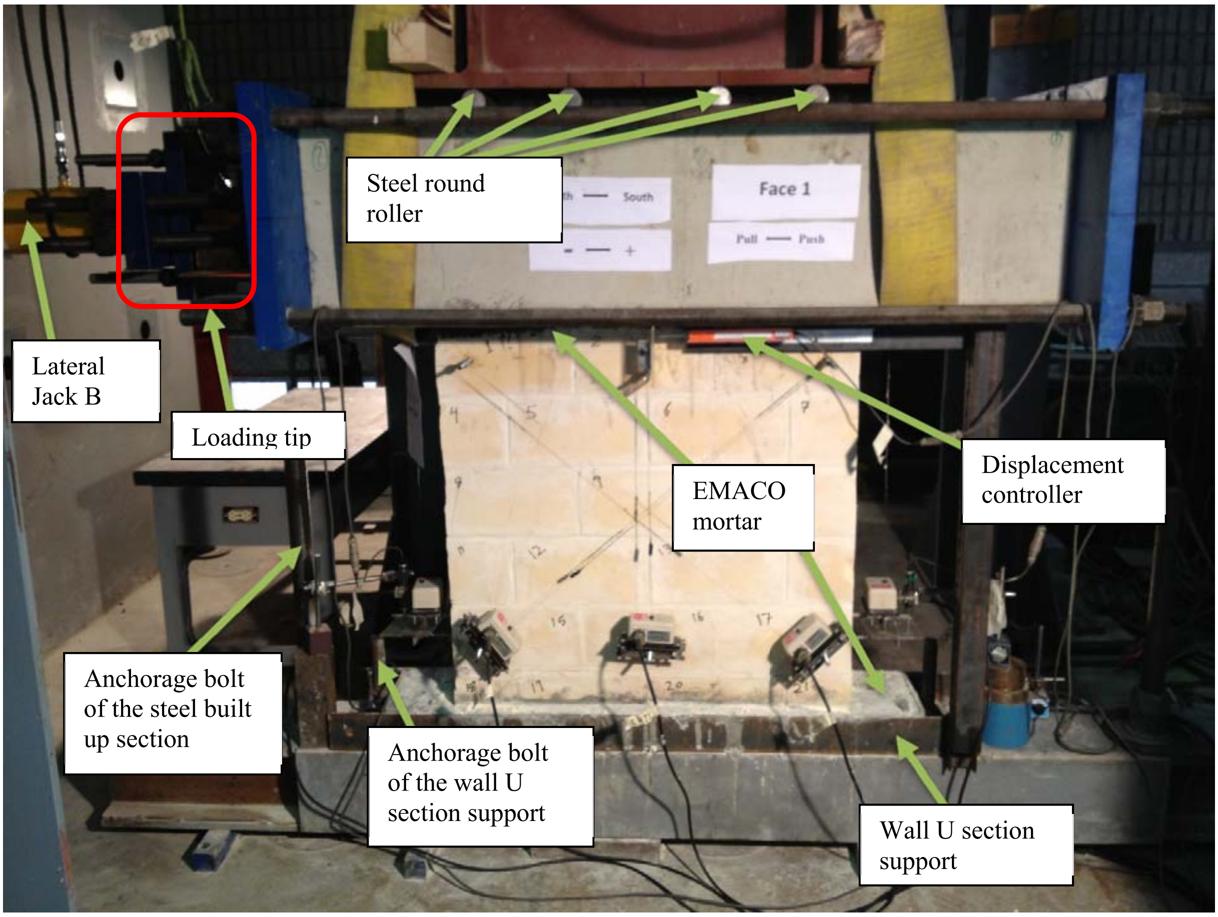

Figure 4.77 Cyclic test setup of Wall-1.7

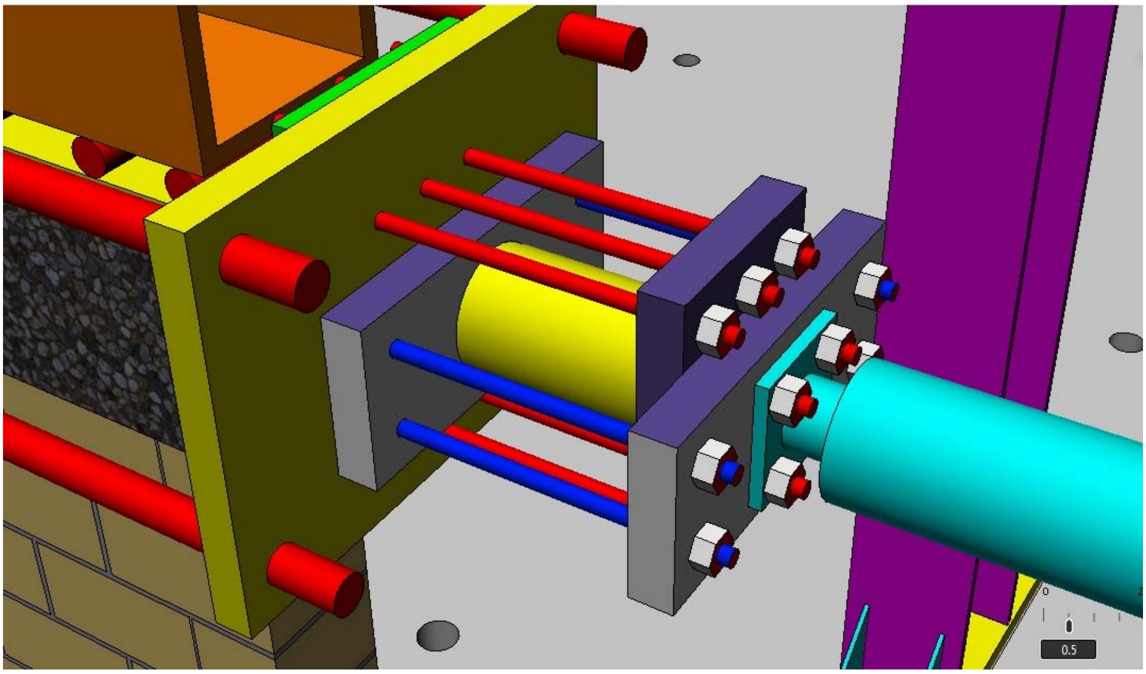

Figure 4.78 Loading tip.

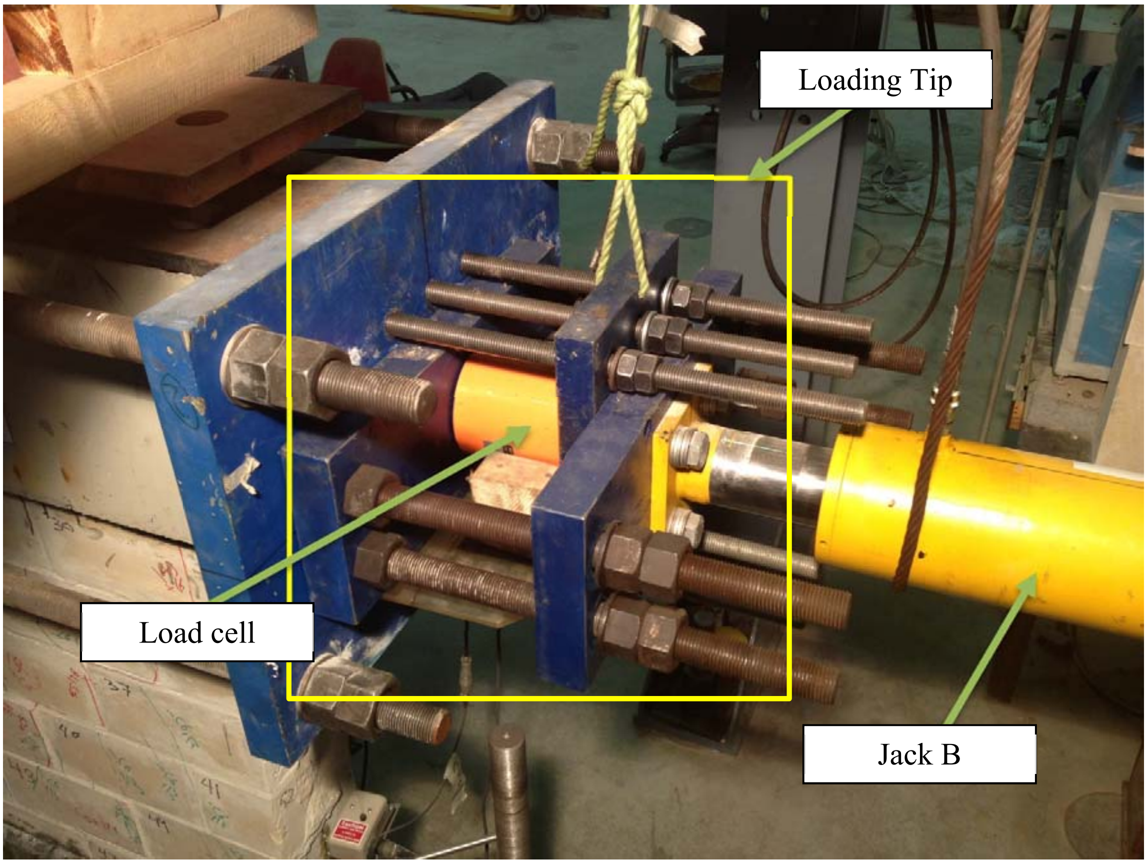

Figure 4.79 Loading tip.

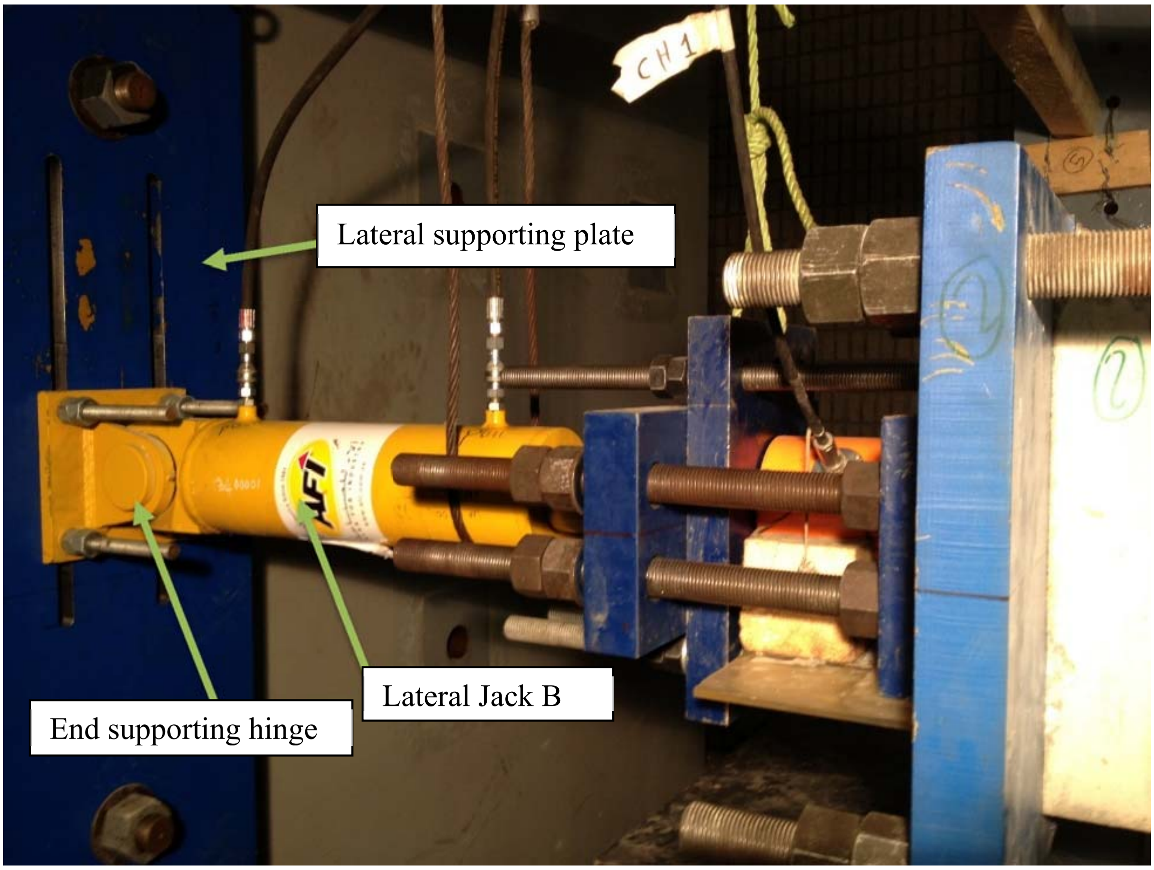

Figure 4.80 Loading tip.

As mentioned before, three walls was tested in the study. Tow to of the walls were tested without any strengthen. The last wall was strengthen with CFRP. The axial stress exerted on the walls are shown in table 4.15.

Table 4.15 Variables used in this study.

Name	Axial stress (MPa)	Reinforcement
Wall-1.35	1.35	No
Wall-1.7	1.7	No
Wall-2.0	2.0	Yes

It has to be mentioned that, wall-1.35 was a trial test as it was the first test to be conducted in this study. The test have experienced many interruptions, misreading and unexpected mistakes. The results of this test was not taken as a guidance to the overall all result of the whole study. It will be presented here as an indication of the overall behavior of the wall as well.

Loading was exerted slowly with a rat of 1.0 KN/s. The wall was then subjected to a cyclic loading using a displacement control load with a loading rate of 0.05 mm/s. The horizontal displacement load was controlled by means of the horizontal LVDT connected to the top center of the wall. The lateral loading adopted in this study was based on drift ratio. Table 4.16 shows the amount of drift ratio that the wall was subjected to and the associated lateral displacement. The lateral displacement measured at the top center of the wall are shown in Fig 4.81

Table 4.16 Lateral displacement loading

Cyclic Loading			
No.	Drift ratio %	Push mm	Pull mm
1	0.05%	0.5	-0.5
2	0.10%	1.0	-1.0
3	0.25%	2.4	-2.4
4	0.50%	4.9	-4.9
5	0.75%	7.3	-7.3
6	1.00%	9.8	-9.8
7	1.25%	12.2	-12.2
8	1.50%	14.6	-14.6
9	2.00%	19.5	-19.5

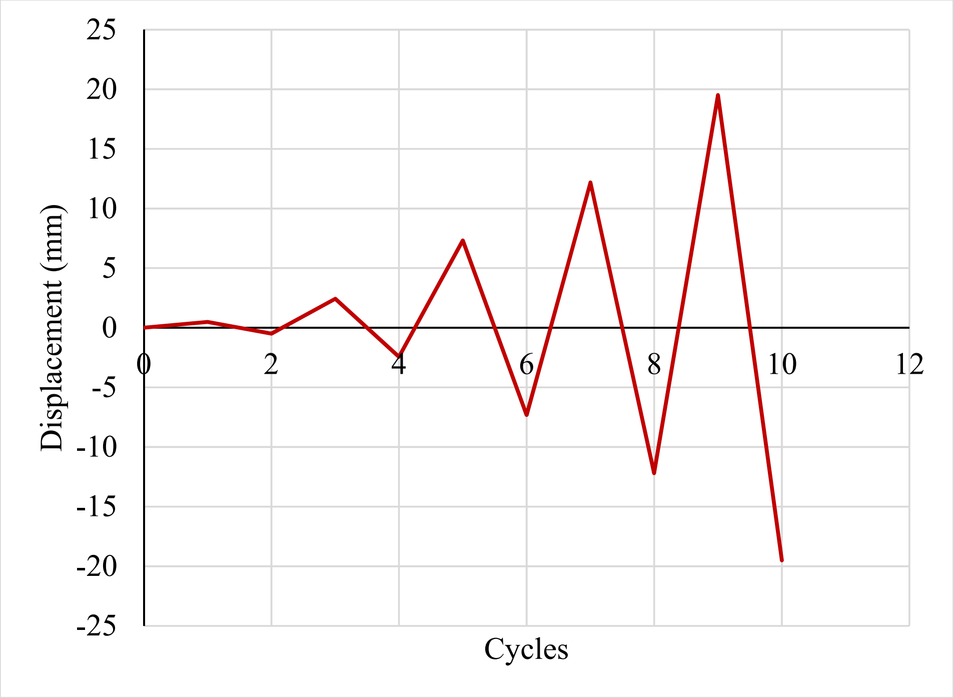

Figure 4.81 Cyclic displacement loading

4.6.1 Wall-1.35.

As mentioned before, the wall under consideration was a trial wall test. Many inconsistent results was observed. The process of test, stop, and retest caused considerable damage to the wall which in turn affected the behavior as well as the capacity of the wall. In the experiment conducted on wall-1.35, the axial load was first exerted so that the axial stress is 1.35 MPa (load of 250 KN). After that lateral displacement load was applied to the wall through the concrete beam. It has been observed that, first cracks noted in the wall was in the lower course of the wall as expected. The wall exhibited high level of rocking behavior. This was because of level of axial load was only 13 % of the axial capacity of the wall. Cracks started to initiate when more cyclic was exerted on the wall. The diagonal crack in the wall was few and they joint together from top to bottom of the wall. Permanent deformation was noted when unloading to zero lateral force. The damage development within the wall body is shown in Figs 4.82-4.84.

Figure 4.82 Damage associated with 4.9 mm push loading, Wall-1.35

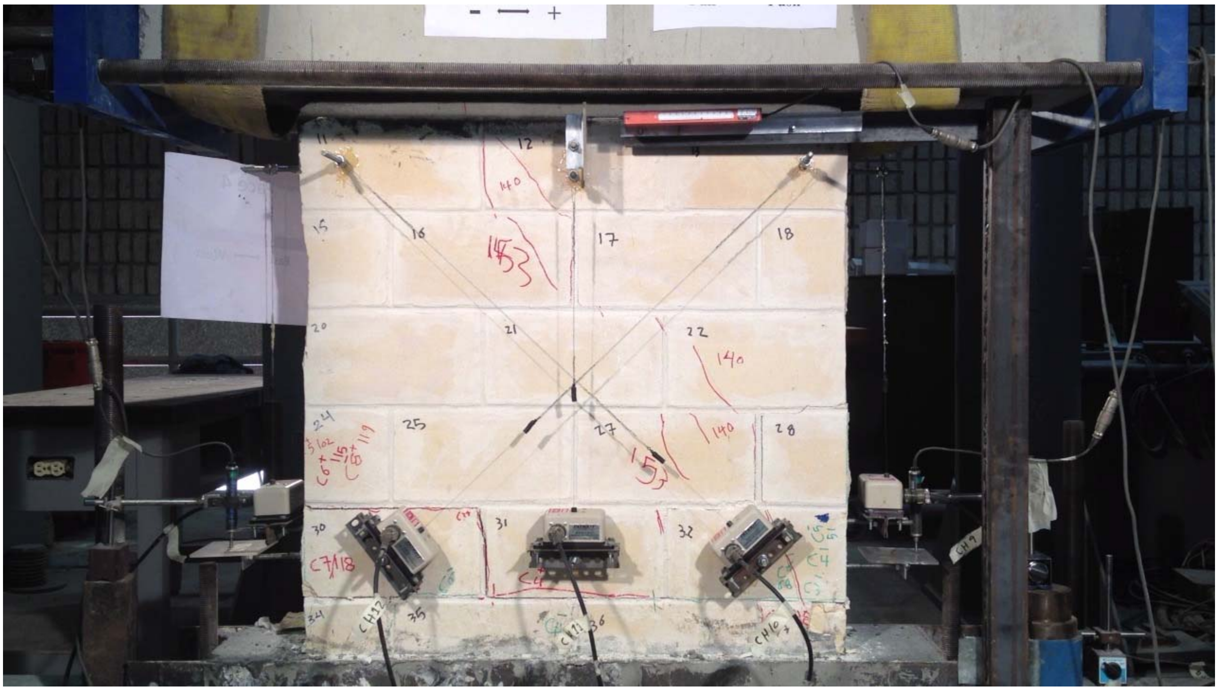

Figure 4.83 Damage associated with 7.3 mm push loading, Wall-1.35

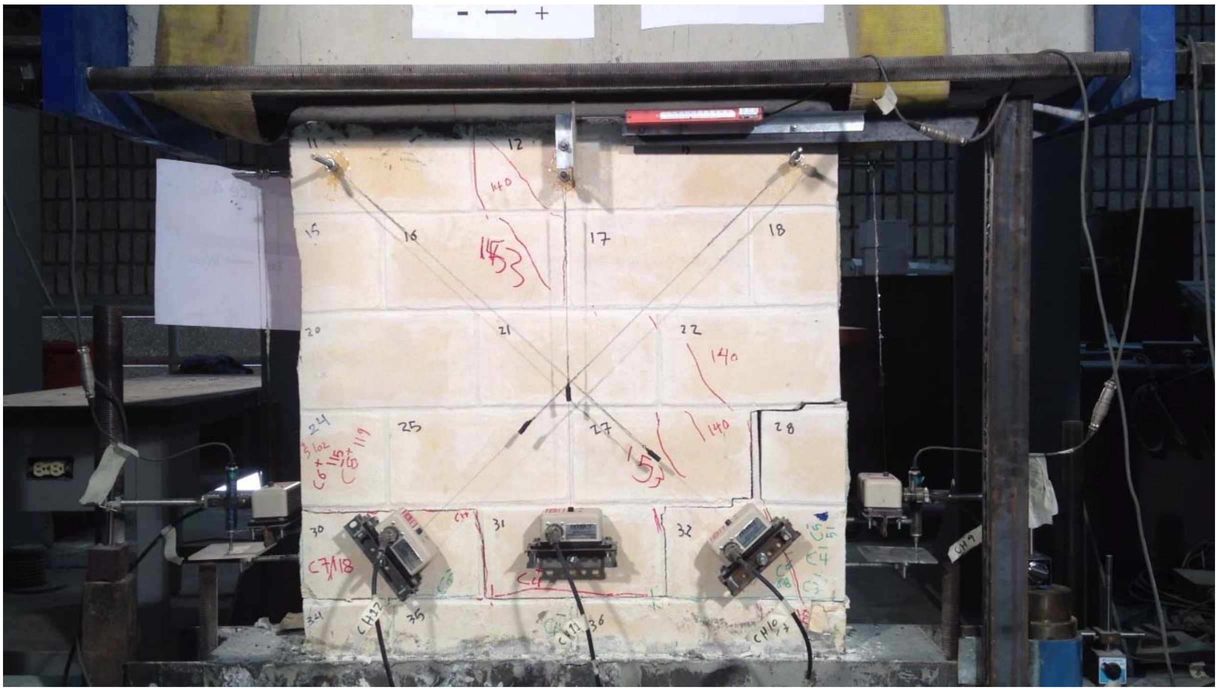

Figure 4.84 Damage associated with 7.3 mm pull loading, Wall-1.35

It has to be mentioned that because this wall was a trial test, the load data captured during the experiment was not correctly captured. Another issue that has to be mentioned is that for safety purposes, only 3 cycles out of 10 was executed. Force displacement hysteresis of the experiment of Wall-1.35 is shown in Fig 4.85.

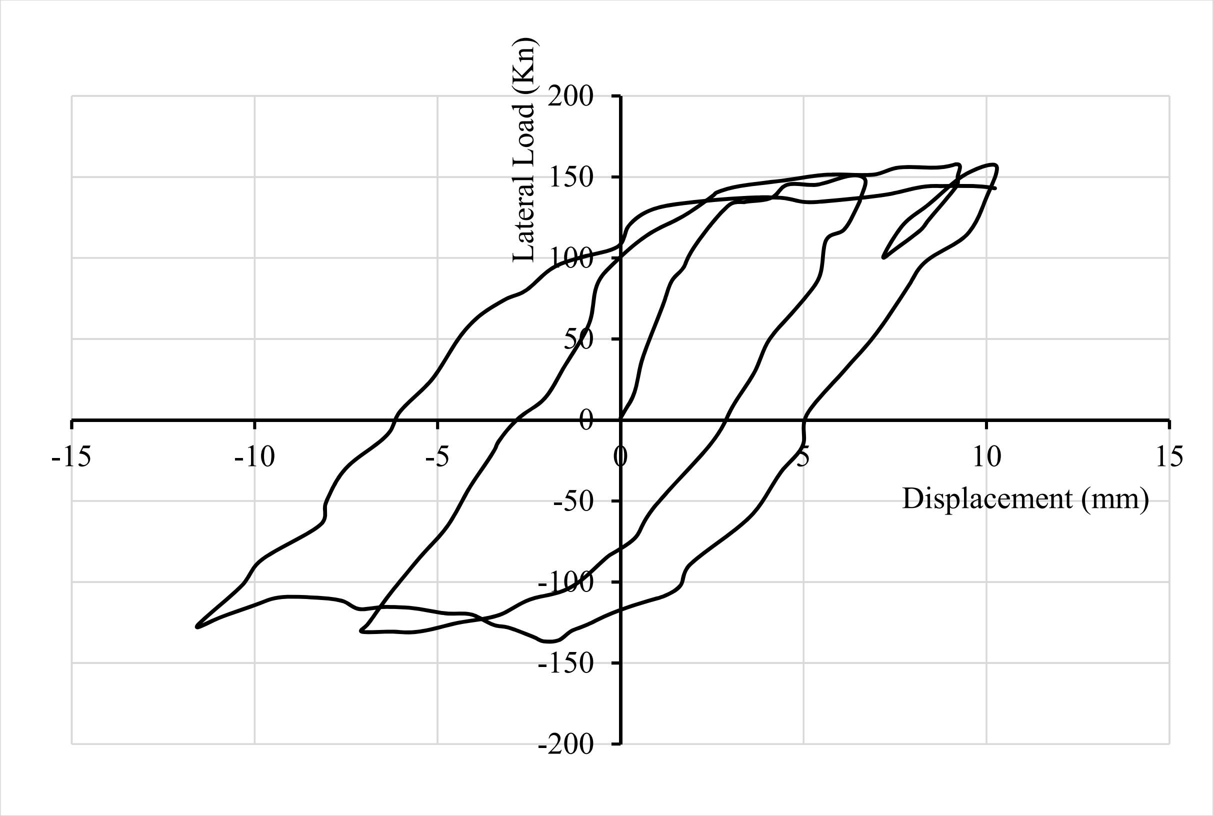

Figure 4.85 Force displacement hysteresis of wall-1.35.

4.6.2 Wall-1.7.

In experiment conducted on wall-1.7, the axial load was first exerted so that the axial stress is 1.7 Mpa (load of 313 KN). After that lateral displacement load was applied to the wall through the concrete beam. The test results of this experiment reveals that, walls behavior is highly depending on the level of axial load excreted on the wall. It has been observed that, first cracks noted in the wall was in the lower course of the wall. These type of cracks repressing a form of rocking failure. The evolution of the damage and cracks on the wall was continue to take another form in which a diagonal cracks was started to initiate within the sandstone brick and also cracks star to initiated in the lime mortar head and bed joints. As the lateral force increase, new cracks were developed and also the existing cracks were getting wider. At first, lateral resistance of the wall was noted to increase in almost linear trend. This indicated that the wall was behaving as a kind of elastic behavior. Very small amount of permanent deformation was recorded at the first few cycles. However, when lateral load started to increase, cracks and damage started to developed and become more pronounced within the wall body. The lateral resistance of the wall was noted to increase in slower rate compare to the previous cyclic which indicated that the wall start to approach the plateou phase of response. Permanent deformation was noted when unloading to zero lateral load. Figs 4.86-4.92 show the wall damage associated with deferent level of lateral load.

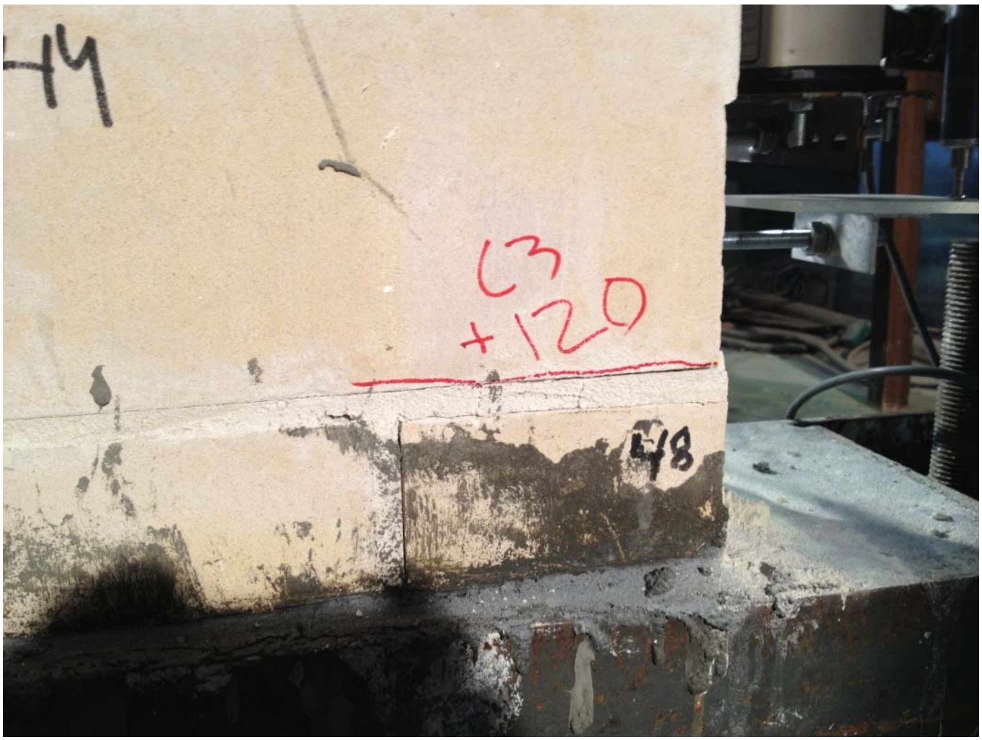

Figure 4.86 Damage associated with 2.4 mm push loading Wall-1.7

Figure 4.87 Damage associated with 2.4 mm pull loading Wall-1.7

Figure 4.88 Damage associated with 7.3 mm push loading Wall-1.7

Figure 4.89 Damage associated with 9.8 mm push loading Wall-1.7

Figure 4.90 Damage associated with 9.8 mm push loading (back side) Wall-1.7

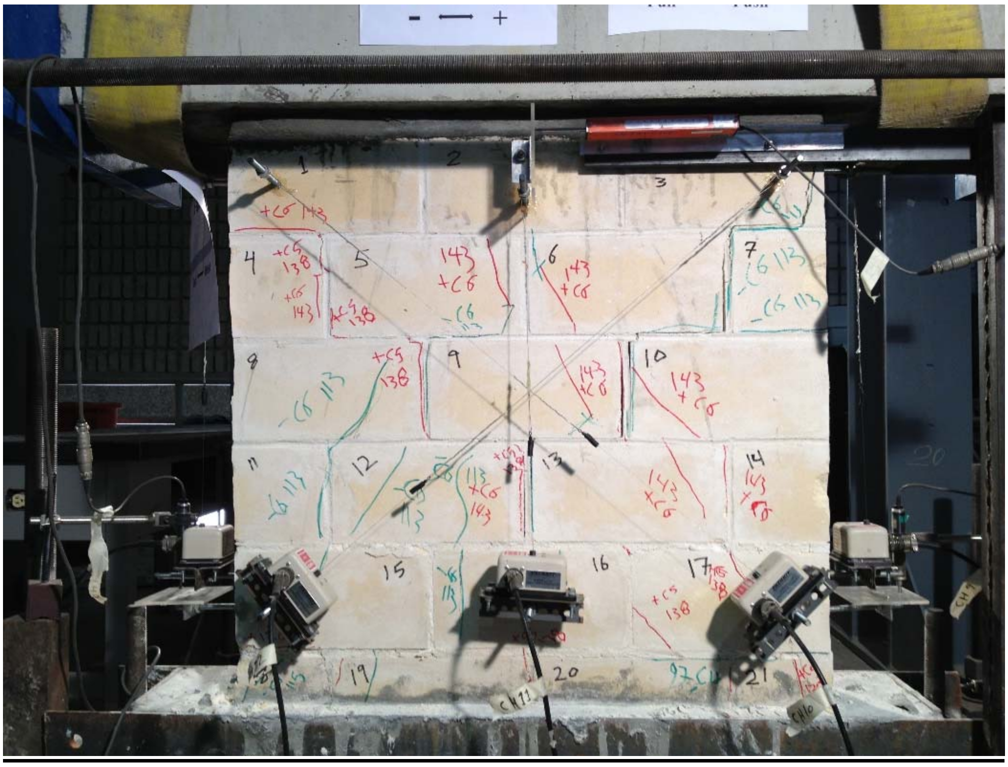

Figure 4.91 Damage associated with 9.8 mm pull loading Wall-1.7

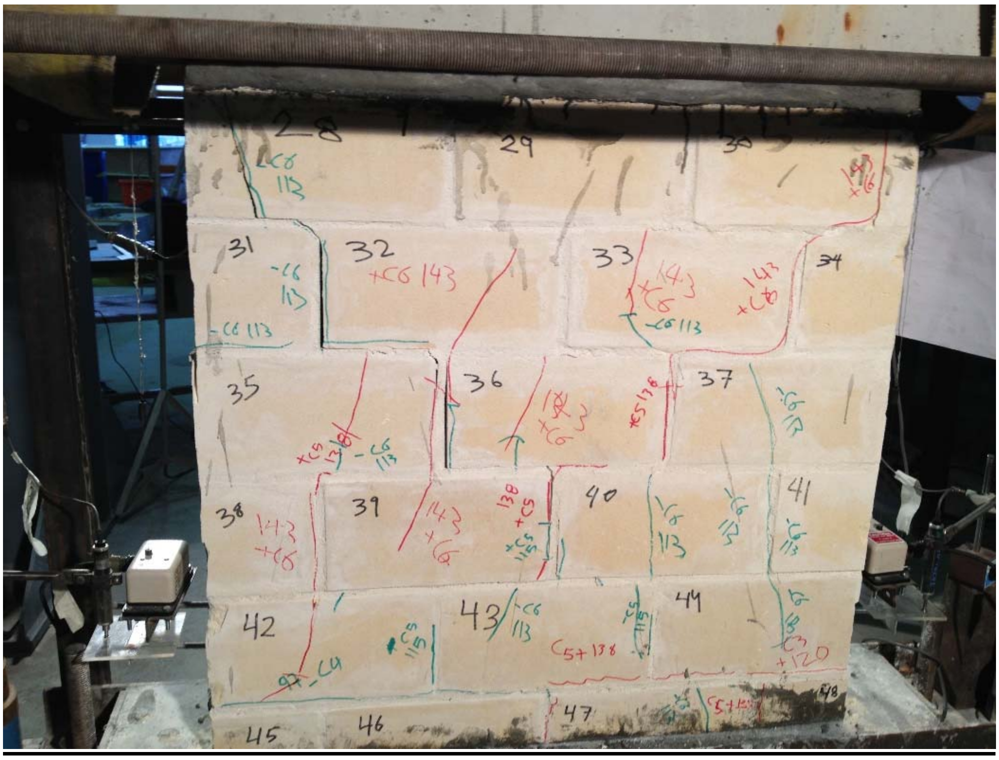

Figure 4.92 Damage associated with 9.8 mm pull loading (back side) Wall-1.7

It has to be mentioned that only 7 cycles out of 10 was executed. The wall had subjected to high level of damage and for the safety issues, the experiment was ended with 7 cycles. Complete force displacement hysteresis of the experiment of Wall-1.7 is shown in Fig 4.93.

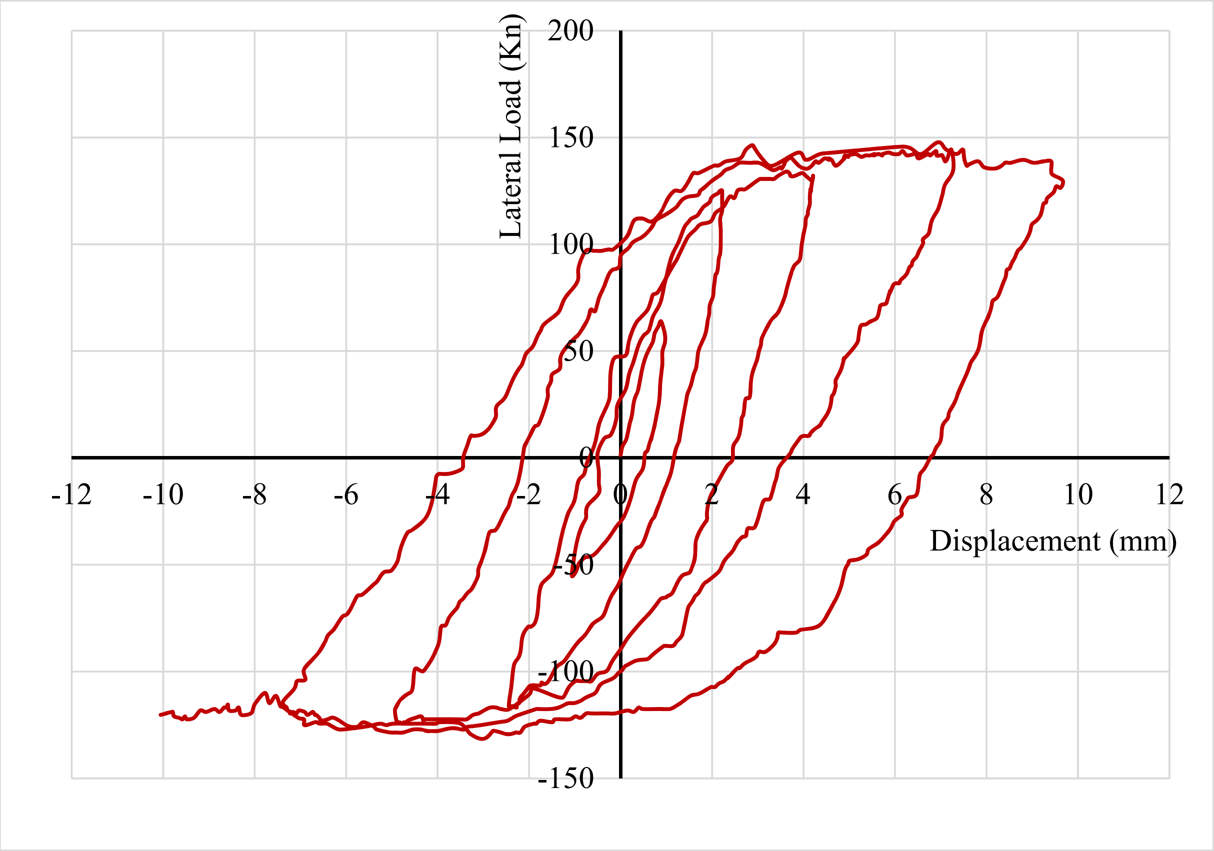

Figure 4.93 Force-Displacement hysteresis loading of Wall-1.7

4.6.3 Strengthening of Masonry Wall.

As mentioned before, masonry wall when subjected to seismic loading, it will experience some damage. To return and rehabilitate walls to function and carry load again, a retrofitting process has to be carried out for the walls.

Several type of retrofitting material and techniques have been adopted and studied by various researchers. One of the most common type of reinforcement is the CFRP (Carbon-Fiber-Reinforced Polymer). This material has a high tensile strength capacity which helps the structure regain strength. In this study, CFRP strengthening process for walls has been adopted and tested experimentally. The purpose of this study is to evaluate the amount of extra strength that is added to the masonry wall due to application of this material. One layer of CFRP lamina was attached to the surface of the wall in a diagonal pattern. The CFRP lamina was attached to the surface using Sika-Dur 300 Epoxy (Fig. 4.94).

Figure 4.94 Sika-Dur 300 Epoxy

The bandwidth of the CFRP lamina was 20 cm. The epoxy was then subjected to dry curing process for a period of 24 hours and then after that cyclic loading test was conducted. In this experiment, the level of axial force was kept equal to the level of axial force in the previous masonry wall. The designation name of this wall was Wall-CFRP-1.7. Configuration of walls strengthened with CFRP is shown in Fig 4.95-4.97.

Figure 4.95 Wall-CFRP-1.7 under test.

Figure 4.96 Wall-CFRP-1.7 under test.

Figure 4.97 Wall-CFRP-1.7 under test.

The wall was then subjected to cyclic loading similar to that exerted on Wall-1.7. The wall exhibit a stiff response in which no cracks was detected within the wall body. The wall exhibited rocking behavior in which a longitudinal crack was observe at the lower cores on the wall (Figs 4.98 and 4.99).

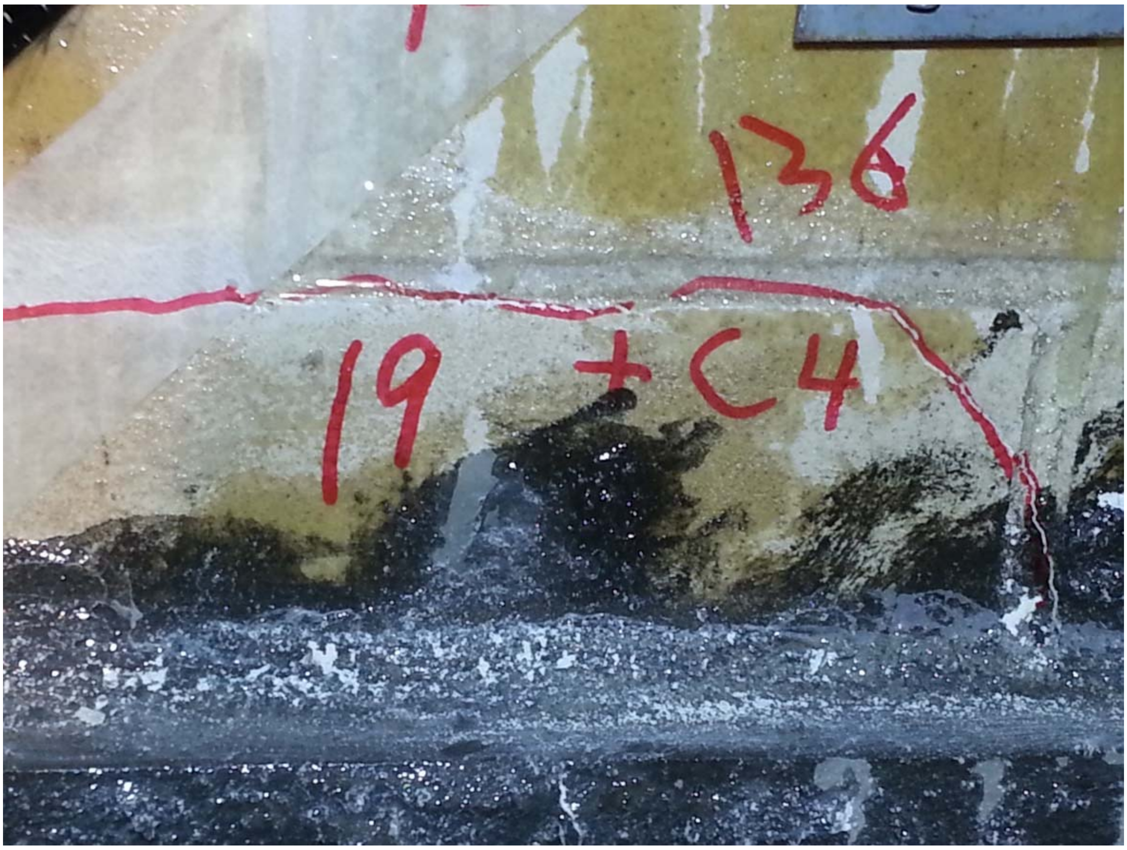

Figure 4.98 Longitudinal crack at the first course of the wall

Figure 4.99 Longitudinal crack at the first course of the wall

It has been noted that the level of lateral strength was high compare to that in Wall-1.7. this observation strengthen the idea of reinforcing masonry wall using CFRP

It has to be mentioned that only 7 cycles out of 10 was executed so that we can compare with Wall-1.7. Complete force displacement hysteresis of the experiment of Wall-CFRP-1.7 is shown in Fig 4.100.

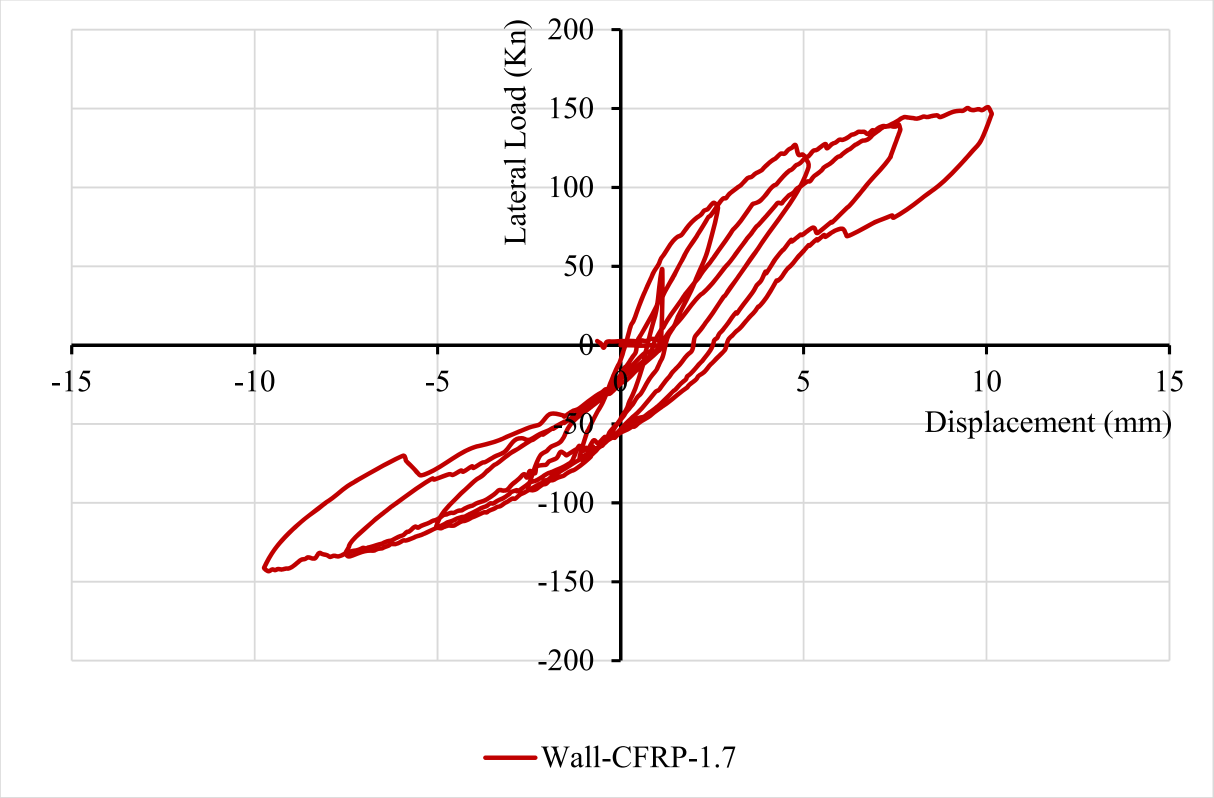

Figure 4.100 Cycle response of Wall-CFRP-1.7

Fig 4.100 shows that walls reinforced with CFRP shows low energy dissipation compare to wall without CFRP. This can be attributed to the absence of damage within the wall body.

CHAPTER 5

COMPUTATIONAL SIMULATION ANALYSIS

5.1 Introduction.

As mentioned earlier, two different numerical approaches were adopted in this study. The first one is based on continuum approach in which both sandstone and lime mortar were modeled as continuum base material. Some of the needed parameters were found form the appropriate tests and some others were assumed using the default values. The interaction between the two material were assumed to be full bond in which no relative movement (separations) in either direction (normal and tangential) was allowed. One of the advantages of the continuum base approach is that it allows capturing the cracks within the lime mortar.

The second approach used was the interface approach using surface base cohesive module available in ABAQUS. In this approach, the sandstone was modeled as continuum base material whereas the lime mortar was modeled as a contact cohesive material with zero thickness.

Effect of axial load on masonry wall has been studied numerically. A generalized behavior of masonry wall subjected to different level of axial loading has been extracted and a proposed correlation that relate the level of axial load to the lateral resistance of the wall has been proposed.

For generalization propose, numerical simulation has been conducted for three different and independent experimental work carried out by various researchers. These include:

- Research work of Demir (2012)
- Research work completed by Li et al (2005)
- Research of Vasconcelos (2005)

All of the above mentioned works were noted to exhibit a common trend in behavior and a general correlation has been proposed for combination of axial and lateral loads that case failure of masonry walls aspect ratio close to unity.

5.2 Numerical Simulation Conducted for Walls Tested in the Study.

In this study, two different approaches were adopted, namely, continuum based approach and interface approach. Emphasis has been given to the continuum approach because the stresses and damage within the mortar body was targeted.

5.3 Continuum Based Approach

As mentioned before, continuum based approach was used in this study to assess the behavior of the masonry wall subjected to axial and lateral loading. The Plastic Damage model incorporated in ABAQUS was used to described the behavior of both sandstone and lime mortar material. In this study, the explicit analysis approach was adopted because the explicit analysis is much more stable and gives good results compared to standard static analysis. The explicit analysis can be used to do quasi-static analysis when the loading time is larger than the vibration period of the structure. Frequency analysis has been carried out for the wall to find the natural period of vibration of the wall related to the axial and lateral vibration mode. The loading time lower limit was set to be at least three times the natural vibration period of the structures to insure that quasi-static analysis was achieved. Table 5.1 shows the vibration modes and the associated frequency and natural period of the masonry wall. The lateral natural vibration period is associated with the 3th mode (Fig 5.1) and the axial natural vibration period is associated with 6th mode (Fig 5.2).

Table 5.1 Mode of vibrations and natural frequencies and period associated with each vibration mode.

Mode of Vibration	Frequency HZ	Vibration Period Sec
1	57.74	0.01732
2	148.24	0.00675
3	247.86	0.00403
4	358.69	0.00279
5	532.73	0.00188
6	640.15	0.00156
7	667.28	0.00150
8	716.38	0.00140
9	932.21	0.00107
10	981.90	0.00102
11	1092.76	0.00092
12	1243.42	0.00080
13	1448.26	0.00069
14	1454.70	0.00069
15	1497.60	0.00067

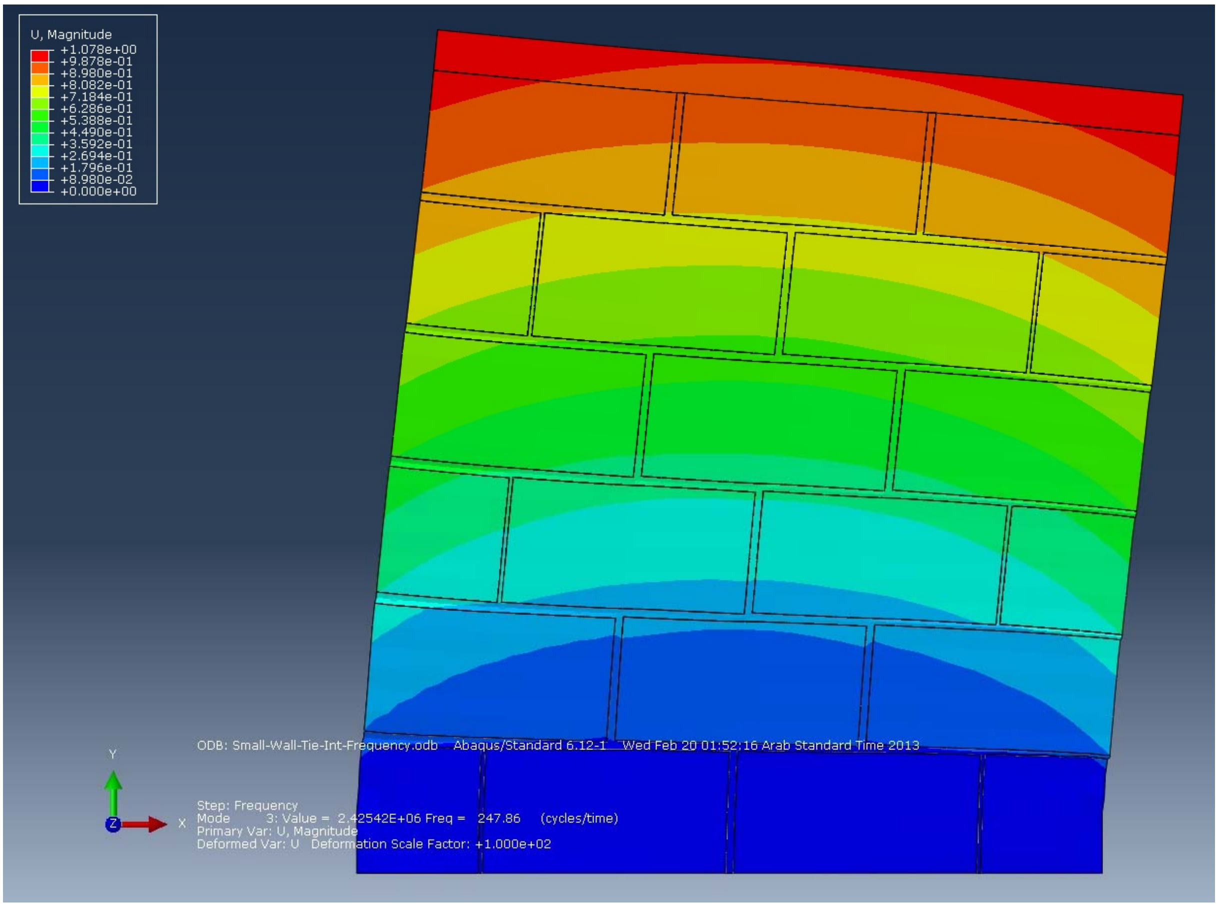

Figure 5.1 3th mode of vibration (Lateral vibration)

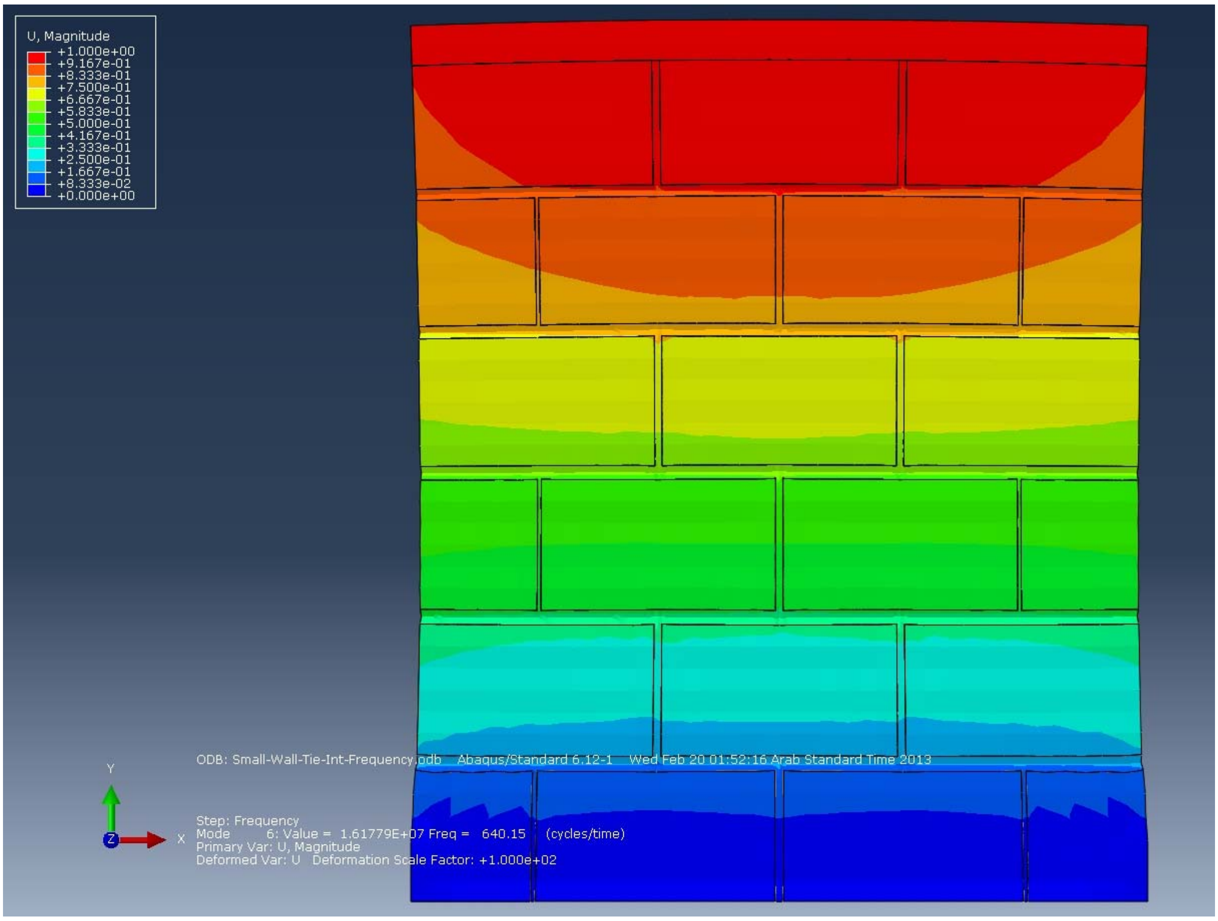

Figure 5.2 6th mode of vibration (vertical vibration)

It is clear form Table 5.1 that each vibration modes has a vibration period way less than one second. Based on that, step time in ABAQUS has been set to equal 1 second.

5.3.1 Computational Simulation of Sandstone Masonry Wall.

As shown in the review of the plastic damage model, several parameters are needed to be input in ABAQUS to carry out the simulations. Some of these parameters were found experimentally and some others were assumed to be the default values. Table 5.2 gives the plastic model parameters associated with sandstone. As seen in the damage model explained in chapter 3, the stress plastic strain for sandstone material is also need in the finite element simulation. Fig 5.3 shows the stress plastic strain in both tension and compression of sandstone.

Table 5.2 Sandstone Parameters Used in Plastic Damage Model.

Mass Density (Tone/mm^3)	Young's Modulus (Mpa)	Poisson's Ratio	Dilation Angle ψ (Degree)	Eccentricity ϵ	f_{b0}/f_{c0}	K	Viscosity Parameter
2.12E-009	27000	0.3	10	0.1	1.16	0.67	0

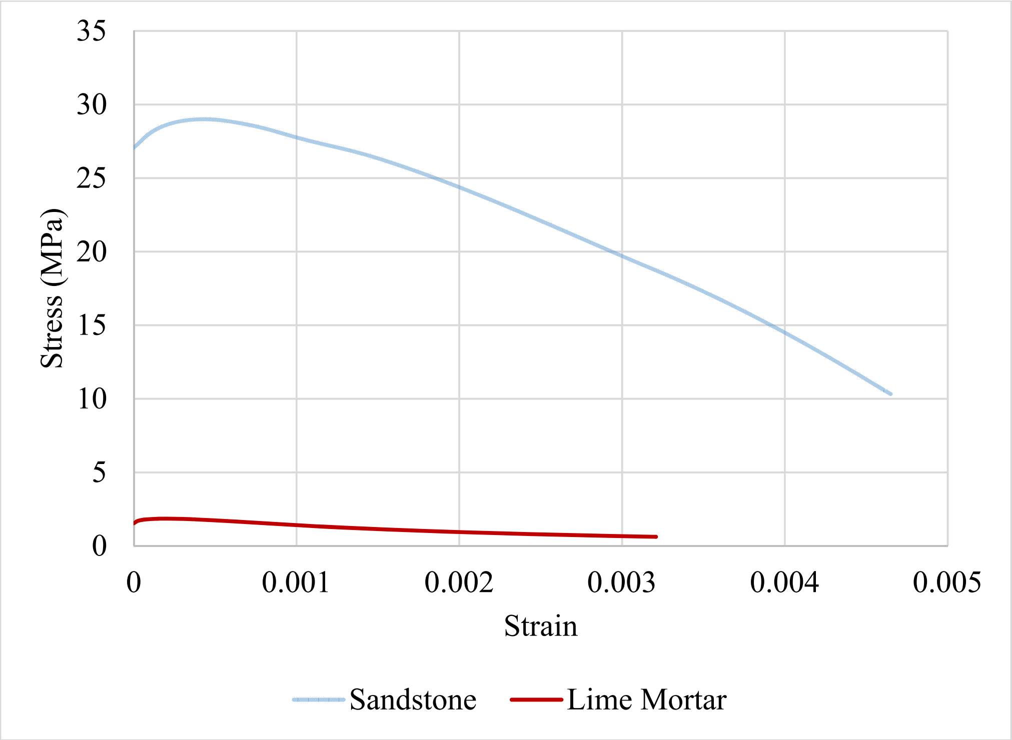

Figure 5.3 Plastic Strain vs Stress in Compression.

Regarding lime mortar, Table 5.3 gives the plastic model parameters associated with needed in the damage model. The stress plastic strain for lime mortar is also need in the finite element simulation. Fig 5.4 shows the stress plastic strain in both tension and compression of lime mortar.

Table 5.3 Lime Mortar Parameters Used in Plastic Damage Model.

Mass Density (Tone/mm^3)	Young's Modulus (Mpa)	Poisson's Ratio	Dilation Angle ψ (Degree)	Eccentricity ϵ	f_{b0}/f_{c0}	K	Viscosity Parameter
1.6E-009	2100	0.25	10	0.1	1.16	0.67	0

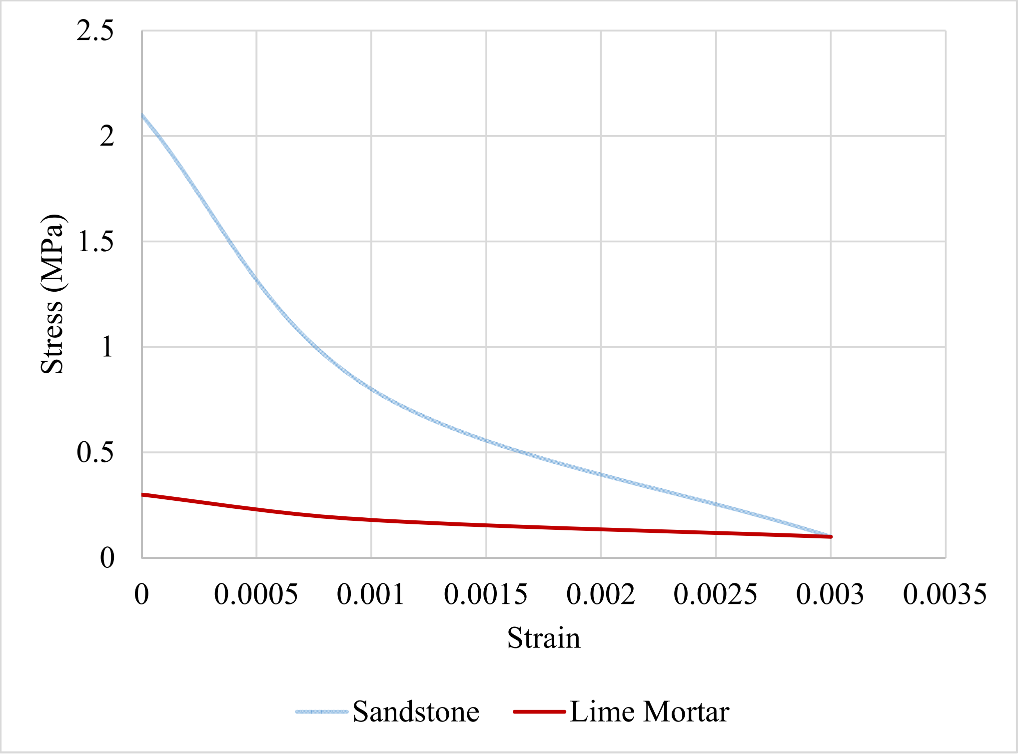

Figure 5.4 Plastic Strain vs Stress in Compression.

5.3.2 Numerical Simulation of Wall-1.7.

For wall-1.7, axial stress applied first to the wall similar to the used on in the experiment (1.7 Mpa) The lateral loading was a displacement control type. The maximum displacement specified in the simulation was 10 mm. The numerical simulation result was compared to the experimental one. A comparison between the envelopes of excremental cyclic test and numerical cyclic simulation is shown is Fig 5.5.

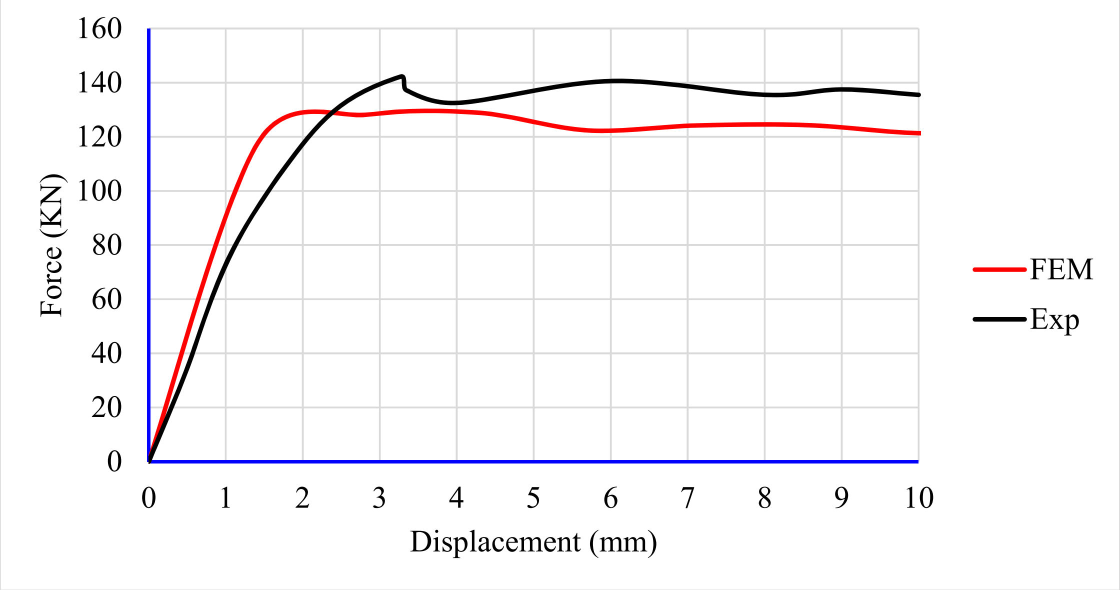

Figure 5.5 Force Displacement of both Experimental and Numerical Results.

From Fig 5.5, it is clear that, there is a good agreement between the experiment test result and the numerical simulation result. The finite element simulation results in a stiffer behavior in the elastic range compare to the experimental result. Figs 5.6 and 5.7 show the failure mode and cracks pattern developed in wall with different level of strain range.

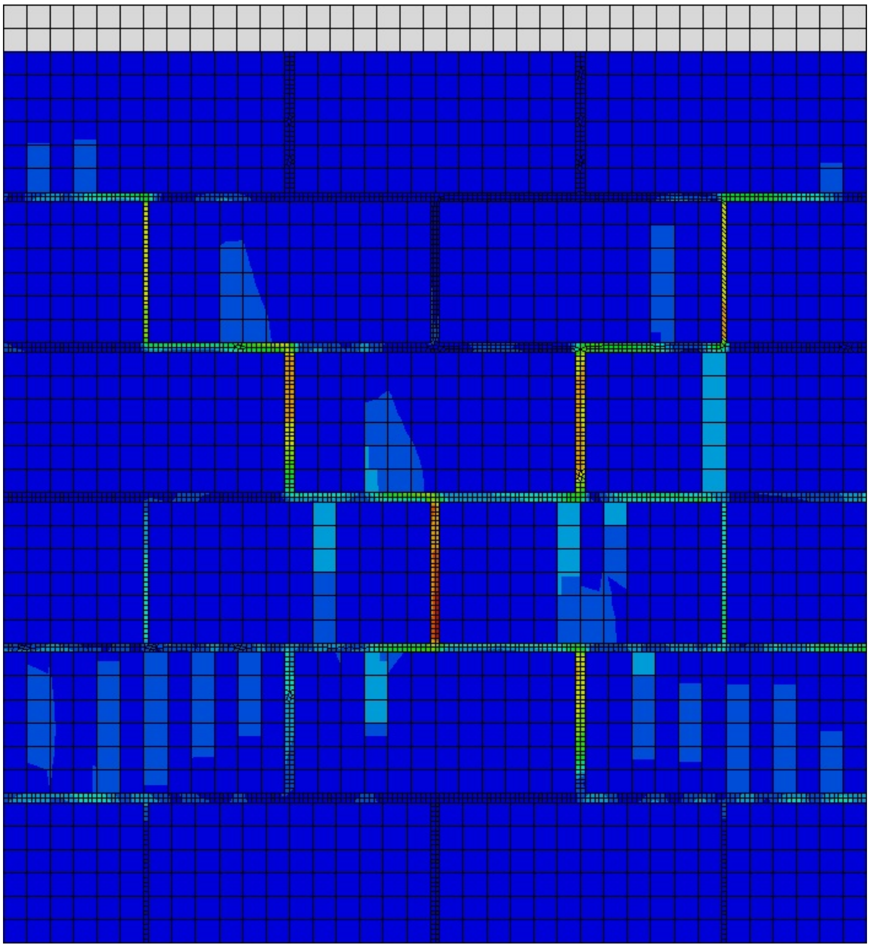

Figure 5.6 Failure mode and crack pattern in the wall after cyclic simulation (large plastic strain range)

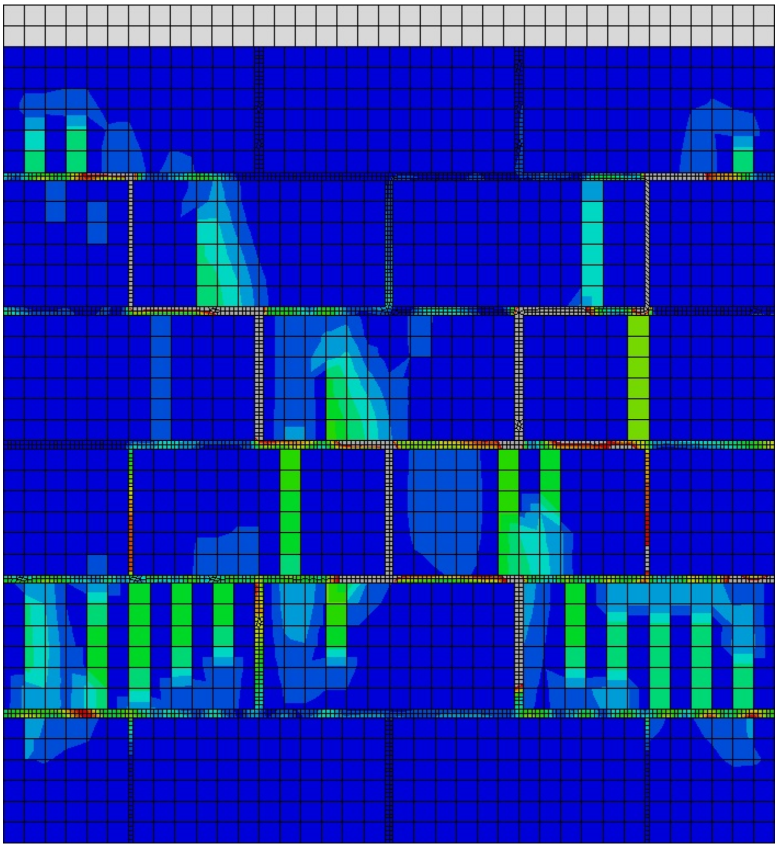

Figure 5.7 Failure mode and crack pattern in the wall after cyclic simulation (low plastic strain range).

It is clear from Figs 5.6 and 5.7 that, almost exact failure mode and crack pattern was achieved from numerical simulation compare to the experimental result

Regarding the stress distribution, Fig 5.8 shows the maximum principle distribution within the wall body for the first cycle. It can be seen that the maximum stress follow a diagonal path in which the cracks formed.

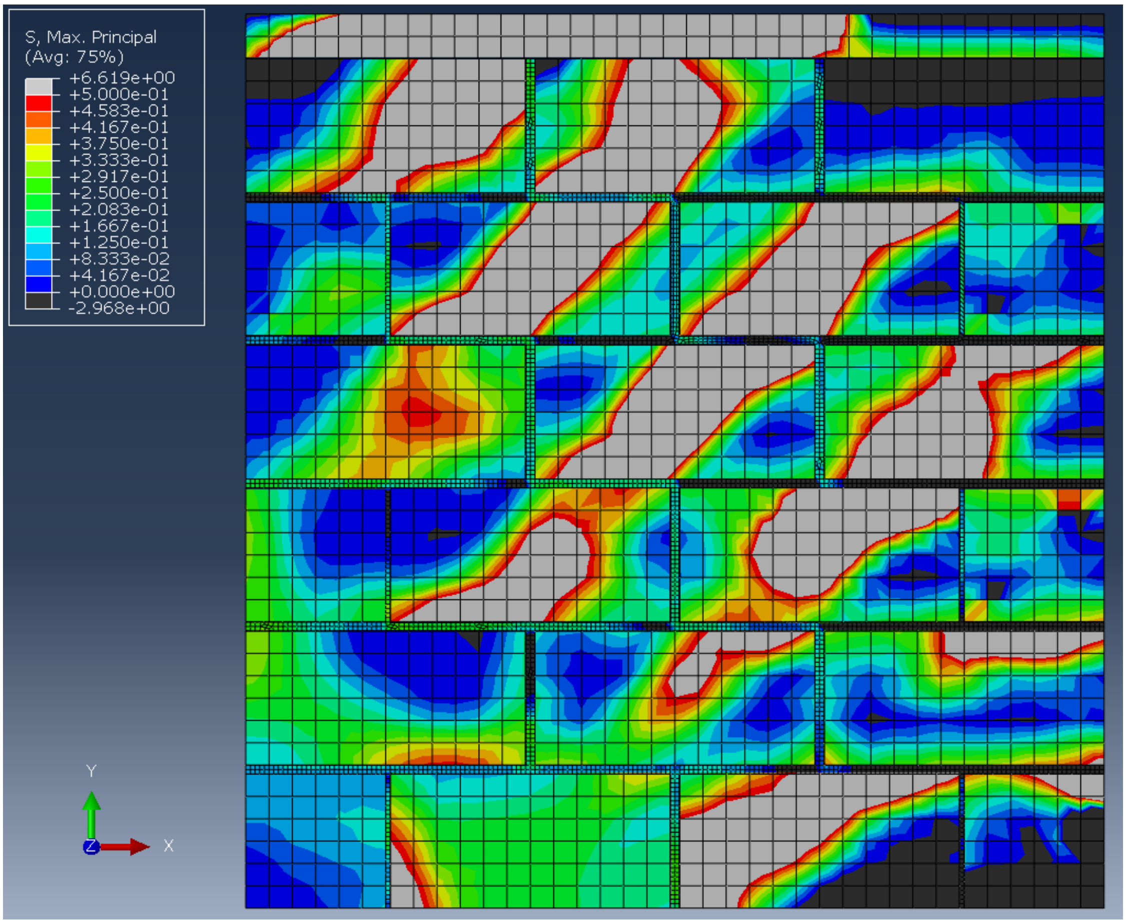

Figure 5.8 Max principle Stress distribution at 0.3 of lateral displacement (Push second cycle)

The maximum principle stress distribution of the consecutive cycles are shown in the appendix. The cyclic response of the wall resulted for numerical simulation is shown in Fig 5.9.

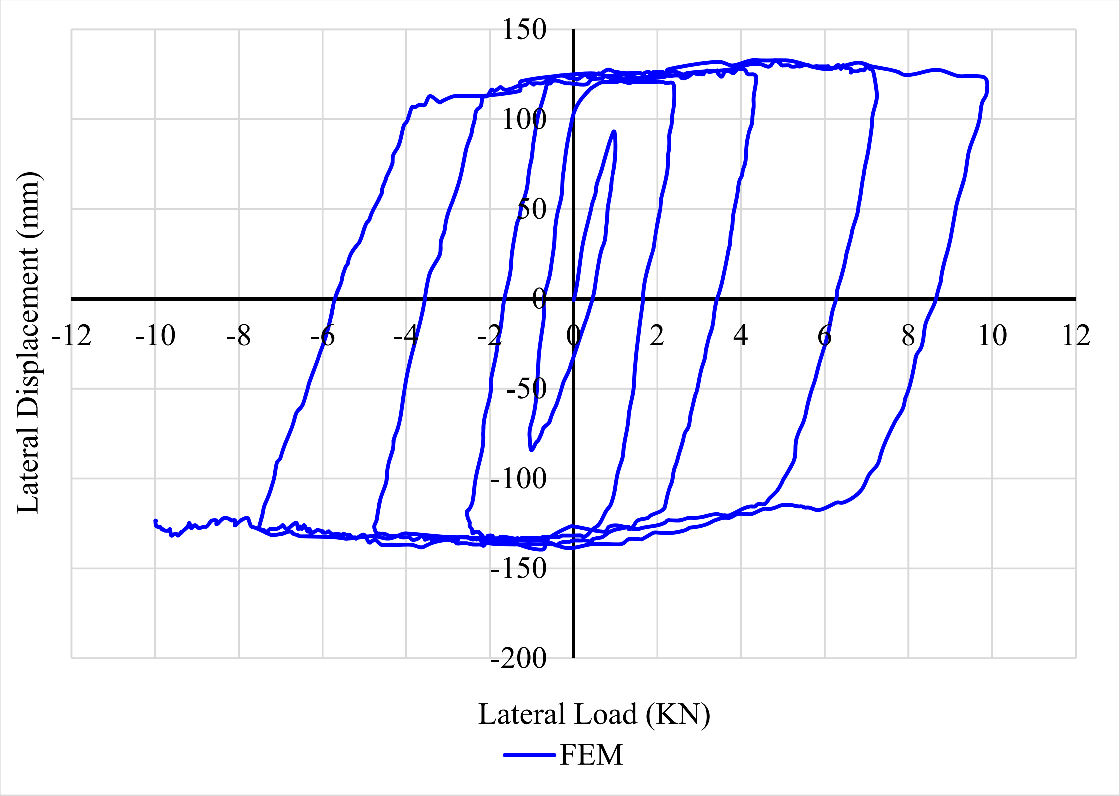

Figure 5.9 Cyclic response of wall resulted from numerical simulation.

In order to know the lateral response of the wall with respect to axial load, a full finite element simulation analysis has been carried out to the wall using all range of axial stress stared with zero axial stress and ended with full axial capacity of the all. In each simulation, lateral strength of the wall associated with lateral displacement was recorded and extracted. This data will help in finding a general relationship between lateral strength and axial stress exerted on the wall. Fig 5.10 shows the relation between lateral displacement and lateral resistance of wall for all different levels of axial load.

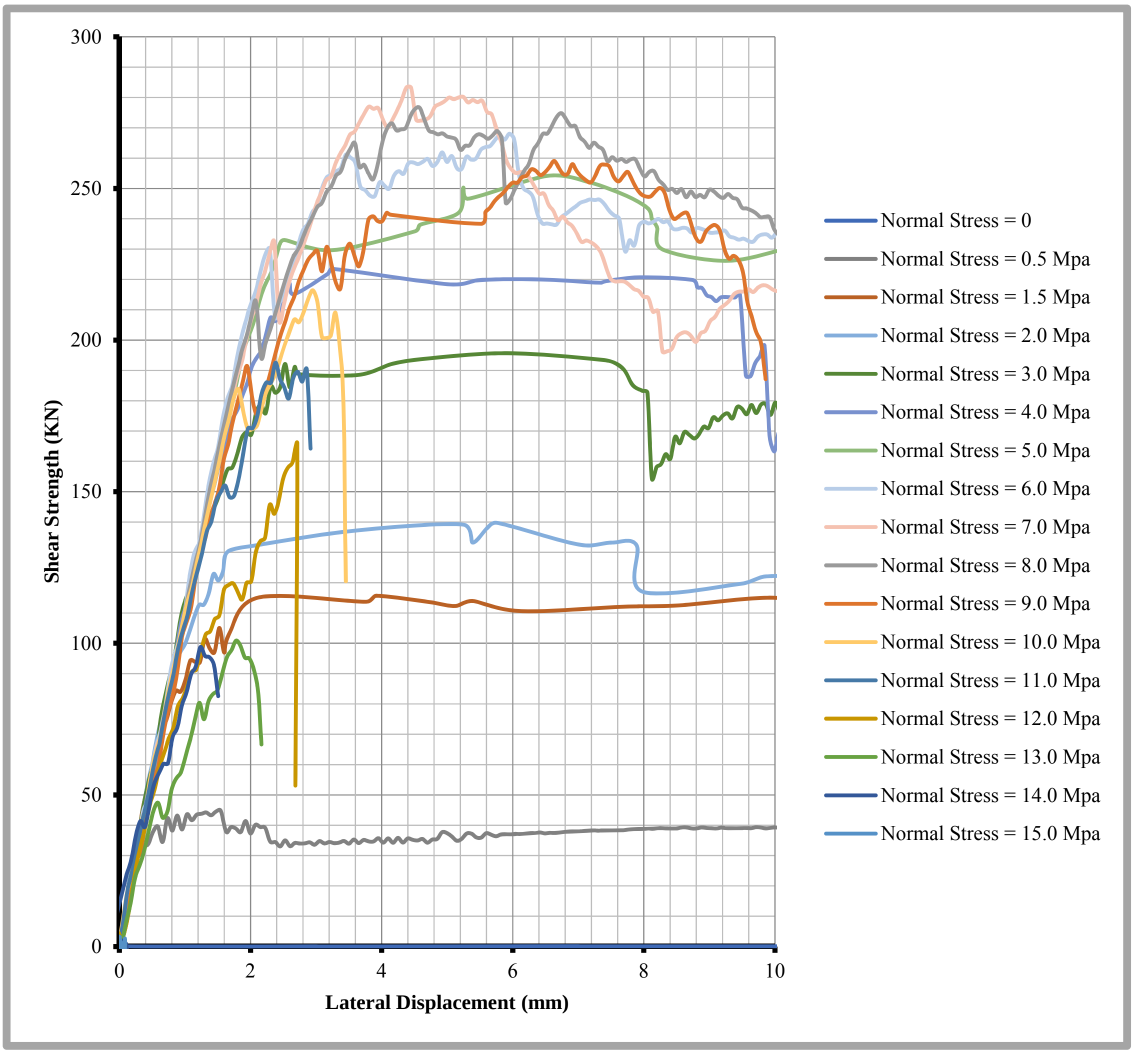

Figure 5.10 Lateral Strength vs Lateral displacement.

From the curves shown in Fig 5.10, it can be seen that the walls exhibit high ductility when the axial pre-compression is small. This ductility decreases as the pre-compression stress increases and the walls tend to exhibit brittle failure. It is also clear from the curves that the lateral strength increases as the axial stress increases. Initially, this trend is true up to a certain level of axial load, following which the walls begin to weaken and lateral resistance decreases as the axial stress increases. The data relating axial forces associated with lateral strengths of the wall is presented in Table 5.4.

Table 5.4 FEM Simulation Results for Normal Stress, Normal Force and Lateral Force for Demir Walls.

Normal Stress	Normal Force-FEM	Max shear force
MPa	KN	KN
0	0	2.32
0.5	100	44.82
1	200	115.68
2	400	139.73
3	600	195.60
4	800	223.48
5	1000	254.02
6	1200	268.06
7	1400	276.56
8	1600	276.56
9	1800	259.08
10	2000	219.96
11	2200	198.24
12	2400	165.66
13	2600	135.25
14	2800	75.15
15	3000	29.41
15.4	3080	0

The data of Table 5.4 has been plotted and is shown in Fig 5.11. Form a regression fit of all data linking the lateral strength of the wall H, coresponding to applied level of pre-compression P, it becomes appearent that the path trend can be simulated by a parablic regression. Similare trend has been reported by Voon (2007).

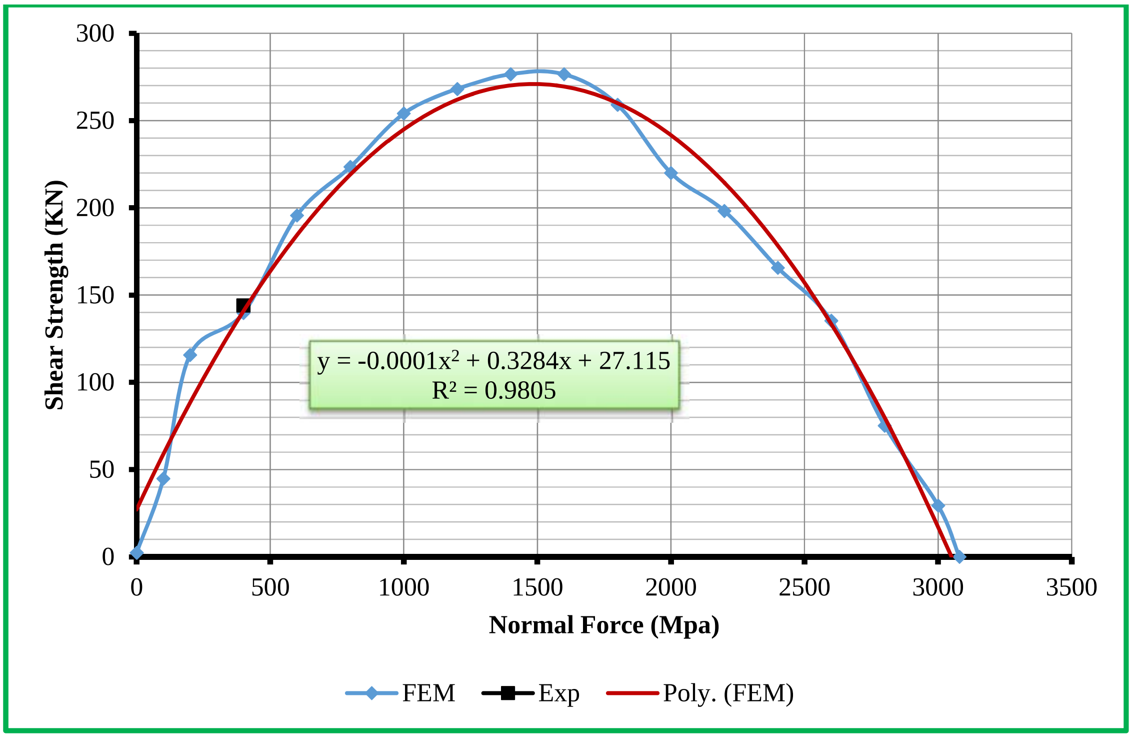

Figure 5.11 Interaction Relation between Lateral Strength H, and Normal Force P.

The regression correspondence resulting from this analysis relates the lateral capacity H to the axial load P on the wall by.

$$H == -0.0001P^2 + 0.3284P + 27.115 \tag{5.1}$$

where:

H is the lateral force at collapse (KN).

P is the applied normal force on the wall (KN).

This relationship may be normalized by taking the ratio of lateral strength to maximum lateral force attained ($H_{max} = 276.56\ KN$) and ratio of axial force applied to maximum applied axial force ($P_{max} = 3080\ KN$). Fig 5.12 shows the normalized curve.

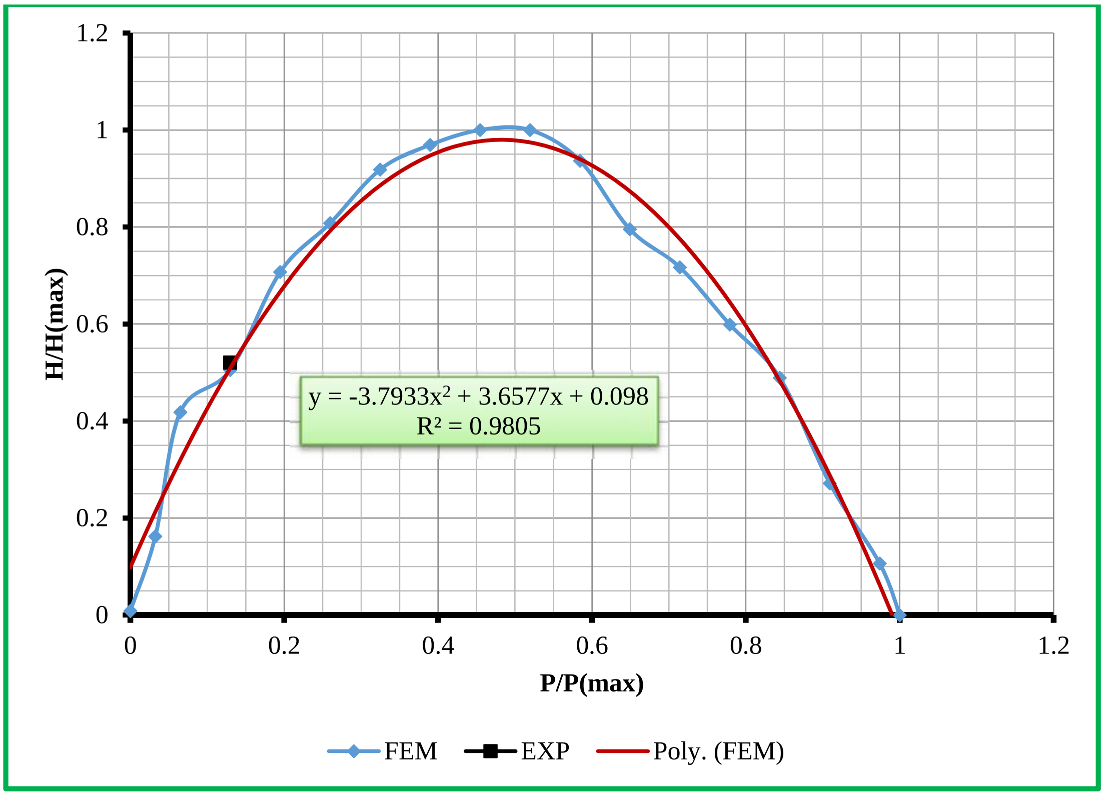

Figure 5.12 Interaction Relation Between Normalized Lateral Force and Normalized Axial Force.

The regression analysis of this curve results in the following equation:

$$y = -3.79x^2 + 3.66x + 0.098 \tag{5.2}$$

where:

$$y = H/H_{max} \quad , \quad x = P/P_{max}$$

When investigating the results of FEM simulation, five failure modes were observed, namely sliding, rocking, head/bed joints opening, cracking in bricks, and crashing of wall. Figs 5.13-5.16, show these failure modes associated with different level of axial force.

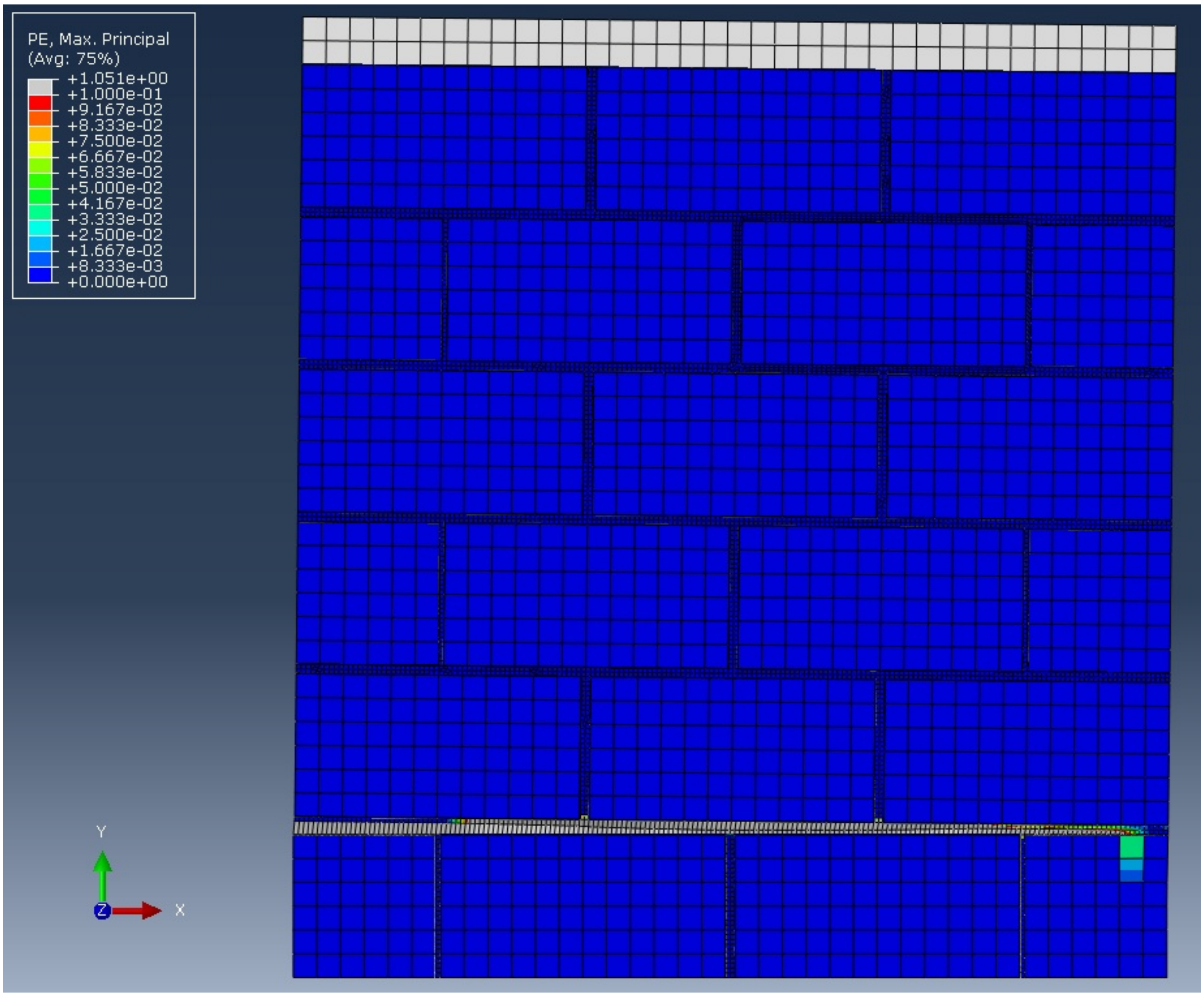

Figure 5.13 Plastic Strain and Failure Mode (0 Axial Stress). (Wall Rocking)

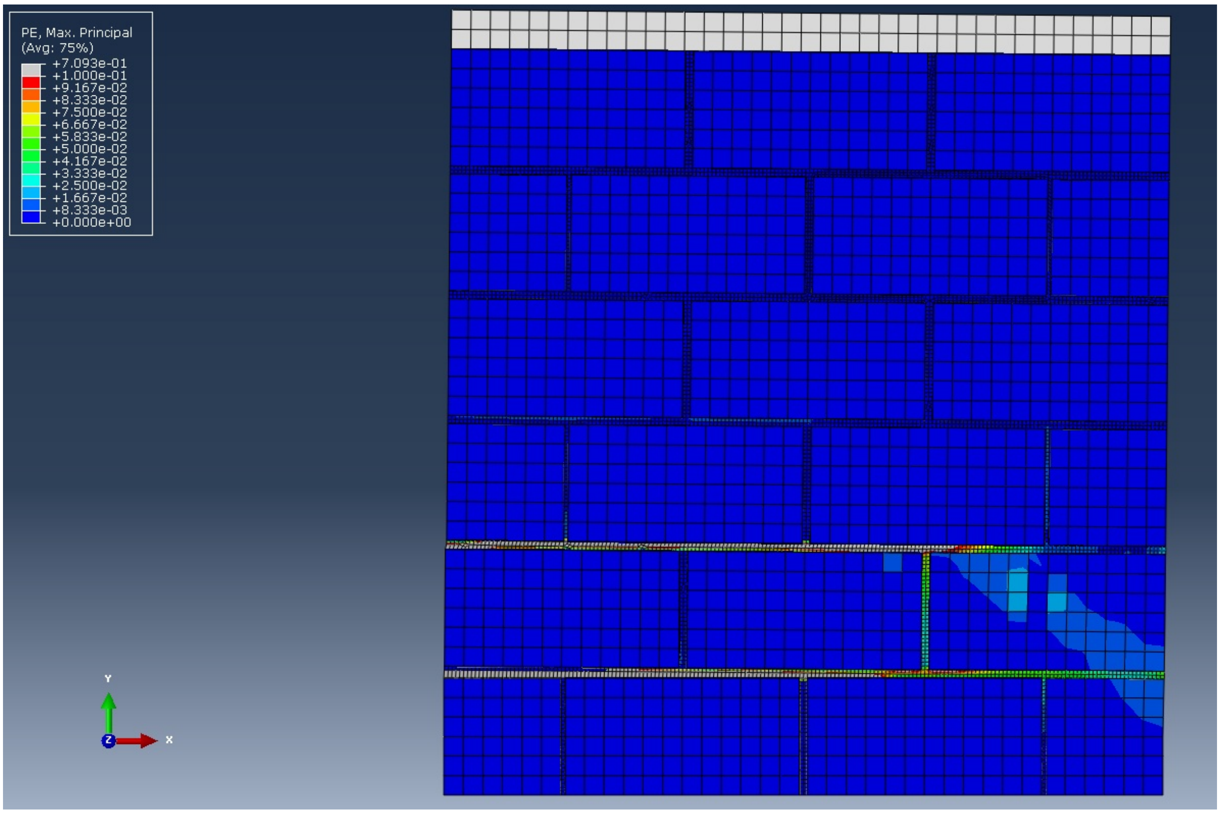

Figure 5.14 Plastic Strain and Failure Mode (2.0 MPa Axial Stress). (Wall head/ bed Joins Opening and Cracking in Bricks)

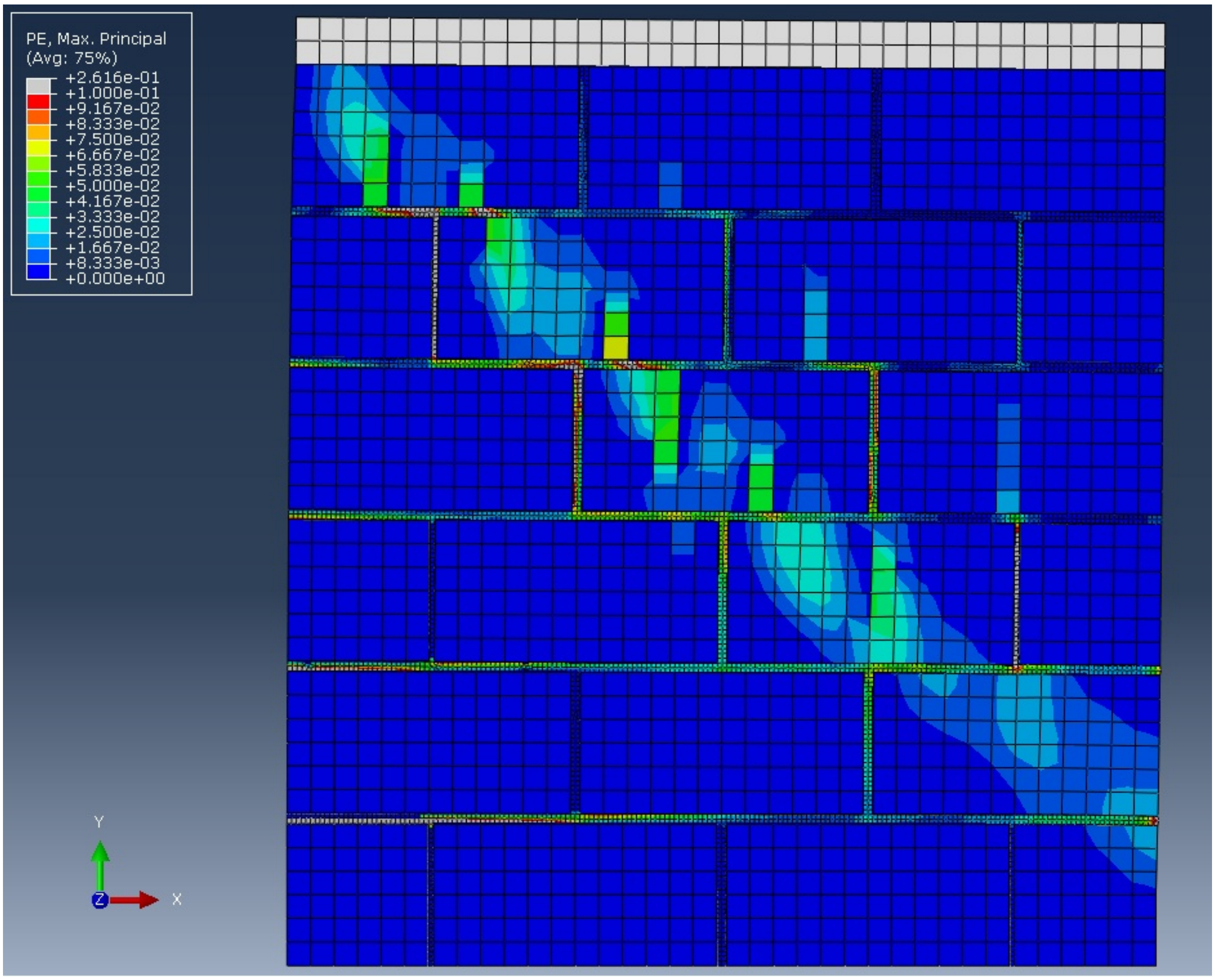

Figure 5.15 Plastic Strain and Failure Mode (4.0 MPa Axial Stress).

(Cracking and Crashing in Bricks)

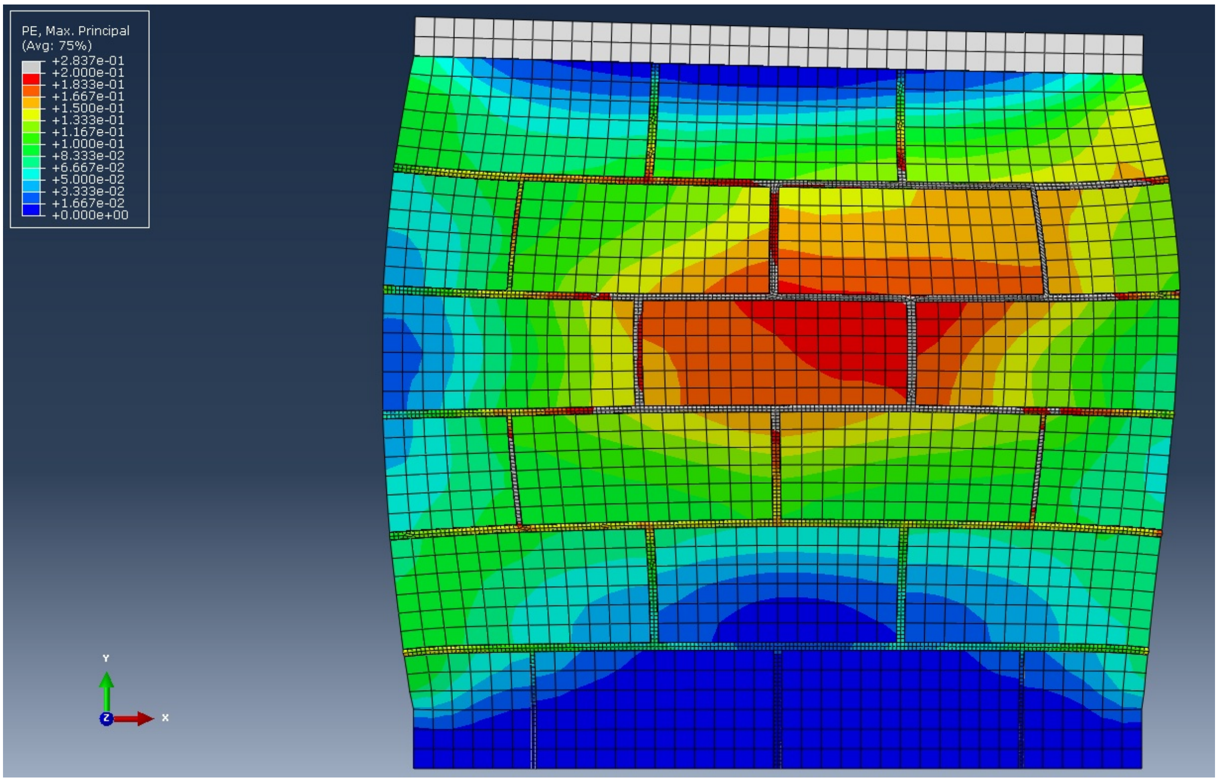

Figure 5.16 Plastic Strain and Failure Mode (15 MPa Axial Stress). (Wall Sliding, Rocking and Toe Crashing)

As can be seen in the previous result, the lateral strength of the wall is highly affected by the level of axial load. The relationship between lateral strength and axial force is investigated more by conducting numerical simulation to walls tested by other researcher.

The stress contour associated with the above mentioned plastic strain cases are shown in the appendix.

5.4 Computational Simulation of Walls Tested by Other Researchers.

As mentioned earlier, finite element simulation have also carried out to walls tested by other researchers. The interaction diagram between axial and lateral loading were found for each of those walls. The goal of this task is to compare the results found in this study and other studies so that a strong and general results can be found. Three type masonry walls were simulated in this study namely:

- walls tested by Demir (2012)
- Walls tested by Li et al (2005)
- Wall tested by Vasconscelos (2005).

5.4.1 Computational Simulation of Demir (2012) Walls.

As mentioned earlier, Demir (2012), conducted a study to examine the response of walls representing an ancient historical mosque in Istanbul (*Bayezid II Mosque*) to seismic loading. In his study, Demir investigated the effect of cyclic loading on a multi-leaf masonry wall representing the ancient heritage mosque. As shown in Fig 5.17, dimensions of the walls were 1.2 by 1.2 m with thickness of 30 cm. Each leaf was built with stone, using dry jointing system.

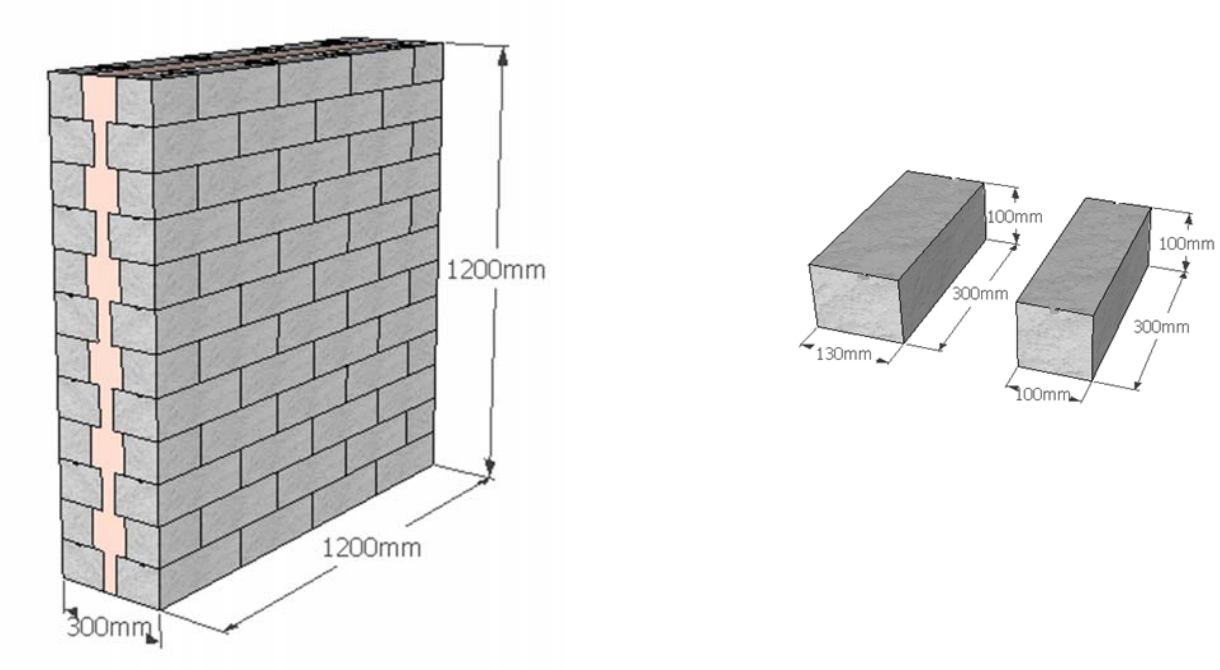

Figure 5.17 Geometric Details of Demir (2012) Walls

The walls were subjected to varying pre-compression axial force prior to the application of cyclic lateral load. The variables are summarized in Table 5.5.

Table 5.5 Variables in Demir's Experiments

Wall Sample	Blocks Clamped or Not	Axial Stress Magnitude (MPa)
M-25-C	Yes	0.25
M-50-C	Yes	0.5
M-75-C	Yes	0.75
M-100-C	Yes	1
M-50	No	0.5

The experimentally observed lateral load versus lateral displacement was recorded for all the walls. Demir has reported different modes of failure of the walls according to the level of axial force. He observed that the walls tended to be stiffer when the axial stress was higher.

In the work presented here, a finite element simulation, using micro-analysis approach, has been conducted, taking the full range of axial stress starting from zero up to the full axial capacity of the wall. In the FEM simulations, fixed support (Ux=0, Uy=0, and Uz=0) were assumed at the base of the walls. In each case of axial load, monotonic lateral displacements and loads have been extracted from the FEM simulations. Uniaxial stress-plastic stain data for both bricks and rubble in uniaxial compression and tension have been used in the plastic damage model incorporated in an ABAQUS environment. Figs 5.18 and 5.19 show this data as based on actual testing carried out by Demir.

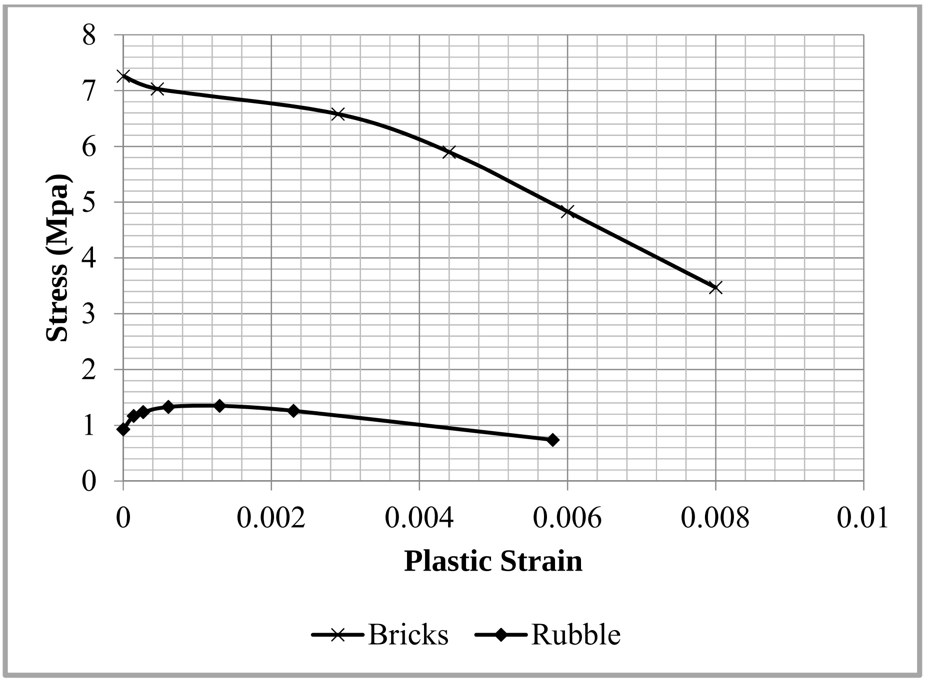

Figure 5.18 Plastic Strain vs Stress in Compression (Demir, 2012).

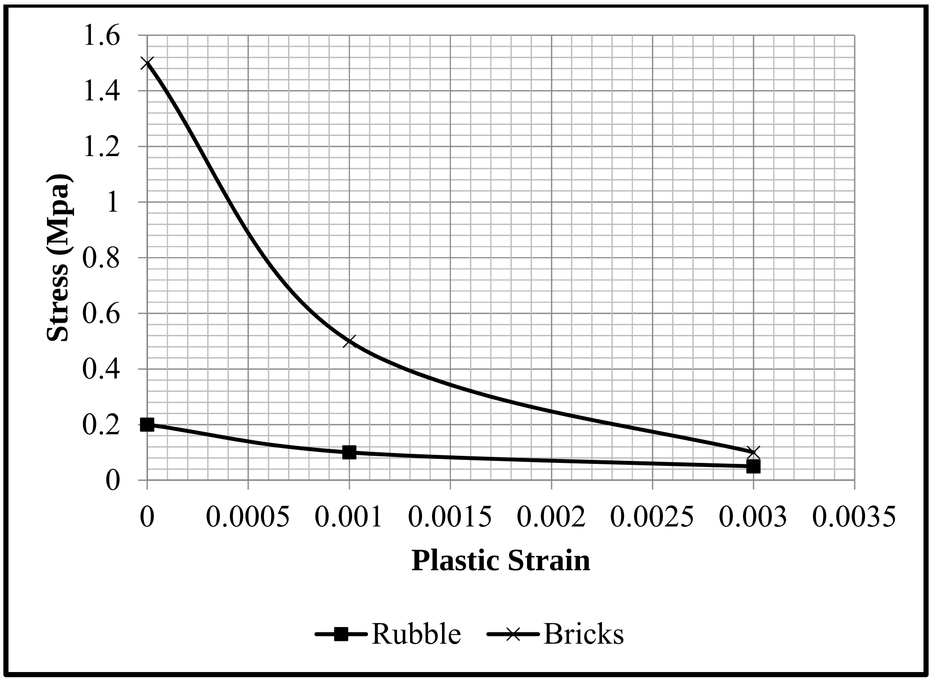

Figure 5.19 Plastic Strain vs Stress in Tension (Demir, 2012).

Plastic damage model, developed by Lubliner et al. (1989) and adopted in the commercial software ABAQUS, needs certain material parameters to be input in carrying out the simulations. Some of these parameters were assumed to be the default values and some others were based on actual experiments. These parameters are shown in Table 5.6.

Table 5.6 Parameters Used in Plastic Damage Model.

Mass Density (Tone/mm^3)	Young's Modulus (Mpa)	Poisson's Ratio	Dilation Angle ψ (Degree)	Eccentricity ϵ	f_{b0}/f_{c0}	K	Viscosity Parameter
2.4E-009	3200	0.18	36	0.1	1.16	0.67	0

The lateral loading was a displacement control type. This maximum displacement specified in the simulation was 10 mm. In the cases associated with low axial stresses, FEM converged up to the end of maximum lateral displacement of 10 mm. However, when axial loads were higher, the lateral displacements, for cases in which the FEM converged, were less than 10 mm. Table 5.7 shows the maximum lateral displacements (in which FEM converged) associated with the applied axial stress.

Table 5.7 Axial Load vs. Lateral Displacement of the FEM Simulation.

Normal Stress (MPa)	Converged Maximum Lateral Displacement (mm)
0 - 2.5*	10
2.75	8.2
3	7.2
3.25	6.6
3.5	5.1
3.75	4.2
4	3.2
4.25	2.7
4.5	2
4.75	1.5
4.85	0 (no solution)

* including of 0.25 MPa

A total of 20 cases were investigated, corresponding to different axial stress level intensities. Due to the high nonlinearity in the problems involved (materials and geometry), the finite element analysis took a long time to complete for each case. A comparison between cyclic test results of wall subjected to axial loading of 0.5 MPa and monotonic FEM simulation results for that wall are as shown in Fig 5.20.

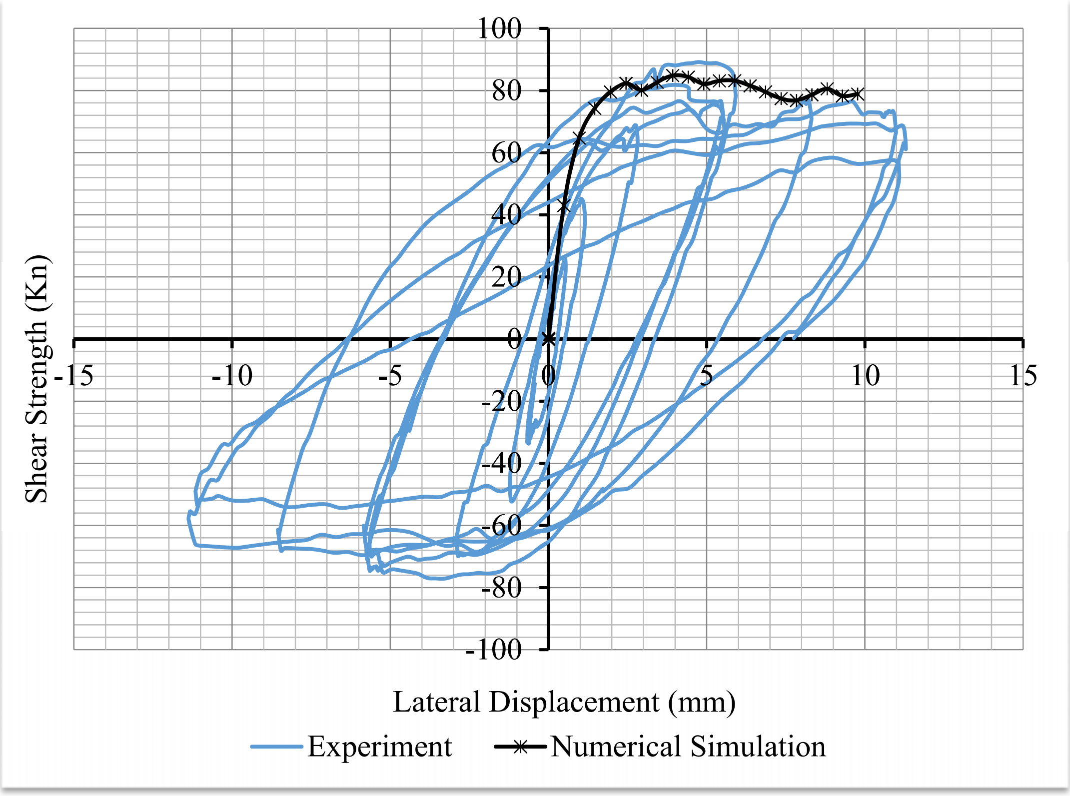

Figure 5.20 Lateral Strength vs Lateral displacement (Axial stress =0.5 MPa)

From the results of Fig 5.20, it is clear that there is a good agreement between envelope of the experimental cyclic loading and the monotonic finite element simulation. The plastic-damage model used in the ABAQUS environment captures the softening behavior (which is usually difficult to simulate using other nonlinear FEM commercial software codes) of the simulated wall up to maximum lateral displacement of 10 mm as recorded during the actual experiment. Fig 5.21 shows the relation between lateral displacement and lateral resistance of wall for all different levels of axial load.

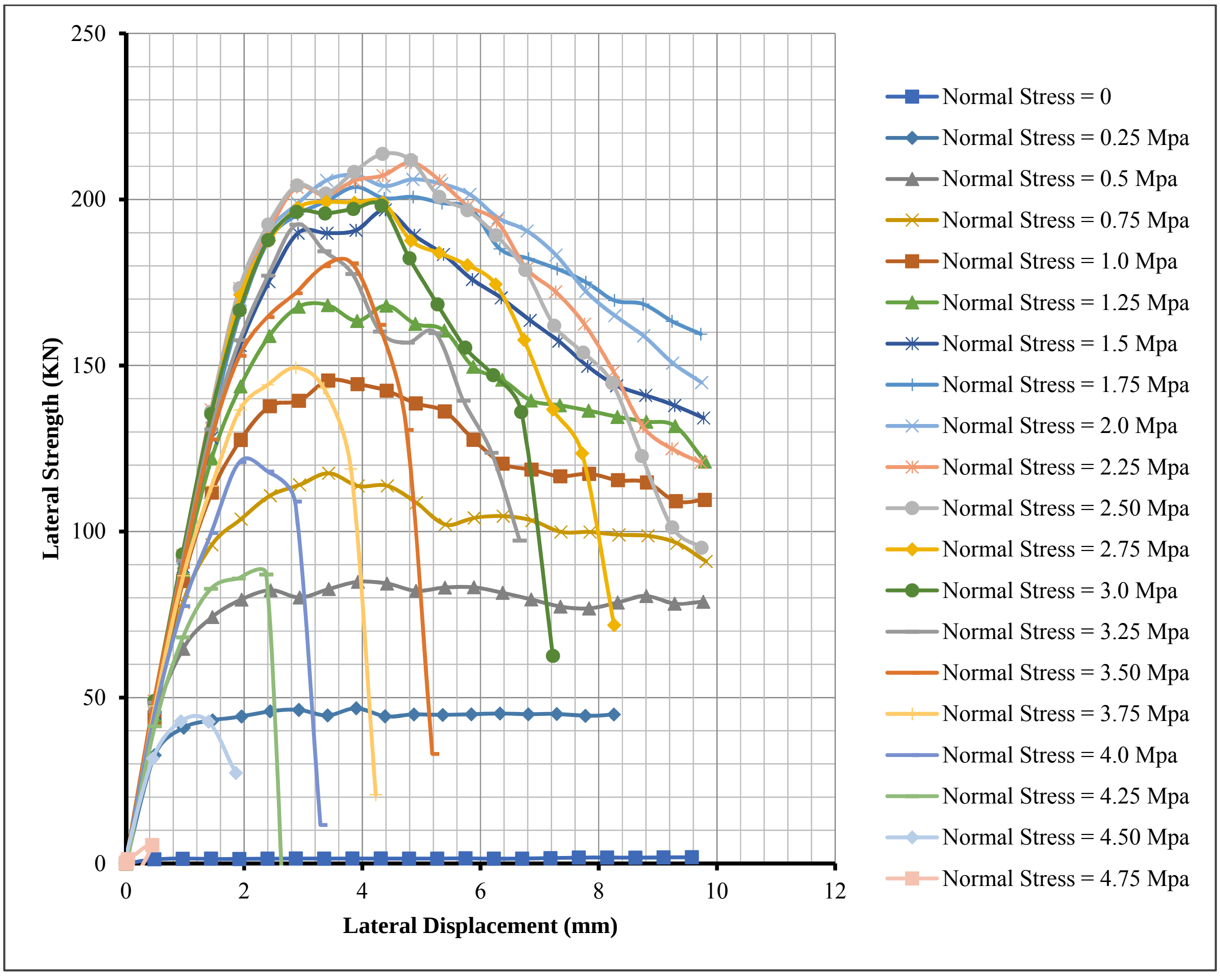

Figure 5.21 Lateral Strength vs Lateral displacement.

From the curves shown in Fig 5.21, it can be seen that the walls exhibit high ductility when the axial pre-compression is small. This ductility decreases as the pre-compression stress increases and the walls tend to exhibit brittle failure. It is also clear from the curves that the lateral strength increases as the axial stress increases. Initially, this trend is true up to a certain level of axial load, following which the walls begin to weaken and lateral resistance decreases as the axial stress increases. The data relating axial forces associated with lateral strengths of the wall is presented in Table 5.8.

Table 5.8 FEM Simulation Results for Normal Stress, Normal Force and Lateral Force for Demir Walls

Normal Stress (MPa)	Normal Force (Kn)	Lateral Force-Exp (Demir 2012) (Kn)	Lateral force-FEM (Kn)	% Difference
0	0	-	1.9	
0.25	90	54	46.8	13%
0.5	180	90	84.8	6%
0.75	270	122.4	117.6	4%
1	360	136.8	145.5	6%
1.25	450		168.2	
1.5	540		196.9	
1.75	630		203.8	
2	720		207.3	
2.25	810		211.2	
2.5	900		213.7	
2.75	990		199.3	
3	1080		198.2	
3.25	1170		192.5	
3.5	1260		180.8	
3.75	1350		149.3	
4	1440		120.9	
4.25	1530		87.1	
4.5	1620		42.8	
4.75	1710		5.5	
4.85	1745		0	

The data of Table 5.8 has been plotted and is shown in Fig 5.22. Form a regression fit of all data linking the lateral strength of the wall H, coresponding to applied level of pre-compression P, it becomes appearent that the path trend can be simulated by a parablic regression. Similare trend has been reported by Voon (2007).

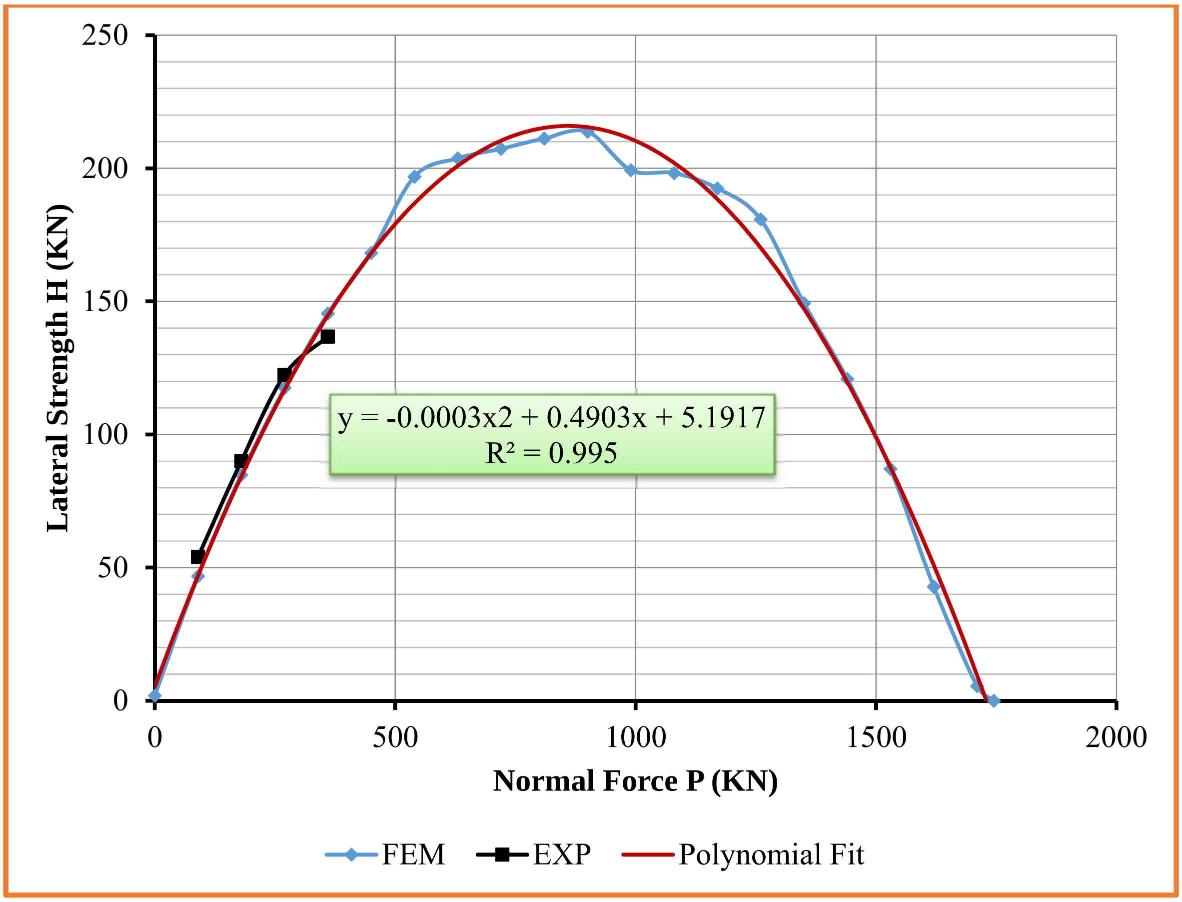

Figure 5.22 Interaction Relation between Lateral Strength H, and Normal Force P.

The regression correspondence resulting from this analysis relates the lateral capacity H to the axial load P on the wall by.

$$H = -0.0003P^2 + 0.4903P + 5.1917 \tag{5.3}$$

where:

H is the lateral force at collapse (KN).

P is the applied normal force on the wall (KN).

This relationship may be normalized by taking the ratio of lateral strength to maximum lateral force attained ($H_{max} = 213.7\ KN$) and ratio of axial force applied to maximum applied axial force ($P_{max} = 1745\ KN$). Fig 5.23 shows the normalized curve.

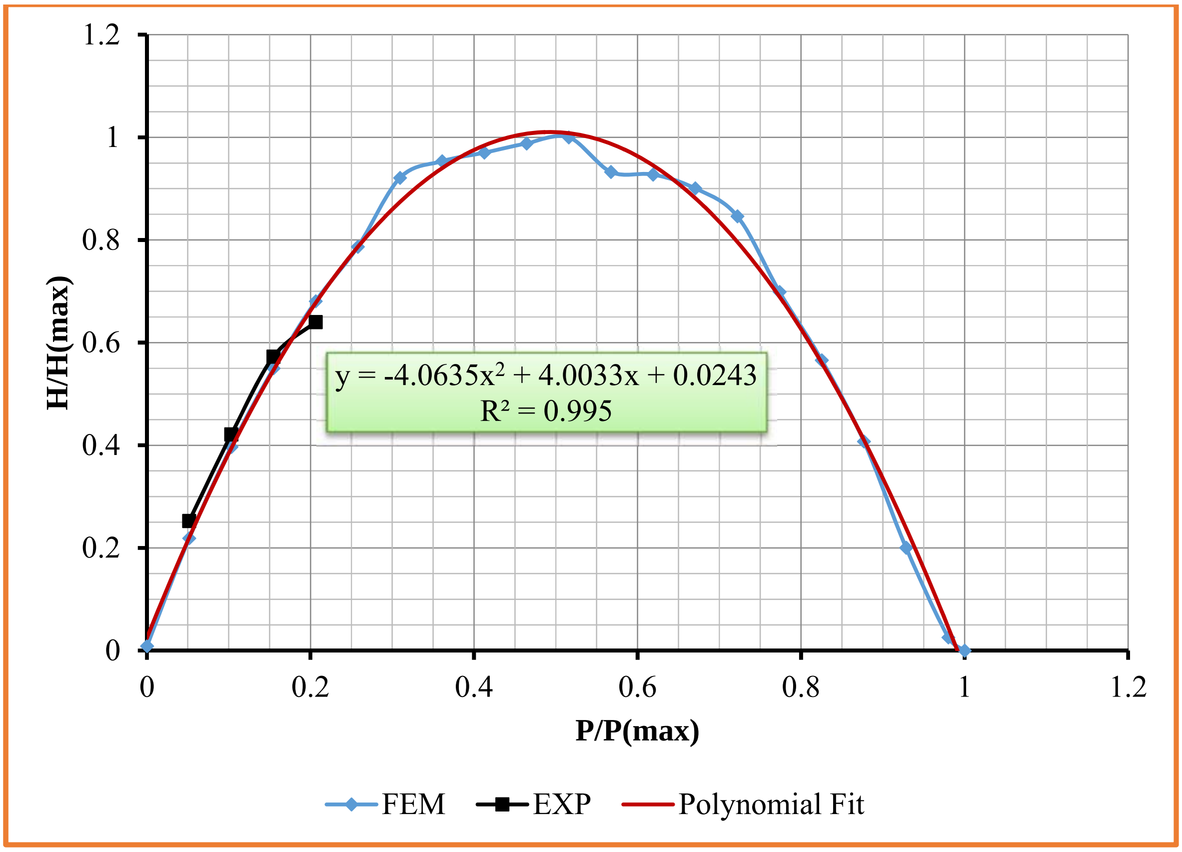

Figure 5.23 Interaction Relation Between Normalized Lateral Force and Normalized Axial Force.

The regression analysis of this curve results in the following equation:

$$y = -4.0635x^2 + 4.0033x + 0.0243 \tag{5.4}$$

where:

$$y = H/H_{max} \quad , \quad x = P/P_{max}$$

When investigating the results of FEM simulation, five failure modes were observed, namely sliding, rocking, head/bed joints opening, cracking in bricks, and crashing of wall. Figs 5.24-5.27, show these failure modes associated with different level of axial force. It has to be noted that displacements shown in Figs 5.24-5.27 have been amplified by factor of 10.

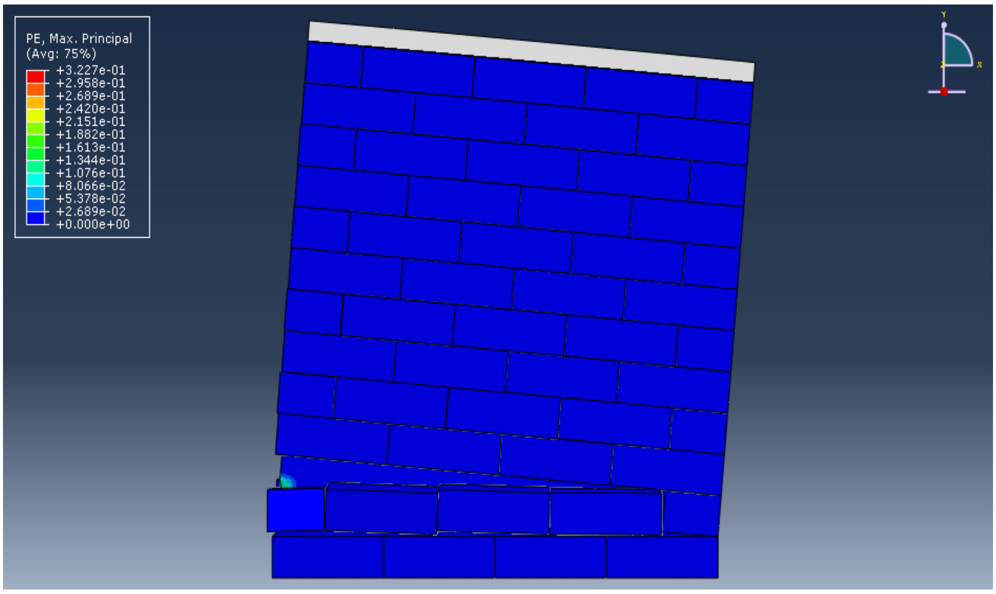

Figure 5.24 Plastic Strain and Failure Mode (0 Axial Stress). (Wall Rocking)

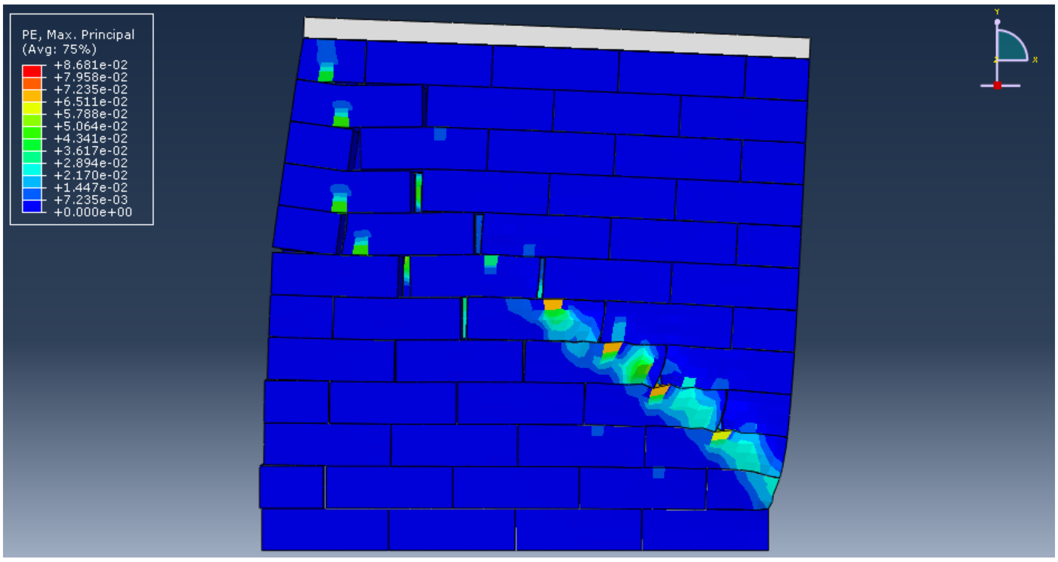

Figure 5.25 Fig 5.25. Plastic Strain and Failure Mode (1.0 MPa Axial Stress). (Wall head/ bed Joints Opening and Cracking in Bricks)

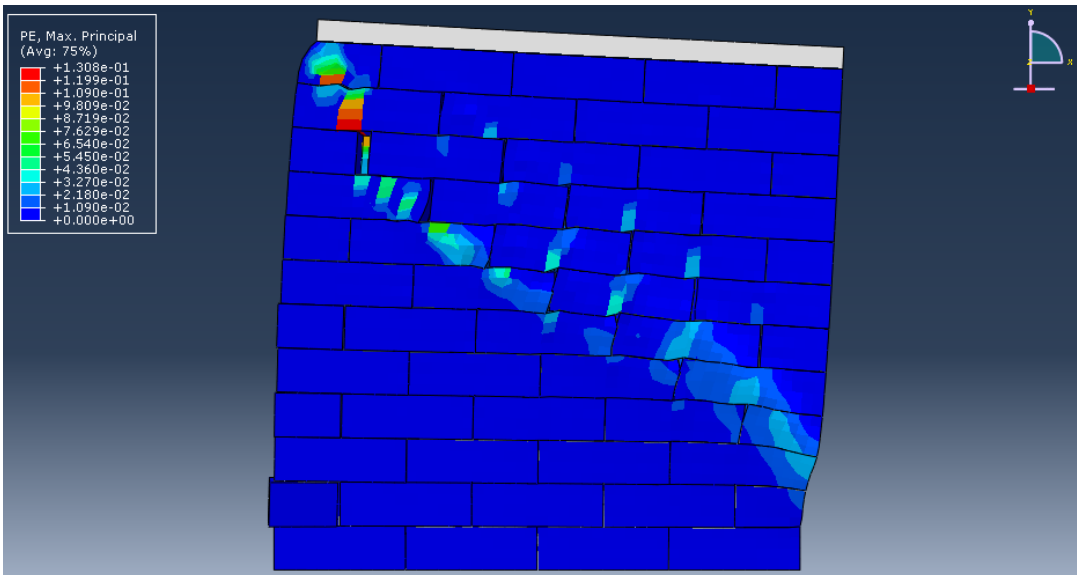

Figure 5.26 Plastic Strain and Failure Mode (2.0 MPa Axial Stress). (Wall head/ bed Joins Opening and Cracking in Bricks)

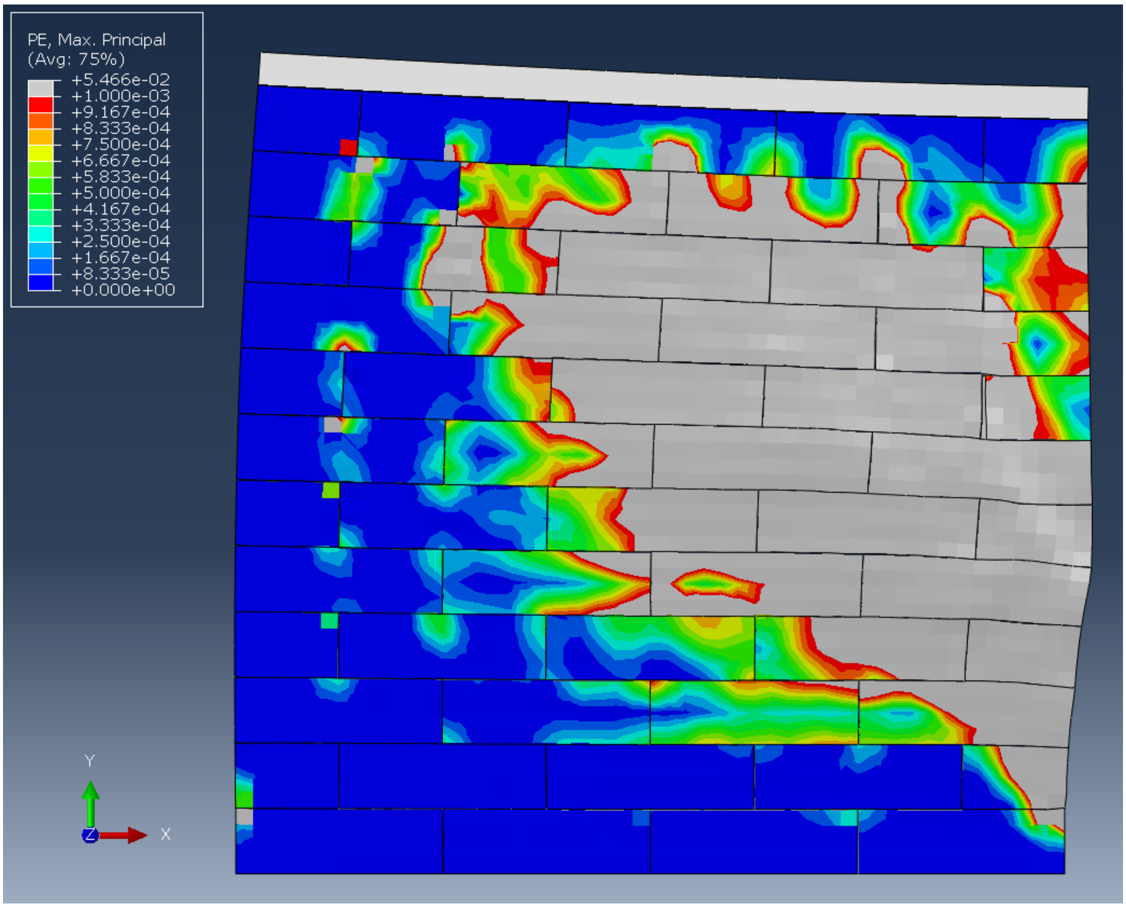

Figure 5.27 Plastic Strain and Failure Mode (4.0 MPa Axial Stress).

(Cracking and Crashing in Bricks)

5.4.2 Computational Simulation of Li et al (2005) Walls.

The second finite element simulation has been done to the wall tested by Li, et al (2005). In his study, Li et al, investigated behavior of masonry concrete walls subjected to diagonal loading. They also investigated the effect of NSM (near surface mounted) reinforcement using GFRP and stainless steel bars on the strength of masonry walls.

In this study, finite element simulations have been conducted on this type of concrete masonry walls. The loading types adopted in this study are axial and lateral loading in which the effect is similar to that when diagonal loading is used. Finite element simulation has been conducted for this type of walls using all range of axial loading starting from zero up to the full axial capacity of the wall so that the interaction between axial and lateral loading can be extracted. The walls geometry adopted by Li was 1625 mm x 1625 mm x 152 mm. The concrete masonry units had dimensions of 406 mm x 203 mm x 152 mm. A type N mortar (ASTM C270) was used to build the walls. The dimensions and configurations of the units and wall are shown in Fig 5.28

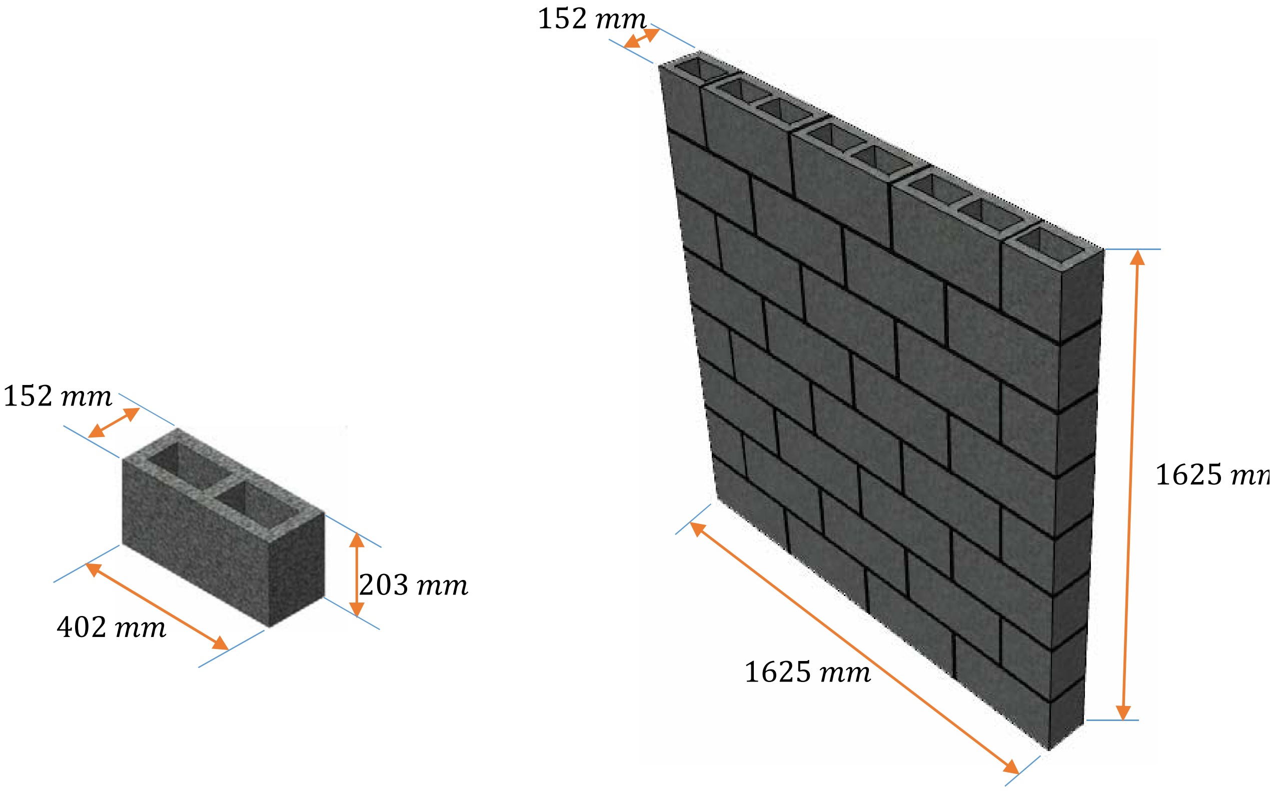

Figure 5.28 Geometry and configuration of Li (2005) walls.

In this study, finite element analysis, using micro-analysis approach, have been conducted to Li's wall by applying pre-compression axial force to each analysis and then applying lateral displacement at the top of the wall. In the FEM simulations, fixed support (Ux=0, Uy=0, and Uz=0) were assumed at the base of the walls. The lateral load versus lateral displacement has been extracted from the finite element simulation. Plastic-Damage model available in ABAQUS is also adopted in the simulations. The materials used in the walls are concrete (concrete brick units) and mortar (head/bed joints between bricks). Both materials have been considered as a continuum media and simulated using continuum damage model. The material properties available in Li's paper are only the concrete and mortar ultimate compression strengths. Other needed data are extracted and calculated based on ACI formulas and others were assumed. The stress plastic strain values needed in the damage model incorporated in ABAQUS environment are shown in Fig 5.29 and 5.30.

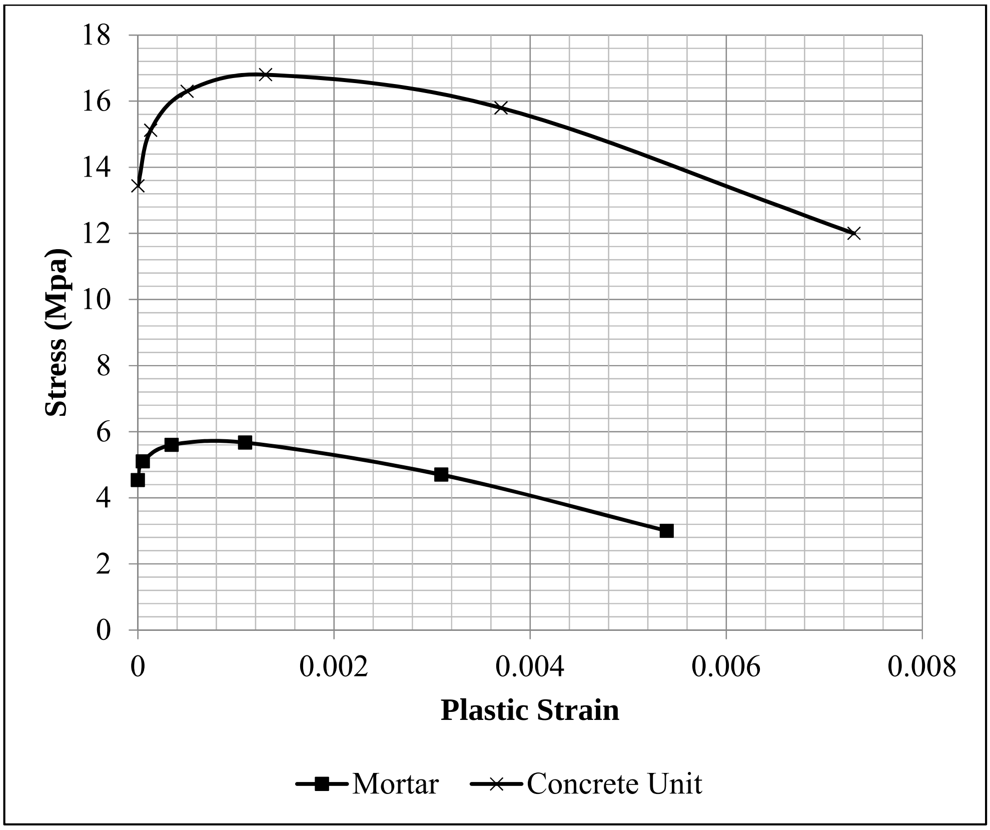

Figure 5.29 Plastic Strain vs Stress in Compression.

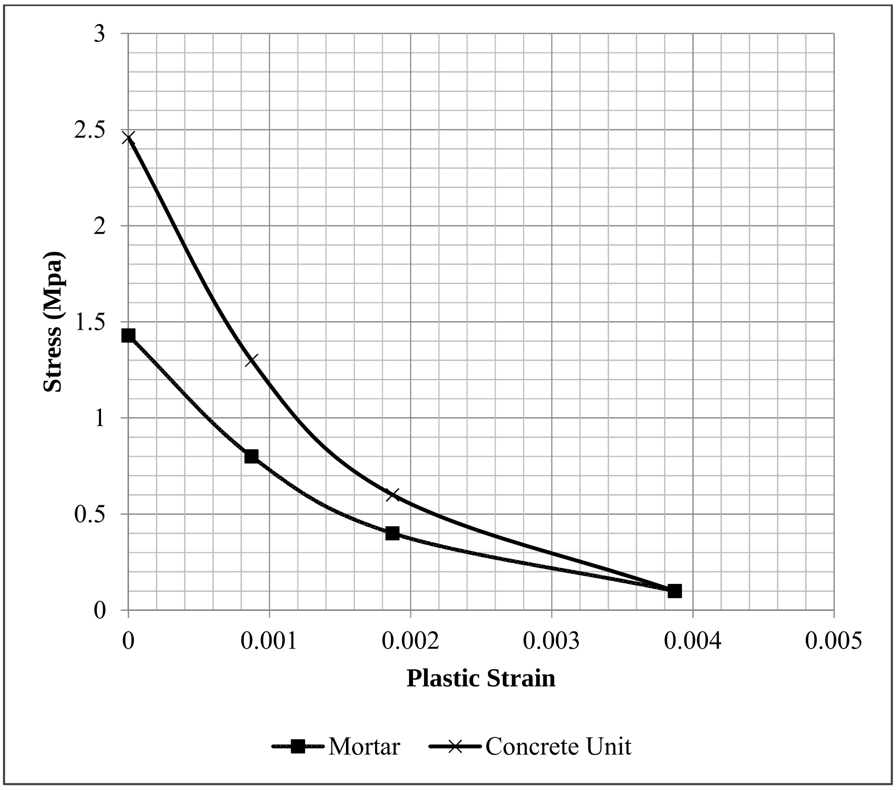

Figure 5.30 Plastic Strain vs Stress in Tension.

Plastic damage model, developed by Lubliner et al. (1989) and adopted in the commercial softwera ABAQUS, needs certain material parameters to be used in simulation. Some of these parameters were assumed to be the default values and some others were calculated based on ACI. These parameters are shown in Table 5.9.

Table 5.9 Parameters Used in Plastic Damage Model.

Mass Density (Tone/mm^3)	Young's Modulus (Mpa)	Poisson's Ratio	Dilation Angle ψ (Degree)	Eccentricity ϵ	f_{b0}/f_{c0}	K	Viscosity Parameter
2.4E-009	19264	0.2	36	0.1	1.16	0.67	0

A monotonic displacement loading was adopted in the simulations with 10 mm maximum lateral displacement. In the cases associated with low axial stresses, FEM converged up to the end of maximum lateral displacement of 10 mm. However, when axial loads were higher, the lateral displacements, for cases in which the FEM converged, were less than 10 mm. Table 5.10 shows the maximum lateral displacements (in which FEM converged) associated with the applied axial stress.

Table 5.10 Axial Load and Lateral Displacements of the FEM Simulation.

Normal Stress (MPa)	Converged Maximum Lateral Displacement (mm)
0 – 4.0	10
4.5	6.5
5	6
5.5	6
6	6
6.5	6
7	5
7.5	2.5
8	1.5
8.47	0 (No solution)

A total of 21 cases were investigated corresponding to different axial stress level. Due to high nonlinearity involved in the problems (materials, geometry, and interaction), the finite element analysis took a long time to complete for each case. The plastic-damage model used in the ABAQUS environment captures the softening behavior (which is usually difficult to simulate using other nonlinear FEM commercial software codes) of the simulated wall up to maximum lateral displacement of 10 mm as recorded during the actual experiment.

Fig. 5.31 shows the relation between lateral displacement and lateral resistance of wall for all different levels of axial load.

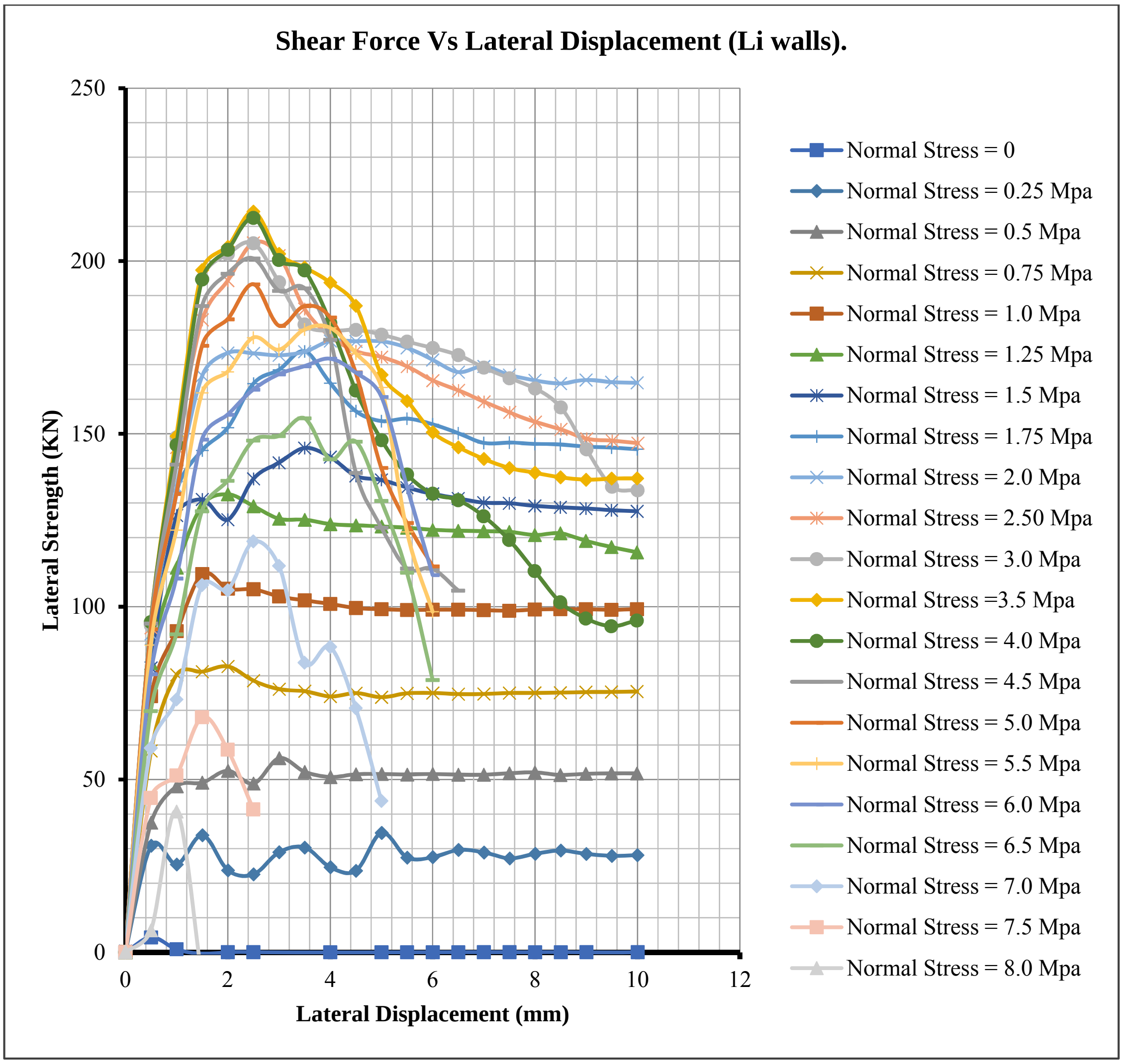

Figure 5.31 Lateral Strength vs Lateral displacement (Li walls).

From the curves shown in Fig. 5.31, it can be seen that the walls exhibit high ductility when the axial pre-compression is small. This ductility decreases as the pre-compression stress increases and the walls tend to exhibit brittle failure. It is also clear from the curves that the lateral strength increases as the axial stress increases. Initially, this trend is true up to a certain level of axial load, following which the walls begin to weaken and lateral resistance decreases as the axial stress increases. The data relating axial forces associated with lateral strengths of the wall is presented in Table 5.11.

Table 5.11 FEM Simulation Results for Normal Stress, Normal Force and Lateral Force for Li Walls

Normal Stress (MPa)	Normal Force (Kn)	Lateral Force-FEM (Kn)
0	0	4.3
0.25	81.5	34.6
0.5	163	56.2
0.75	244.5	82.7
1	326	109.4
1.25	407.5	132.5
1.5	489	145.9
1.75	570.5	173.9
2	652	176.9
2.5	815	205.3
3	978	205.1
3.5	1141	214.3
4	1304	212.5
4.5	1467	200.8
5	1630	193.3
5.5	1793	180.7
6	1956	171.7
6.5	2119	154.5
7	2282	118.9
7.5	2445	68.1
8	2608	40.7
8.47	2763	0

The data of Table 5.11 has been plotted and is shown in Fig 5.32. Form a regression fit of all data linking the lateral strength of the wall H, coresponding to applied level of pre-compression P, it becomes appearent that the path trend can be simulated by a parablic regression. Similare trend has been reported by Voon (2007).

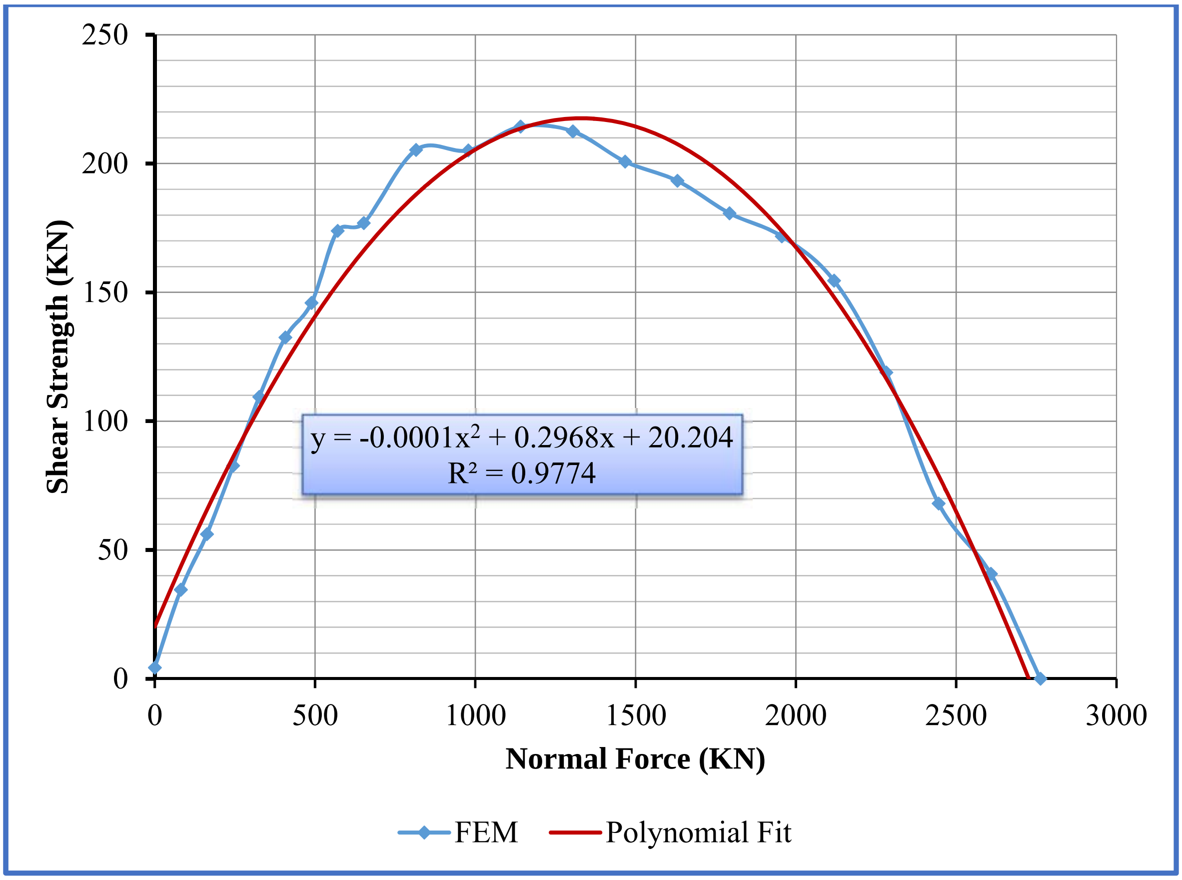

Figure 5.32 Interaction Relation between Lateral Strength H, and Normal Force P.

The regression correspondence resulting from this analysis relates the lateral capacity H to the axial load P on the wall by.

$$H = -0.0001P^2 + 0.2968P + 20.204 \tag{5.5}$$

where:

H is the lateral force at collapse (KN).

P is the applied normal force on the wall (KN).

This relationship may be normalized by taking the ratio of lateral strength to maximum lateral force attained ($H_{max} = 214.3\ KN$) and ratio of axial force to maximum applied axial force ($P_{max} = 2763\ KN$). Fig 5.33 shows the normalized curve.

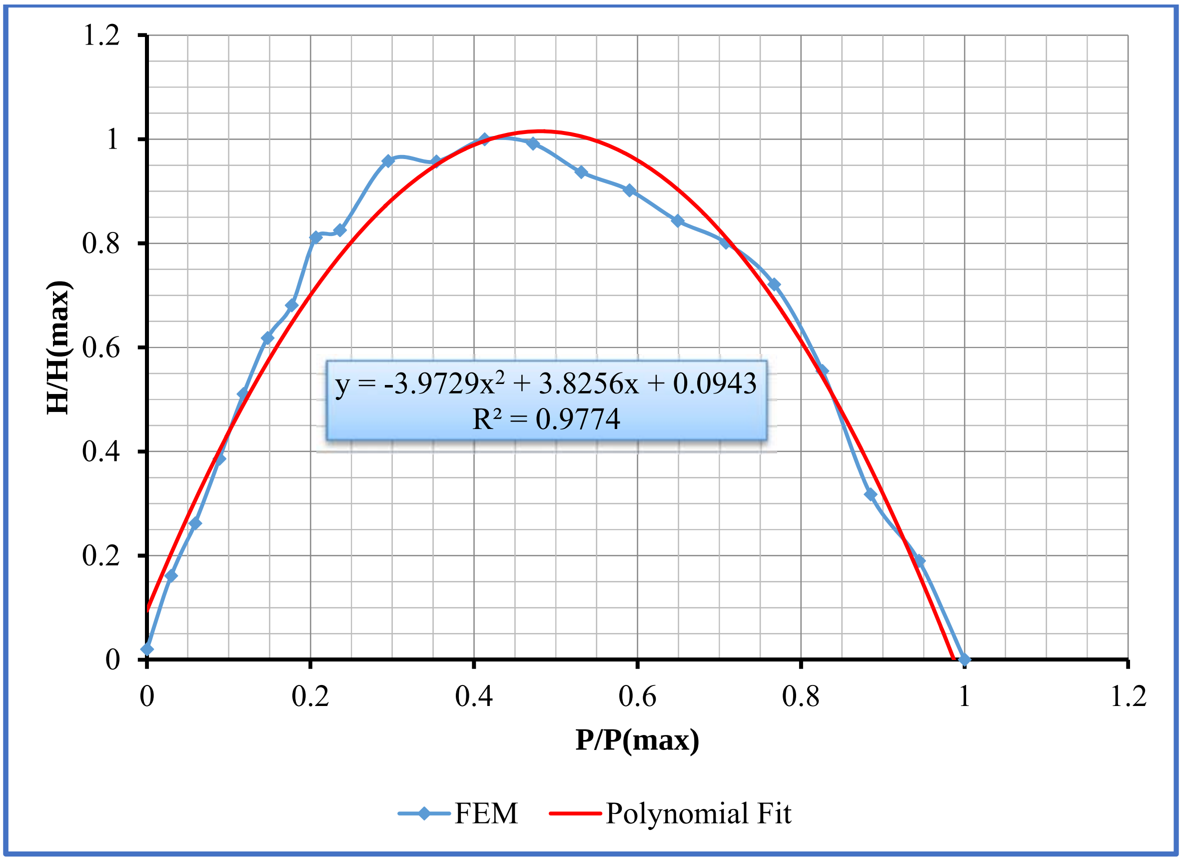

Figure 5.33 Interaction Relation between Normalized Lateral Force and Normalized Axial Force.

The regression analysis of this curve results in the following equation:

$$y = -3.9729x^2 + 3.8256x + 0.0943 \tag{5.6}$$

where:

$$y = H/H_{max} \quad , \quad x = P/P_{max}$$

When investigating the results of FEM simulation, five failure modes were observed, namely sliding, rocking, head/bead joints opening, cracking in bricks, and crashing of wall. Figs 5.34-5.37, show these failure modes associated with different level of axial force. It has to be noted that displacements shown in Figs 5.34-5.37 have been amplified by factor of 10.

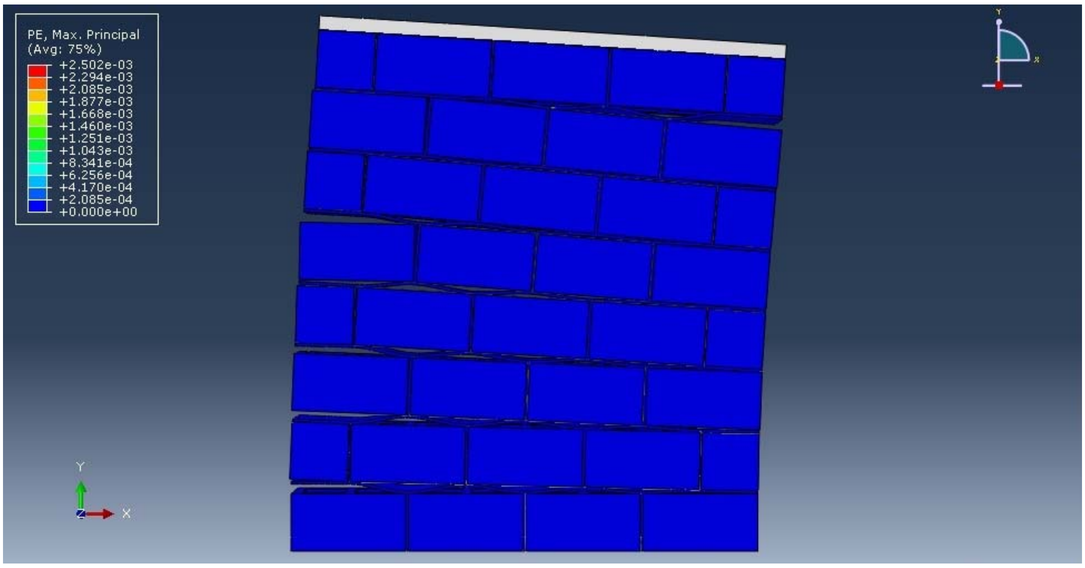

Figure 5.34 Plastic Strain and Failure Mode (0 MPa Axial Stress). (Wall Rocking)

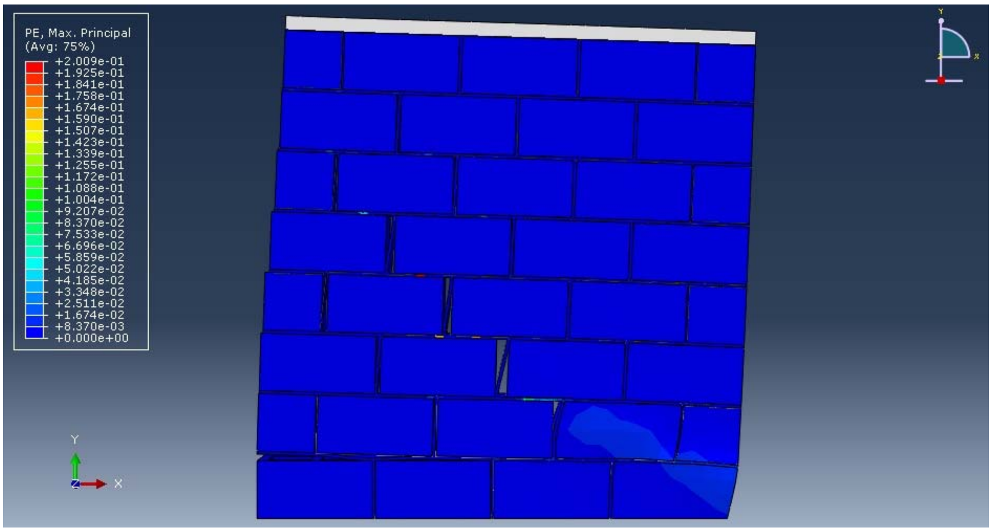

Figure 5.35 Plastic Strain and Failure Mode (2.0 MPa Axial Stress). (Wall head/ bed Joins Opening and Cracking in Bricks)

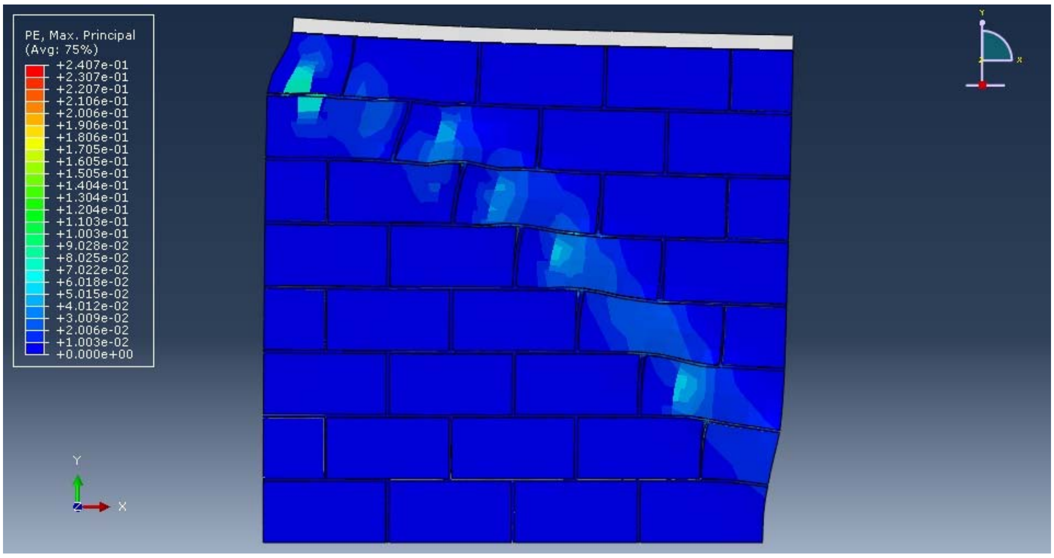

Figure 5.36 Plastic Strain and Failure Mode (4.0 MPa Axial Stress). (Wall Bricks Cracking and Crushing)

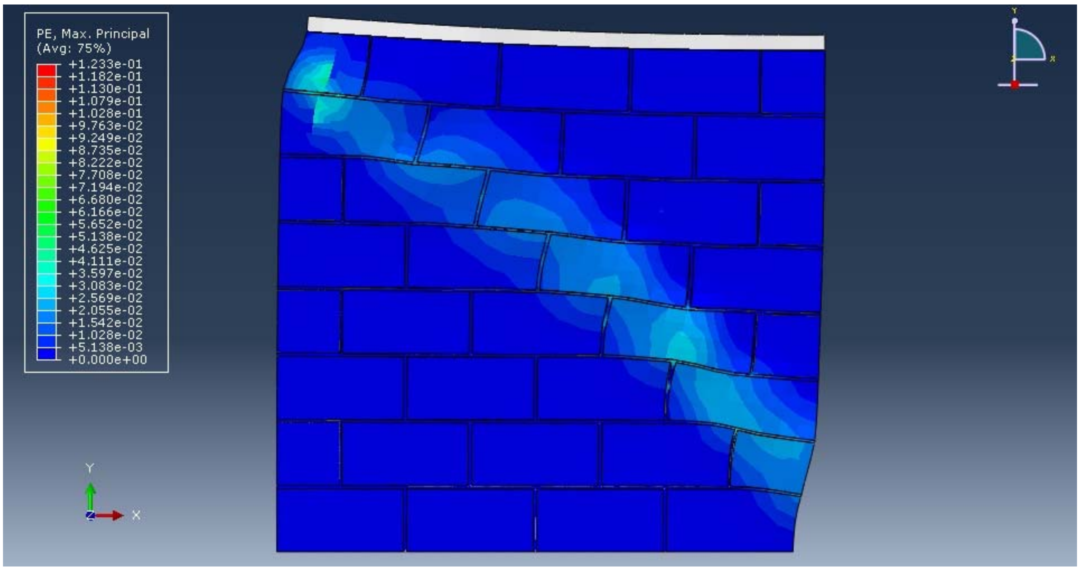

Figure 5.37 Plastic Strain and Failure Mode (6.0 MPa Axial Stress). (Wall Bricks Cracking and Crushing)

5.4.3 Simulation of Walls Tested by Vasconcelos (2005).

The third finite element study has been done to the walls tested by Vasconscelos in her PhD work. In her study, Vasconscelos studied the effect of cyclic loading on different kinds of masonry walls. She investigated walls made of granite (representing the main material used for constructing the historical strictures). Three main categories of walls have been investigated:

- WS walls which are composed of units with regular shape and dimensions and dry joints.
- WI walls which consist of the assembly of irregular hand-cut units with similar shape but variable dimensions with low strength mortar filling in the head and bed joints
- WR rubble masonry walls which are composed by units with variable shape and dimensions randomly assembled with low strength mortar

Vasconscelos tested masonry walls of 1200 mm height X 1000 mm width, corresponding to a height to length ratio of 1.2. The walls thicknesses were 200 mm. The adopted dimensions for the walls and stone units are about 1:3 scale for single leaf walls found in the northern region of Portugal. Fig 5.38 bellow shows schematic representation of the three types of walls.

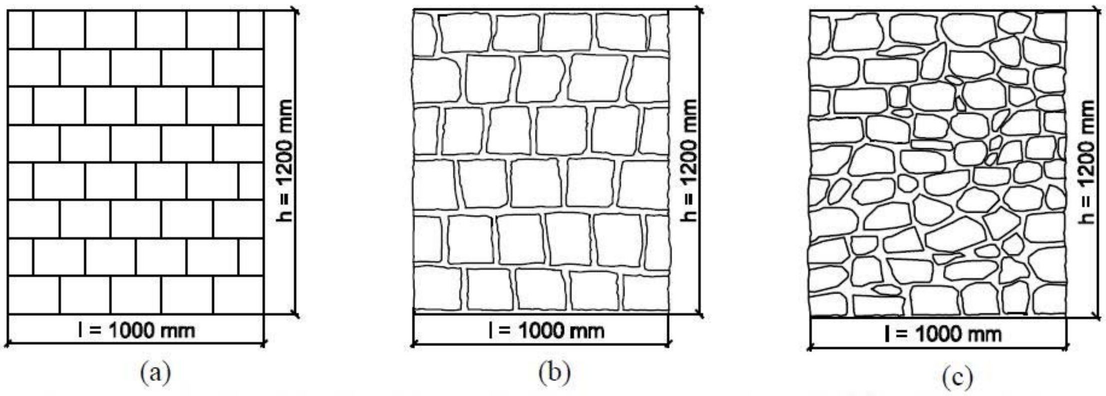

Figure 5.38 Geometry and bond details of Vasconscelos walls; (a) sawn stone units walls, WS; (b) irregular walls, WI; (c) rubble walls, WR

n the simulation study, finite element simulations have been conducted to WS wall only using all range of axial loading staring with zero axial loading up to full axial capacity of the wall so that the interaction between axial and lateral loading can be extracted. As mentioned before, the walls were 1200 mm X 1000 mm X 200 mm. The granite masonry units had dimensions of 200 mm X 150 mm X 200 mm (Fig 5.39).

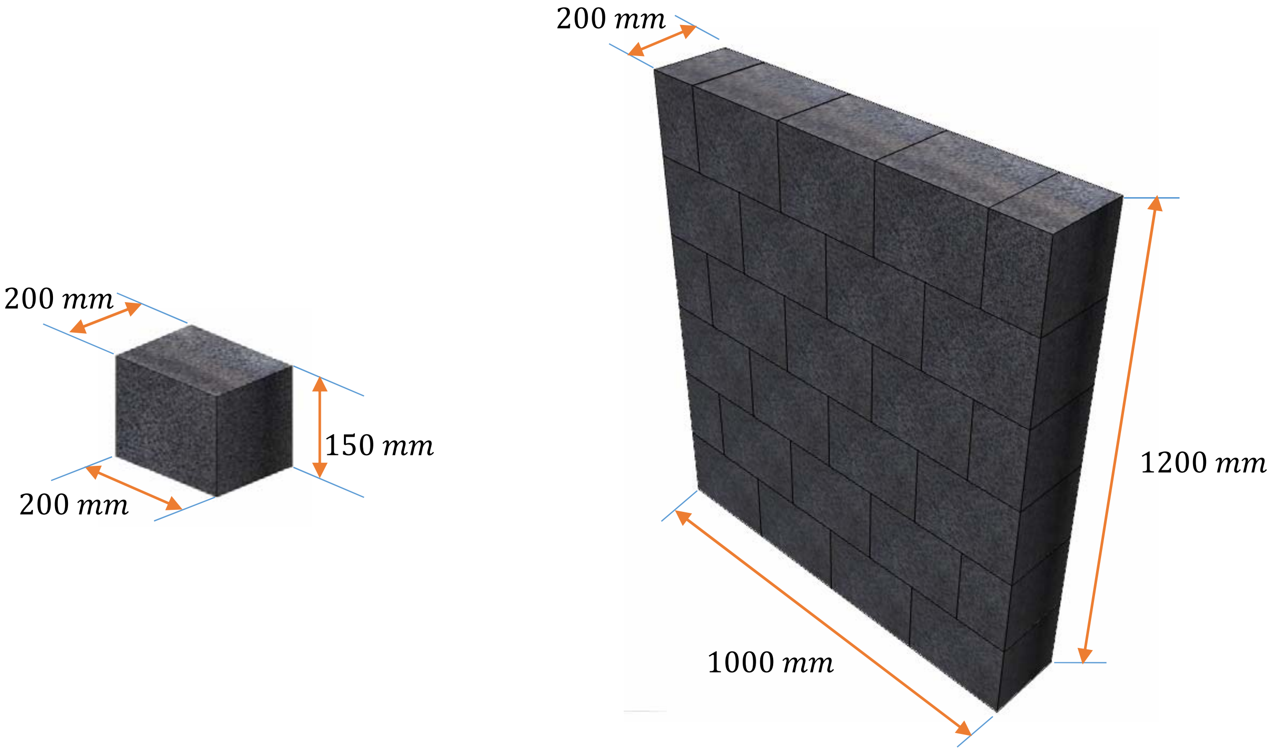

Figure 5.39 Geometry and bond details of sawn stone walls, WS; (Vasconscelos walls)

As mentioned before, WS walls are composed of units with regular shape and dimensions and dry joints. In the FEM analysis, granite stone has been considered as a continuum media and simulated using continuum damage model. The stress plastic strain values needed in the damage model incorporated in ABAQUS are as shown in Figs 5.40 and 5.41.

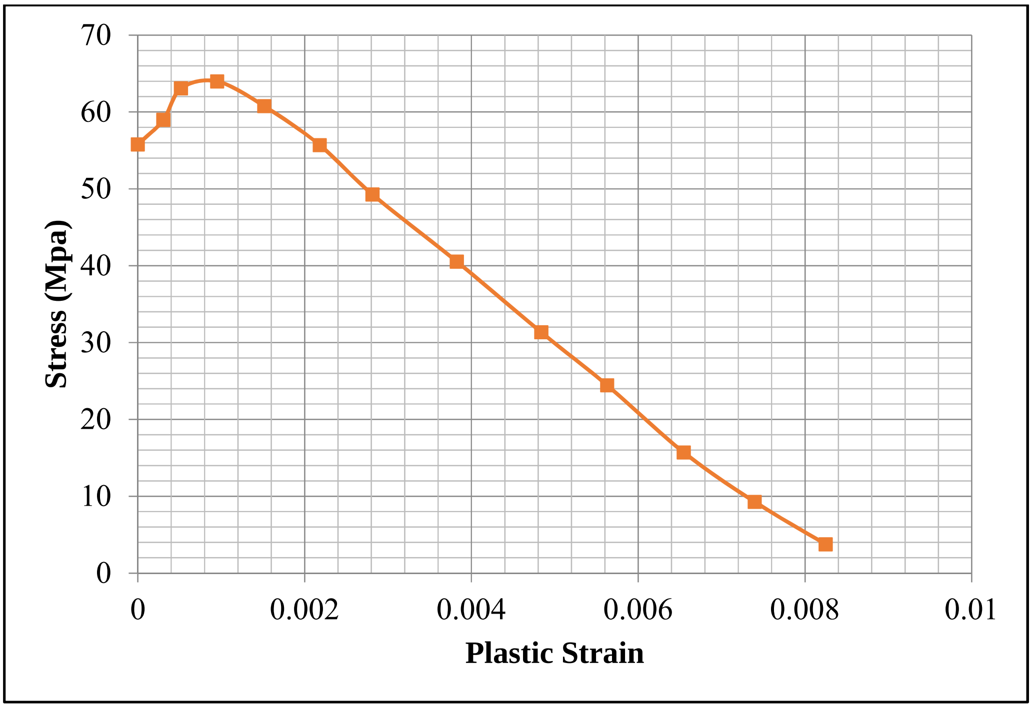

Figure 5.40 Plastic Strain vs Stress in Compression (Vasconscelos walls).

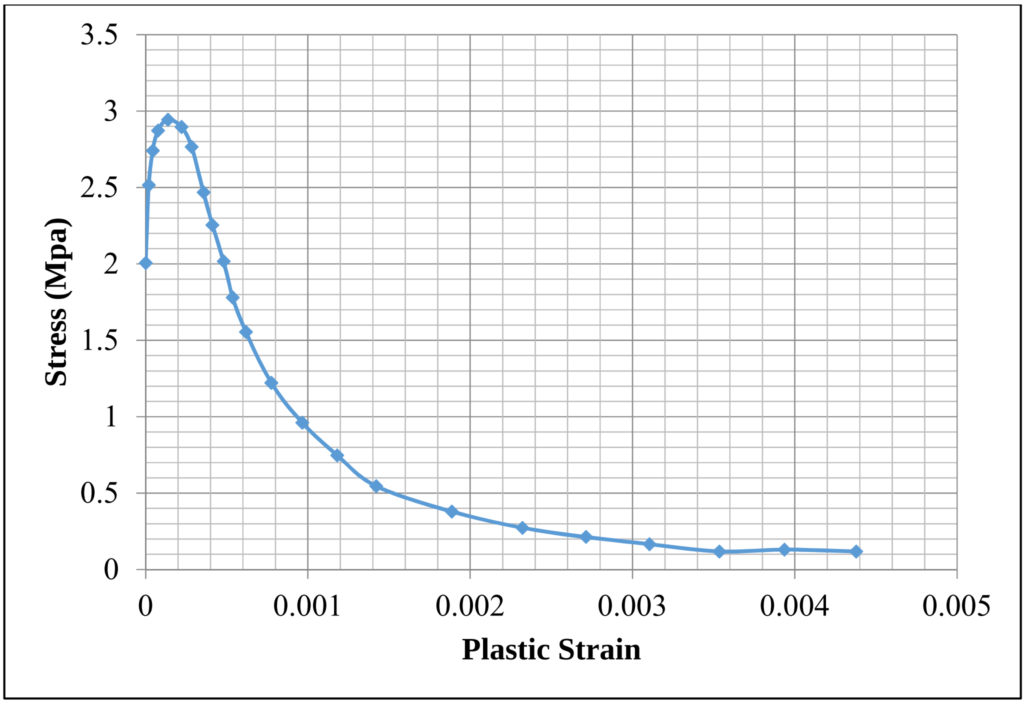

Figure 5.41 Plastic Strain vs Stress in Tension (Vasconscelos walls).

Plastic damage model, developed by Lubliner et al. (1989) and adopted in the commercial softwera ABAQUS, needs certain material parameters to be used in simulation. Some of these parameters were assumed to be the default values and some others were calculated based on ACI. These parameters are shown in Table 5.12.

Table 5.12 Parameters Used in Plastic Damage Model.

Mass Density (Tone/mm^3)	Young's Modulus (Mpa)	Poisson's Ratio	Dilation Angle ψ (Degree)	Eccentricity ϵ	f_{b0}/f_{c0}	K	Viscosity Parameter
2.6E-009	20200	0.2	36	0.1	1.16	0.67	0

In her study, Vascolncelos tested the WS walls under both cyclic and monotonic loading. Three WS walls were tested under monotonic lateral loading. The axial stresses that were exerted on the walls were 0.5, 0.875 and 1.25 Mpa for each wall. The lateral displacement verses lateral strength of the walls has been recorded. Fig 5.42 bellow shows the behavior of the walls under the mentioned loads.

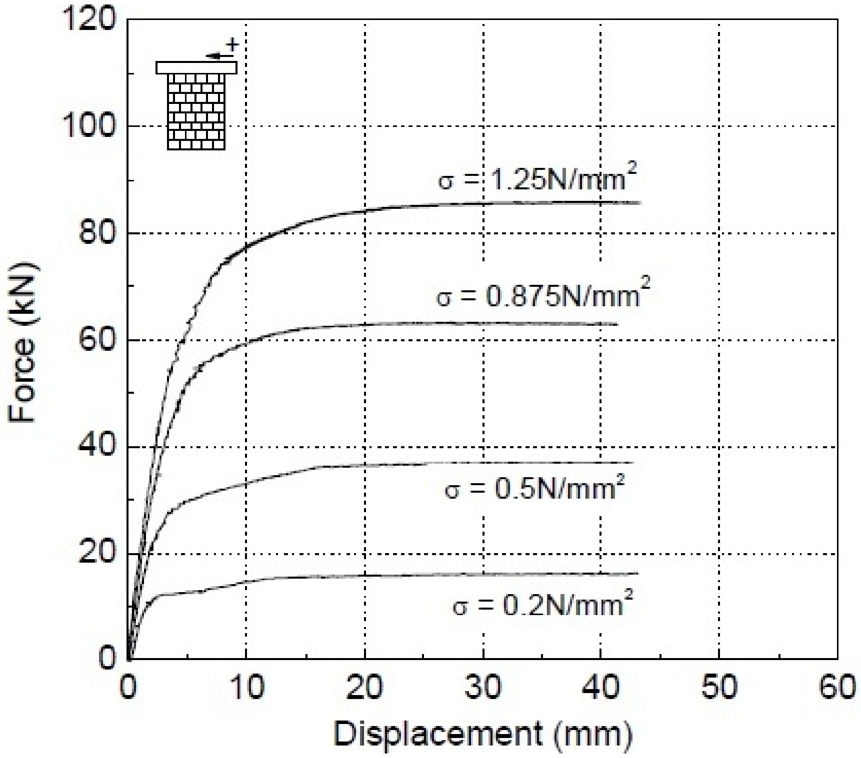

Figure 5.42 Monotonic force-displacement diagrams of walls WS under distinct pre-compression levels (Vasconscelos walls).

In this study, finite element simulations have been conducted to the WS walls. Axial stresses applied to the walls were starting from zero axial stress up to the full axial capacity of the wall. Fig 5.43 shows results of finite element simulation and the experimental results for those WS walls that were tested under monotonic loading.

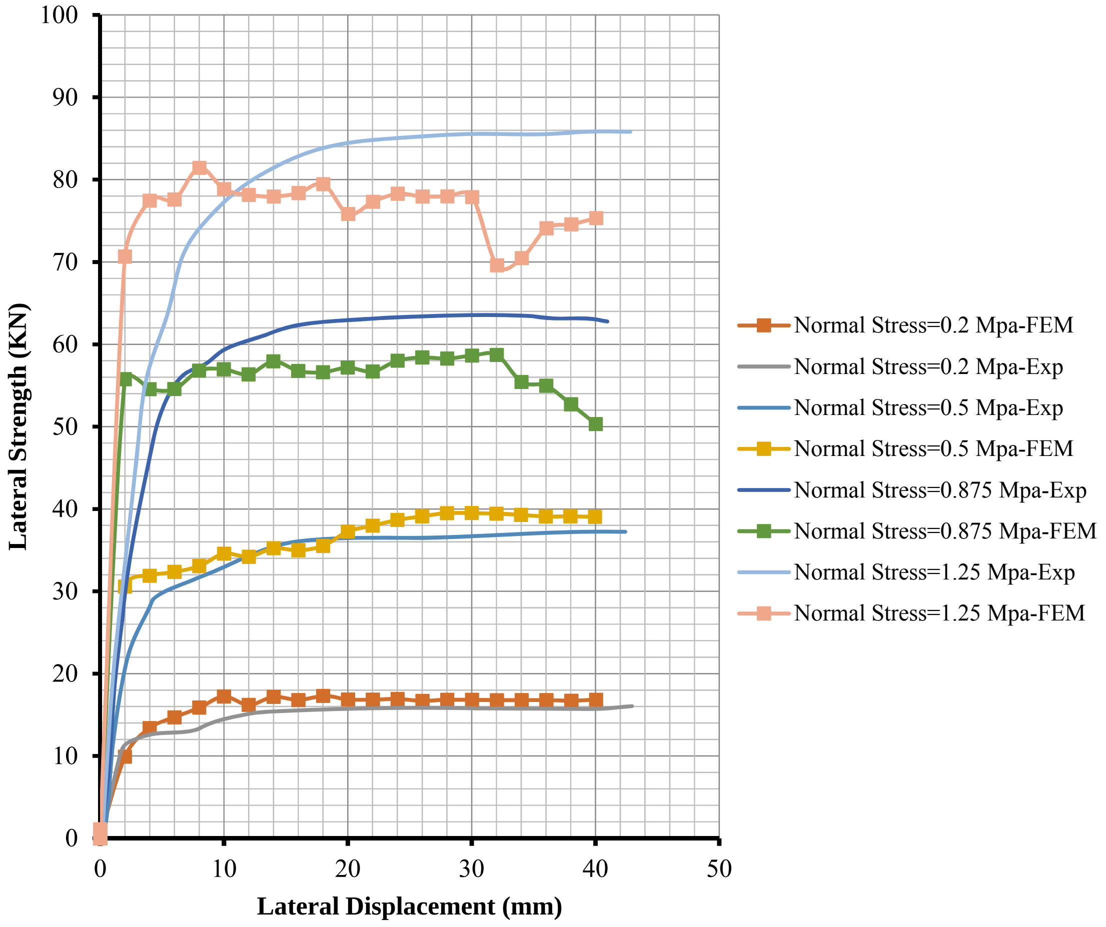

Figure 5.43 Lateral Strength vs Lateral displacement (Vasconscelos walls).

From Fig 5.43, it is clear that there is a good agreement between the experimental results and the FEM results.

As mentioned before, the walls have been subjected to a pre-compression axial force of taking the full range starting from zero up to full axial capacity of the wall. The lateral load verses lateral displacement has been extracted from the finite element simulation.

Following are the axial stresses and lateral displacements cases that have been investigated using finite element.

Table 5.13 Axial load and Lateral displacements of Vasconscelos walls.

Normal Stress (MPa)	Max lateral displacement (mm)
0.2	10
0.5	40
0.875	40
1.25	40
2	10
3	10
4	10
6	10
8	4.5
9	2.6
11	1.9
12	3.0
13	3.0
14	1.9
15	2.7
16	1.4
17	1.5
18	1.0
19	0

A total of 19 simulations have been conducted in which axial stress is different in each simulation. The simulations took a long duration to complete.

From the analysis of all load cases mentioned in Table 5.13, the results of this simulation also reveal that, the interaction between axial force and lateral resistance follow a parabolic curve. Fig 5.44 shows lateral displacement verses lateral force of walls simulated using finite element.

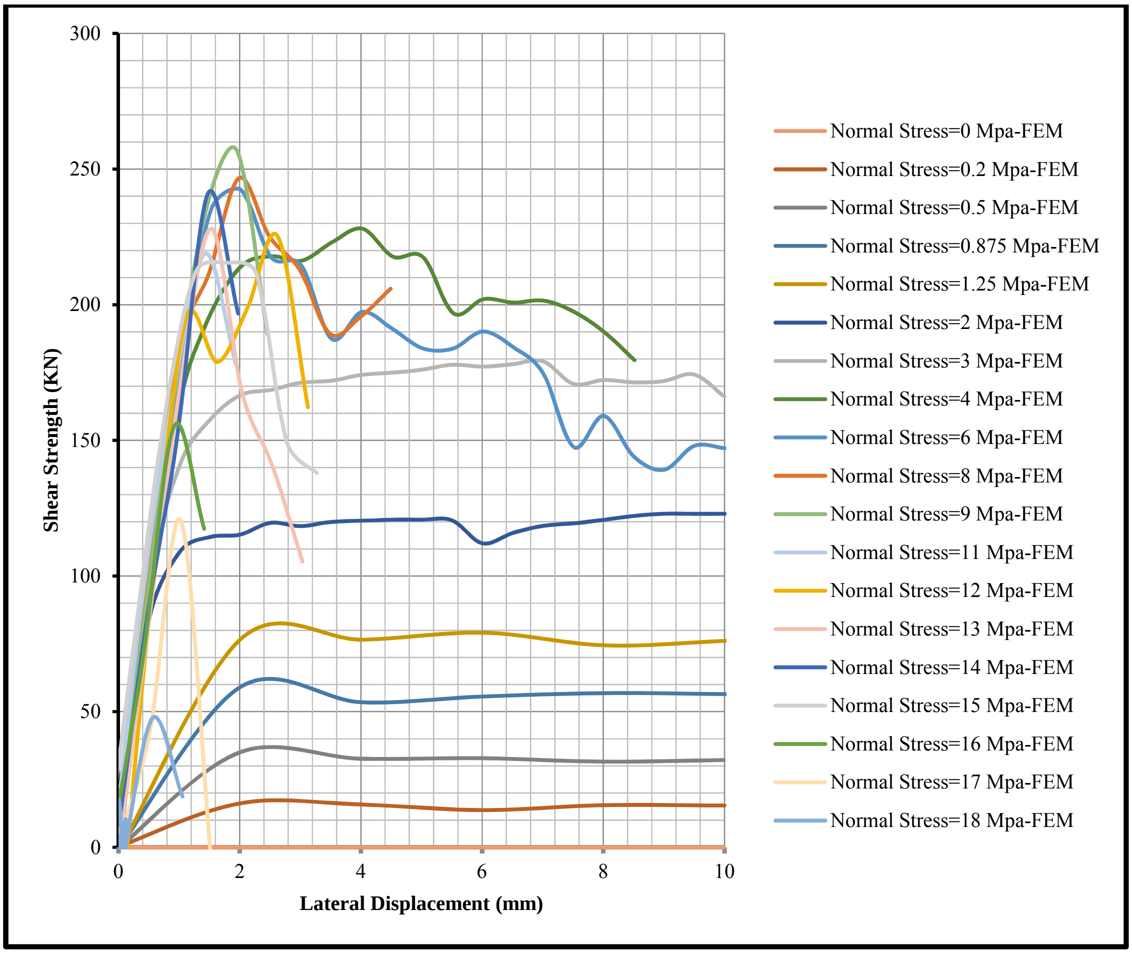

Figure 5.44 Lateral Strength vs Lateral displacement (Vasconscelos walls).

From the curves above, it is clear that the walls exhibit high ductility when the axial force is low. This ductility decreases as the pre-compression stress increases and the walls tend the exhibit brittle failure. It is also clear from the curves that the lateral strength increases as the axial stress increases. This trend is true up to certain level after which the walls begin to weaken and lateral resistance decreases as the axial stress increases. The data relating axial forces and lateral strengths of the walls are presented in Table 5.14:

Table 5.14 Axial load, axial force and Maximum shear force (Vasconscelos walls).

Normal stress (MPa)	Normal Force (Kn)	Lateral Strength-Exp (Kn)	Lateral Strength-FEM (Kn)
0	0		0.017
0.2	40	16.05	17.11
0.5	100	37.23	36.09
0.875	175	63.51	59.13
1.25	250	85.84	79.10
2	400		122.96
3	600		179.15
4	800		228.03
6	1200		242.41
8	1600		246.70
9	1800		256.64
11	2200		218.89
12	2400		225.23
13	2600		228.03
14	2800		240.97
15	3000		215.41
16	3200		182.43
17	3400		120.30
18	3600		47.50
19	3800		0

This data has been plotted as shown in Fig 5.45.

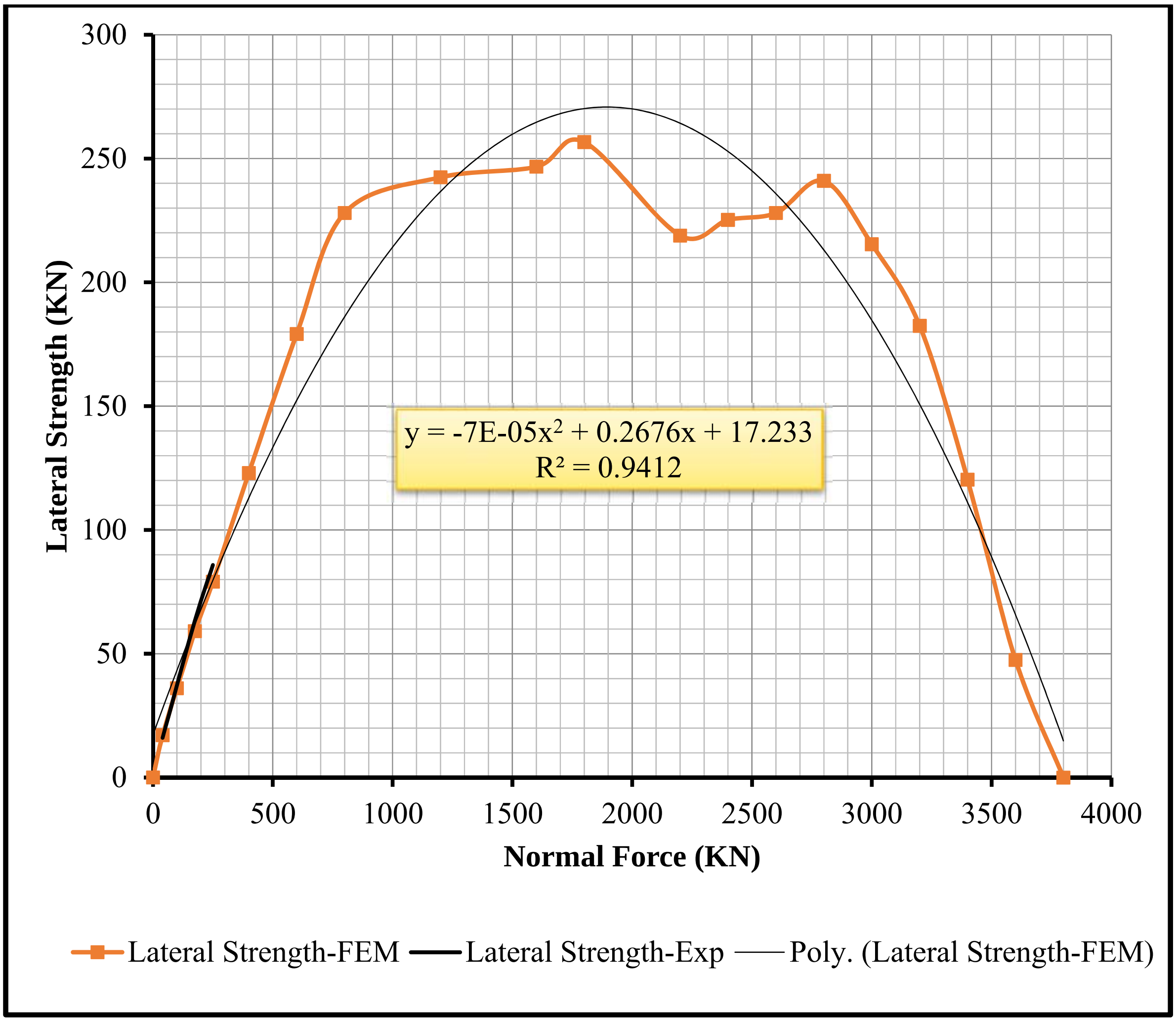

Figure 5.45 Lateral Shear Strength vs Normal force (Vasconscelos walls).

It is clear from Fig 5.45 above that the relationship between axial force and lateral strength of the wall follows a parabolic curve. A regression analysis has been done for the data collected from the simulation. The formula result from this analysis is:

$$H = -0.00007P^2 + 0.2676P + 17.233 \tag{5.7}$$

This curve has been normalized by dividing lateral forces by maximum lateral force and axial forces by maximum axial force. The result of the curve is shown in Fig 5.46.

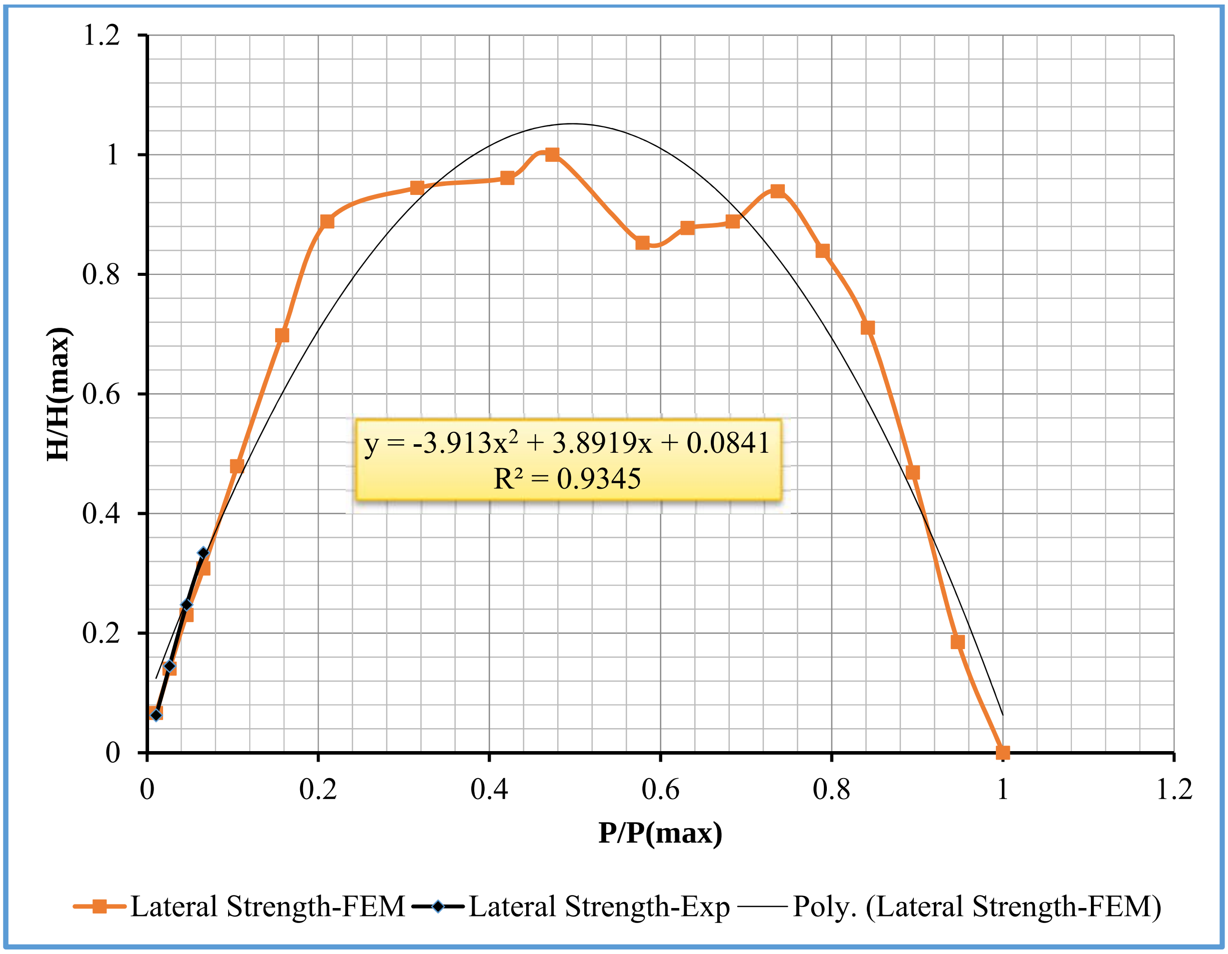

Figure 5.46 Normalized Lateral Shear Strength vs Normalized Axial Force (Vasconscelos walls).

Normalizing Eq 5.7 results in the following equation:

$$y = -3.913x^2 + 3.8919x + 0.0841 \tag{5.8}$$

Where:

$$y = \frac{H}{H_{max}} \quad and \quad x = \frac{P}{P_{max}}$$

When investigating the results of FEM simulation, five failure modes were observed, namely sliding, rocking, head/bead joints opening, cracking in bricks, and crashing of wall.

Figs 5.48-5.51, show these failure modes associated with different level of axial force. It has to be noted that displacements shown in Figs 5.47-5.50 have been amplified by factor of 10.

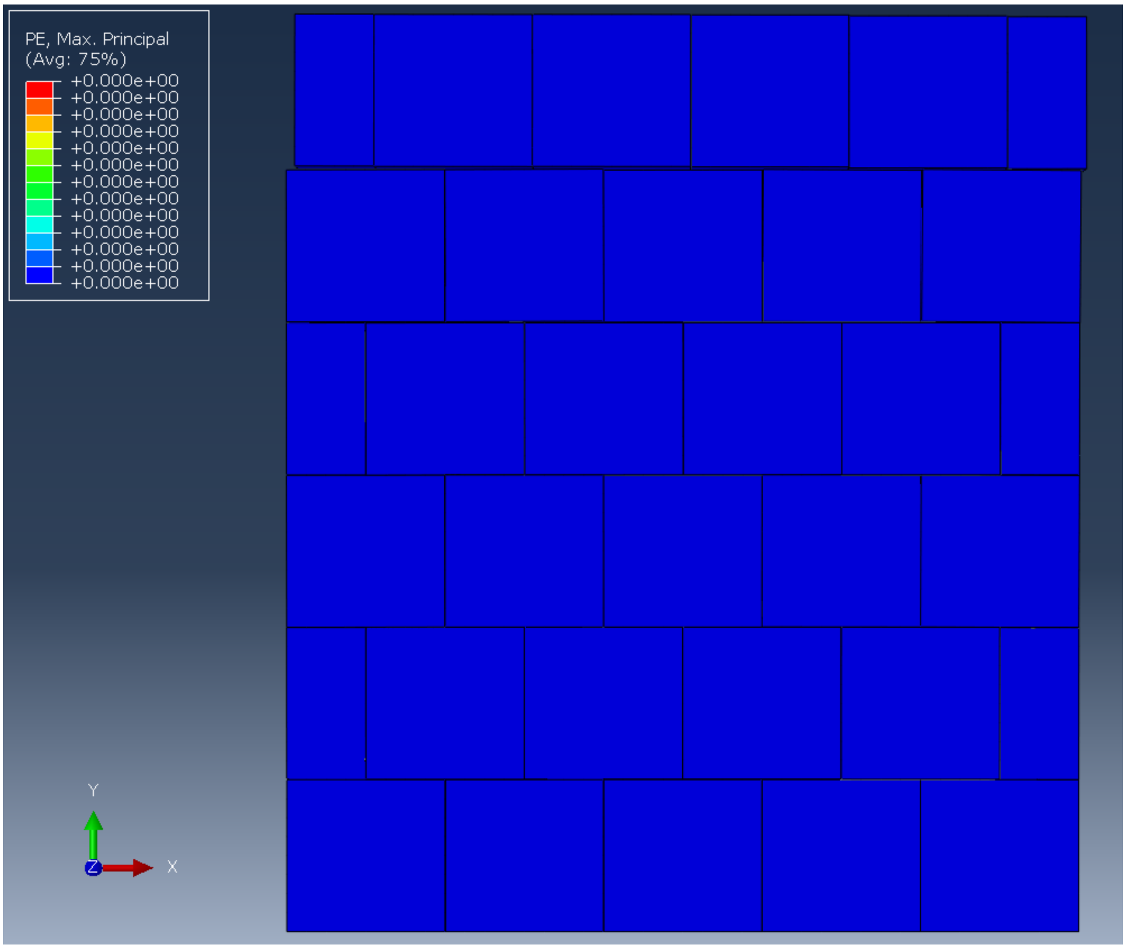

Figure 5.47 Plastic Strain and Failure Mode (0 MPa Axial Stress). (Wall Sliding)

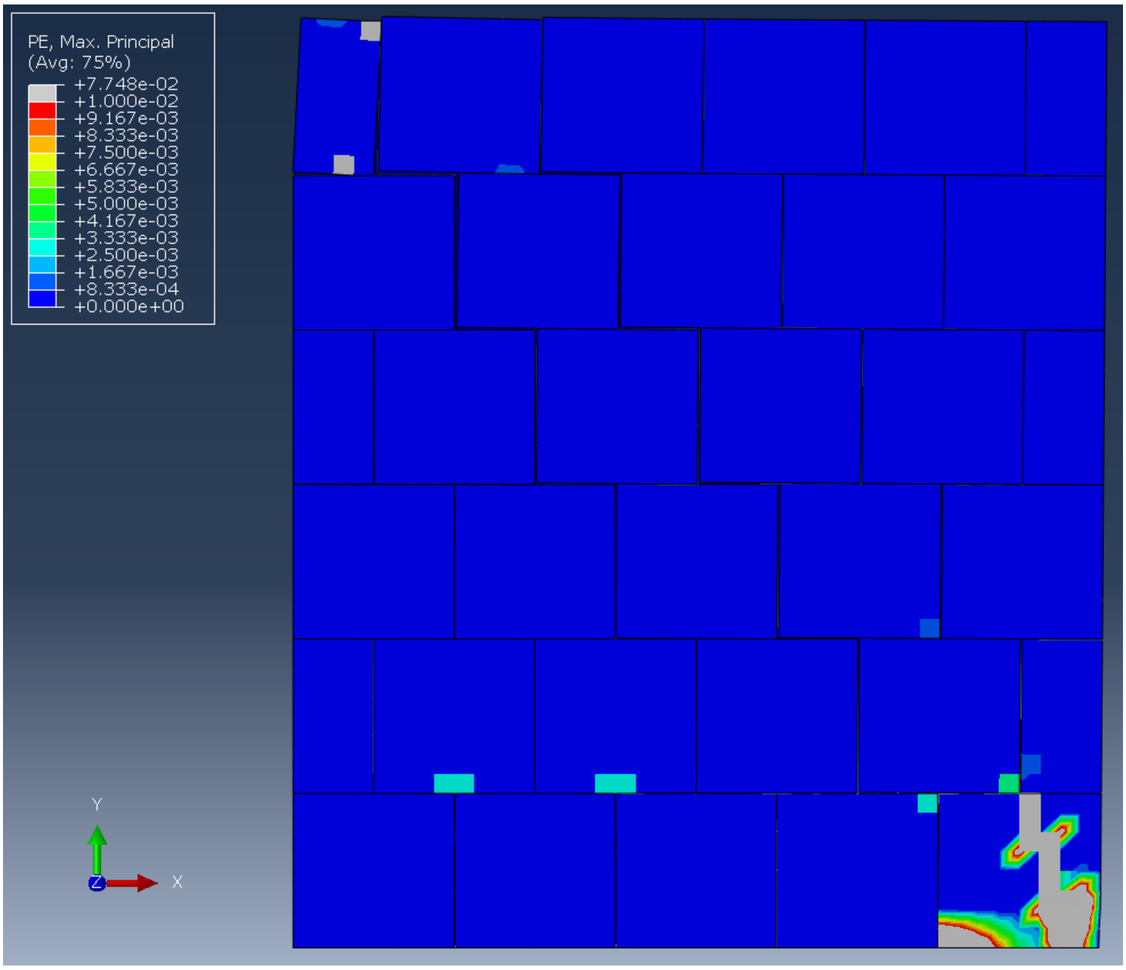

Figure 5.48 Plastic Strain and Failure Mode (2.0 MPa Axial Stress). (Wall head/ bed Joins Opening and Toe Crushing)

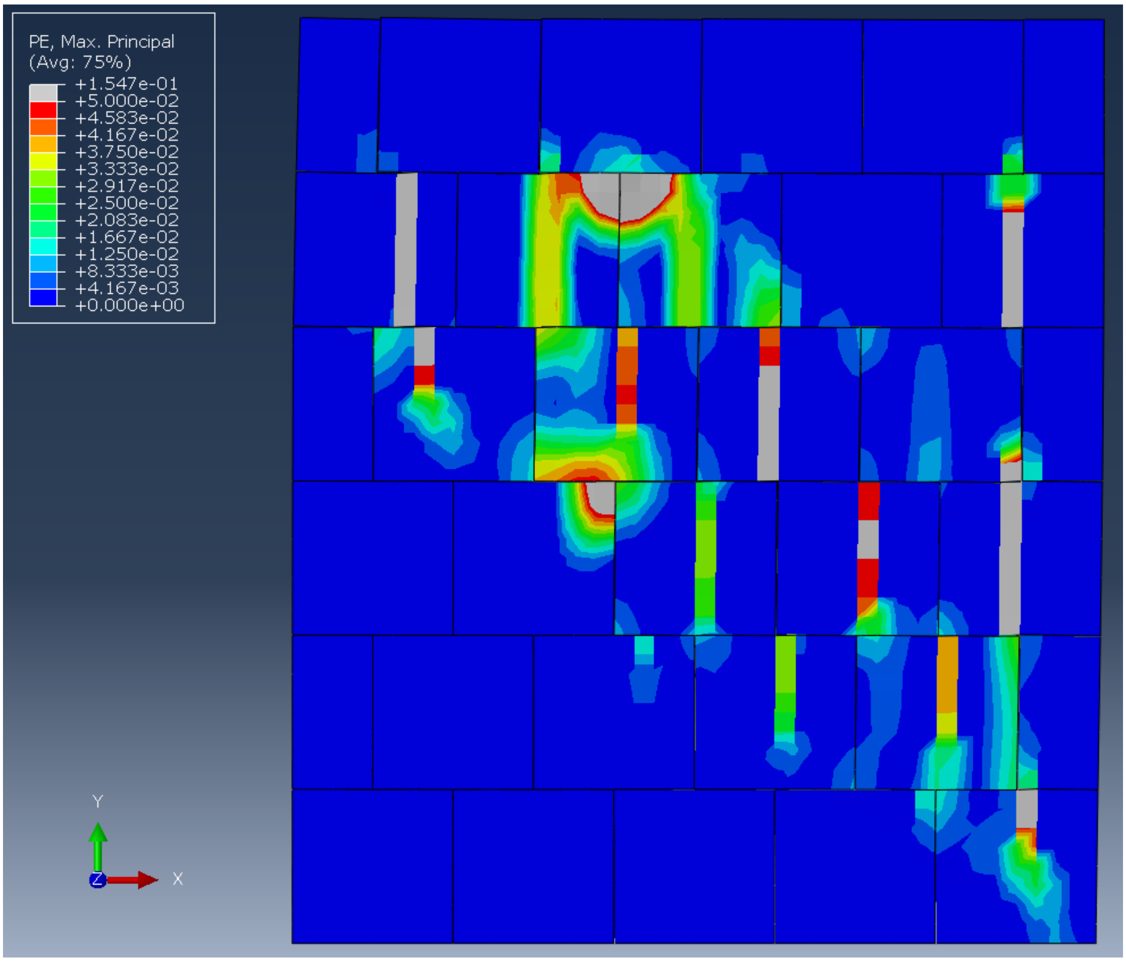

Figure 5.49 Plastic Strain and Failure Mode (6.0 MPa Axial Stress). (Wall Bricks Cracking and Crushing)

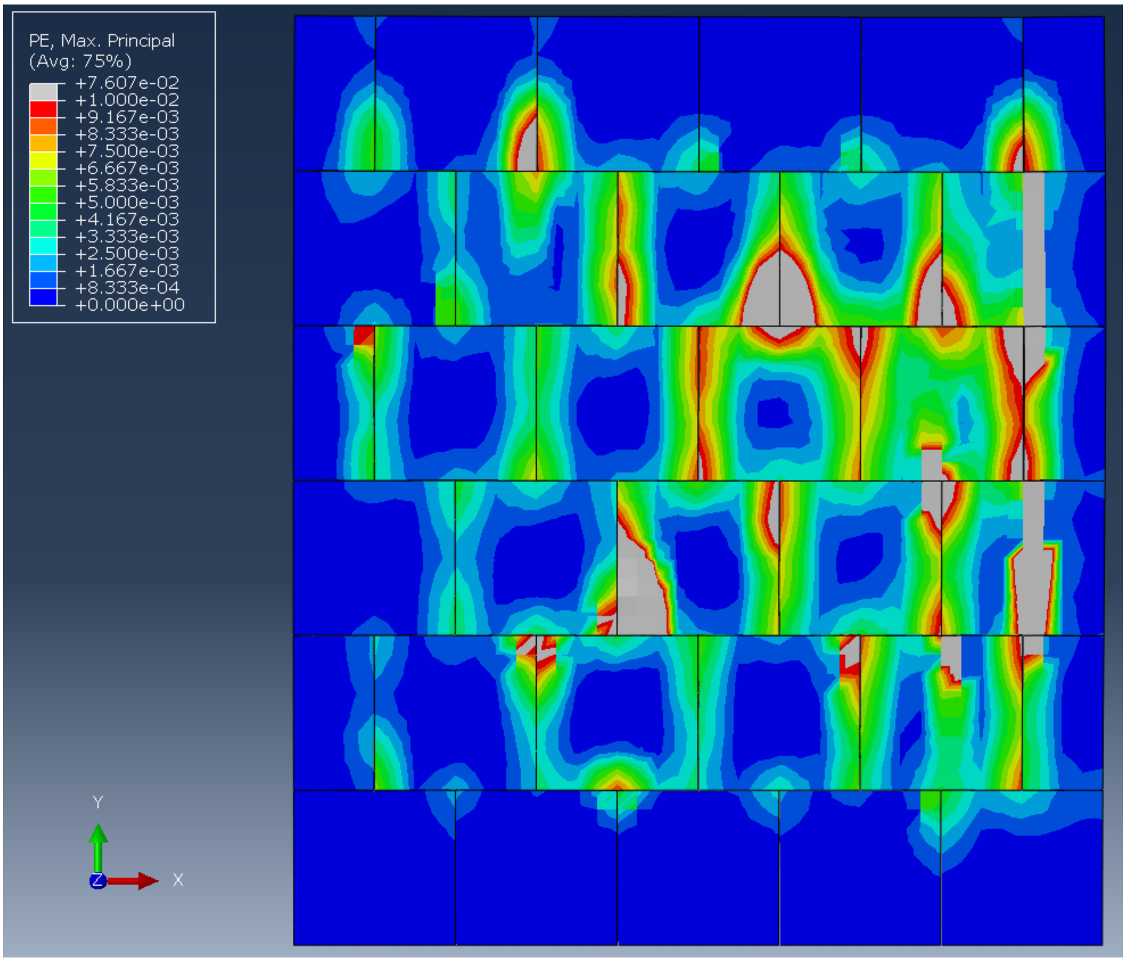

Figure 5.50 Plastic Strain and Failure Mode (16.0 MPa Axial Stress). (Wall Bricks Cracking and Crushing)

The stress contour associated with the above-mentioned plastic strain cases are shown in the appendix.

5.5 Generalized Interaction Diagram

As shown in the above analysis of all walls simulated, the relationship between axial force and lateral strength follows parabolic curves. The normalized equations of these walls seem to be similar. The normalized interaction curves of all walls type are gathered in one curve. The results are shown in Fig 5.51.

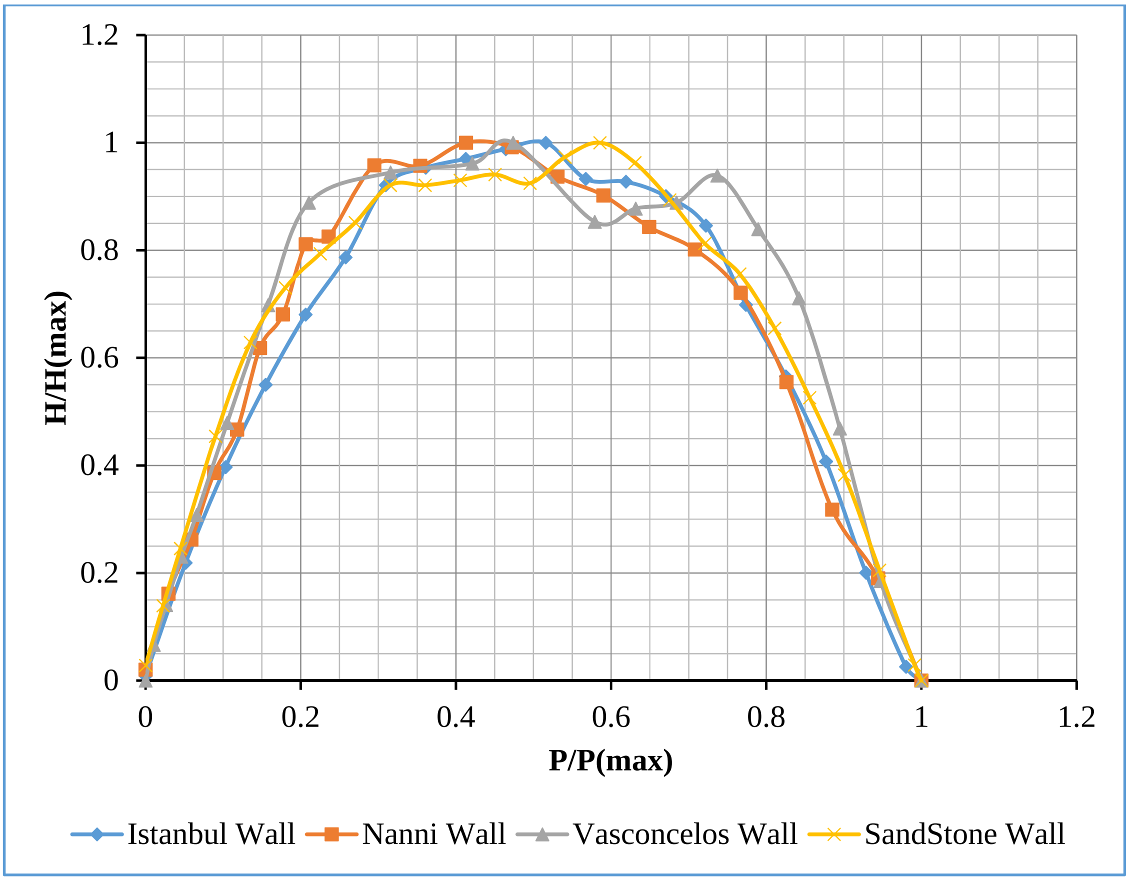

Figure 5.51 Normalized Lateral Shear Strength vs Normalized Axial Force curves (Sandstone, Demir, Li and Vasconscelos walls).

Regression analysis has been done to all data to get a one general normalized equation. The regression and fitted curve are shown in the Fig 5.52.

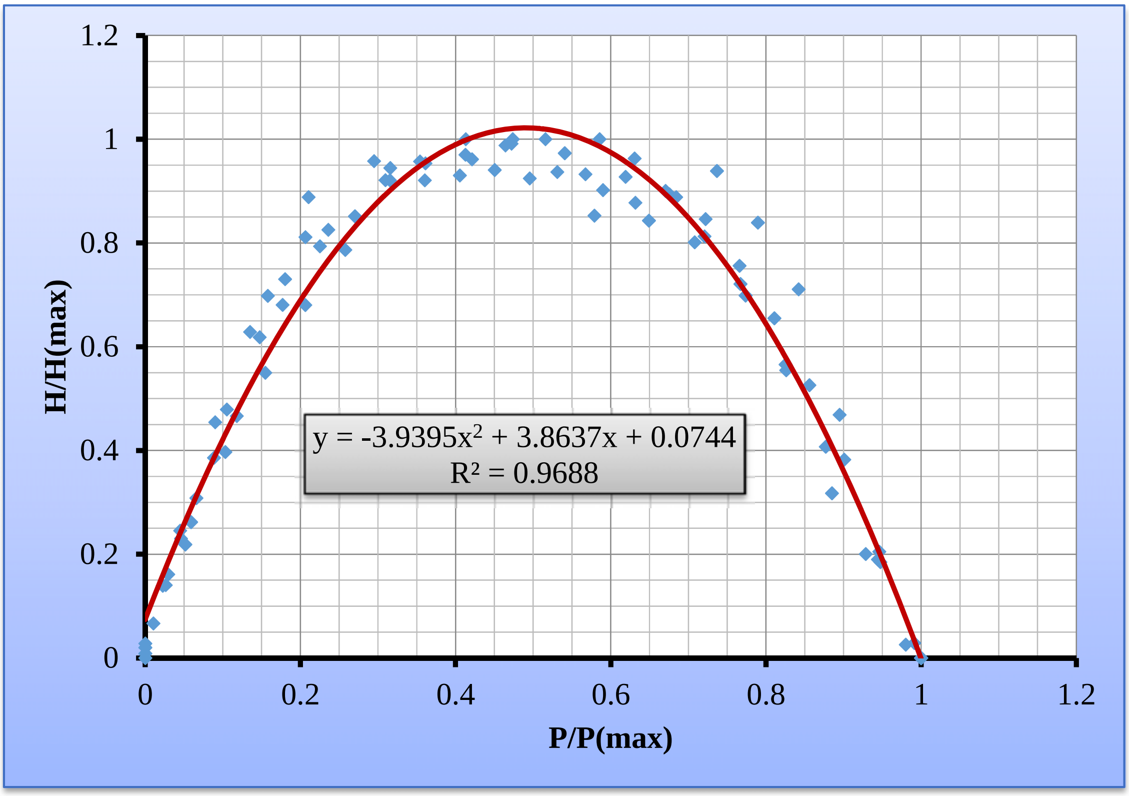

Figure 5.52 Normalized Lateral Shear Strength vs Normalized Axial Force (Sandstone, Demir, Li and Vasconscelos walls).

The normalized general equation is:

$$Assuming\ y = \frac{H}{H_{max}} \quad and \quad x = \frac{P}{P_{max}}$$

$$\boldsymbol{y = -3.9395x^2 + 3.8637x + 0.0744} \qquad (5.9)$$

This equation is very similar to Eqs 5.2, 5.4, 5.6, and 5.8 of all normalized interaction curves of all walls simulated above. This equation can extend to be used for any masonry wall subjected to in-plane loading. An analysis and design procedure can be proposed using this generalized normalized interaction equation.

5.6 Mechanistic Approach for Predicting Behavior of Masonry Wall.

This behavior has been reported indirectly by some researchers. The main theory that they used is the bending and static equilibrium theory to find the maximum lateral capacity of the wall.

Abrams (1992) from University of Illinois has investigated the behavior of unreinforced masonry element. In his work, Abrams performed an experimental study on five walls specimens. Each one the walls was subjected to axial stress. As he reported, the axial stress applied on the five walls was ranging from 0.52 Mpa up to 0.99 Mpa. The results showed that, substantial increase in lateral strength could exist past initial crack whether it be for older walls tested with force that increased monotonically, or failure of for newer walls subjected to repeated and reversed cyclic lateral forces.

Abrams used the bending theory and static equilibrium to find the lateral capacity of the wall. Fig 5.53 shows the basic assumption the he used in his analysis.

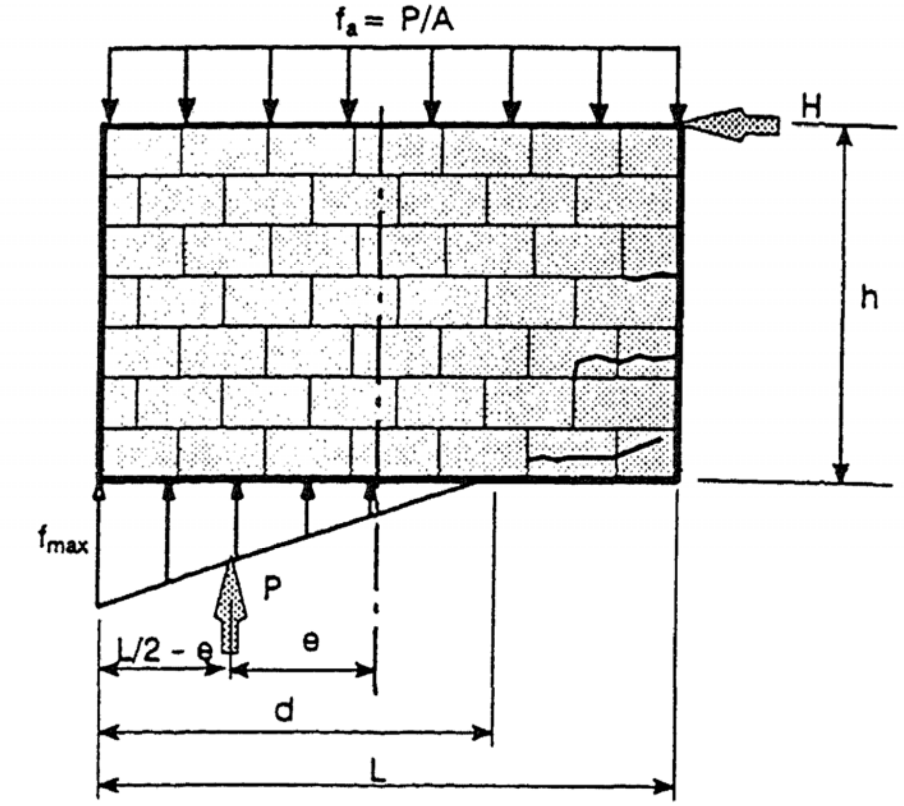

Figure 5.53 Free body diagram of wall cracked at base.

In our study, we used the equation that Abrams (1992) used to verify his result. The static equilibrium equation using bending theory is as follows:

$$H = \frac{P}{3bh\,f_{max}}\left(\frac{3bL}{2}f_{max} - 2P\right) \tag{5.10}$$

This equation has been derived based on three assumptions:

- The material behavior is linear,
- The wall self-weight is not considered
- Beam bending theory is applicable.

This means that when applied normal axial force P is zero, the lateral resistance force of the wall H is zero. In order to account for the self-weight of the wall, this equation can be reformulates as follows:

$$H = \frac{(P + P_0)}{3bh\, f_{max}}\left(\frac{3bL}{2} f_{max} - 2(P + P_0)\right) \tag{5.11}$$

Where:

H is the lateral horizontal strength force of the wall.

P is the external applied normal force on the wall

f_{max} is the maximum axial capacity of the wall.

P_0 is the total weight of the wall

L is the width of the wall

h is the height of the wall

b is the thickness of the wall.

This equation can be normalized using the maximum horizontal force and maximum axial force that can be carried by the wall. The maximum horizontal and axial forces are shown in Eqs, 5.12 and 5.13

$$H_{max} = \frac{3bL^2 f_{max}}{32h} \tag{5.12}$$

$$P_{max} = \frac{3bLf_{max} - 4P_0}{4} \tag{5.13}$$

To compare our result with the result coming from Abrams approach, we can apply the above equations to the four wall cases mentioned above (sandstone wall, Demir wall, Li wall, and Vasconcelos wall). Important note has to be taken into consideration when using the above equations which is that these equations have been derived based on the assumptions that the material behavior is elastic linear. This means that for high axial load, these equations are not applicable because the material of the wall goes in the nonlinear phase of its behavior. Excluded the last part of the curve represents the above equations we will get the following results:

5.6.1 Sandstone Wall.

$L = 1.0\ m, \qquad h = 1.0m, \qquad b = 0.2m, \qquad f_{max} = 22.2\ Mpa$

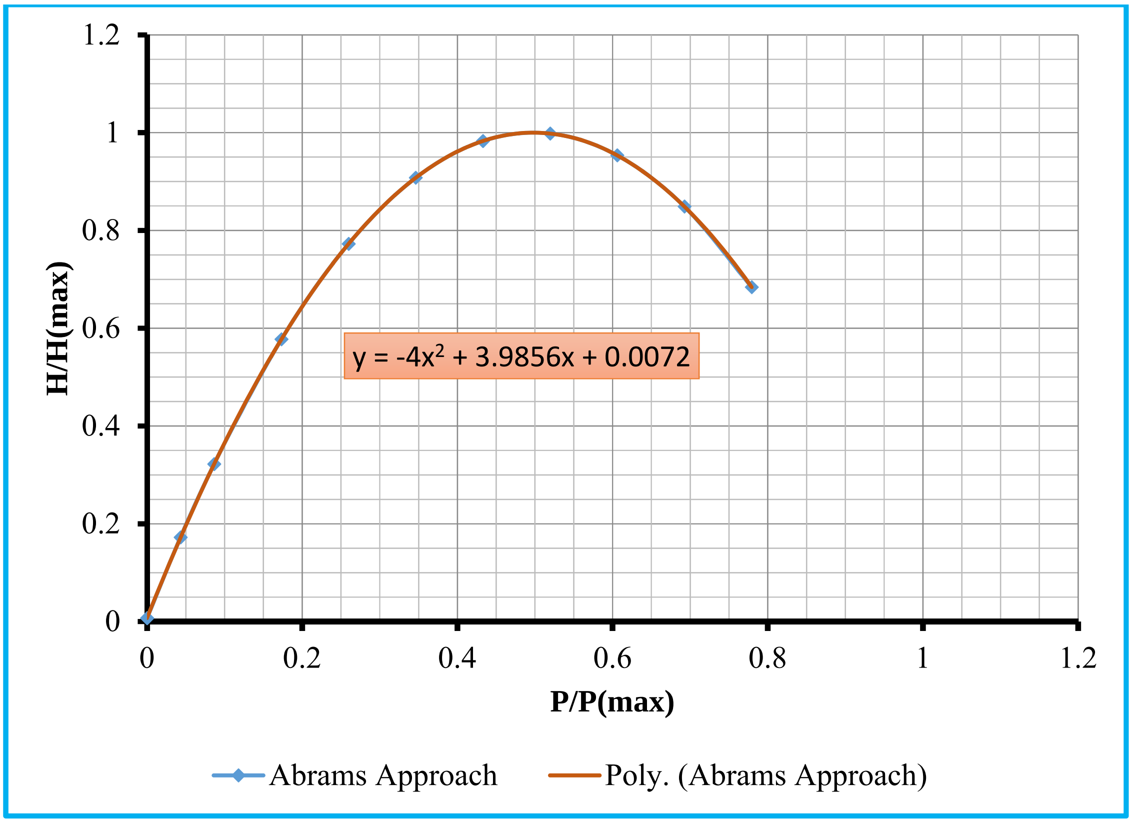

Figure 5.54 Normalized Lateral Shear Strength vs Normalized Axial Force using Abrams approach (Sandstone walls).

5.6.2 Demir Experiments

$$L = 1.2\ m, \qquad h = 1.2m, \qquad b = 0.3m, \qquad f_{max} = 4.8\ Mpa$$

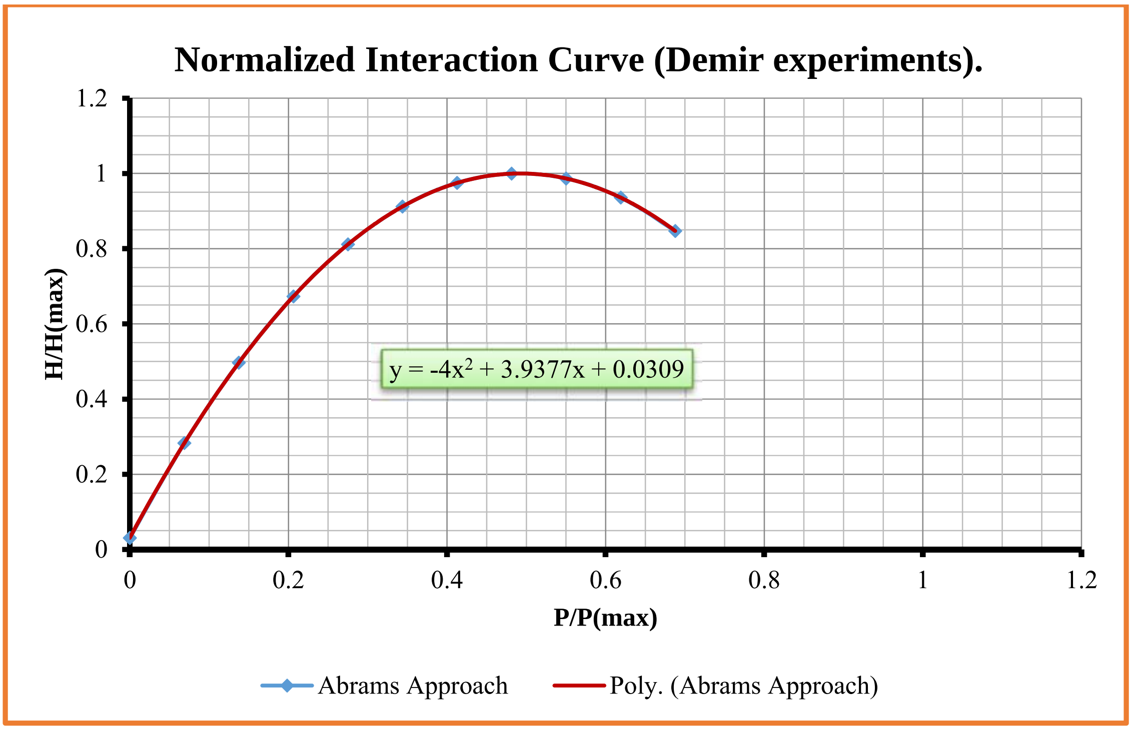

Figure 5.55 Normalized Lateral Shear Strength vs Normalized Axial Force using Abrams approach (Demir walls).

5.6.3 Li Experiments

$L = 1.625\ m, \qquad h = 1.625m, \qquad b = 0.2m, \qquad f_{max} = 8.47\ Mpa$

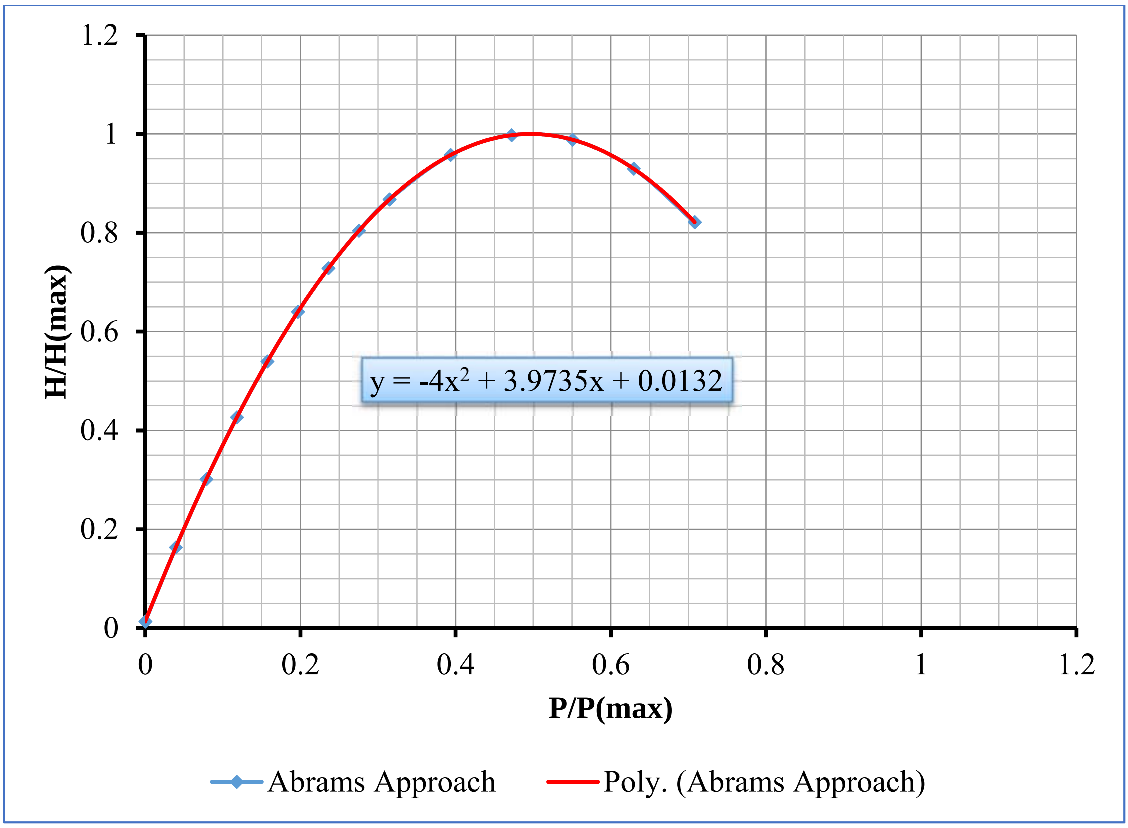

Figure 5.56 Normalized Lateral Shear Strength vs Normalized Axial Force using Abrams approach (Li walls).

5.6.4 Vasconcelos Experiments:

$L = 1.0\ m, \qquad h = 1.2m, \qquad b = 0.3m, \qquad f_{max} = 19\ Mpa$

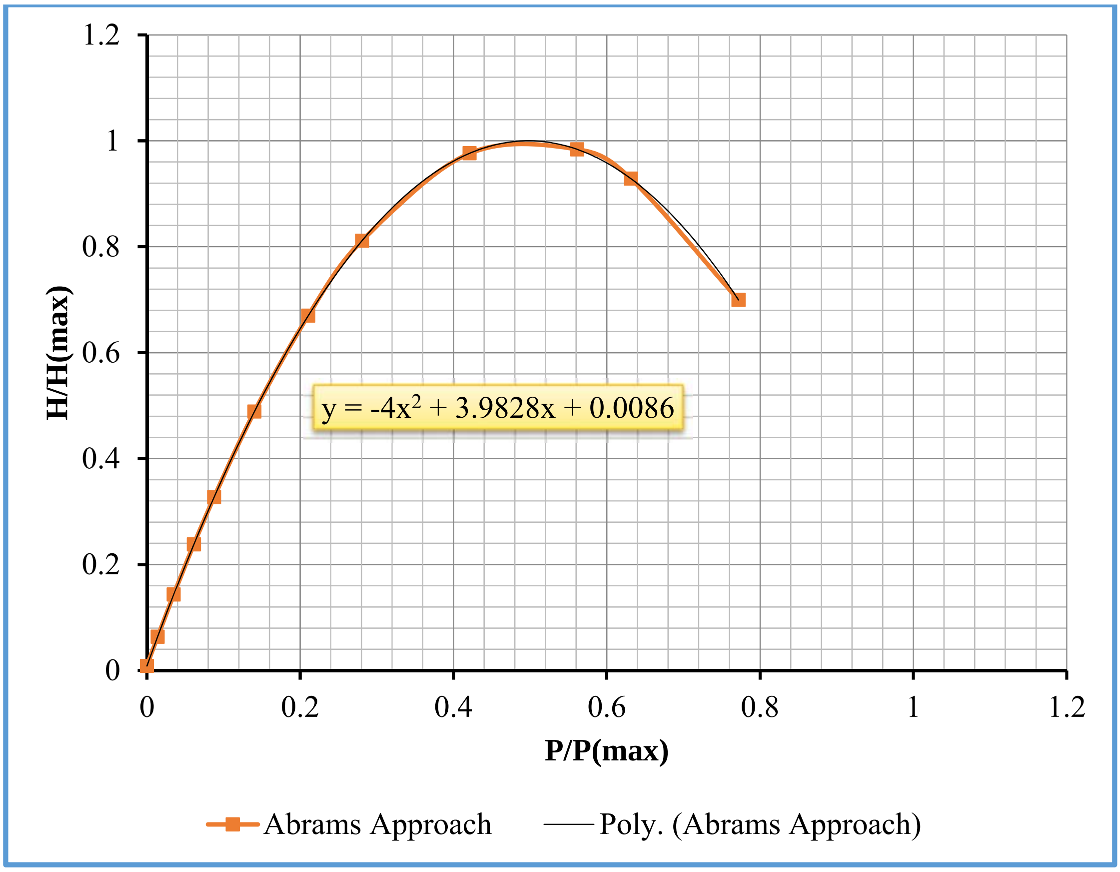

Figure 5.57 Normalized Lateral Shear Strength vs Normalized Axial Force using Abrams approach (Vasconcelos walls).

If we plot the data results from the simulation of walls, we will get Fig 5.58.

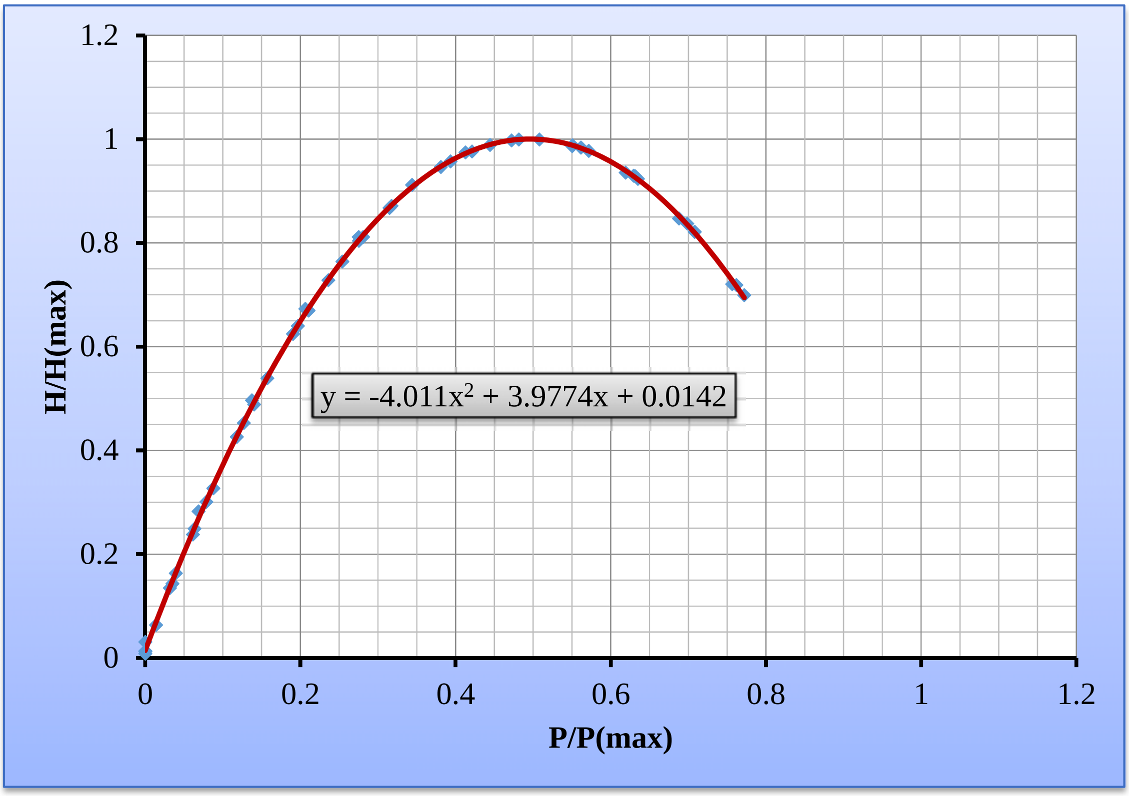

Figure 5.58 Normalized Lateral Shear Strength vs Normalized Axial Force using Abrams approach (Sandstone, Demir, Li, and Vasconcelos walls).

From the above results, it is clear that the interaction equation between normal and lateral forces is:

$$Assuming\ y = \frac{H}{H_{max}} \quad and \quad x = \frac{P}{P_{max}}$$

$$y = -4.011x^2 + 3.9774x + 0.0142 \tag{5.14}$$

Plotting equations 5.9 and 5.14, we will get the following curves:

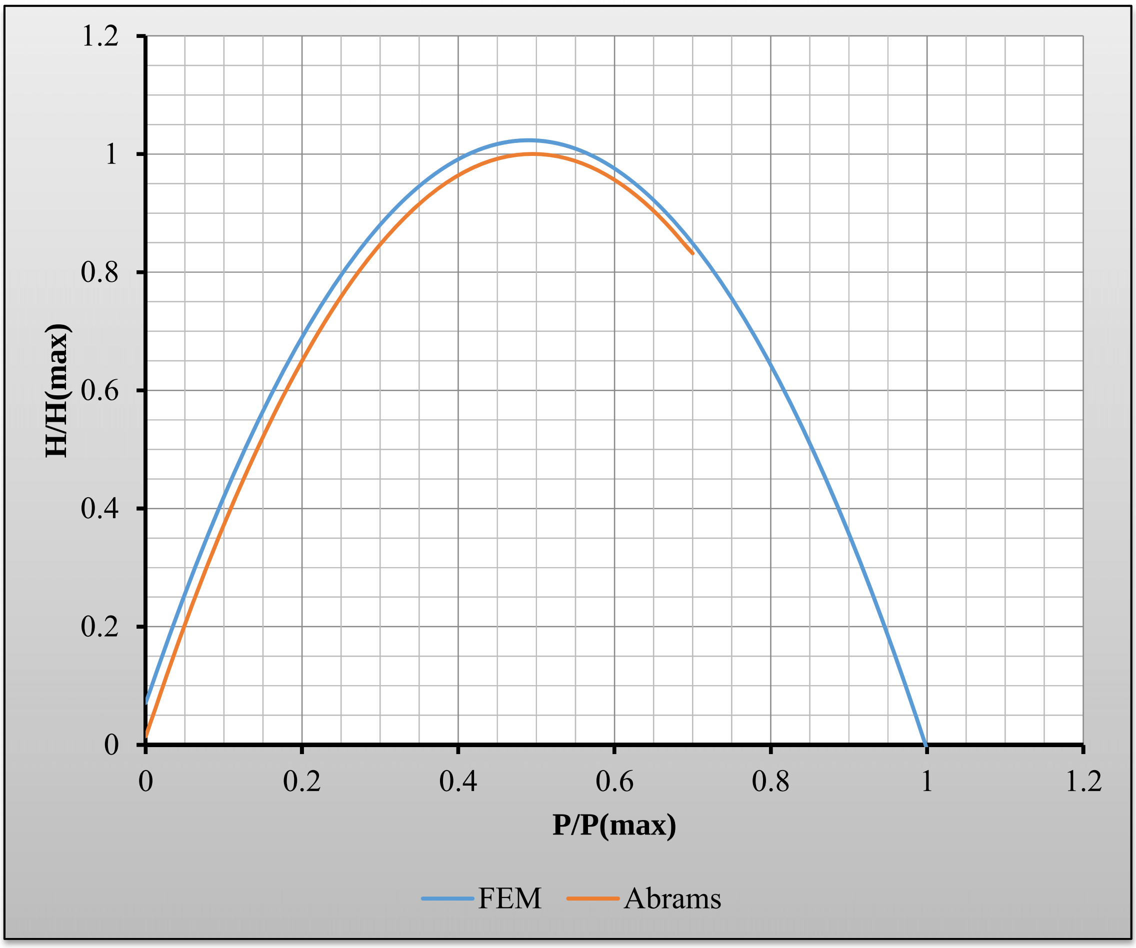

Figure 5.59 Normalized Lateral Shear Strength vs Normalized Axial Force using both FEM analysis and Abrams approach (Sandstone Demir, Li, and Vasconcelos walls).

It is clear that there is a good agreement between the two equations resulted from both finite element analysis and the static equilibrium equation investigated by Abrams. The deference between them may be attributed to bending theory adopted in static equilibrium equation. It is clear that the walls have a big value of width/length ration. This high ration means that the bending theory is not any more accurate to be used for describing the wall behavior.

In general, if we exclude the first part of the curves, the average differences between the two curves is with the range 2-3% which means that there is a good agreement between the interaction equations result from two deferent approaches.

5.7 Interface Modeling Approach.

As mentioned before, two different approach was adopted in this study. The first approach was continuum-based approach in which both sandstone and lime mortar was modeled as continuum material. The interface between the two material was assumed perfect bond. The second approach was an interface base approach. In this approach the head joints behave totally under cohesive action while the bed joints behave under pure friction. This approach is valid because of the fact that in the vertical direction the head joints are only subjected to baling stress without any friction effect. In the bead joints however, two diffident sources of strength are acting. The first one is the friction reaction. This friction force is high due to the high value of the coefficient of friction and also due to the nature of axial loading on the wall. Another source of strength in the bed joints is the shear cohesive. The shear cohesive in the bead joints is very low because of the low fracture energy in the tangential direction. Based on that only, only friction action has been adopted in the bead joints. The sandstone was modeled as continuum material. In ABAQUS/Explicit, the surface-base-cohesive approach was adopted to model the cohesive behavior of the head joints. Surface based cohesive behavior is primarily intended for situations in which the interface thickness in negligibly small. In this surface-based behavior adopted in this model, the contacted surfaces are the surfaces of the adjacent bricks themselves which means that, the lime mortar thickness have been assumed to be zero as the nature of the surface-based cohesive behavior suggested.

Due the n nature of surface based behavior, the lime mortar thinness was assumed zero. The traction separation behavior is the main property that is needed to define the interface response.

In this model, the separation starts to accrue when the traction applied on the surface reaches the maximum traction property of the interface. After that, damage evolution controls the final separation of the surfaces.

In this study, a monotonic simulation was conducted on sandstone wall for the comparison purposes with continuum-based approach. Simulation using interface approach was done to Wall-1.7 with only monotonic loading. Table 5.15 shows the parameters adopted in this study.

Table 5.15 Parameters adopted in the interface modeling approach.

Item		value
Friction coefficient		0.7
Damage initiation values	Normal peak traction	0.3
Damage Evolution values	Normal Fracture Energy	0.0015
	Power law exponent	2.284

The force displacement curve is shown in Fig. 5.60.

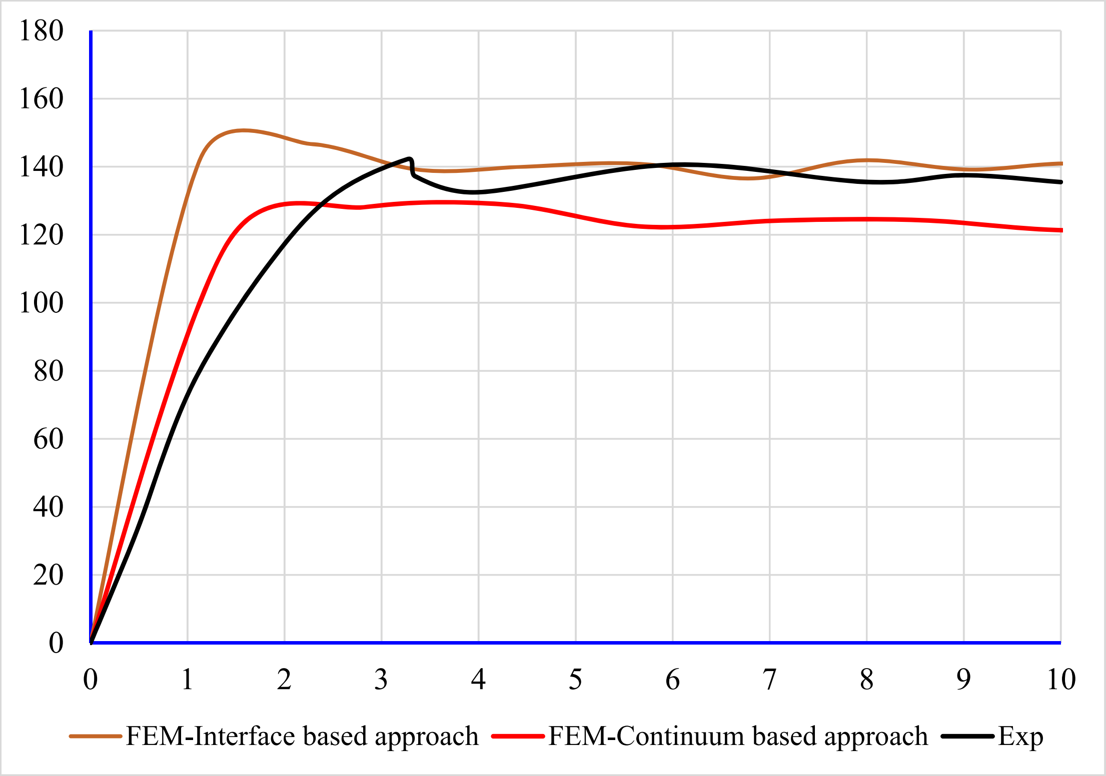

Figure 5.60 Compression between experimental and both continuum based and interface based numerical approaches.

As can be seen from Fig 5.60 there is a good agreement between the continuum based approach, interface approach and experimental results. The interface approach predicts little stronger response of the wall compare to the continuum based approach and experimental results. The initial stiffness of the wall is also higher in the case of interface approach compare to other results.

Regarding the crack pattern of the wall, the interface approach predict the cracking pattern of the wall quite well. The damaged captured using this approach is shown in Fig 5.61.

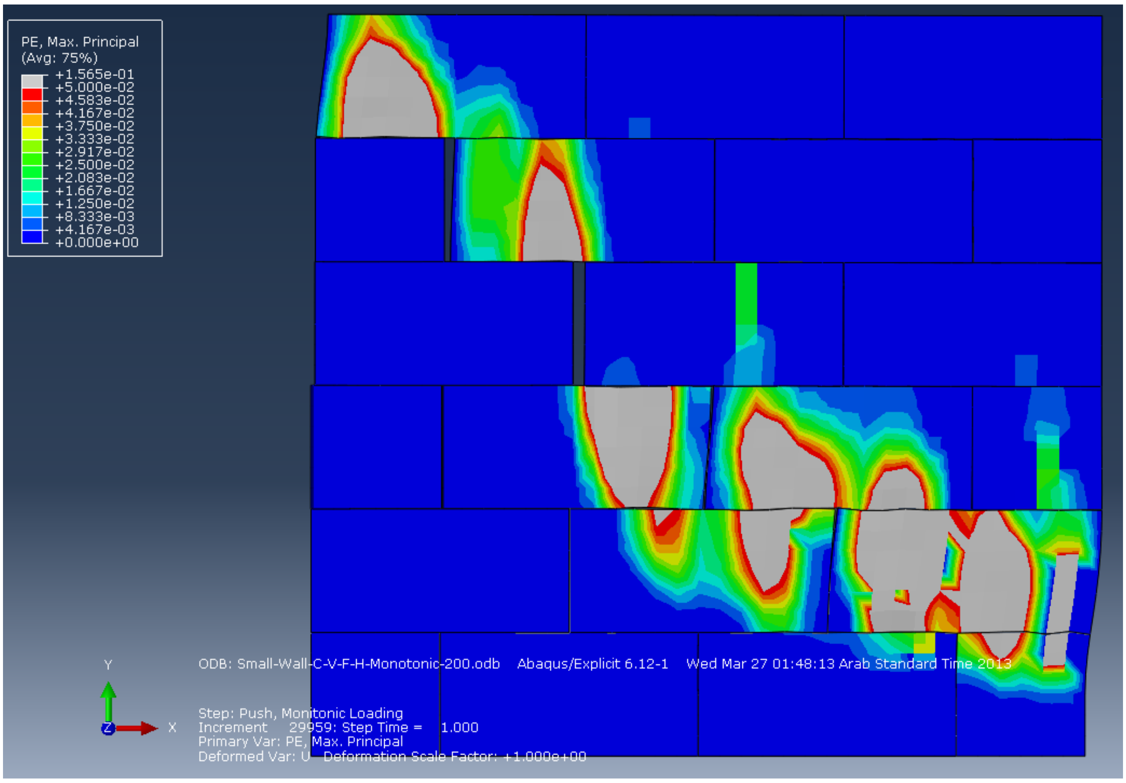

Figure 5.61 Crack Pattern in Wall Simulated Using Interface Based Approach

From Fig 5.61, it is clear that the interface approach predict the crack pattern quite well compare to experimental results. The stress contour related to this case is shown in Fig 5.62.

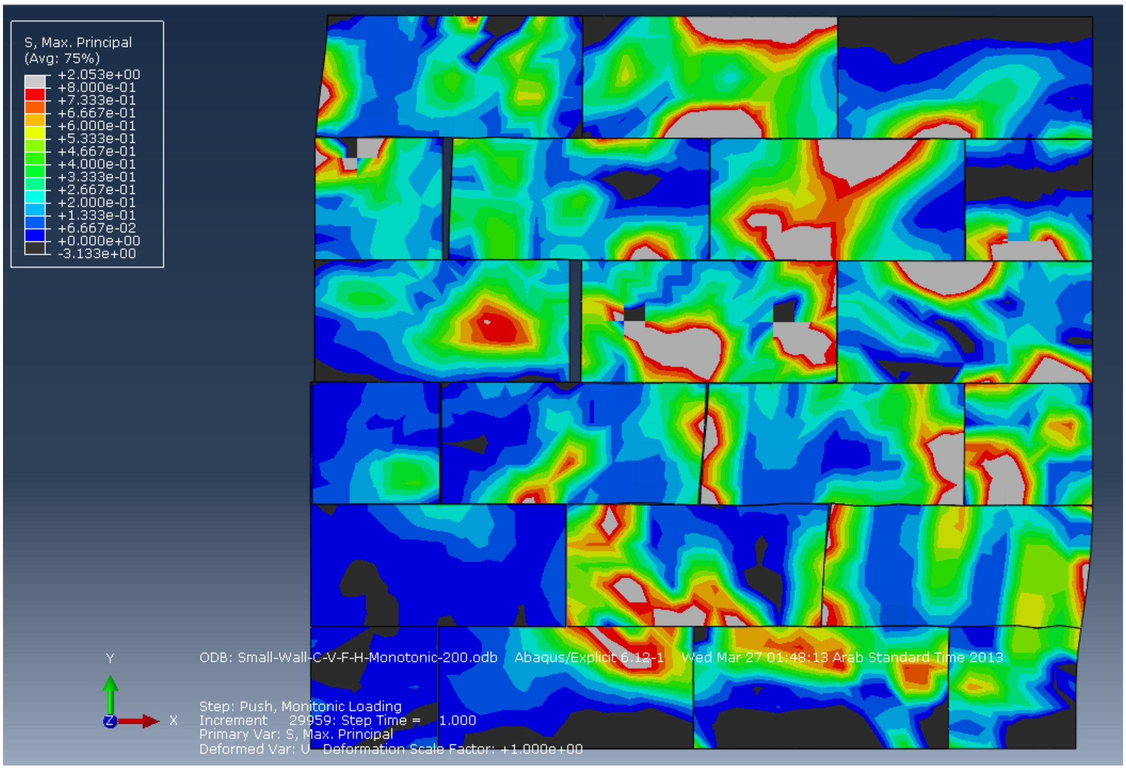

Figure 5.62 maximum principles stress (interface modeling, 1.7.0 MPa axial stress).

5.8 CFRP Strengthen

As mentioned before, masonry walls need to be strengthened and retrofitted to withstand any seismic loading that can destroy them. Several technique have been prosed to strength and retrofit that masonry walls. Among these technique is the CFRP. In this study, the effects of strengthening of walls with carbon fibre reinforced plastics (CFRP) sheets was investigated numerically to walls tested by Demir (2012). The wall strengthened with CFRP was modelled in an ABAQUS environment. Only one axial load case in which the wall is subjected to 0.5 MPa axial loading was studied.

The Plastic damage model parameters for the wall are same as those presented in Figs 5.18 and 5.19 and Table 5.6. The CFRP properties adopted in this study are shown in Table 5.16.

The CFRP sheet used in this study is a SikaWrap-230C, which is a woven carbon fiber fabric recommended for structural strengthening and improved seismic performance of masonry walls. The SikaWrap-230C uses mid-strength unidirectional carbon fibers. The laminate itself is of thickness 1 mm impregnated with Sikadur-330 epoxy. In this study, only one CFRP laminate of thickness 1.0 mm and a width of 50 mm were used. The CFRP laminate stripes were placed in both sides of the wall and extended vertical and horizontal though the whole dimensions of the wall. It should be mentioned that, the subscripts in Table 5.16 represent the principal material directions of the CFRP lamina. The wall reinforced with CFRP is shown in Fig 5.63.

Table 5.16 Proprieties of CFRP lamina.

E_1 (MPa)	E_2 (MPa)	ν_{12}	G_{12} (MPa)	G_{13} (MPa)	G_{23} (MPa)	σ_u (MPa)
28000	2800	0.25	5000	5000	5000	350

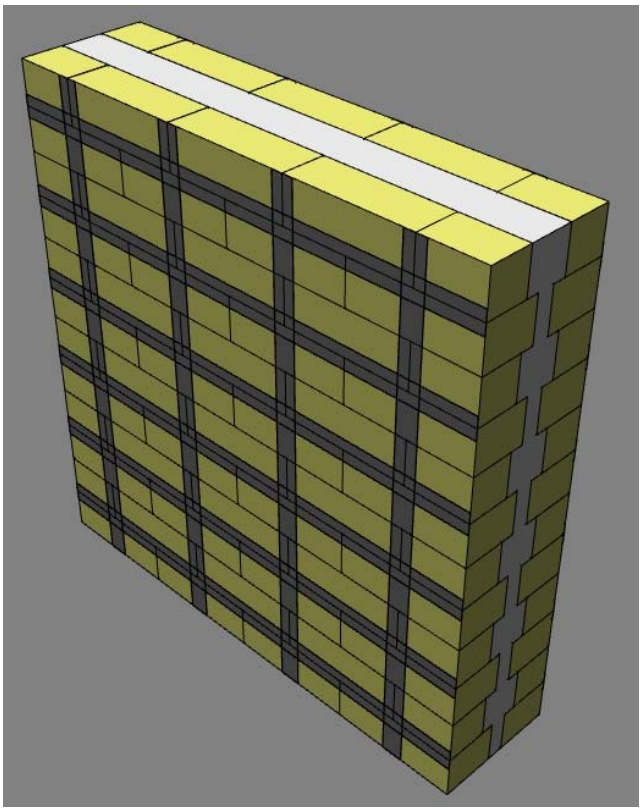

Figure 5.63 Pattern of CFRP lamina on both sides of the wall

The lateral loading was a displacement control type. This maximum transverse displacement specified in the simulation was 10 mm. Experimental and numerical results for lateral load-displacement are shown in Fig 5.64. It can be seen that the wall lateral load response was enhanced 16% as a result of reinforcing with CFRP.

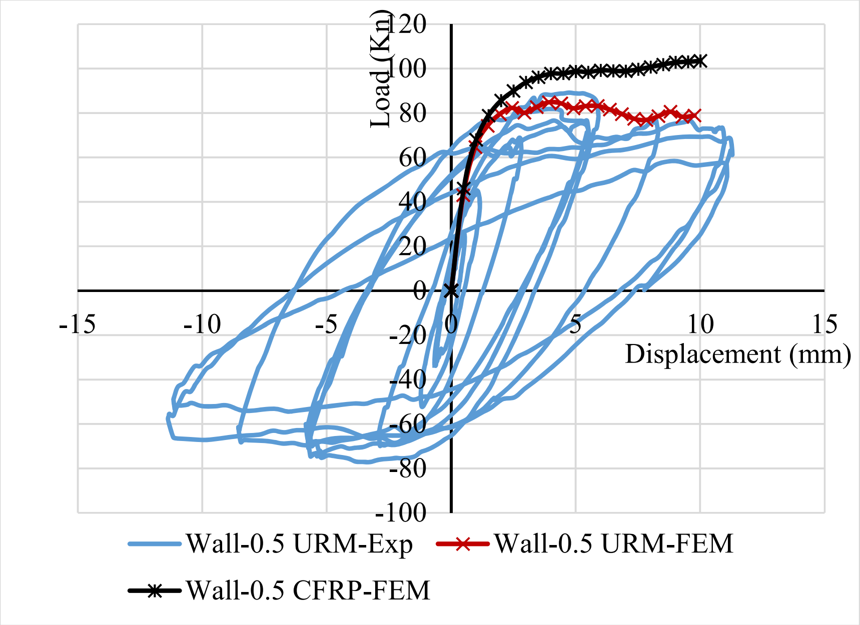

Figure 5.64 Lateral Response of the Wall with Axial Stress of 0.5 Mpa

A comparison of stress and deformation patterns (at drift=10 mm) between unreinforced and reinforced masonry walls is shown in Figs. 5.65 to 5.70. It can be seen from Figs . 5.65 to 5.70 that the failure mode of the wall has changed. In the URM case, failure resulted due to rocking and separation at lower base course levels driven by peeling tensile stress on one side, whereas the other side exhibited high compression/shear driven damage at the lower base course levels.

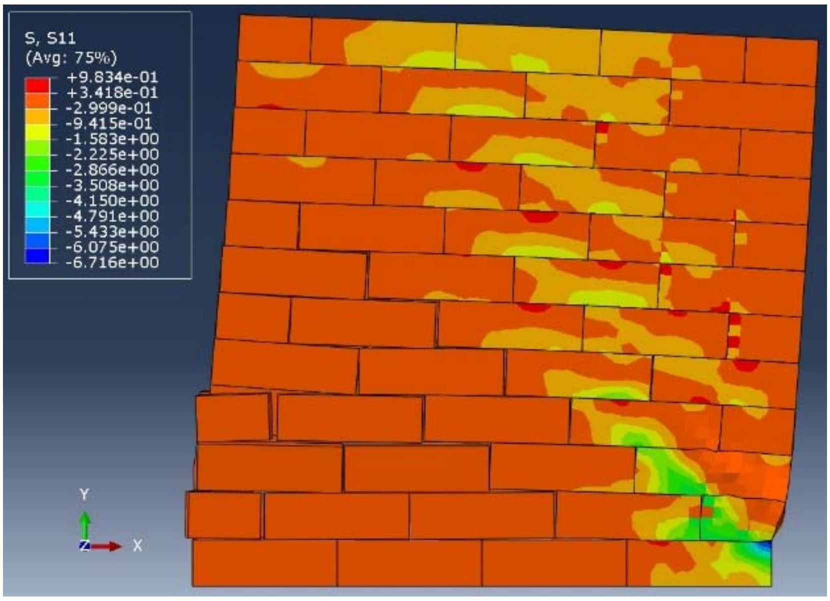

Figure 5.65 Stress (S11) in the Bricks (URM)

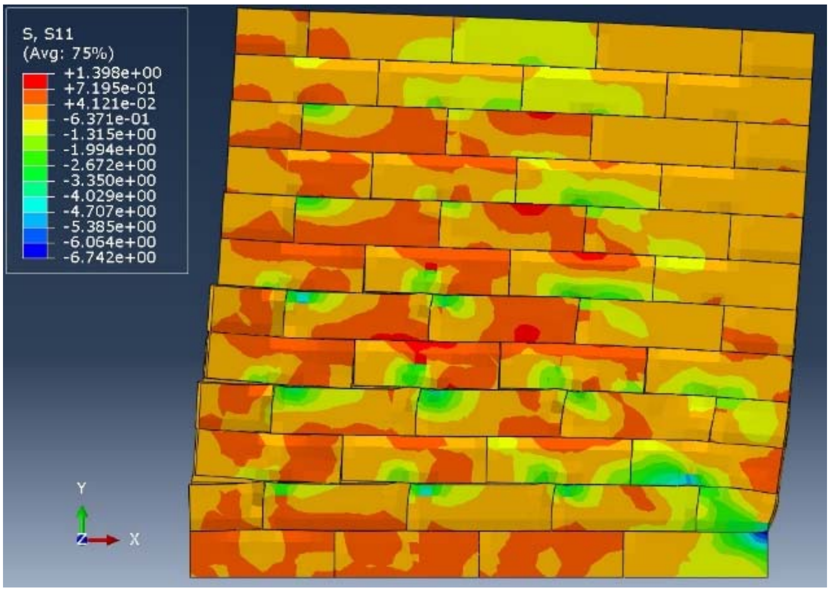

Figure 5.66 Stress (S11) in the Bricks (RM)

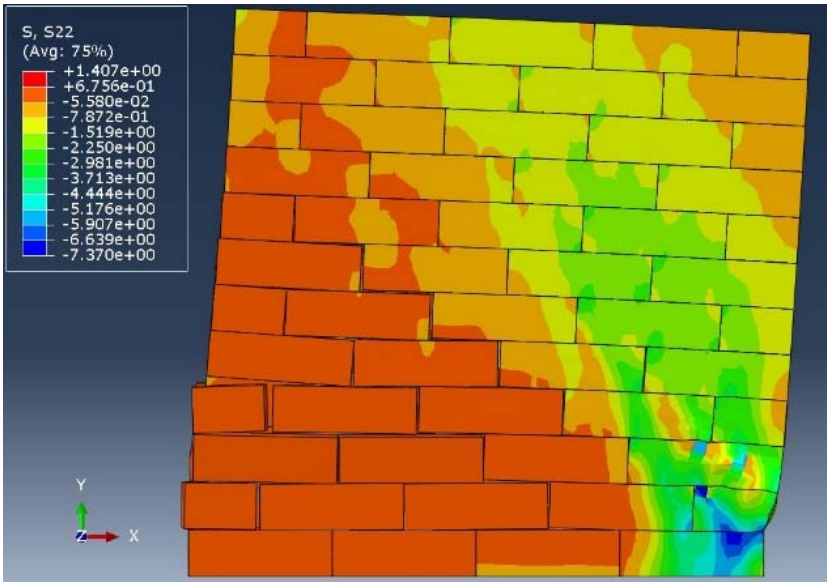

Figure 5.67 Stress (S22) in the Bricks (URM)

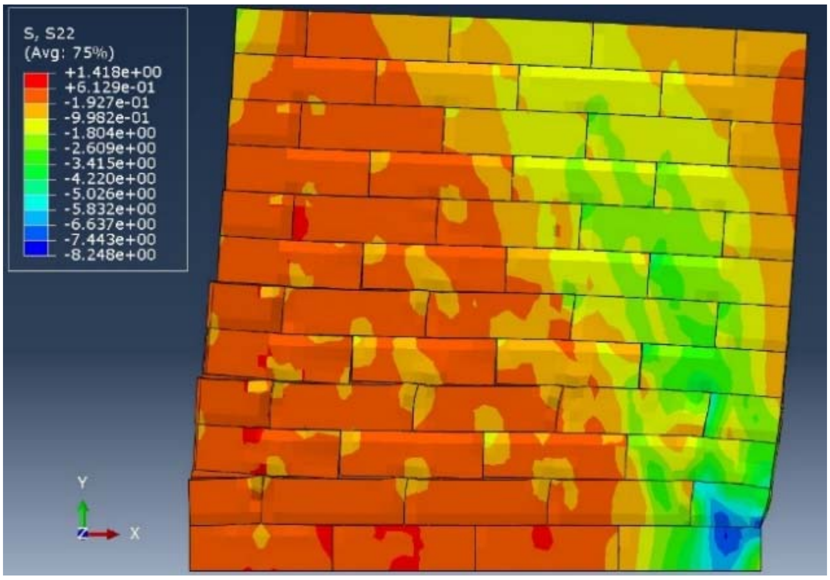

Figure 5.68 Stress (S22) in the Bricks (RM)

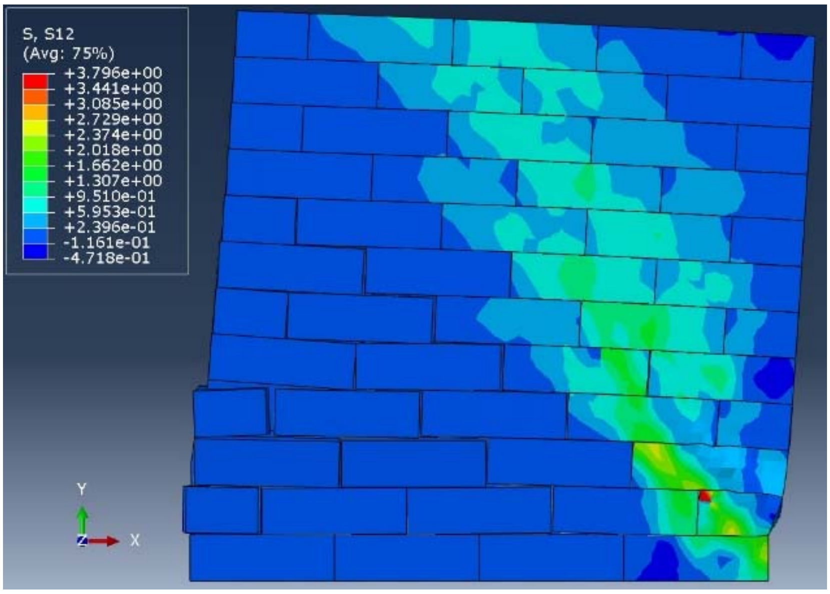

Figure 5.69 Stress (S12) in the Bricks (URM)

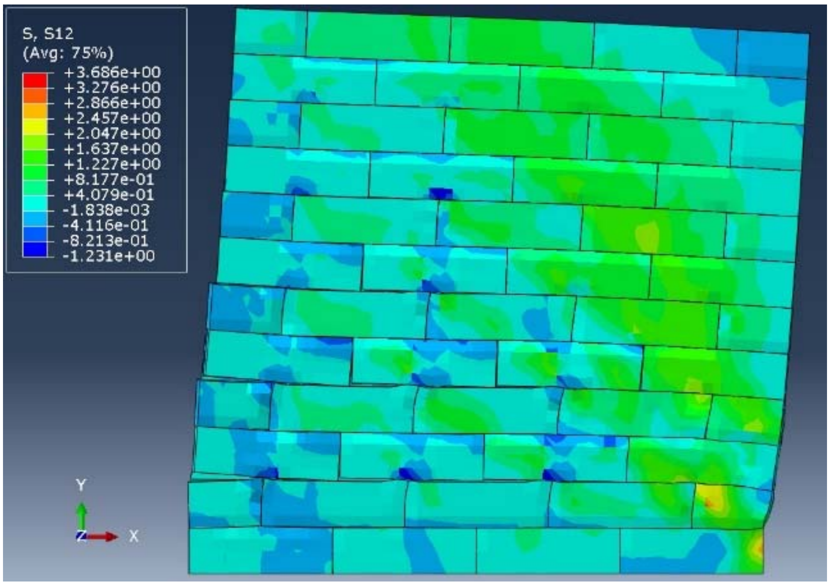

Figure 5.70 Stress (S12) in the Bricks (RM)

For the CFRP reinforced wall, it can be seen that the left side of the wall was prevented from excessive rocking and bed course separation was minimized. Head joint separation was also reduced significantly. The reinforced wall retained the integrity up to the maximum drift level. The stress distribution in CFRP in reinforced masonry wall (RM) is shown in Figs. 5.71 to 5.73. It can be seen that the CFRP effectively holds the wall together as one unit. The stress in y-direction (S22) in the left side of the wall is high which means that the CFRP is acting to reduce the phenomenon of the bed rocking.

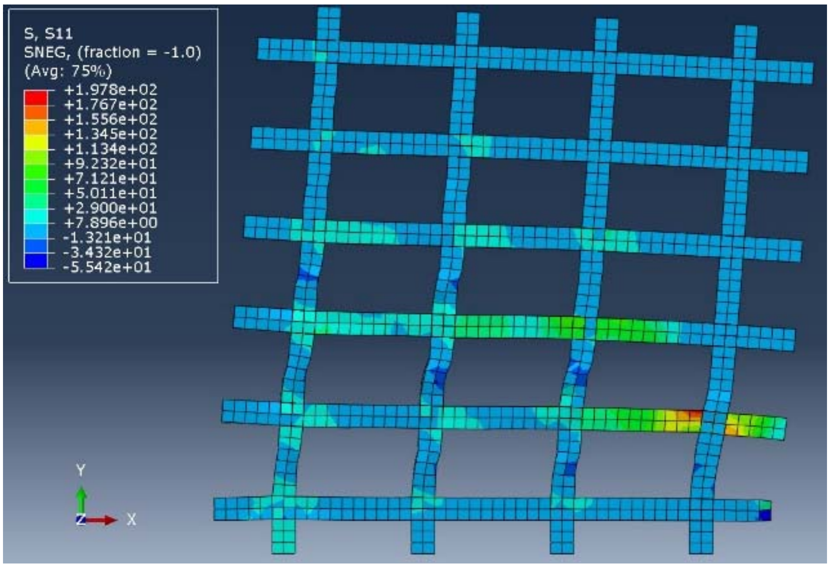

Figure 5.71 Stress (S11) in the CFRP lamina.

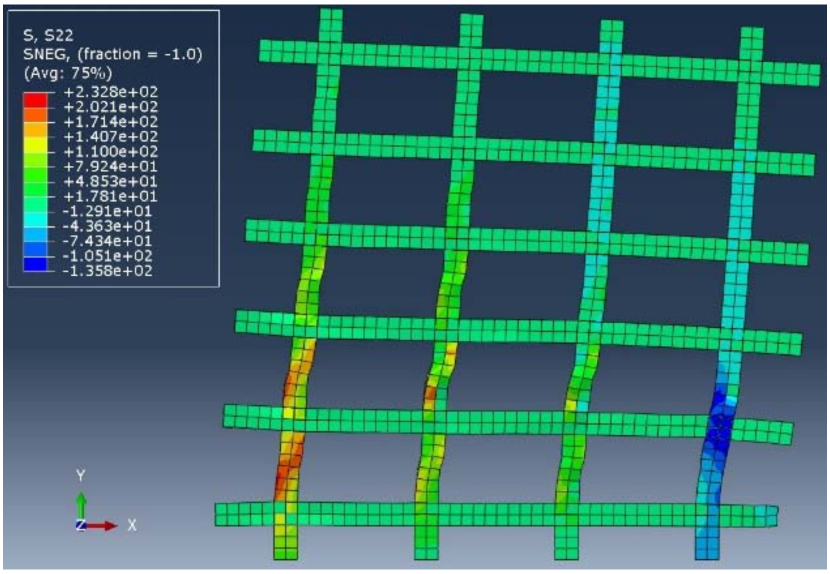

Figure 5.72 Stress (S22) in the CFRP lamina.

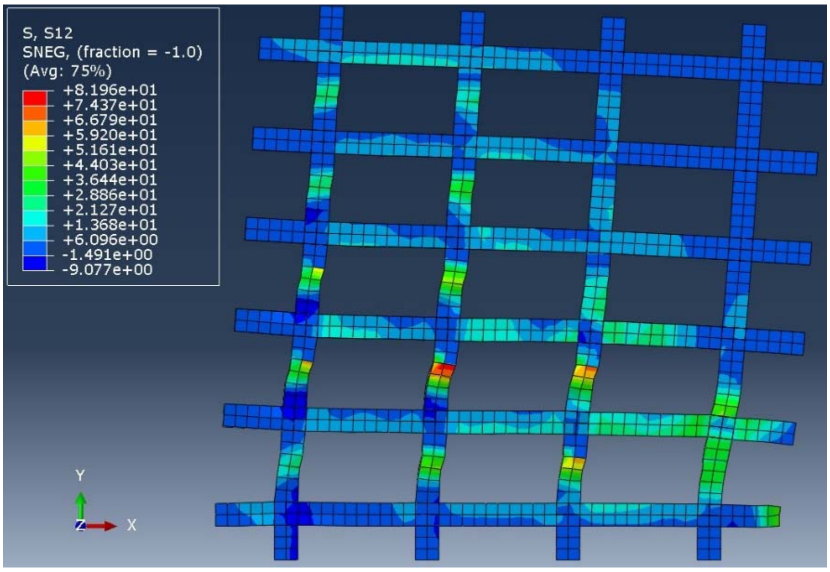

Figure 5.73 Stress (S12) in the CFRP lamina.

CHAPTER 6

RESULTS AND DISCUSSIONS

6.1 Introduction.

As shown in the previous chapters, the masonry walls are one of the importation existing structures. These type of structures are needed to be maintained and persevered against any damage that can happen to them. In Saudi Arabia there exists a rich heritage construction that spared all over the contrary.

A lot of researches have been conducted on wall subjected to combination of axial and lateral cyclic loading. Masonry reinforcement has also attracted attention by research community.

6.2 Mechanical Properties of Material.

From the experimental program presented in Chapter 4, it is clear that the sandstone materials exhibit quit good strength in compression. However the sandstone material is weak in tension which means that any masonry structure built from sandstone, are needed to be maintained against any loading that can cause high tensile stress on the material.

On the other hand, the lime mortar shows a weak response to loading in both compression and tension. This means that the lime mortar is the weakest element in the masonry construction. It was chosen to be weak in order to represent a form of heritage construction in Riyadh.

The compensation of such different material adds many complications to the problem under investigation in which this difference in material properties makes masonry wall to be highly heterogeneous structures. This adds a real challenge when performing the numerical simulation. All type of mechanical tests have been done to extract the needed material properties needed in the finite element simulation.

6.3 Prism Uniaxial Compression Test.

In this study, a compression test to sandstone prism has been carried out. It can be seen that the prism compression strength is less than the compression strength of the sandstone material. In fact, two factors affect the uniaxial strength of the masonry prism in comparison to the uniaxial strength of the masonry unit. Those two factors are:

1. Presence of weak material (Lime mortar)
2. Effect of large scale of prism compare to sandstone cylinders

It is clear that the presence of the weak material will reduce the capacity of the prism. The more the weak material in the prism, the more the reduction in the uniaxial strength of the prism. Regarding the effect of large scale, this phenomena has been observed by several researchers in which the increase in size of prism or wall leads to reduction of compression strength.

6.4 Unreinforced Sandstone Wall (Wall-1.7).

When investigating the results found from excremental test, it can be seen that the wall response to lateral load is highly affected by the level of axial force on the wall. This reason of the wall can be attributed to two factors namely: material factor and geometry factor. When loading the wall axially and by assuming no damage will accrue to the wall materials, the lateral force need to displace the wall to certain lateral displacement will increase by increasing the axial force. This axial force will increase the wall rocking response as shown in Fig 6.1.

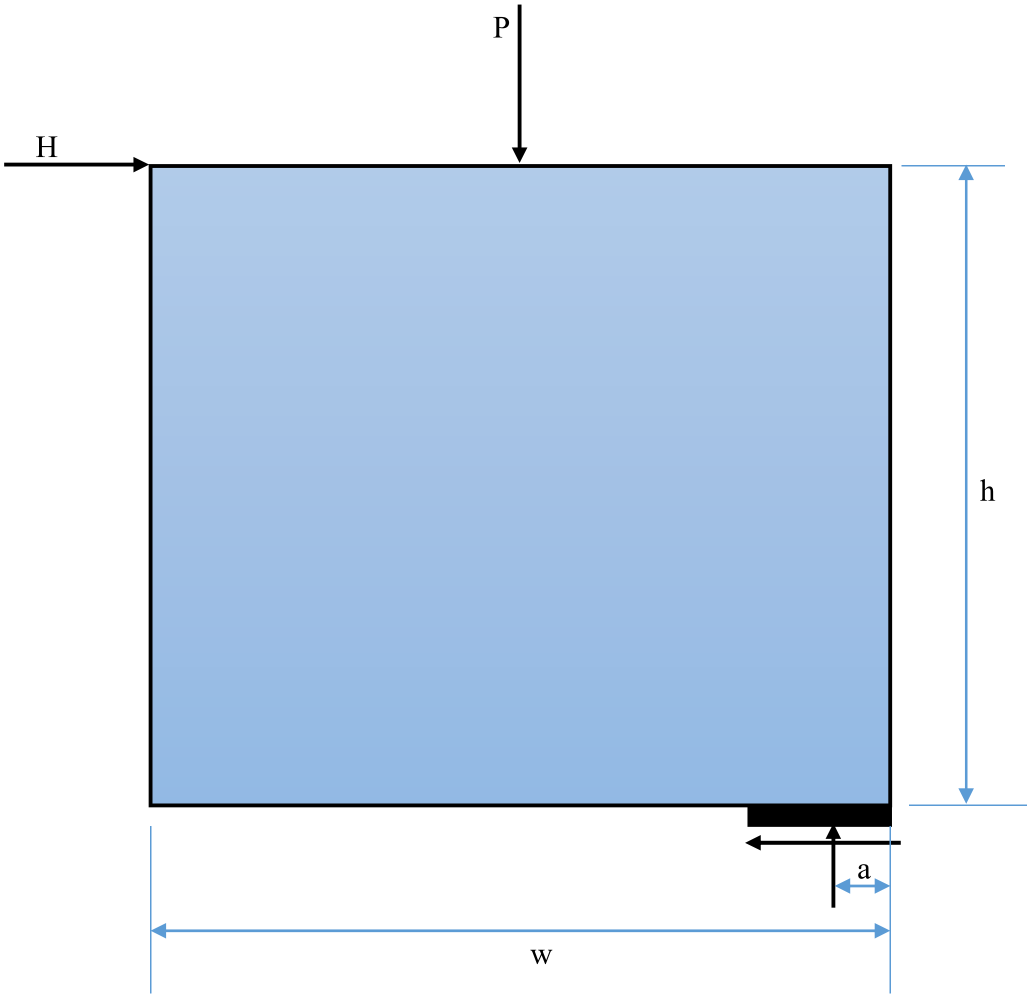

Figure 6.1 Simple Mechanistic model of wall behavior for undamaged wall.

The second factor that is also help in increasing the lateral strength of the wall is that based on wall's material strength. More confinement of the material lead to more resistance to internal stress and more resistance to internal damage. This means that the wall acts as a one unit. In particular, the resistance of the wall material will help increase the lateral resistance by enhancing the geometry factor that leads to increase the lateral strength of the wall. The geometry factor that lead to increase of lateral force as a result of increasing axial force, this factor holds up to a certain limit. After that, the internal stress lead to cracks initiation of the wall material and then relaxation of the wall and redistribution of the support reactions area. In this case, the supports will be taken by larger area compare to the case of small supporting area (Fig 6.2.).

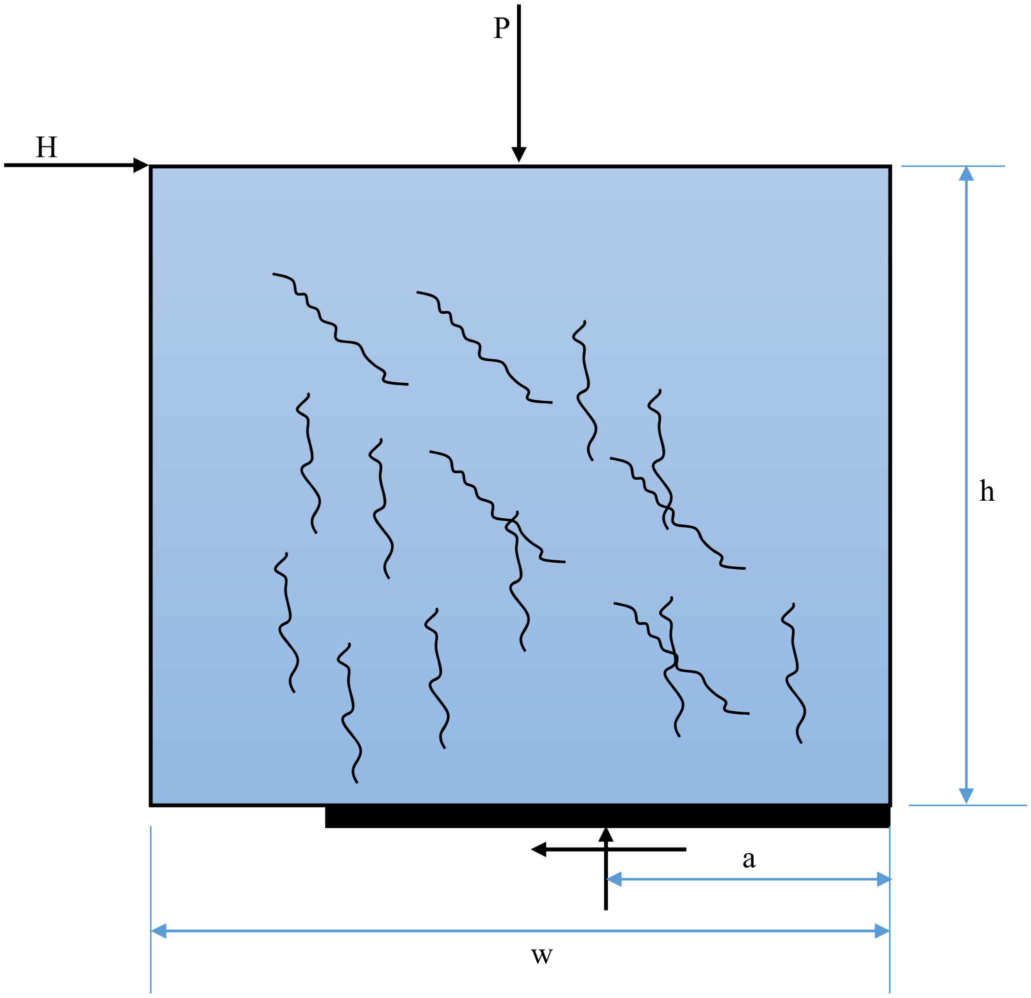

Figure 6.2 Simple Mechanistic model of wall behavior for damaged wall.

It has also to be mentioned that when analyzing the imitation and propagation of the cracks within the wall, the first crack started at the lower left corner of the wall. In this area the longitudinal or vertical stress is high compared to other points in the wall and the shear stress is zero at the outer face. This makes the maximum principal stress approach the vertical direction. However, when looking at the wall body in places where the shear stress is high (toward the middle of the wall), when the axial stress start to increase, the principal stress starts to approach 45 degree angle leading to diagonal cracks in the wall body. When the total external axial stress applied on the wall increases, the vertical stress in all points in the wall increases also in compressive , which lead to increase in the overall all lateral strength of the wall.

Regarding the cyclic behavior of the wall, it can be seen from Fig 6.3 that the wall exhibit a linear response in the first few cycles. This trend changed as the lateral load increase. Nonlinear behavior of the wall was observed and permanent deformation was recorded as seen in Fig 6.3. It is also clear that the wall stiffness reduced in the later cycles compare to the former one. This reduction can be attributed to the damage of the wall in both sandstone and lime mortar material.

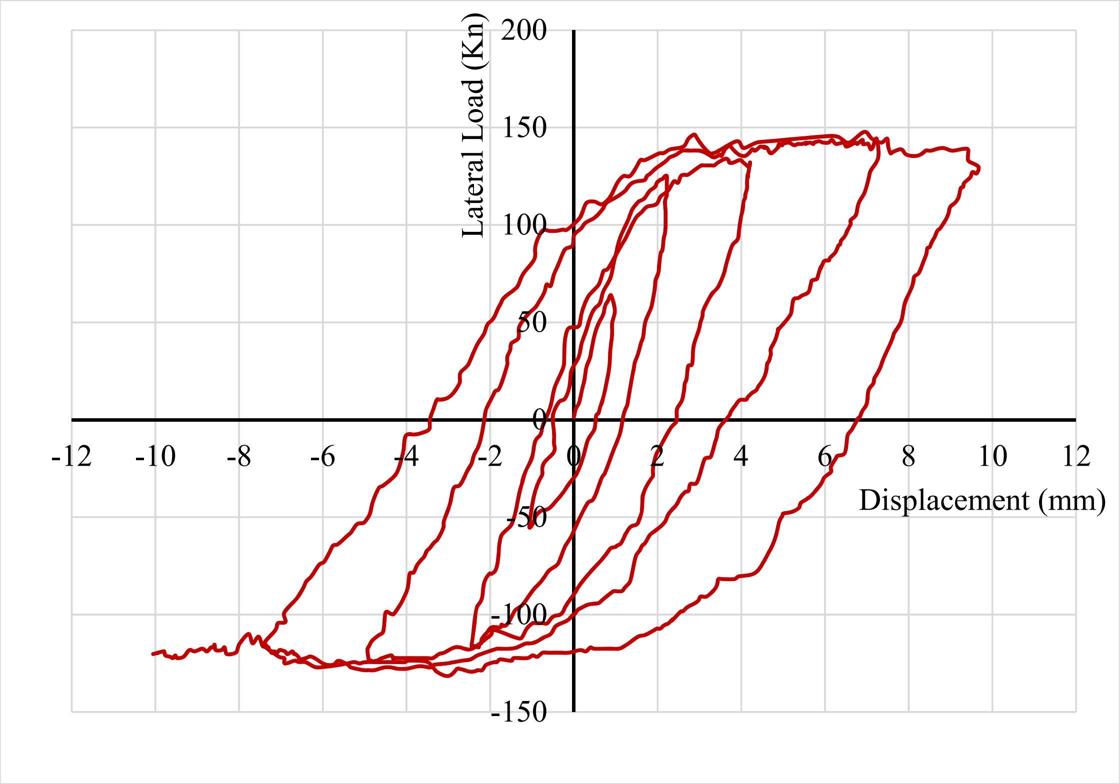

Figure 6.3 Lateral Force-Displacement response of Wall-1.7.

6.5 Numerical Simulation of Wall-1.7.

Two goals were tagged in this sturdy in terms of numerical simulation. The first one is related to simulating the response of the wall subjected to same load the have been exerted in the experimental work. The second goal is related to prediction of lateral response of the wall as a function of axial load exerted on the wall. In the first goal, several trails have been made for finding the best parameters so that perfect matching between excremental and numerical results is achieved. Several numerical simulations trails have been carried out to get those parameter. As shown in Chapter 4, the finite element simulation was quite difficulty due to the complexity of the problem under consideration. The results of numerical simulation have shown that a good match was achieved between excremental and numerical results as shown in Fig 6.4.

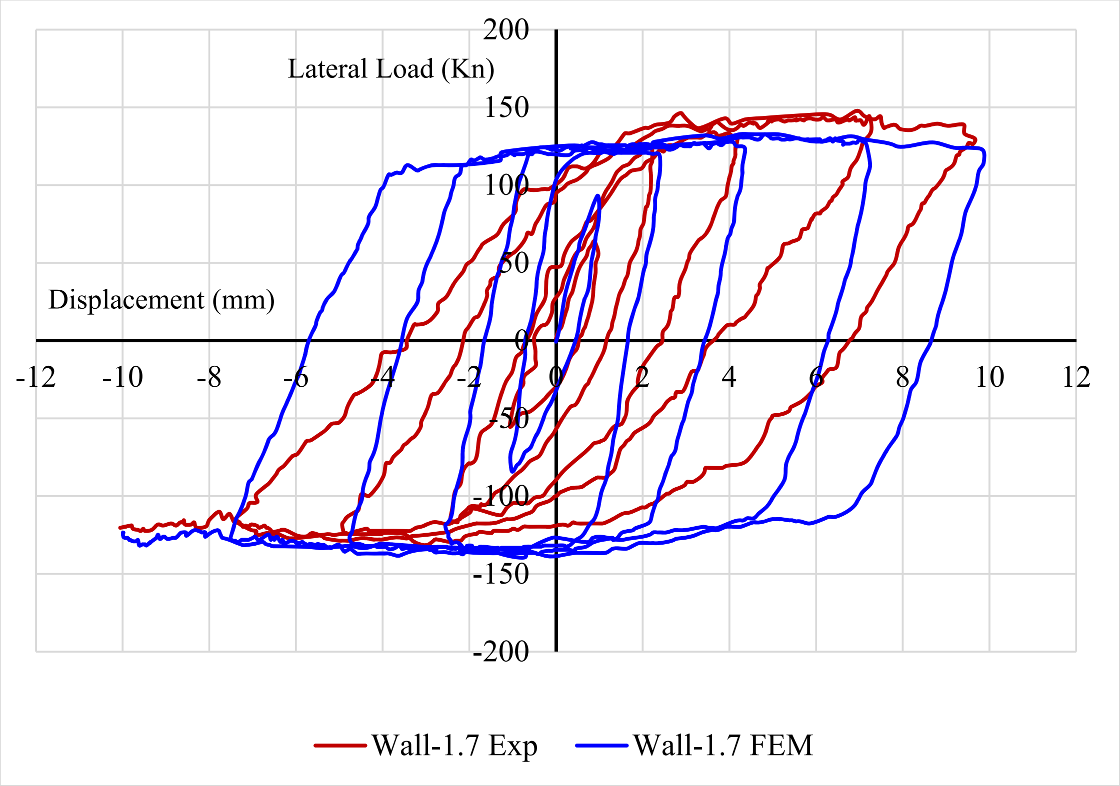

Figure 6.4 Lateral Force-Displacement response of Wall-1.7 from experimental and numerical results

As shown in Fig 6.4 theirs is a good match between the experimental and numerical results. In the first few cycles, the FEM simulation predicted stronger response of the wall compare to excremental result. However, this difference between the two results started to vanish with more cycles applied on the wall. When more cyclic excreted on the wall, the numerical simulation predicted less strength of the wall in pushing compare to experiment and predicted matching result with experiment in pulling.

The FEM numerical simulation predicted stiff response of the wall compare to the excremental results in almost all cycles. This can be attributed to the face that the bond between sandstone and lime mortar was assumed perfect bond. In reality, the de-bonding process between the two materials happened due to the lower cohesion between lime mortar and sandstone. This de-bonding intern reduce the lateral stiffness of the wall. This de-bonding can be seen in Figs 6.5-6.9

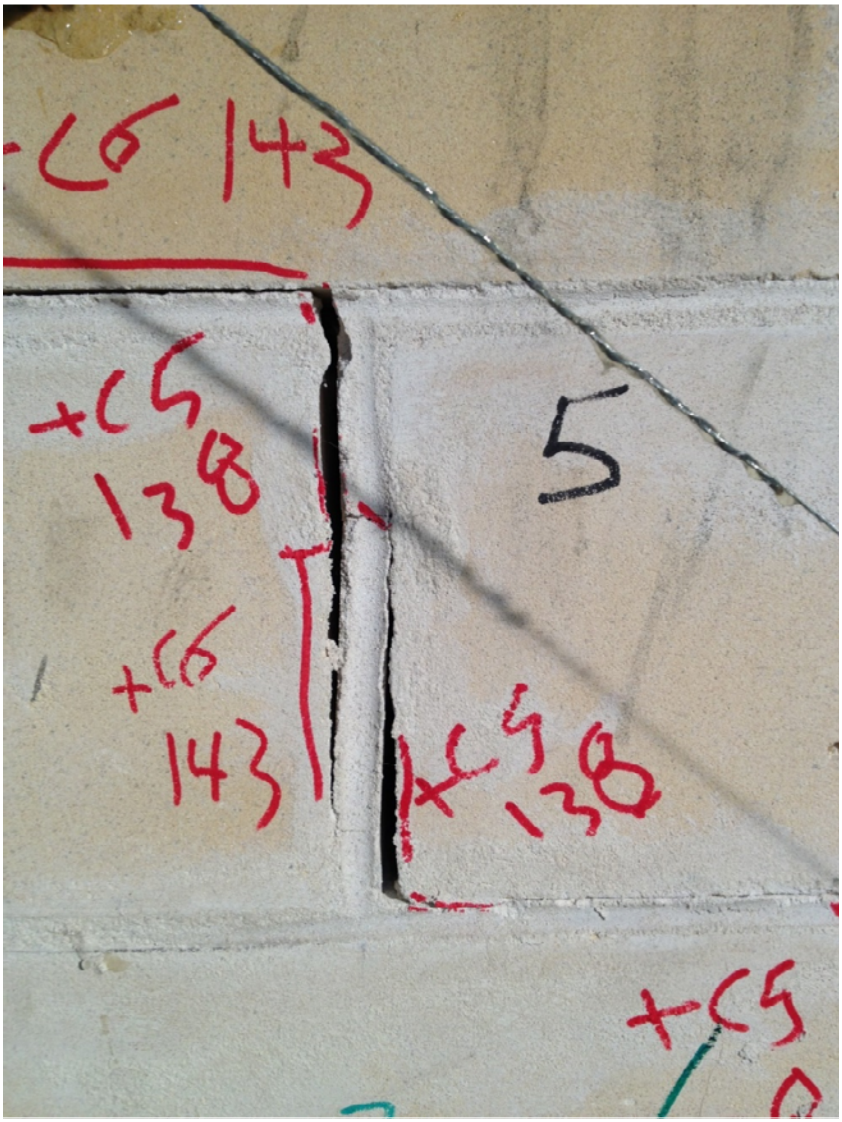

Figure 6.5 Debonding between sandstone and lime mortar.

Figure 6.6 Debonding between sandstone and lime mortar.

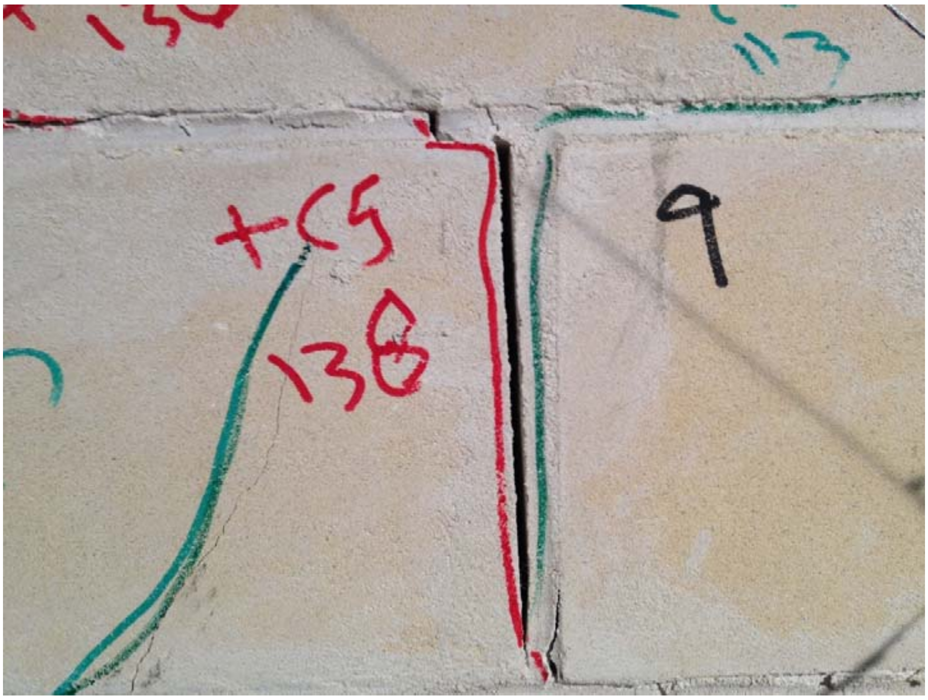

Figure 6.7 Debonding between sandstone and lime mortar.

Figure 6.8 Debonding between sandstone and lime mortar.

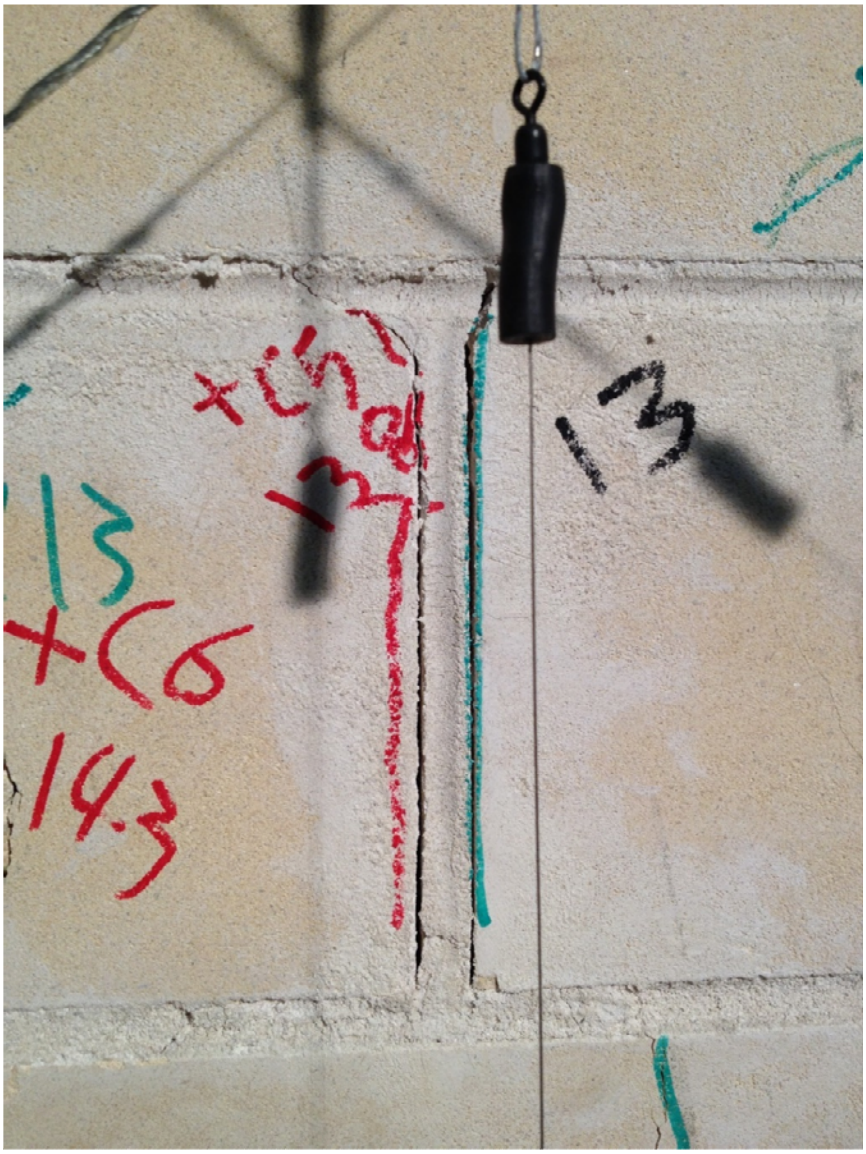

Figure 6.9 Debonding between sandstone and lime mortar.

In this study, the effect of axial force level of lateral strength was examined

As shown in the Figs 6.5-6.9, the de-bonding process between sandstone and lime mortar means that the surface interaction between the two material one of the weak points in the wall. This de-bonding may be attributed to the weakness of the lime mortar. This de-bonding process will reduce the lateral resistance of the wall and at the same time it will increase the lateral drift of the wall. This reduction in strength and increasing in drift means reduction in lateral stiffness of the wall. It has to be mentions in this regard that the de-bonding may accrue due to poor work in which the lime mortar was not placed correctly and acutely at the time of wall construction.

In the second goal, the lateral repose of the wall as a function of axial force exerted on the wall was studied extensively. Several numerical simulations have been carried out to fined such relationship. The whole range of axial force was applied on the wall and with each axial force maximum lateral strength was recorded. This analysis was done for walls tested in the study and on walls tested by other researcher. The reason for that is the ideas of getting a uniform relationship that relates lateral strength of the wall to the axial force exerted on the wall regardless of the material and dimensions of the wall. One constrain was placed in the analysis which is the aspect ratio of the wall was limited to be close to one.

The resulted universal formula shows that the wall exhibit increasing trend in lateral strength of wall as the axial force exerted on the wall increases. This relationship reverse when the axial force exerted on the wall reached a certain value which is approximately 40-60% of wall axial capacity. As mentioned earlier, this formula can be used as a guideline for engineers to predict the lateral strength of masonry wall subjected to axial and lateral forces.

This behavior of wall have been studied using the framework of mechanistic modeling by several researchers. The found results from this study have been matched with one of the mechanistic model proposed by Abrams (1992). A god matching between the data resulted from FEM approach and the results found using Abrams (1992) mechanistic approach. This matching strengthen the idea of universal behavior of walls when subjected to axial and lateral loading. This newfound property of the walls response to axial and lateral load can lead to design guidance foe engineers toward estimation of that capacity of the wall without testing them.

6.5 Experimental Results of Wall-CFRP-1.7.

As mentioned before, the CFRP was used in masonry walls for the purpose of strengthen and retrofitting damaged wall. In this study the CFRP was targeted to be used as a strengthen material in which the CFRP was add to the wall before any damage happen to the them. Two factors affecting the behavior of the CFRP when add to the structures. The first one is the CFRP strength and its stress-strain behaviors. In this factor, the CFRP is well known to be so stiff and has a high tensile capacity. This strength will go in action immediately after loading which will add a new strength to the wall.

The second facto is the bond strength between the CFRP and the wall. This is the most critical point in the interaction process between CFRP and the lime mortar. In this experiment no Debonding was noted to happen between CFRP and the wall except at the end of CFRP.

When using the CFRP lamina to strengthen the wall, a strength enhancement was observed in walls strengthened with CFRP compare to wall without any reinforcement. Cyclic lateral response of both walls is shown in Fig 6.10.

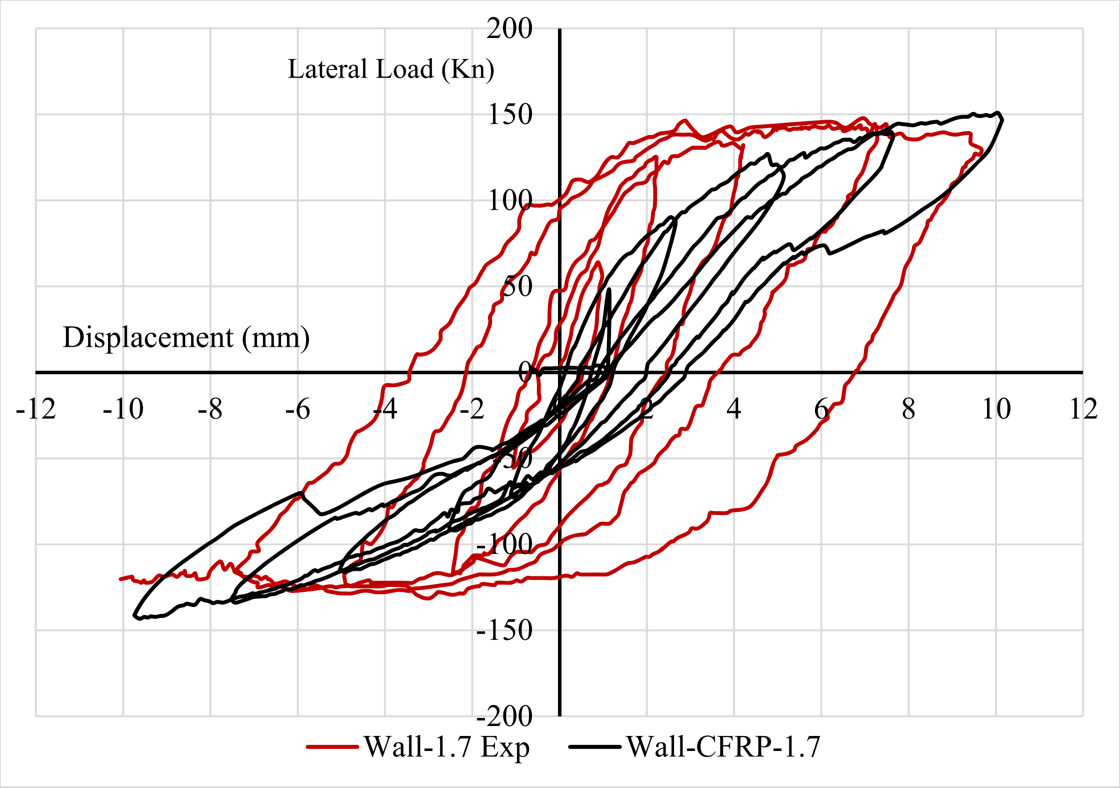

Figure 6.10 Lateral Force-Displacement response of Wall-1.7 and Wall-CFRP-1.7.

From Fig 6.10, it is clear that the wall gain an extra strength due to the presence of CFPR. The wall behaved in a stiff manner and moved as one unite. This behavior is clear in Fig 6.10 above in which when loading level is low, the wall response in stiff manner. However, when load exceed certain threshold, the response started to be more ductile. This ductility in the case of CFRP is due to the rocking behavior of the wall in which smaller lateral force is needed to drift the wall laterally.

The lateral response of the wall were enhanced compare to wall without CFRP as shown in Fig 6.10. From Fig 6.10 it is clear that less area within hysteresis has been generated in case of wall reinforced with CFRP compare to wall without CFRP. This means that less energy was dissipated which is the case due to less damage initiation within the wall body in case of Wall-CFRP-1.7 compare to Wall-1.7 where a lot of damage happened within the wall body. The stiffness of the wall is also enhanced as can be seen. Form all of that it can be seen that adding CFRP as a reinforcing material to the wall helps in increasing the lateral strength of the wall.

In this test, the wall was noted to behavior as one unite without any damage within the wall body. Cracks were noted at the first lower course of the wall within the wall passing only though the uncoated sandstone bricks as shown in Figs 6.11 and 6.12.

Figure 6.11 cracks at the lower cores of the wall.

Figure 6.12 cracks at the lower cores of the wall.

CHAPTER 7

CONCLUSIONS AND RECOMMENDATIONS

As seen in this study several experiments as well as several numerical simulations have been carried out. All of this work was aiming at better understanding the response of masonry wall to axial and lateral loading. Several studies are just completed and others are started and all of those studies are representing a great changes for adding a new things and new ideas to the world of masonry mechanics.

7.1 Conclusions

It can be concluded that sandstone material exhibits quite good strength in compression but weak strength in tension. This weakness can be compensated by using any type of reinforcement. Regarding lime mortar, this material is very weak in both tension and comparison when compared with sandstone.

It can be also concluded that walls in general exhibit good strength in the lateral action compared to out of plane action. This in-plane strength increase in a direct proportion manner with increase of axial force on the wall. The proportionality between the axial and lateral force is then reversed after certain limit in which the increase in axial force is adversely affecting the lateral strength of the wall.

This study also has demonstrated the simulation of unreinforced masonry heritage walls using an elasto-plastic damage developed by Lubliner (1989) and further extended by Lee, and Fenves (1998) and made available in ABAQUS environment. The use of this model requires certain material parameters, including the stress-plastic strain data for hardening and softening in uniaxial compression and a corresponding one for uniaxial tension in addition to other parameters related to defining the yield surface and plastic potential function. Those parameters can be found using the appropriate testes including uniaxial and biaxial tension and compression tests.

Two approaches were adopted in simulating the masonry wall. The first approach is that the wall has been treated as a strong/weak material combination, with blocks being represented as the strong material and the mortar as the weak material. The interaction between the two material was assumed to be perfect bond.

The results for interaction of lateral strength of the wall to the axial pre-compression show that masonry walls behave in a systematic manner to in-plane loading, regardless of wall size, patterns, and wall materials. Based on output of FEM simulations, an interactive response equation has been proposed for use in masonry walls of aspect ratio close to 1.0.

Generally, when axial stress exerted is low, the wall tends to fail in rigid type modes of sliding and rocking. However, when axial stress is a slightly higher, the wall tends to fail by head/bed joints opening and mortar cracking. This mode of failure is common when dry contact system is adopted or when the mortar strength is weak.

For walls with moderate to high axial stress, cracks start to initiate within the bricks themselves due to diagonal tension in the bricks exceeding the tensile strength of the bricks. These cracks are also often complemented by staggered step cracking in head and bed joints, especially with wet mortar construction.

For cases where the axial load becomes excessive, the lateral strength of the walls is severely compromised. In this case, the wall is pre-damaged due to presence of cracks within the wall as a consequence of high pre-compression, and failure on lateral loading of the wall is primarily due to extension of existing cracks in shear-compression.

It can be also concluded that, Concrete Damage mechanics approach implemented in ABAQUS can be used efficiently to model masonry wall structures. The continuum-based technique adopted for both sandstone and lime mortar results in good agreement between experimental and numerical load-deflection response of the wall, although fine mesh is required so that the aspect ratio of the elements are within the acceptable range. The mode of failure and development of cracks in the wall were also captured with significant accuracy using the plastic-damage model.

The second approach used in simulating the behavior of the masonry wall inclusion of interface elements between masonry blocks. The used of interface element for numerical simulation is also one of the possible approach that can be used to tackle the problem. The parameters needed for modeling using interface elements are found based on the mechanical properties of the lime mortar. The lime mortar is geometrically not included in the model, which does not allow seeing the damage within the mortar layers. This approach however, reduces the fineness of the finite element mesh and a significant reduction in simulation time without affecting the response of the wall under applies loads. The interface model in ABAQUS requires data including the fracture energy in normal and tangential directions, traction-separation curves in normal and tangential directions, and coefficient of friction. These parameters can be found using the appropriate tests including tensile and direct shear test.

It is found that the interface approach is very efficient when the cohesive strength of layers that connects the components of the structure is high. This means that the fracture energy needed to create the crack is high. This interface element would be very efficient in case of simulation for CFRP attached to the wall. Using interface elements, it is observed that the bed joints is clearly acting under the friction force whereas the head joints act under peeling action. This hybrid action of bed and head joints gives better results in terms of cracks and failure patterns. The relation between lateral strength and lateral displacement was also observed to be better.

Using CFRP is one of the major methods of strengthening and retrofitting the masonry wall. The only thing that has to be taking into account is the bonding strength between CFRP and masonry wall. The use of CFRP enhanced the lateral strength of the wall and also the lateral stiffness of the wall. CFRP helps to eliminate premature rocking failure of the wall, and allows for the mobilization of the entire wall continuum in participation of resistance to the applied forces.

From the FEM simulation, it can be concluded that the CFRP sheets have a pronounced effect in enhancing the strength and integrity of the wall. The lateral strength capacity is increased and also the failure mode changes. Adoption of suitable configuration of the CFRP has been shown to reduce premature failure driven by rocking and separation at lower base course levels, and allows for greater mobilization and participation of the entire wall in resisting the applied lateral load. The numerical model for the CFRP reinforced heritage wall shows that with proper configuration of the CFRP the failure mode of the unreinforced wall can be modified so as to enhance the strength and integrity of the wall.

7.2 Engineering Guidelines for Assessment of Heritage Structures

For typical heritage stone masonry building requiring strengthening or retrofitting, the following approach can be adopted.

- Identification of material properties
- Evaluation axial load on the walls of the existing structure.
- Development of finite element model of the wall and its simulation using plastic damage model the existing level of applied load and the experimentally determined material properties.
- Based on the mode of failure and cracking patterns observed in the finite element simulation, a strategy for strengthening or retrofitting the walls can be developed using CFRP or any other strengthening technique
- Finite element simulation of strengthened walls using plastic damage model to ascertain the enhancement in the load capacity of the masonry walls.
- The procedure for strengthening the wall be determined numerically and implemented at job site.

7.3 Recommendations for Future Work.

It can be seen that, there are several things that have to be investigated as future work. Some of these topics can be summarized as follows:

- Uniaxial compression tests have also to be conducted on larger sizes of wall prism to find out the exact effect of size on the uniaxial strength of the prisms. This will help predicting axial capacity of large wall sizes.

- Monotonic loading experimental study has to be conducted on walls using the full range of axial force staring with zero axial force up to the full axial capacity of the wall. In each axial force, the lateral strength has to be found so that the interaction between axial force and lateral strength can be extracted experimentally.

- Regarding the strengthen techniques; investigation has to be done on different pattern of CFRP laminate sheets. Another possible sturdy is using other type of material for strengthen purposes.
- Numerical investigation can has to be conducted one walls strengthen with CFRP and also on walls retrofitted with CFRP. In fact, numerical simulation of damaged wall retrofitted with CFRP is quit challenging as the wall experiences previous damage prior to placemen of CFRP.
- Experimental characterization of the out-of-plane behavior of sandstone masonry walls.
- Investigating different bricks pattern and different brick sizes is also one of the possible future work.
- When looking at the plastic damage model developed by Lubliner (1989) and further extended by Lee, and Fenves (1998), the two damage parameters (compression damage and tension damage) are assumed to be a scalar quantities in which they are similar at any direction. In reality, the compression damage can be accurately assumed as a scalar quantity because the partial crush in the microstructure of concrete due to loading in one direction is defiantly 100% affecting the compression capacity in the other directions. Based on that, the assumption of compression

damage parameter to be scalar is valid however, the tension damage cannot be accurately assumed to be a scalar quantity in which that when loading in one direction, the damage evolved in the loading direction is not really affecting the other directions. Based on that, the damage quantity in tension has to be assumed as a vector in which each one of the three principle directions has to have its own tension damage parameters.

- Investigating the interaction relation between lateral and axial force of walls with aspect ratio greater and less than 1.0.

APPENDIX

A.1 Stain Gauges Details

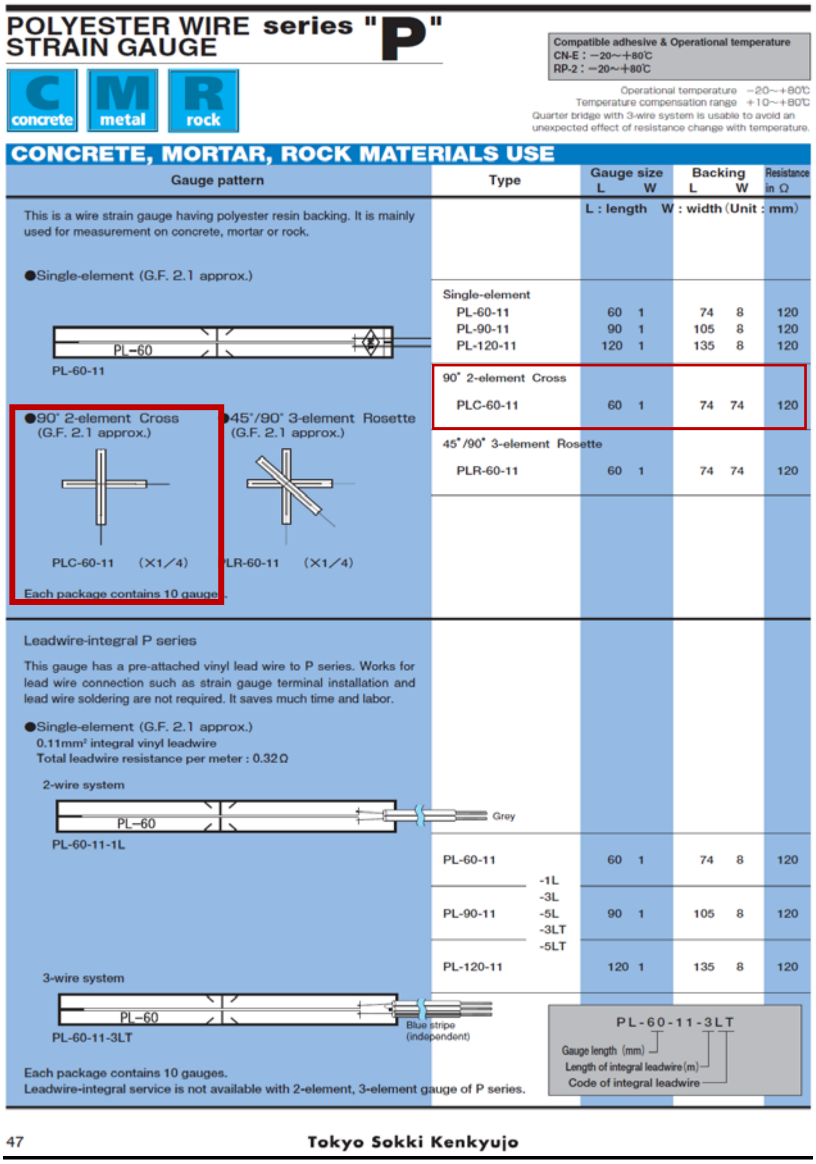

POLYESTER WIRE series "P" STRAIN GAUGE

Compatible adhesive & Operational temperature
CN-E : −20∼+80℃
RP-2 : −20∼+80℃

Operational temperature −20∼+80℃
Temperature compensation range +10∼+80℃
Quarter bridge with 3-wire system is usable to avoid an unexpected effect of resistance change with temperature.

CONCRETE, MORTAR, ROCK MATERIALS USE

Gauge pattern

This is a wire strain gauge having polyester resin backing. It is mainly used for measurement on concrete, mortar or rock.

●Single-element (G.F. 2.1 approx.)

PL-60-11

●90° 2-element Cross (G.F. 2.1 approx.)

PLC-60-11 (×1/4)

●45°/90° 3-element Rosette (G.F. 2.1 approx.)

PLR-60-11 (×1/4)

Each package contains 10 gauges.

L : length W : width (Unit : mm)

Type	Gauge size L	Gauge size W	Backing L	Backing W	Resistance in Ω
Single-element					
PL-60-11	60	1	74	8	120
PL-90-11	90	1	105	8	120
PL-120-11	120	1	135	8	120
90° 2-element Cross					
PLC-60-11	60	1	74	74	120
45°/90° 3-element Rosette					
PLR-60-11	60	1	74	74	120

Leadwire-integral P series

This gauge has a pre-attached vinyl lead wire to P series. Works for lead wire connection such as strain gauge terminal installation and lead wire soldering are not required. It saves much time and labor.

●Single-element (G.F. 2.1 approx.)
0.11mm² integral vinyl leadwire
Total leadwire resistance per meter : 0.32Ω

2-wire system

PL-60-11-1L

3-wire system

PL-60-11-3LT

Type		Gauge size L	Gauge size W	Backing L	Backing W	Resistance in Ω
PL-60-11	-1L -3L -5L -3LT -5LT	60	1	74	8	120
PL-90-11		90	1	105	8	120
PL-120-11		120	1	135	8	120

PL-60-11-3LT
Gauge length (mm)
Length of integral leadwire (m)
Code of integral leadwire

Each package contains 10 gauges.
Leadwire-integral service is not available with 2-element, 3-element gauge of P series.

47 Tokyo Sokki Kenkyujo

Figure A.1 Details of PLC-60-11 cross type strain gauges

A.2 Stress Contour in The Cyclic Loading of Wll-1.7.

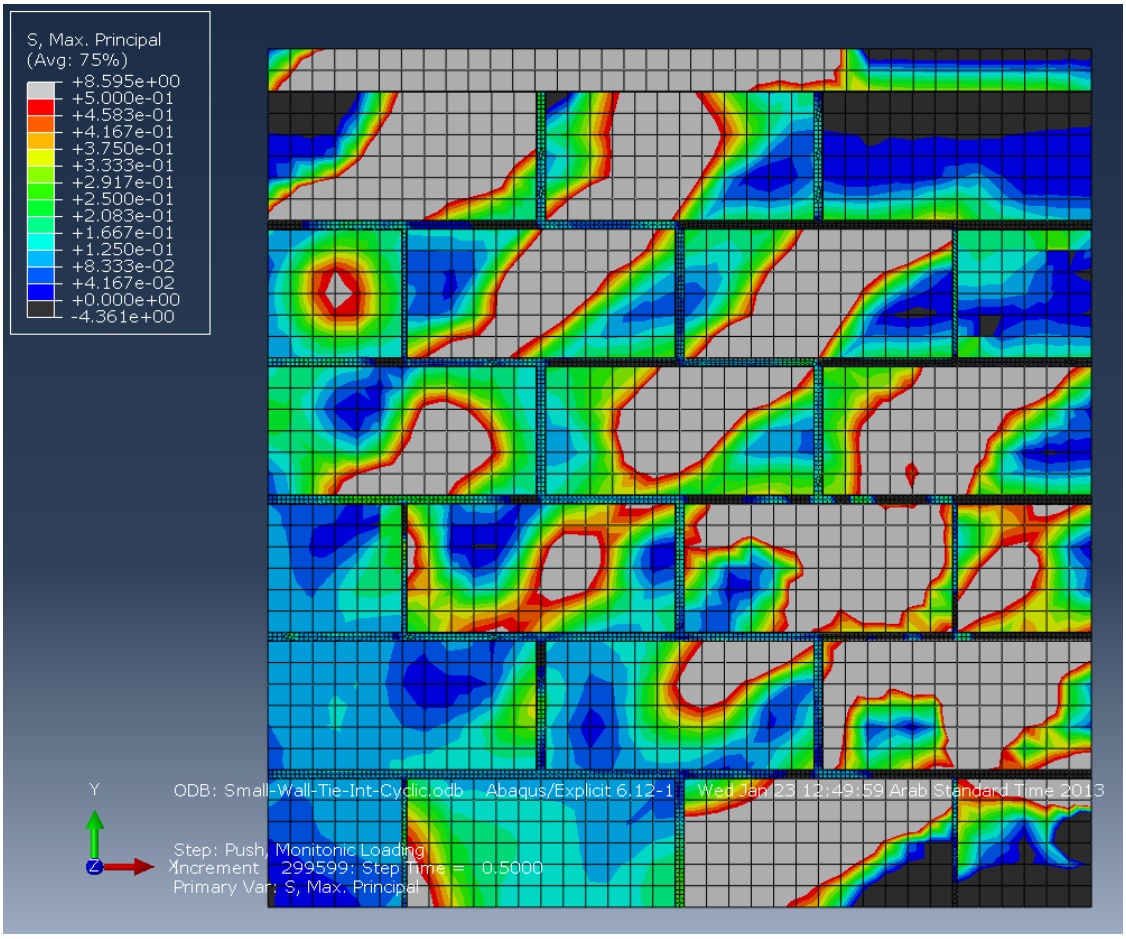

Figure A.2 Max principle Stress distribution at 0.5 time of lateral displacement (Push, first cycle)

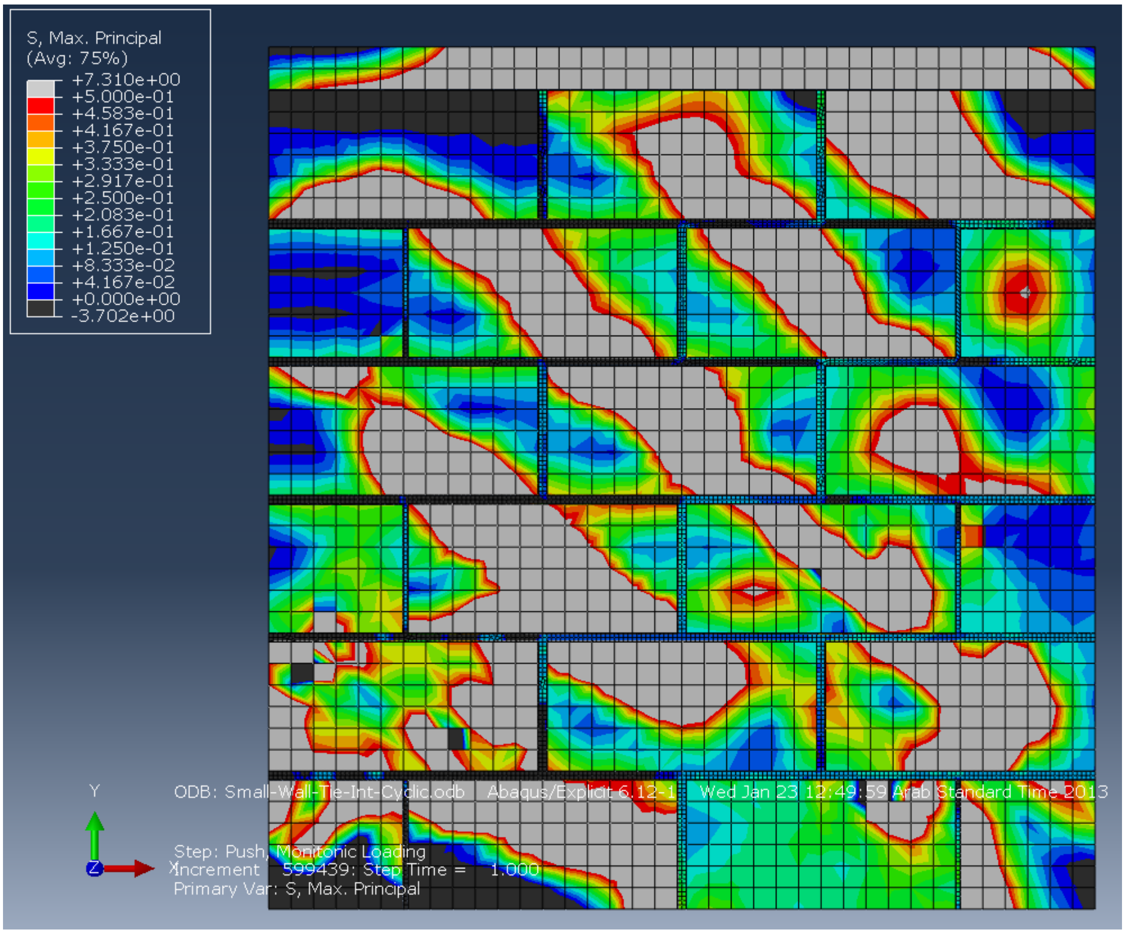

Figure A.3 Max principle Stress distribution at 1.0 time of lateral displacement (Pull, first cycle)

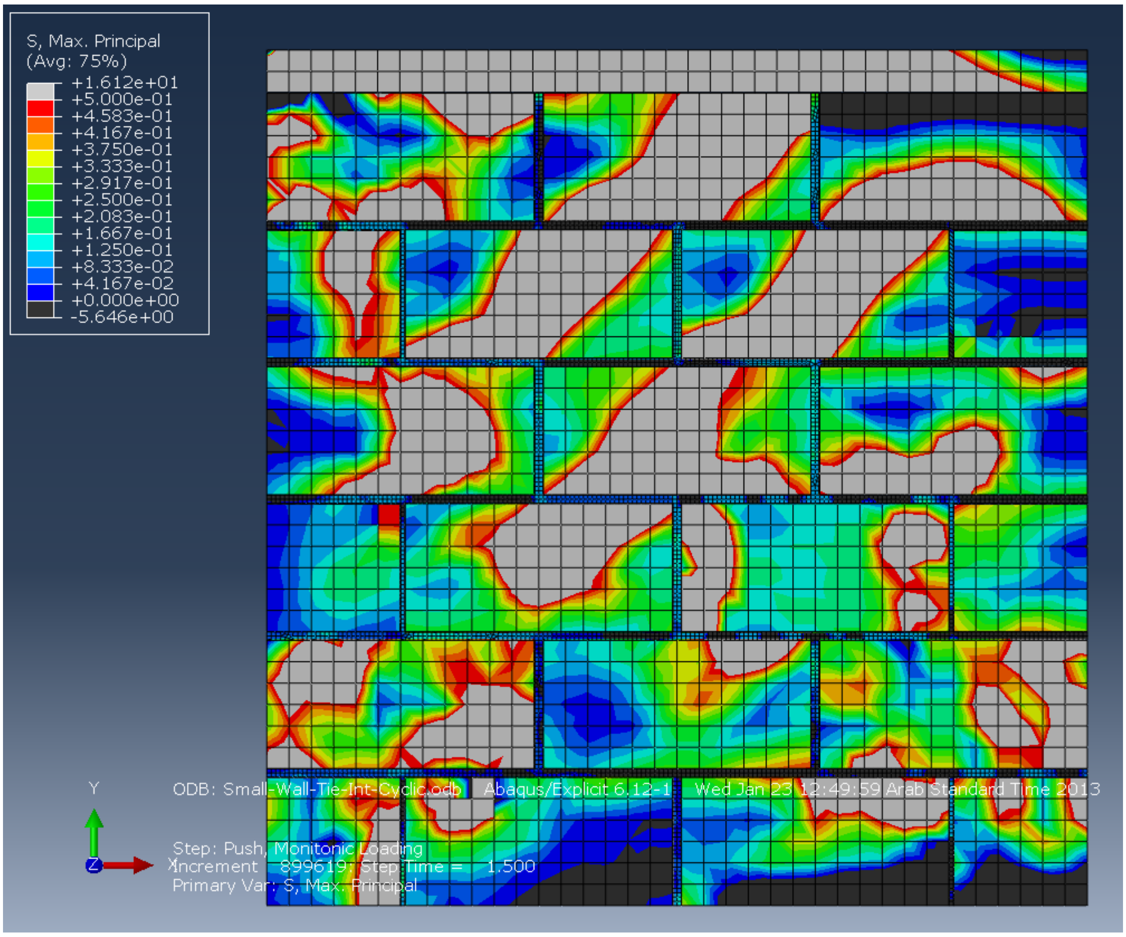

Figure A.4 Max principle Stress distribution at 1.5 time of lateral displacement (Push, second cycle)

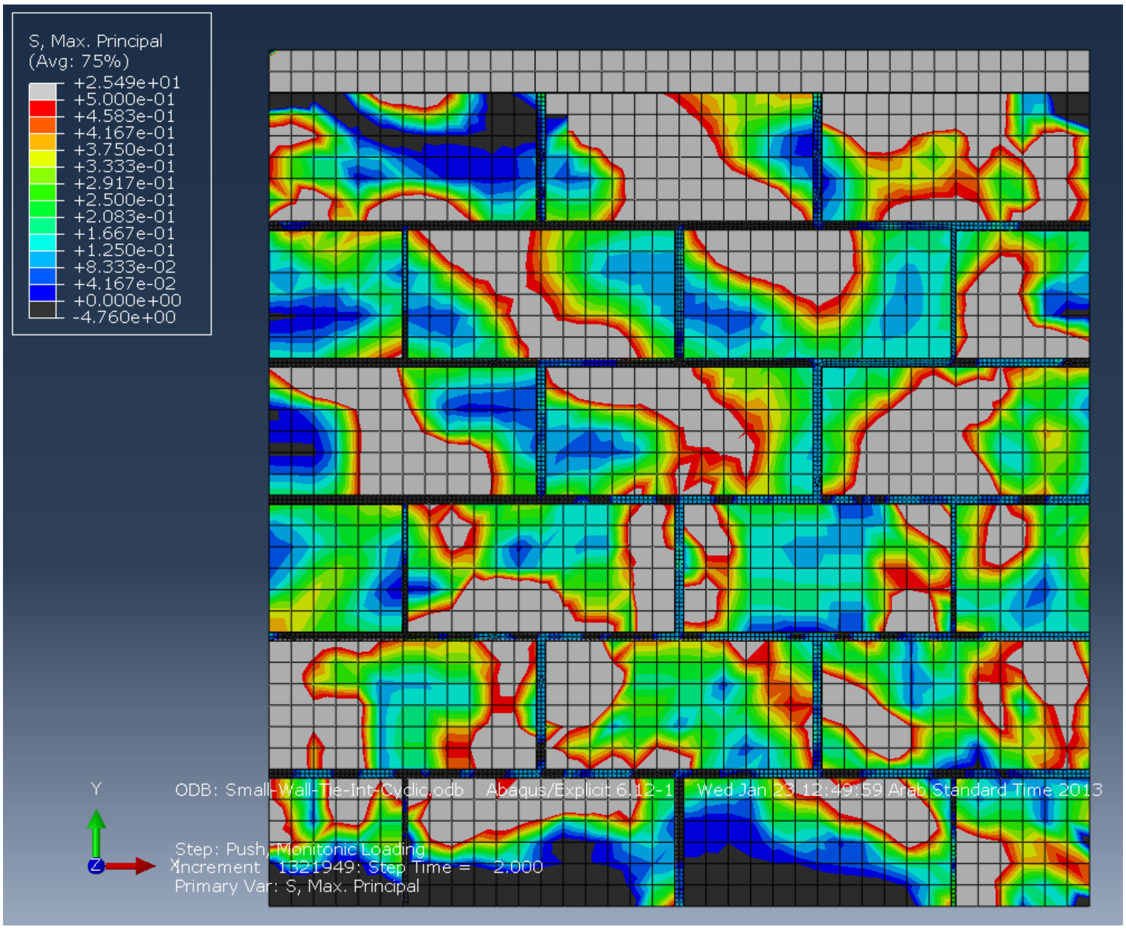

ODB: Small-Wall-Tie-Int-Cyclic.odb   Abaqus/Explicit 6.12-1   Wed Jan 23 12:49:59 Arab Standard Time 2013

Step: Push, Monitonic Loading
Increment   1321949: Step Time =   2.000
Primary Var: S, Max. Principal

Figure A.5 Max principle Stress distribution at 2.0 time of lateral displacement (Pull, second cycle)

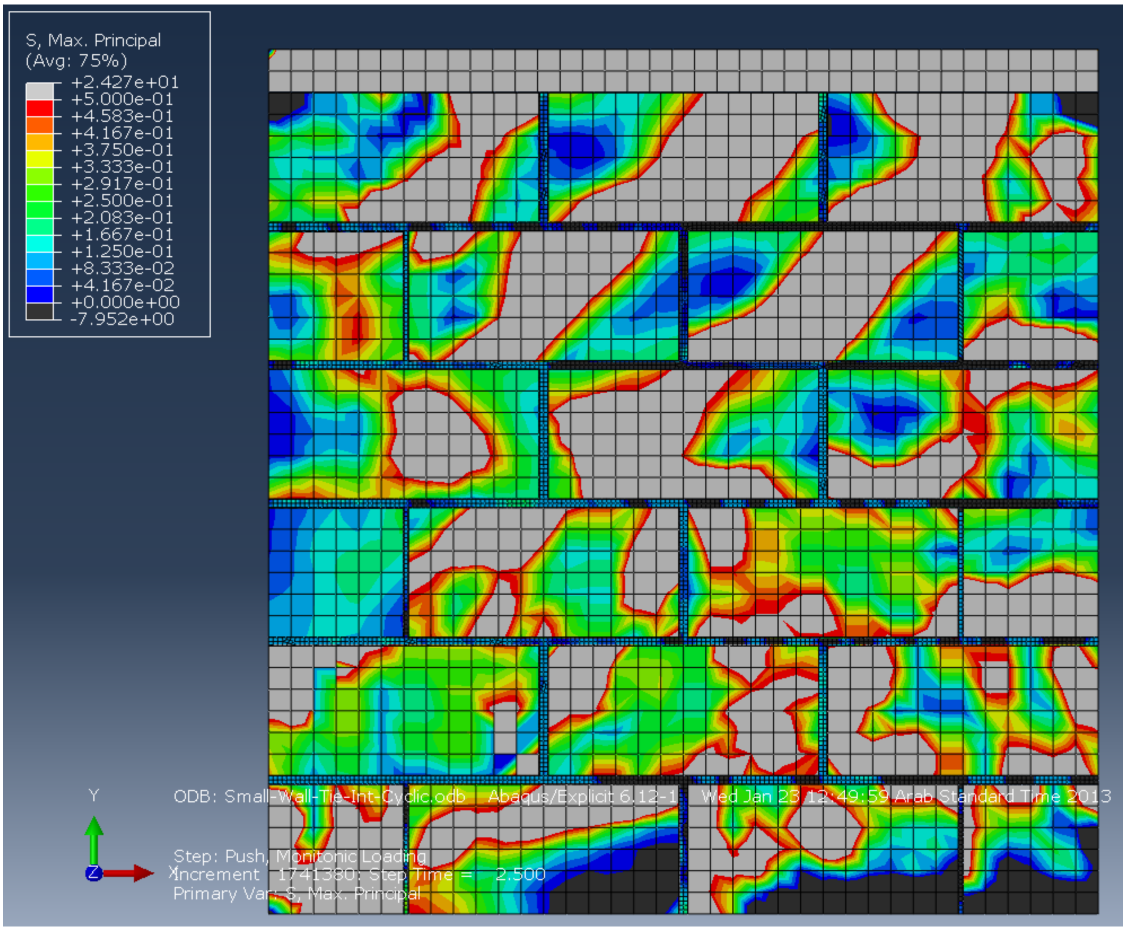

ODB: Small-Wall-Tie-Int-Cyclic.odb   Abaqus/Explicit 6.12-1   Wed Jan 23 12:49:59 Arab Standard Time 2013

Step: Push, Monitonic Loading
Increment   1741380: Step Time =   2.500
Primary Var: S, Max. Principal

Figure A.6 Max principle Stress distribution at 2.5 time of lateral displacement (Push, Third cycle)

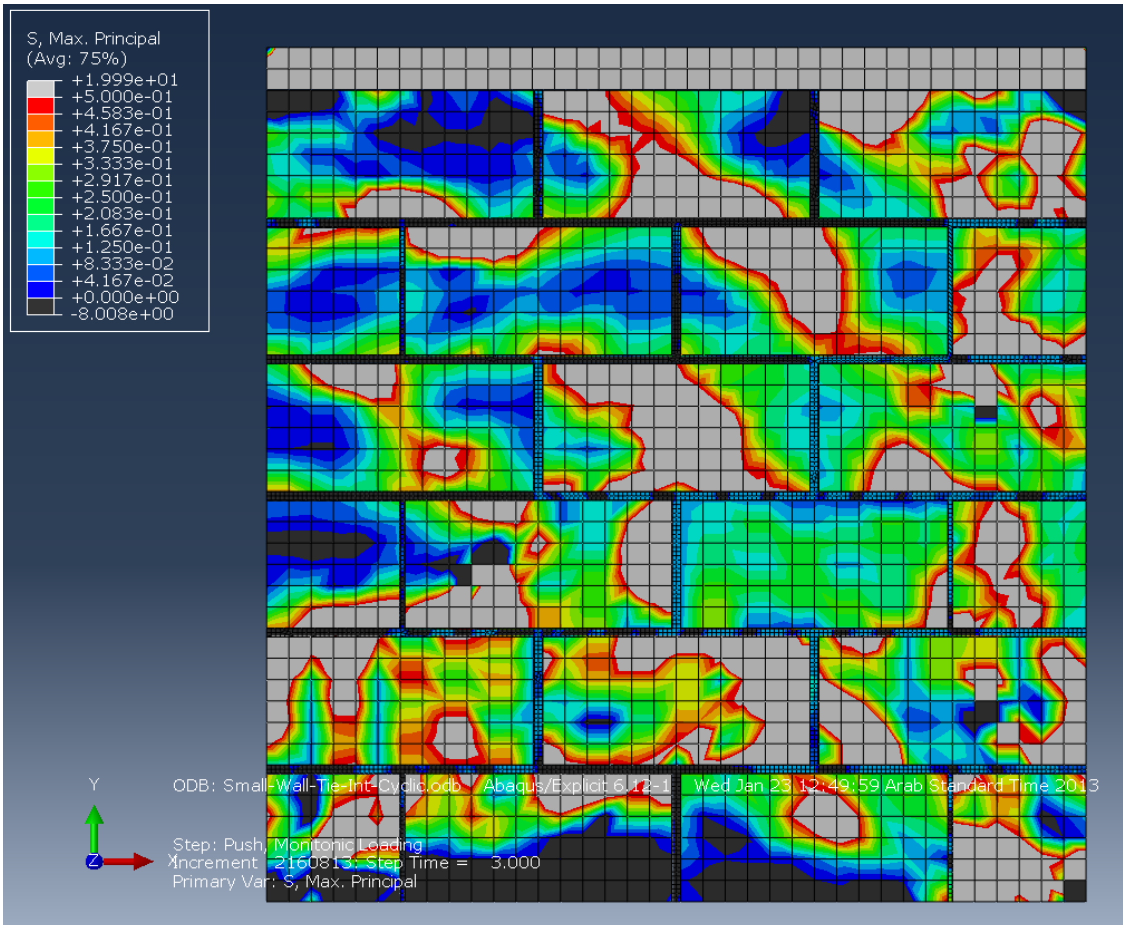

Figure A.7 Max principle Stress distribution at 3.0 time of lateral displacement (Pull, Third cycle)

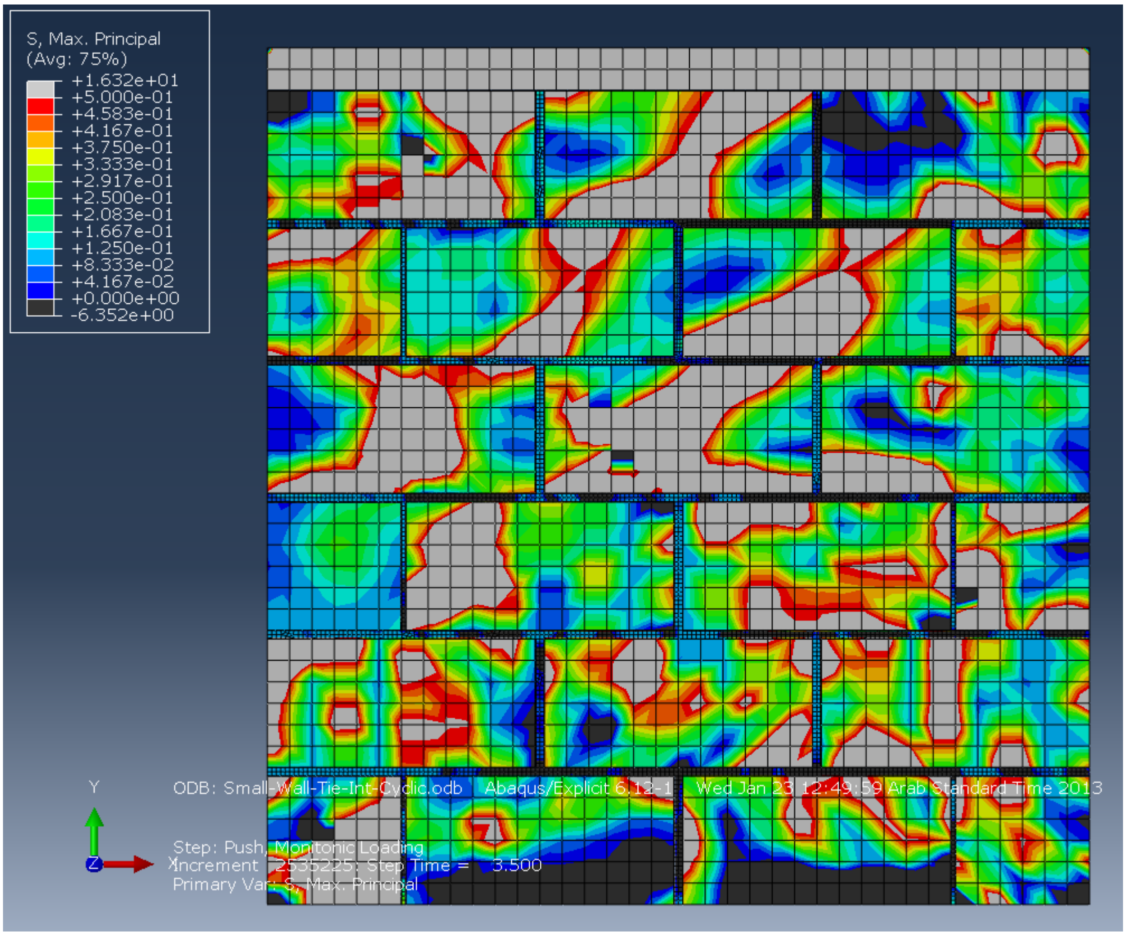

Figure A.8 Max principle Stress distribution at 3.5 time of lateral displacement (Push, fourth cycle)

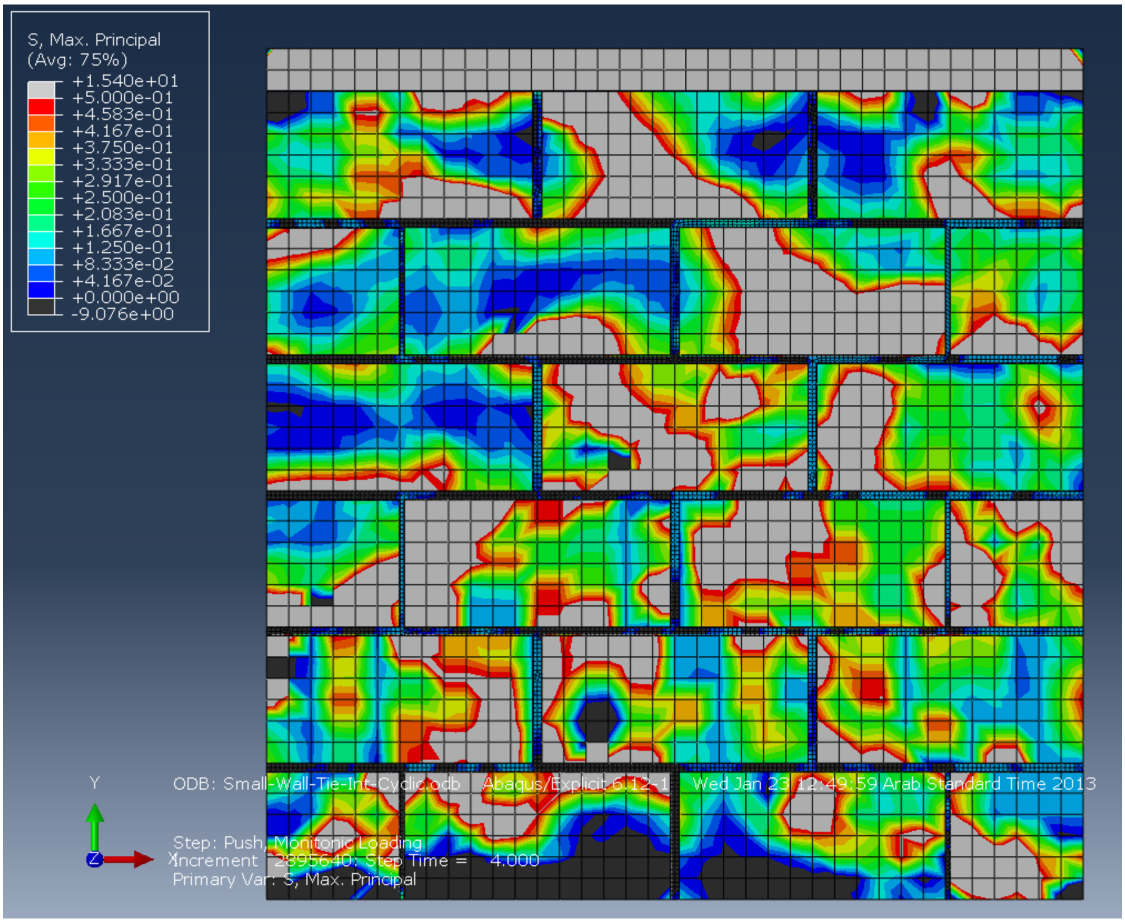

Figure A.9 Max principle Stress distribution at 4.0 time of lateral displacement (Pull, fourth cycle)

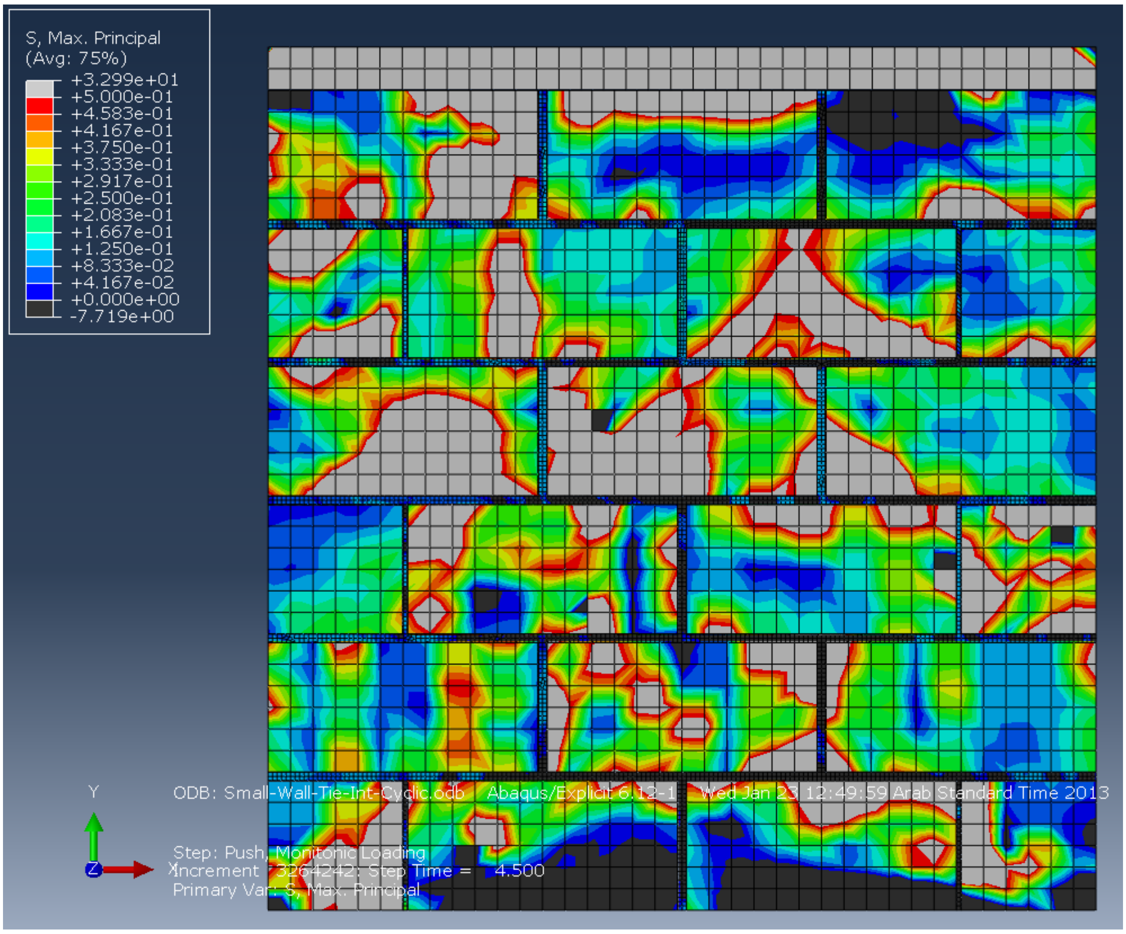

Figure A.10 Max principle Stress distribution at 4.5 time of lateral displacement (Push, fifth cycle)

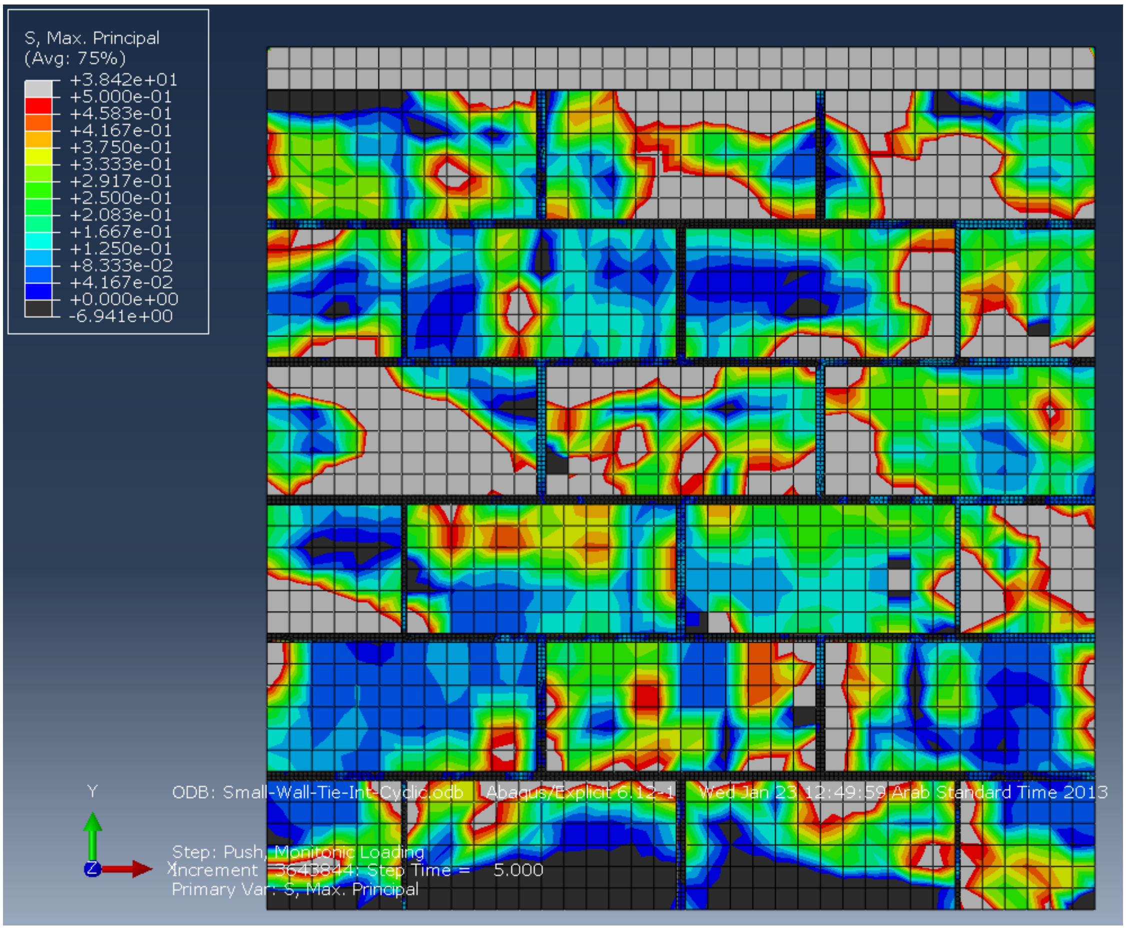

Figure A.11 Max principle Stress distribution at 5.0 time of lateral displacement (Pull, fifth cycle)

A.3 Stress Contour of Sandstone Wall With Different Axial Stress.

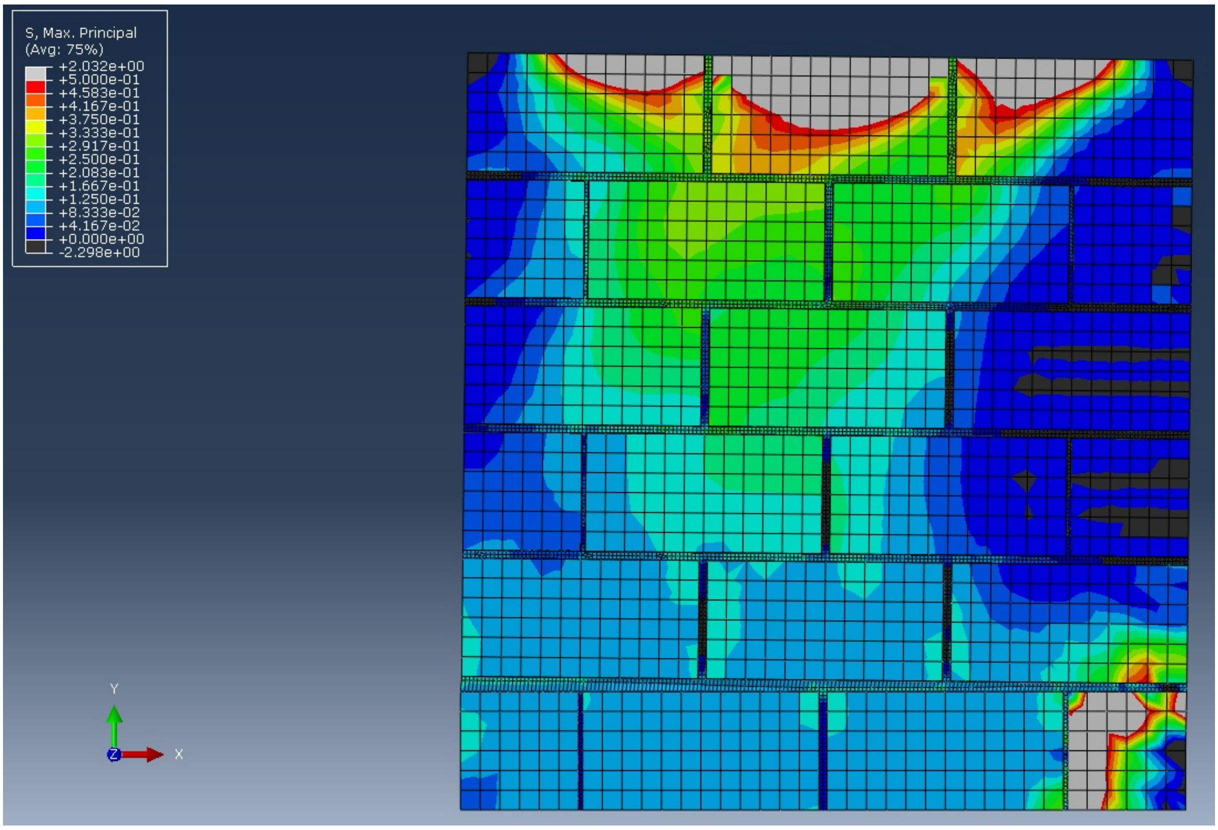

Figure A.12 Stress contours (0 Mpa Axial Stress) sandstone wall.

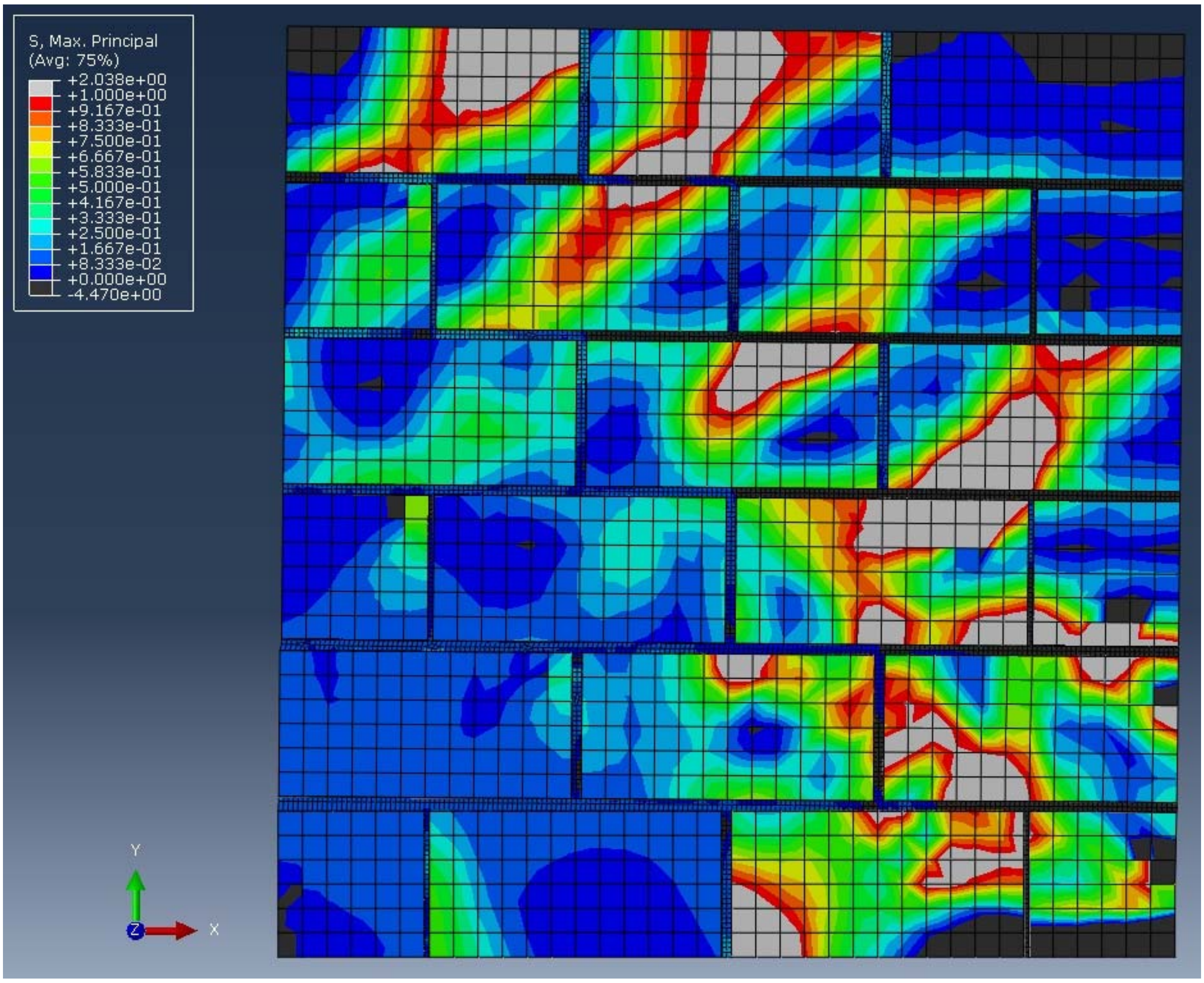

Figure A.13 Stress contours (2.0 MPa Axial Stress) sandstone wall

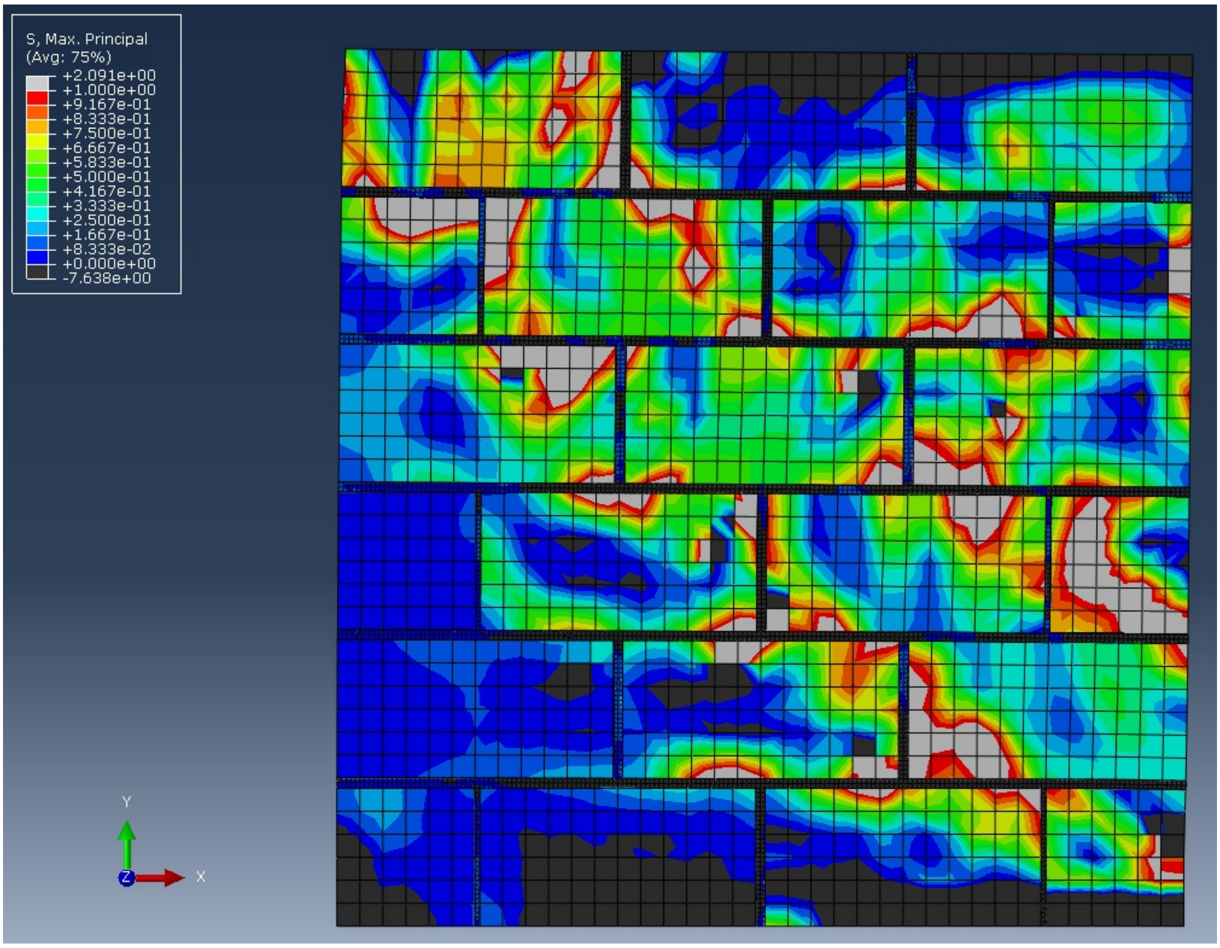

Figure A.14 Stress contours (4.0 MPa Axial Stress) sandstone wall

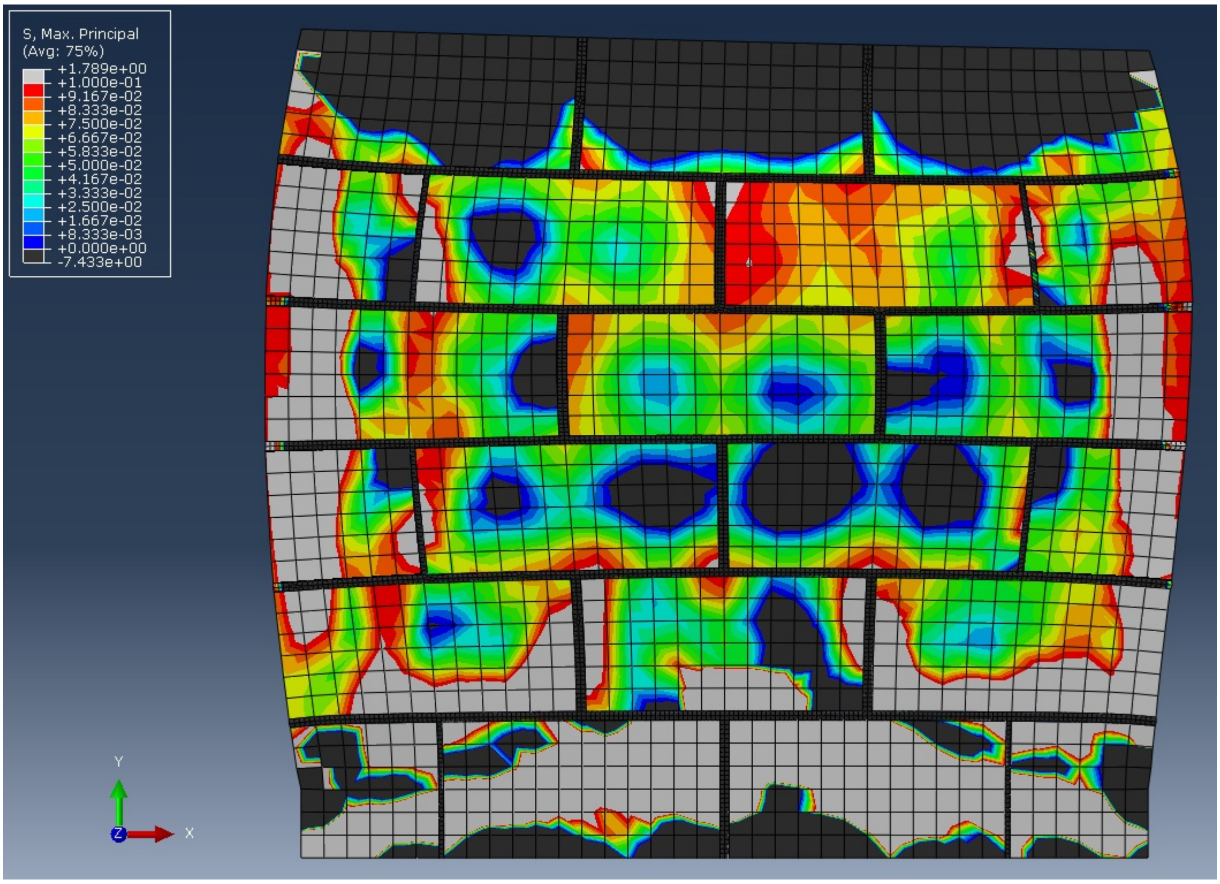

Figure A.15 Stress contours (15.0 MPa Axial Stress) sandstone wall

A.4 Stress Contour of Walls Tested by Demir (2012).

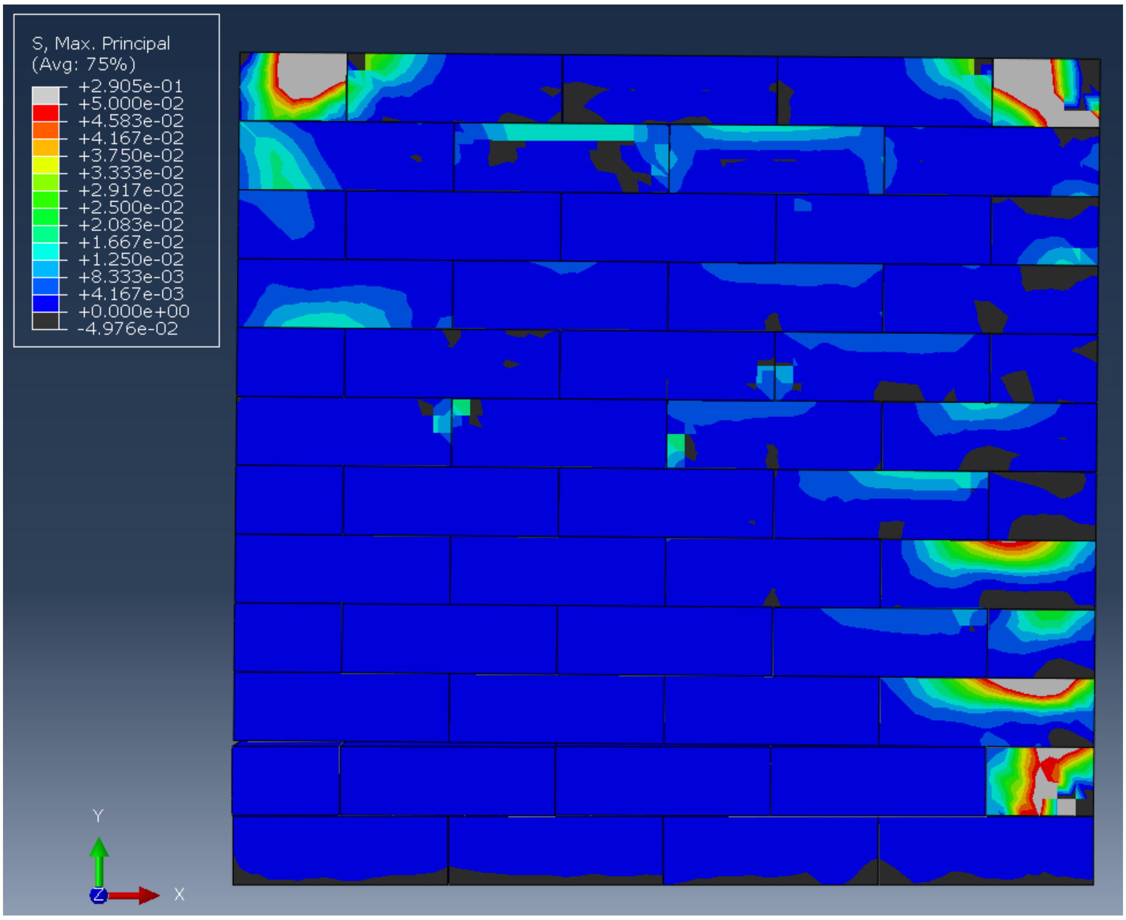

Figure A.16 Stress contours (0 MPa Axial Stress) Demier’s wall.

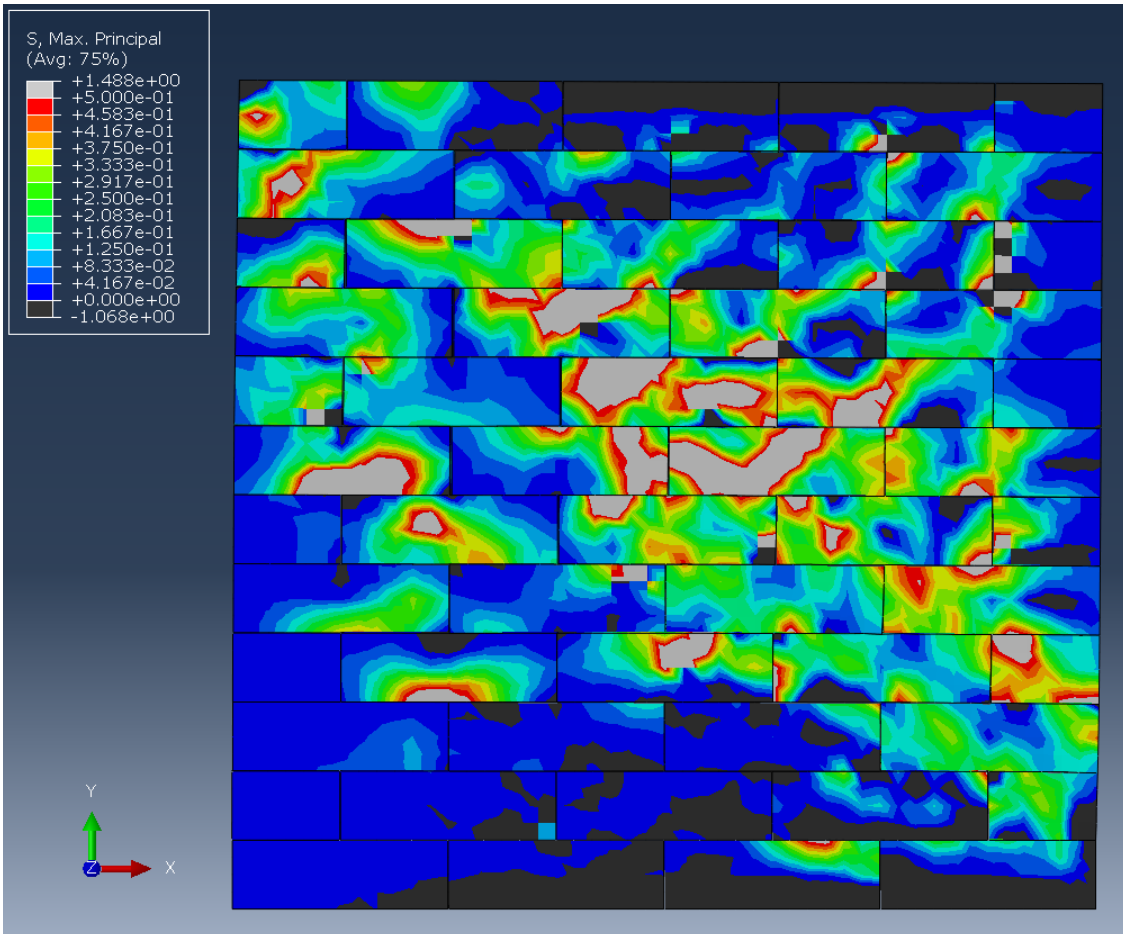

Figure A.17 Stress contours (1.0 MPa Axial Stress) Demier’s wall.

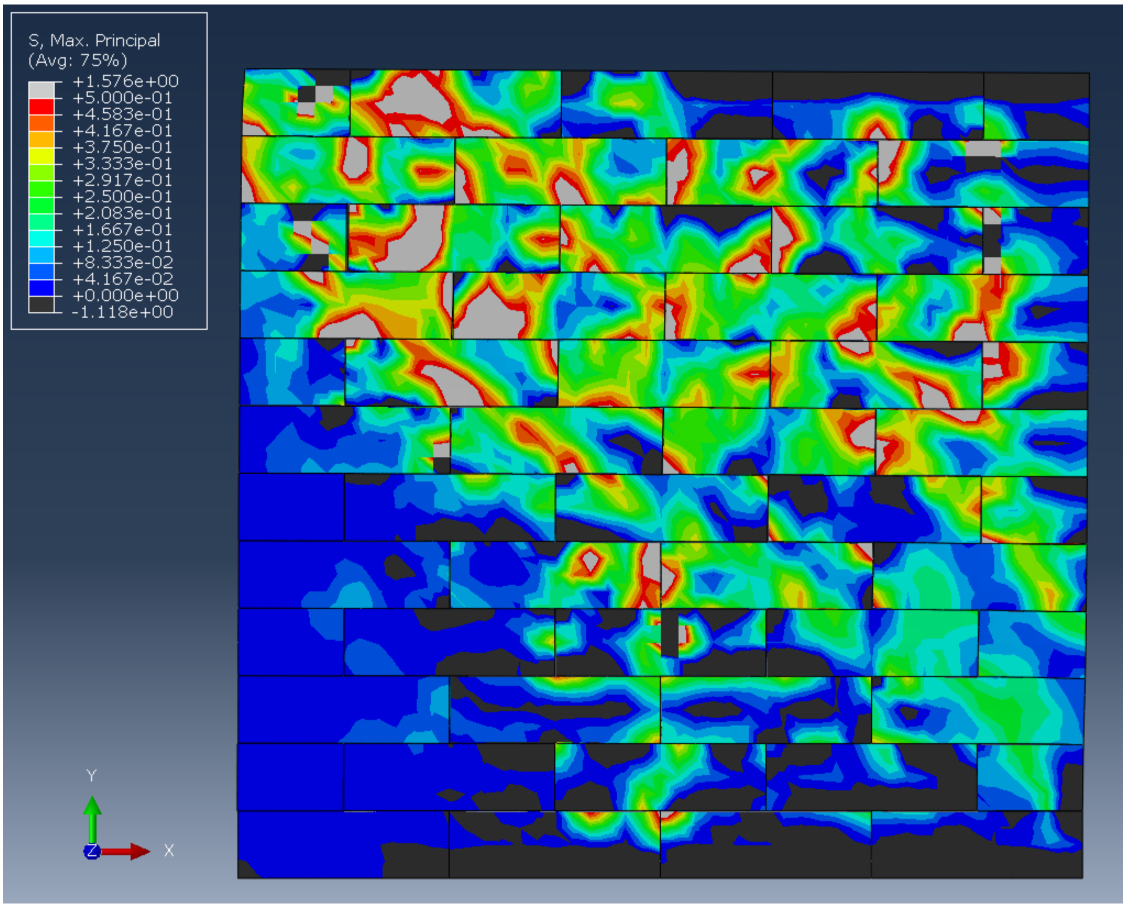

Figure A.18 Stress contours (2.0 MPa Axial Stress) Demier's wall.

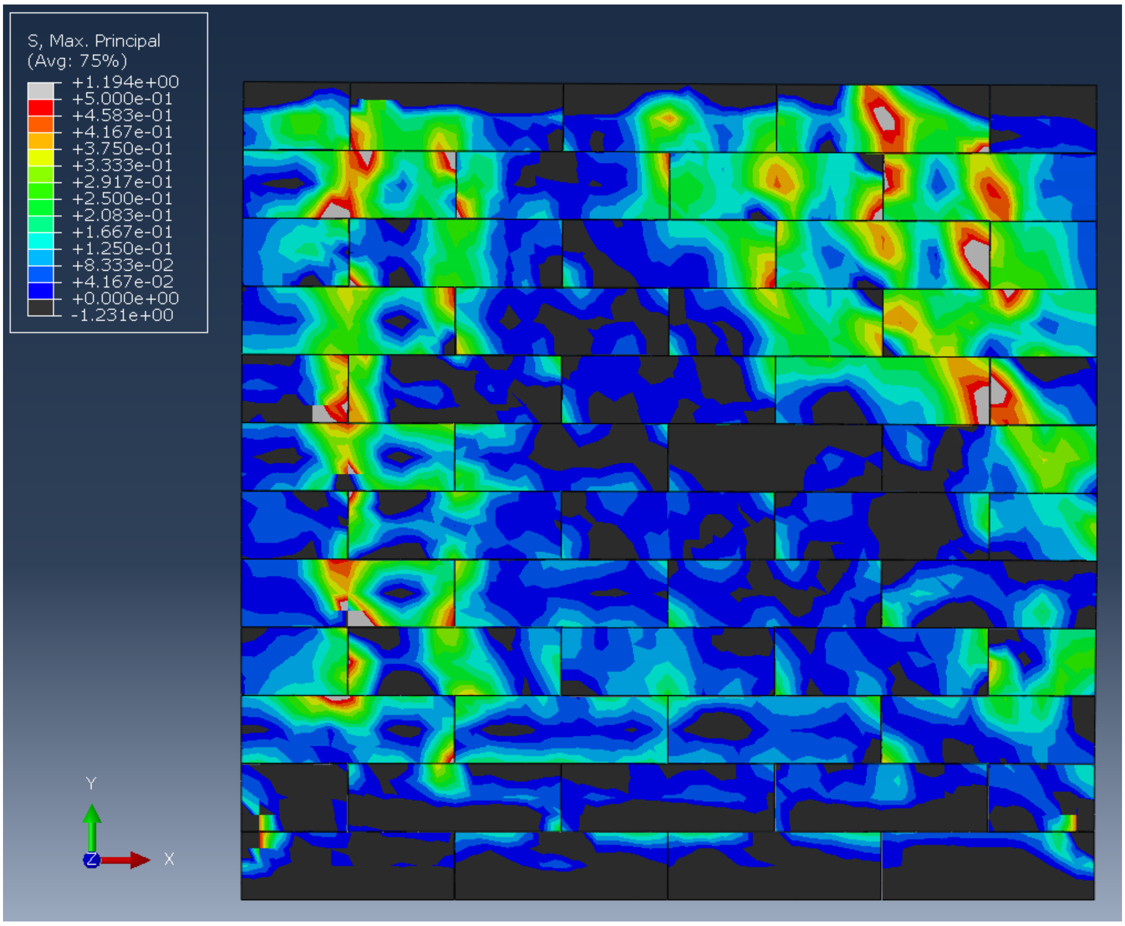

Figure A.19 Stress contours (4.0 MPa Axial Stress) Demier's wall.

A.5 Stress Contour of Wall Tested by Li (2005).

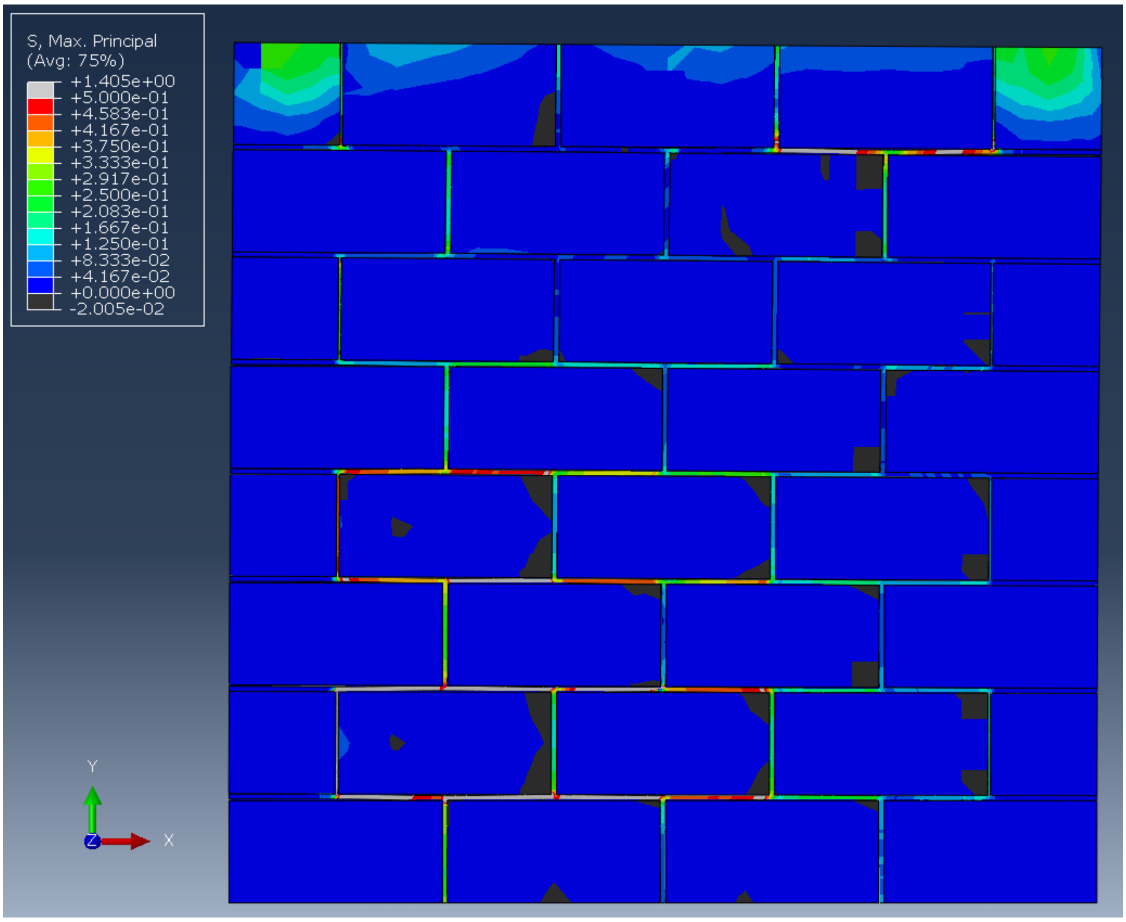

Figure A.20 Stress contours (0 MPa Axial Stress) Lee’s wall.

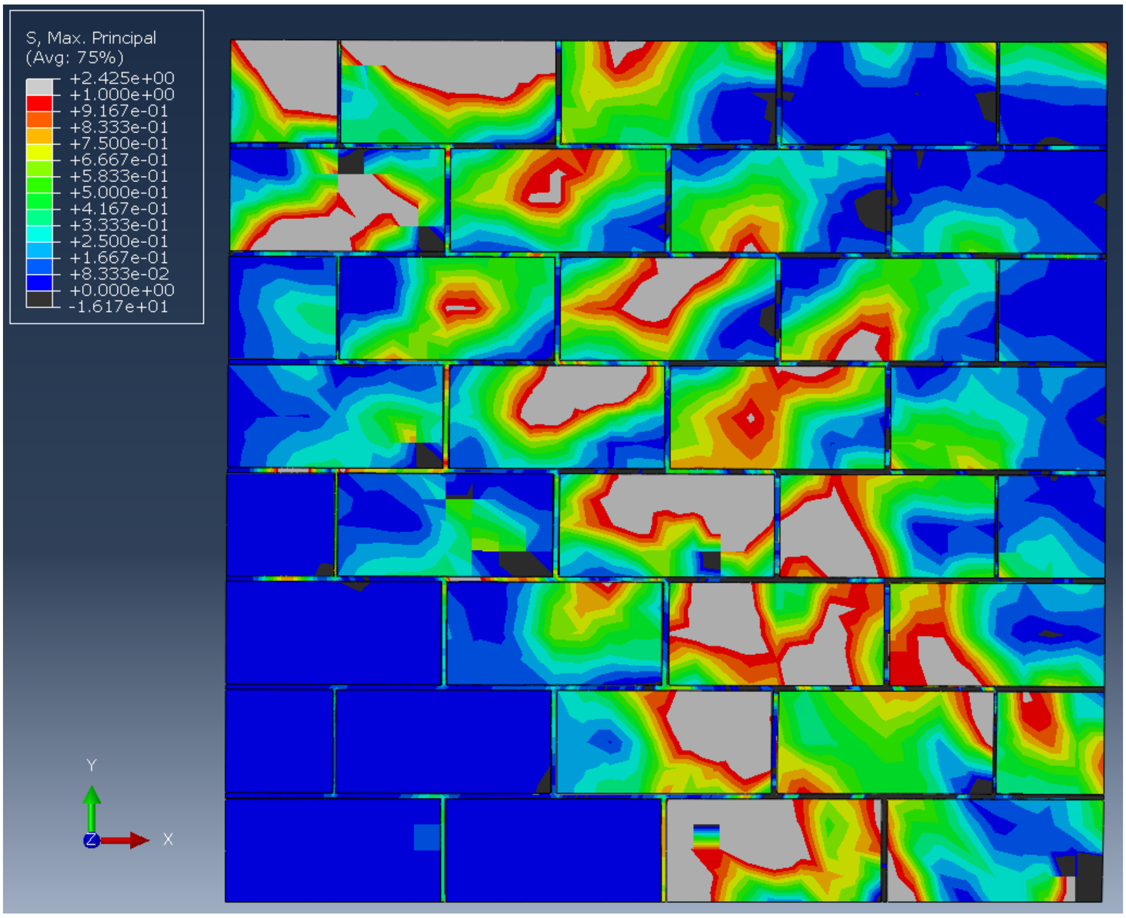

Figure A.21 Stress contours (2 MPa Axial Stress) Lee’s wall.

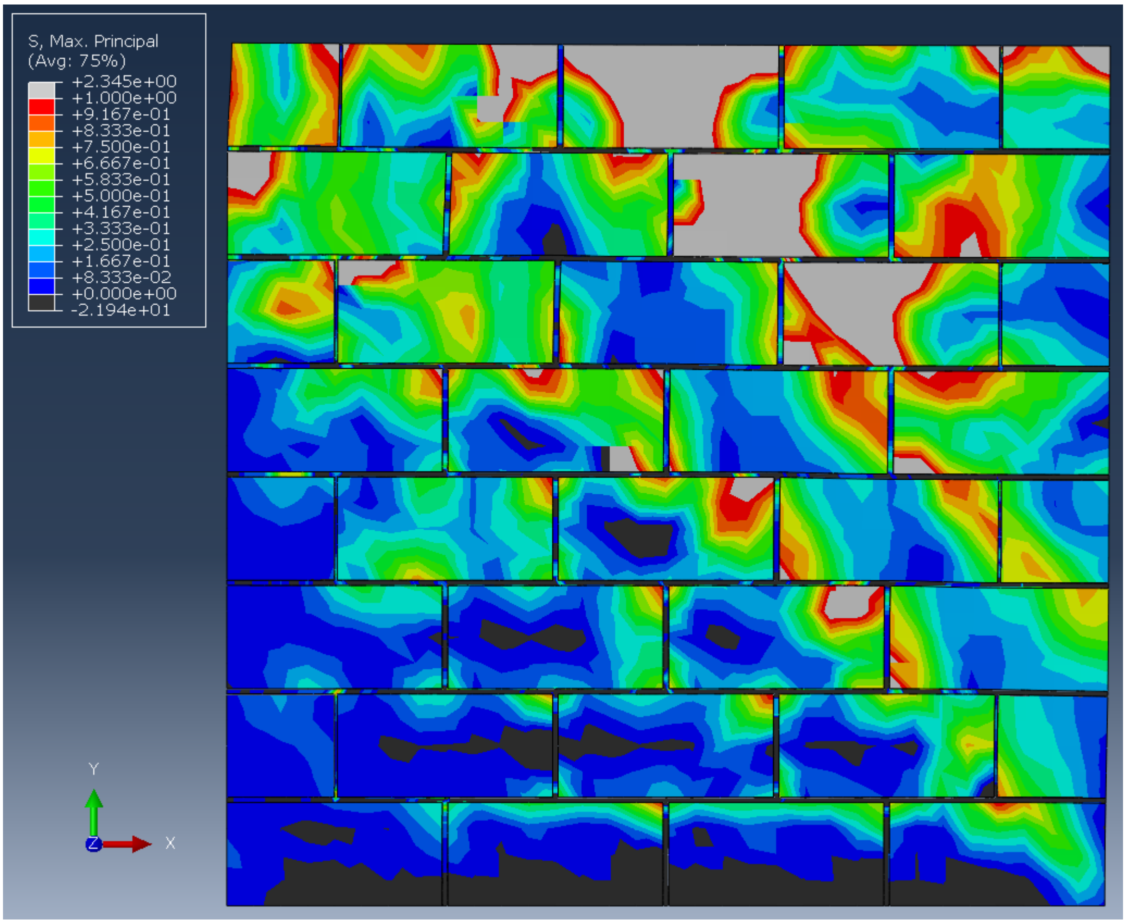

Figure A.22 Stress contours (4 MPa Axial Stress) Lee’s wall.

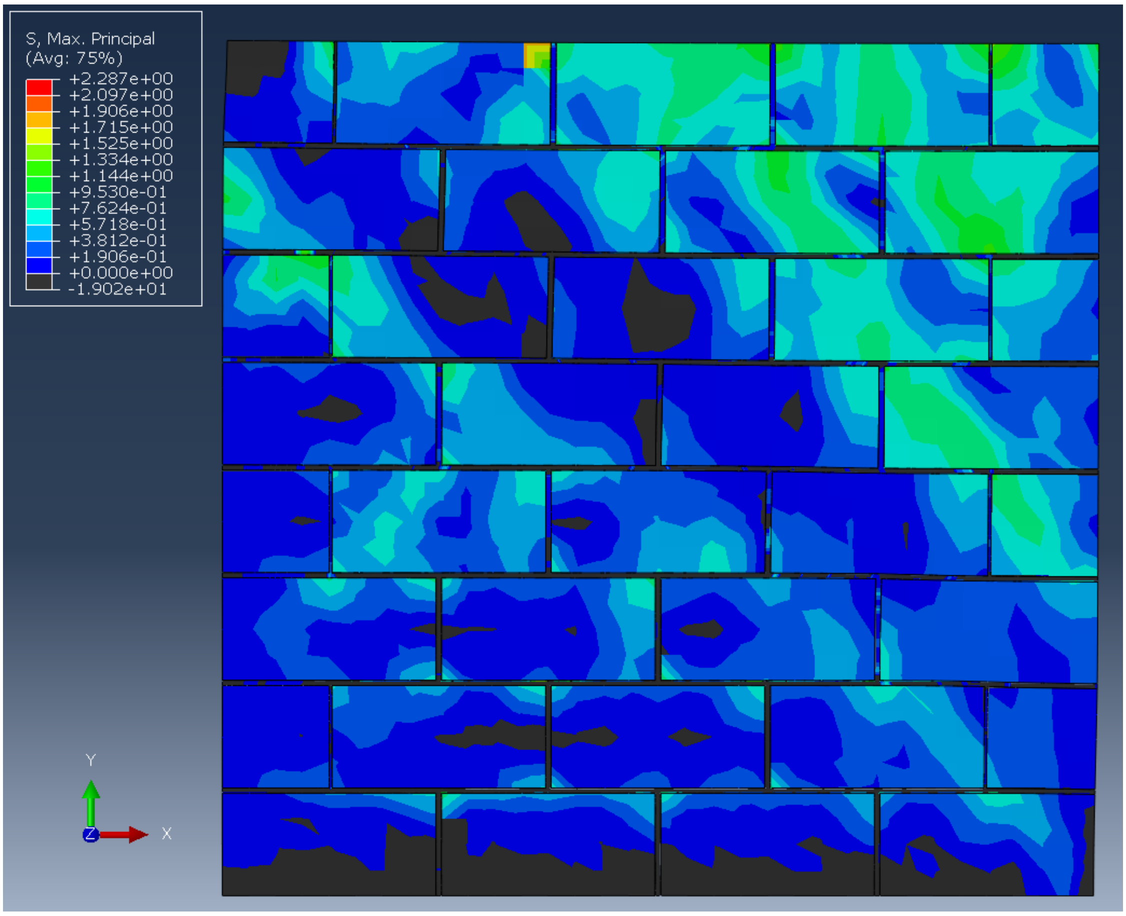

Figure A.23 Stress contours (6 MPa Axial Stress) Lee's wall

A.6 Stress Contour of Wall Tested by Vasconcelos (2005).

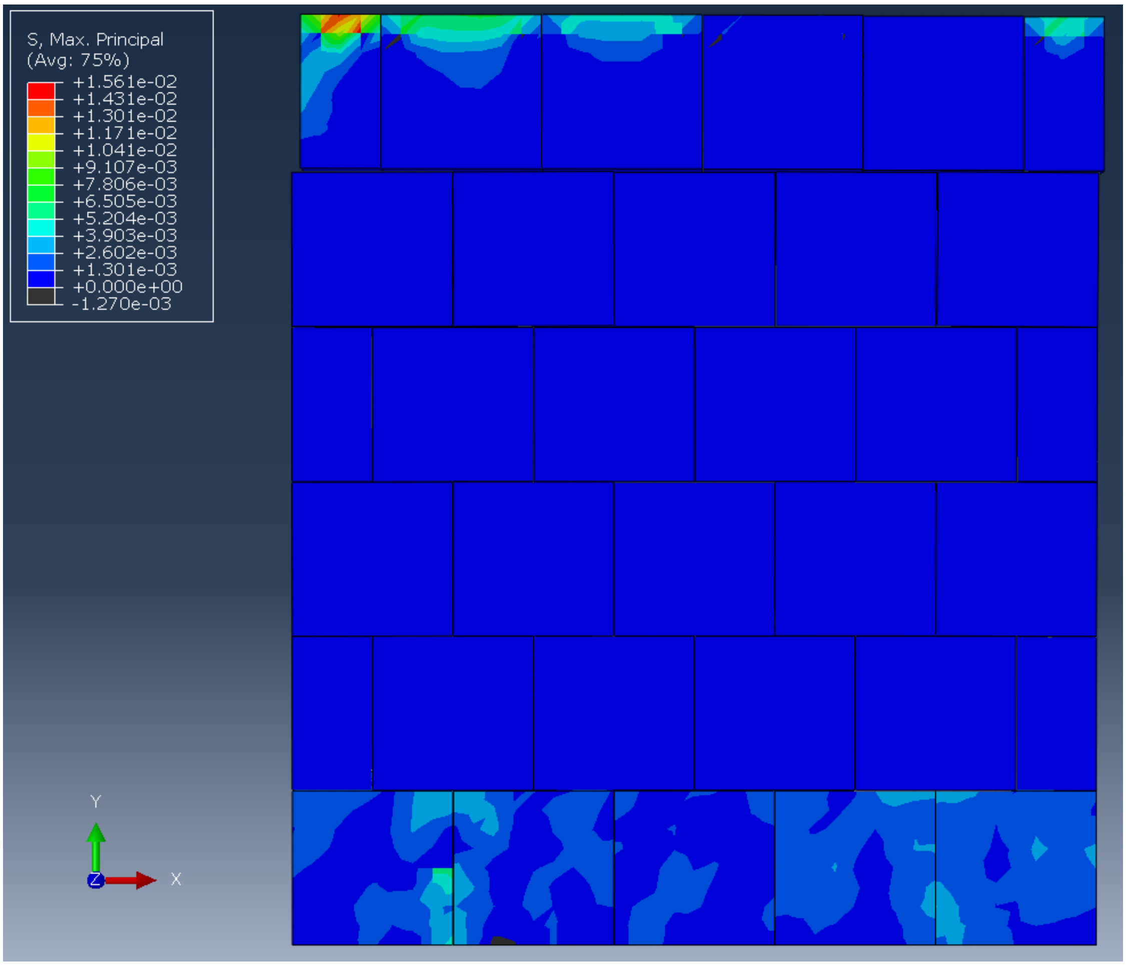

Figure A.24 Stress contours (0 MPa Axial Stress) Vasconselos wall.

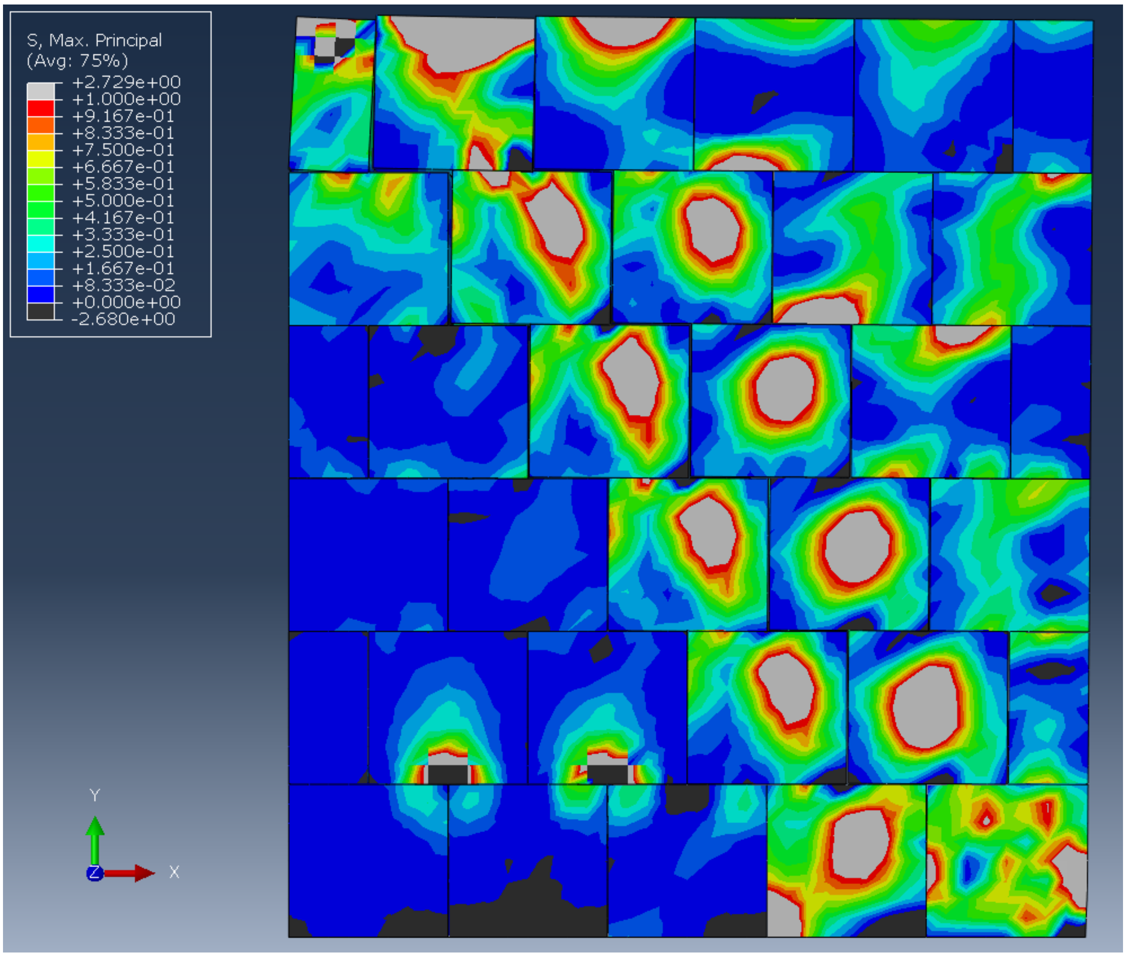

Figure A.25 Stress contours (2 MPa Axial Stress) Vasconselos wall.

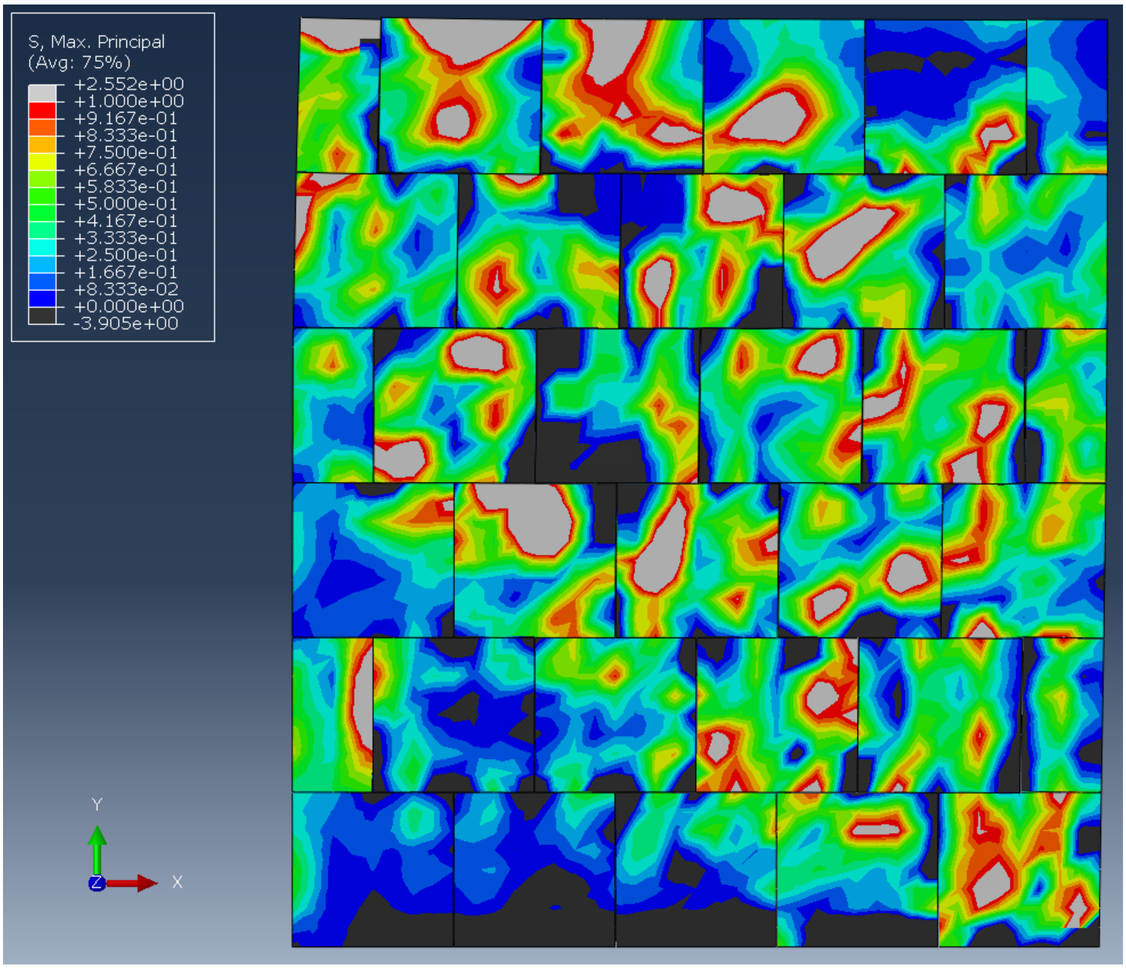

Figure A.26 Stress contours (6 MPa Axial Stress) Vasconselos wall.

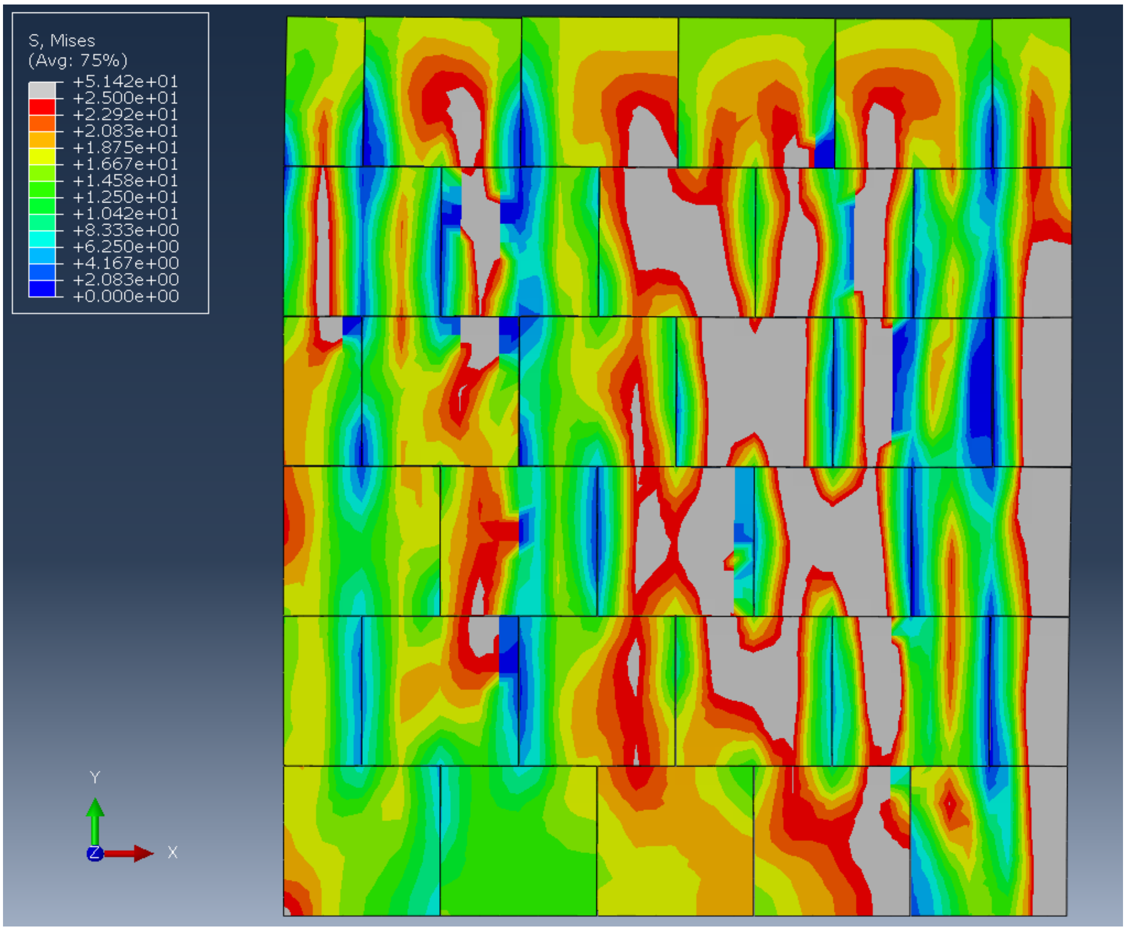

Figure A.27 Stress contours (16 MPa Axial Stress) Vasconselos wall.

References

[1] A. Gabor, E. Ferrier, E. Jacquelin, P. Hamelin “Analysis and modelling of the in-plane shear behavior of hollow brick masonry panels” journal of Construction and Building Materials, Vol. 20, No. 5, June 2006, 308–321

[2] A. Lucas & J. Harris ”Ancient Egyptian Materials and Industries”, Dover Publications, 4th edition, November 30, 2011.

[3] ABAQUS Theory Manual, version 6.12.

[4] Abrams, D. (2001), “Performance-Based Engineering Concepts for Unreinforced Masonry Building Structures”, Progress in Structural Engineering and Materials Journal, Elsevier, John Wiley & Sons, 3, 48-56.

[5] Al-Gohi, B., Rahman, M. K, and Baluch, M. H., “A Review of Seismic Retrofit of Masonry Walls”, Turkish Saudi Workshop on Structural and Earthquake Engineering, Istanbul, June, 2010.

[6] ACI Committee 440 (2002). Guide for the Design and Construction of Externally Bonded FRP Systems for Strengthening Concrete Structures (ACI440.2R-02), American Concrete Institute, Farmington Hills, Michigan, 45 pp.

[7] BS EN 459-1:2010 Building lime. Definitions, specifications and conformity criteria Supersedes BS EN 459-1:2001

[8] Basoenondo, E. A., “Lateral Load Response of Cikarang Brick Wall Structures-an Experimental Study”, PhD (2008) , Queensland University of Technology, Australia.

[9] Cem Demir” SEISMIC BEHAVIOUR OF HISTORICAL STONE MASONRY MULTI-LEAF WALLS “, PhD Dissertation. Turkey: Istanbul Technical University (ITU). 2012

[10] Crisafulli, F. J.; Carr, A. J.; and Park, R., "Shear Strength of Unreinforced Masonry Panels," Pacific Conference on Earthquake Engineering, Melbourne, Australia, Nov. 20-22, 1995, pp. 77-86.

[11] D.P.Abrams “Strength and behavior of unreinforced masonry elements” Earthquake Engineering, Tenth world Conference, 1992 Balkema, Rotterdam. ISBN 90 5410 060 5.

[12] Da Porto, F., Guidi, G., Garbin, E., and Modena, “In-Plane Behavior of Clay Masonry Walls: Experimental Testing and Finite-Element Modeling” Journal of Structural Engineering, Vol. 136, No. 11, November 1, 2010, 1379–1392

[13] Davies J., “Observation of Fracture Path Development in Mortar Beam Specimens”, Advn. Cem. Bas. Mat., 3(1996)31-36.

[14] Edgell, G. 2005: Edgell, G., Haseltine, B.A., "Building mortar for low rise housing recommendations, problems and solutions", British Masonry Society Publication, pp.29.

[15] Filiatrault, A., Uang, C., Folz, B., Chrstopoulos, C., and Gatto, K. (2001), “Reconnaissance Report of February 28, 2001 Nisqually (Seattle-Olympia) Earthquake”, Report No. SSRP-200102, Structural Systems Research Project, Dept. of Structural Engineering, University of California, San Diego, USA.

[16] Graça de Fátima Vasconcelos “Experimental investigations on the mechanics of stone masonry: Characterization of granites and behaviour of ancient masonry shear walls” PhD dissertation. Portugal: University of Minho; 2005. Available at http://www.civil.uminho.pt/masonry/.

[17] Green S.J., Swanson S.R., “Static Constitutive Relations for Concrete”, AWFLTR-72-244, U.S.Air Force Weapon Laboratory, Kirtland Air Force Base, NM, 1973.

[18] Geers M.G.D., Borst R. de, Peerlings R.H.J., “Damage and Crack Modelling in Single-Edge and Double-Edge Notched Concrete Beams”, Engineering Fracture Mechanics, 65(2000), 247-261.

[19] Haider. W., “Inplane Response of Wide Spaced Reinforced Masonry Shear Walls”, PhD, 2007, Central Queensland University, Australia

[20] Haach, V. G., “Development of a Design Method for Reinforced Masonry Subjected to In-Plane Loading Based on Experimental and Numerical Analysis”, PhD (2009), University do Minho, Portugal.

[21] Jankowiak, T., Lodygowski, T., “Identification of Parameters of Concrete Damage Plasticity Constitutive Model”, Publishing House of Poznan University of Technology, Poznań, Poland, 2005, ISSN 1642-9303.

[22] Kmiecik, P., Kamiński, M., “Modelling of Reinforced Concrete Structures and Composite Structures with Concrete Strength Degradation Taken Into Consideration”, Wrocław University of Technology, Wybrzeże Wyspiańskiego 25, 50-370 Wrocław, Poland, 2011.

[23] Krit Chaimoon, Mario M. Attard “Modeling of unreinforced masonry walls under shear and compression”, Engineering Structures, Volume 29, Issue 9, September 2007, Pages 2056–2068.

[24] Kiarash, M. D., “Computational, Analytical and Experimental Modeling of Masonry Structures”, PhD, 2012, State University of New York at Buffalo.

[25] Kachanov,L.,M., Introduction to Continuum Damage Mechanics, Springer; 1986 Edition.

[26] Kupfer H., Hilsdorf H.,K., Rusch H., “Behavior of Concrete Under Biaxial Stresses”, ACI Journal, 65, 8(1979), pp. 656-666.

[27] Lourenço PB. “A user/programmer's guide for the micro-modelling of masonry structures”, Relatório no 03.21.1.31.35. Universidade Técnica de Delft. Delft, Países Baixos e Universidade do Minho. Guimarães (Portugal); 1996.

[28] Lourenco, P. B. , “Computational Strategies for Masonry Structures”, PhD (1996), Delft University of Technology, Netherlands.

[29] Lubliner, J., Oliver, J., Oller, S., and Oñate, E., “A Plastic-Damage Model for Concrete”, International Journal of Solids and Structures, V. 25, No. 3, pp. 299-326, 1989.

[30] Lee, J. and Fenves, G.L., “Plastic-Damage Model for Cyclic Loading of Concrete Structures”, Journal of Engineering Mechanics, ASCE, V. 124, No. 8, pp. 892-900, 1998.

[31] Li, T., Galati, N., Tumialan, G., and Nanni, A., “Analysis of Unreinforced Masonry Concrete Walls Strengthened with Glass Fiber-Reinforced Polymer Bars”, Structural Journal, Vol 102, No. 4, July 1, 2005, pp. 569-577.

[32] Mann, W., and Miller, H., "Failure of Shear-Stressed Masonry- An Enlarged Theory, Tests and Application to Shear Walls", Proceedings of the British Ceramic Society, V. 30, 1982, pp. 223-235.

[33] MM Attard, A Nappi, F Tin-Loi (2007) Modelling fracture in masonry, Journal of Structural Engineering 133: 1385-1392.

[34] Paul T. Nicholson, & Ian Shaw Ian Shaw "Ancient Egyptian Materials and Technology", Cambridge University Press; 1 edition (October 1, 2009)

[35] Paulay, T., and Priestley, M.J.N. (1992). "Seismic Design of Reinforced Concrete and Masonry Buildings", John Wiley & Sons, Inc., New York, 744 pp.

[36] R. Senthivel, P.B. Lourenço "Finite element modelling of deformation characteristics of historical stone masonry shear walls" Journal of Engineering Structure, Vol. 31, No. 9, September 2009, pp. 1930-1943.

[37] Rabotnov Y.N., "Creep Problems in Structural Members", North-Holland, Amsterdam, 1969.

[38] Schlangen, E., "Experimental and Numerical Analysis of Fracture Processes in Concrete", Ph.D. Thesis, Delft University of Technology, 1993.

[39] Senthivel, R., Lourenço P. B. "Finite Element Modelling of Deformation Characteristics of Historical Stone Masonry Shear Walls", Journal of Engineering Structures, Vol. 31, No. 9, September 2009, pp. 1930-1943.

[40] SikaWrap®-230C, Product Data Sheet.

[41] Vasconcelos, G. F., "Experimental Investigations on the Mechanics of Stone Masonry: Characterization of Granites and Behaviour of Ancient Masonry

Shear Walls", PhD dissertation. Portugal: University of Minho; 2005. Available at http://www.civil.uminho.pt/masonry/.

[42] Voon, K. C., "In-Plane Seismic Design of Concrete Masonry Structures", PhD (2007), University of Auckland, New Zealand.

[43] Yi, T "Experimental Investigation and Numerical Simulation of an Unreinforced Masonry Structure with Flexible Diaphragms" PhD (February 2009), Georgia Institute of Technology, USA.

Vitae

Name :Basheer Hasan Ali Al-Gohi

Nationality :Yemeni

Date of Birth :7/9/1976

Email :basheer_algohi@hotmail.com

:algohi@kfupm.edu.sa

Address :Ibb City, Taiz Street, Yemen

Academic Background :PhD in Civil Engineering , King Fahd University of Petroleum and Minerals (KFUPM), Dhahran, Saudi Arabia.

:M.S in Civil Engineering , King Fahd University of Petroleum and Minerals (KFUPM), Dhahran, Saudi Arabia.

:B.S in Civil Engineering, Alanbar University , Al-Ramadi, Alanbar, Iraq